Thermal Dynamic Imaging and Thermal Management for Quantum Cascade Lasers

by

Siyi Wang

A thesis
presented to the University of Waterloo
in fulfillment of the
thesis requirement for the degree of
Doctor of Philosophy
in
Electrical and Computer Engineering (Nanotechnology)

Waterloo, Ontario, Canada, 2022

© Siyi Wang 2022

Examining Committee Membership

The following served on the Examining Committee for this thesis. The decision of the Examining Committee is by majority vote.

External Examiner: Qiying Chen
Professor, Dept. of Physics and Physical Oceanography,
Memorial University of Newfoundland

Supervisor(s): Dayan Ban
Professor, Dept. of Electrical and Computer Engineering,
University of Waterloo

Internal Member: Bo Cui
Professor, Dept. of Electrical and Computer Engineering,
University of Waterloo

Youngki Yoon
Associate Professor, Dept. of Electrical and Computer Engineering,
University of Waterloo

Internal-External Member: Jonathan Baugh
Professor, Dept. of Chemistry, Institute for Quantum Computing,
University of Waterloo

Author's Declaration

This thesis consists of material all of which I authored or co-authored: see Statement of Contributions included in the thesis. This is a true copy of the thesis, including any required final revisions, as accepted by my examiners.

I understand that my thesis may be made electronically available to the public.

Statement of Contributions

Chapter 3 of this thesis consists of a paper [Siyi Wang *et al.*, "Thermal dynamic imaging of mid-infrared quantum cascade lasers with high temporal–spatial resolution," *Journal of Applied Physics* 128(8), 083106 (2020)] that was co-authored by Siyi Wang (1st author), Dr. Chao Xu (former Ph.D. student), Dr. Fei Duan (former Ph.D. student), Dr. Boyu Wen (former Ph.D. student), Dr. S. M. Shazzad Rassel (Post-doc fellow), Dr. Man Chun Tam (former Ph.D. student), Dr. Zbigniew Wasilewski (Professor), Dr. Lan Wei (Professor), and Dr. Dayan Ban (Professor, my supervisor). Siyi Wang developed and documented the methodology, conducted device fabrication, data acquisition, analysis, and manuscript drafting. Dr. Chao Xu assisted in L-I-V measurement setup, device fabrication, thermal simulation, and manuscript revision. Dr. Fei Duan assisted in data acquisition on TDTR imaging system. Dr. Boyu Wen assisted in data acquisition on laser spectrum by FTIR measurements. Dr. S. M. Shazzad Rassel assisted in data acquisition on L-I-V measurements. Dr. Man Chun Tam conducted the epitaxial growth on MIR QCLs (wafer#: G0241) by MBE. Dr. Zbigniew Wasilewski supervised on MBE growth. Dr. Lan Wei supervised the TDTR imaging system. Dr. Dayan Ban (my supervisor) assisted in manuscript revision and provided funding resources. This work has also been presented on a conference [Siyi Wang *et al.*, "Time resolved Thermoreflectance Imaging for Mid infrared Quantum Cascade Laser," *CLEO: Applications and Technology*, JTu2G. 2, San Jose, CA, USA (May 2020)].

Part of the contents in chapter 4 has been published and presented on a conference [Siyi Wang *et al.*, "Localized Facet Joule Heating of Mid-infrared Quantum Cascade Lasers," *Photonics North 2022*, Niagara Falls, Canada, 24-26 May 2022.]. This work was co-authored by Siyi Wang (1st author), Dr. Chao Xu (former Ph.D. student), Dr. Zbigniew Wasilewski (Professor), and Dr. Dayan Ban (Professor, my supervisor). Siyi Wang developed and documented the methodology, conducted device fabrication, data acquisition, analysis, and manuscript drafting. Dr. Chao Xu assisted in device fabrication and advised on methodology. Dr. Zbigniew Wasilewski supervised on MBE growth. Dr. Dayan Ban (my supervisor) assisted in manuscript revision and provided funding resources.

Chapter 5 has been incorporated within a manuscript that has been accepted for publication [Siyi Wang *et al.*, "Visualization of Localized Facet Joule Heating induced Optical Degradation on Mid-infrared Quantum Cascade Lasers"] on *Optics Express* (Manuscript Accepted, Oct-27-2022). This manuscript was co-authored by Siyi Wang (1st author), Dr. Chao Xu (former Ph.D. student), Dr. Man Chun Tam (former Ph.D. student), Ms. Kailyn Vaillancourt (Undergraduate Research Assistant), Dr.

Zbigniew Wasilewski (Professor), Dr. Lan Wei (Professor), and Dr. Dayan Ban (Professor, my supervisor). Siyi Wang developed and documented the methodology, conducted device fabrication, data acquisition, analysis, and manuscript drafting. Dr. Chao Xu assisted in device fabrication and advised on methodology and manuscript drafting. Ms. Kailyn Vaillancourt assisted in conceptual visualization and manuscript editing. Dr. Man Chun Tam conducted the epitaxial growth on MIR QCLs (wafer#: G0241) by MBE. Dr. Zbigniew Wasilewski supervised on MBE growth. Dr. Lan Wei supervised the TDTR imaging system. Dr. Dayan Ban (my supervisor) assisted in manuscript revision and provided funding resources.

Part of the contents in chapter 6 has been published and presented on a conference [Siyi Wang *et al.*, "Heterogeneous integration of transfer bonded terahertz quantum cascade lasers for improved heat management and light coupling," *Optoelectronic Devices and Integration X*. Vol. 11894. 118941J, *SPIE* (October 2021)]. This work was co-authored by Siyi Wang (1st author), Dr. Chao Xu (former Ph.D. student), Dr. Zbigniew Wasilewski (Professor), and Dr. Dayan Ban (Professor, my supervisor). Siyi Wang developed and documented the methodology, conducted device fabrication, data acquisition, analysis, and manuscript drafting. Dr. Chao Xu assisted in device fabrication, simulation, and advised on methodology. Dr. Zbigniew Wasilewski supervised on MBE growth (wafer#: G0226, G0312, and G0405). Dr. Dayan Ban (my supervisor) assisted in manuscript revision and provided funding resources.

Publications relevant to this thesis during the Ph.D. program are listed below.

Journal Articles

[1] **Siyi Wang**, Chao Xu, Man Chun Tam, Kailyn Vaillancourt, Zbigniew Wasilewski, Lan Wei, and Dayan Ban, "Visualization of Localized Facet Joule Heating induced Optical Degradation on Mid-infrared Quantum Cascade Lasers," *Optics Express* (Manuscript Accepted, October 2022).

[2] **Siyi Wang**, Siyi Wang, Chao Xu, Fei Duan, Boyu Wen, S.M. Shazzad Rassel, Man Chun Tam, Zbigniew Wasilewski, Lan Wei, and Dayan Ban, "Thermal dynamic imaging of mid-infrared quantum cascade lasers with high temporal–spatial resolution," *Journal of Applied Physics* 128(8), 083106 (2020).

[3] Fei Duan, Kai Chen, **Siyi Wang**, Lan Wei, Yonglin Yu, and Dayan Ban, "Temperature profile and transient response of thermally tunable ridge waveguides with laterally supported suspension," *Applied Physics Letters* 116(1), 011102 (2020).

[4] Boyu Wen, Chris Deimert, **Siyi Wang**, Chao Xu, S.M. Shazzad Rassel, Zbigniew Wasilewski, and Dayan Ban, "Six-level hybrid extraction/injection scheme terahertz quantum cascade laser with suppressed thermally activated carrier leakage," *Optics Express* 28(18), 26499-26508 (2020).

[5] Boyu Wen, Chao Xu, **Siyi Wang**, Kaixi Wang, Man Chun Tam, Zbigniew Wasilewski, and Dayan Ban, "Dual-lasing channel quantum cascade laser based on scattering-assisted injection design," *Optics Express*, 26(7), 9194-9204 (2018).

Conference Proceedings

[1] **Siyi Wang**, Chao Xu, Zbigniew Wasilewski, and Dayan Ban**,** "Localized Facet Joule Heating of Mid-infrared Quantum Cascade Lasers," *2022 Photonics North (PN)*, IEEE, 2022.

[2] **Siyi Wang**, Chao Xu, Zbigniew Wasilewski, and Dayan Ban**,** "Heterogeneous integration of transfer bonded terahertz quantum cascade lasers for improved heat management and light coupling," *Optoelectronic Devices and Integration X*, (Vol. 11894, pp. 158-165), SPIE, October 2021.

[3] **Siyi Wang**, Chao Xu, Fei Duan, Boyu Wen, S.M. Shazzad Rassel, Zbigniew Wasilewski, Lan Wei, and Dayan Ban, "Time resolved Thermoreflectance Imaging for Mid infrared Quantum Cascade Laser," *CLEO: Applications and Technology*, pp. JTu2G-2, Optical Society of America, 2020.

[4] Chao Xu, **Siyi Wang**, HoSung Kim, Zbigniew Wasilewski and Dayan Ban, "A 3.3 THz Patch Antenna Terahertz Photodetector," *2019 Infrared Terahertz Quantum Workshop (ITQW 2019)*, Ojai, CA, USA, 15-20 September 2019.

[5] Boyu Wen, Chao Xu, **Siyi Wang**, S.M. Shazzad Rassel, Chris Deimert, Zbigniew Wasilewski, Dayan Ban, "Novel 4-well THz QCL with double injection/extraction channels," *2019 Infrared Terahertz Quantum Workshop (ITQW 2019)*, Ojai, CA, USA, 15-20 September 2019.

[6] Boyu Wen, Chao Xu, **Siyi Wang**, Kaixi Wang, Man Chun Tam, Zbigniew Wasilewski, and Dayan Ban, "Lasing channels switching in dual color scattering assisted THz quantum-cascade laser," *The 14th International Conference On intersubband Transition in Quantum Wells*, Sands Expo and Convention Center, Singapore, 11-15 September 2017.

[7] Boyu Wen, Chao Xu, **Siyi Wang**, Kaixi Wang, Man Chun Tam, Zbigniew Wasilewski, and Dayan Ban, "Scattering Assisted dual color THz quantum cascade laser operating up to 144 K with large dynamic range," *The 18th Canadian Semiconductor Science and Technology Conference*, Waterloo, Ontario, Canada, 24-27 August 2017.

[8] Xiaoliang He, **Siyi Wang**, Seyed Ghasem Razavipour, Guocheng Liu, Chao Xu, Boyu Wen, Alam Mahmud, Denise Gosselink, Man Chun Tam, Zbigniew Wasilewski, and Dayan Ban, "Characterization for mid-infrared quantum cascade lasers operating up to 350 K on pulse-mode," *Canadian Semiconductor Science and Technology Conference* Waterloo, Ontario, Canada, 24-27 August 2017.

[9] Chao Xu, **Siyi Wang**, Boyu Wen, Xiaoliang He, Yue Zhuo, Denise Gosselink, Man Chun Tam, Zbigniew Wasilewski, and Dayan Ban, "Broad-band Terahertz Quantum Cascade Lasers," *The 18th Canadian Semiconductor Science and Technology Conference*, Waterloo, Ontario, Canada, 24-27 August 2017.

Abstract

Recent advances in quantum cascade lasers (QCLs) development are pushing lasing performance towards higher output power, higher operating temperature, and higher wall-plug efficiency (WPE). However, Joule heating and insufficient heat dissipation are the main issues limiting QCLs towards higher lasing performance, especially when the devices are operating on continuous-wave (cw) mode. For mid-infrared (MIR) QCLs, although the record high WPE has been achieved up to 31% on pulsed mode and 22% on cw mode at room temperature (RT), the devices still emit more heat than light. For terahertz (THz) QCLs, the maximum operating temperature (T_{max}) on cw mode is 129 K, much lower than 250 K, the T_{max} on pulsed mode operation. As a result, to understand the thermal dynamics and to optimize the thermal management to further improve QCLs lasing performance are highly requisite.

In order to better understand the internal heat dynamics of such laser devices, it is requisite to directly observe the transient temperature profile on device's active region (MQWs heterostructure), where heat is generated and dissipated in the surrounding medium, providing insights based on where the best strategy on device thermal management can be found. However, early works on direct observations of temperature imaging profiles on QCLs are still insufficient and limited by accurately monitoring the thermal dynamics in high spatial and temporal resolution simultaneously. Recently, CCD-based time-domain thermoreflectance (TDTR) microscopy have been employed to monitor pulse injected MIR QCLs. This technique provides a non-intrusive methodology capable of measuring real-time two-dimensional (2D) temperature profiles measurements with high temporal and spatial resolution simultaneously.

In this study, a series of transient temperature imaging profiles of an actively biased ridge-waveguide MIR QCL were obtained with ultrafast temporal resolution down to 50 ns and sub-micrometer spatial resolution down to 390 nm simultaneously at RT. This study reveals that heat accumulates and temperature starts to rise in device's active region up to ~100 degree above RT within 500 ns under a short pulsed high current injection (~112W of peak power injection, I=6A, V=18.7V). Further study reveals that, with epi-side up mounting strategy, within 1-2 μs, the heat dissipation to the top cladding layer is substantially suppressed, and most of the heat is drained to the substrate through the bottom cladding layer. This insufficient heat dissipation eventually leads to thermal-induced lasing quenching after 2 μs, which is also confirmed by combining light-current-voltage (L-I-V) measurements and theoretical thermal modeling.

In addition, localized Joule heating on the laser facet is detrimental to MIR QCLs when long-term operation and reliability are requisite in high output power applications. In this study, reversible lasing performance degradation is investigated on an uncoated actively- biased $GaAs/Al_{0.45}Ga_{0.55}As$ mid-infrared quantum cascade laser (MIR-QCL) facet. The surface temperature rises (ΔT) on the MIR QCL are characterized before and after the device undergoes an accelerated aging burn-in test, followed by hydrogen plasma treatment. The data is visualized by spatially resolved time-domain thermoreflectance (SR-TDTR) microscopy. On the laser facet, ΔT decreases with a drop in lasing performance and ΔT increases with an increase in lasing performance. Along the laser cavity, the thermal property change is negligible before and after the aging test, independent of the optical performance change. The results verify that thermal-induced facet oxidation is the main reason for the rapid degradation of the lasing performance in the early aging stage.

Another primary work is to develop novel thermal management strategy for THz QCLs towards higher operating temperature on cw mode. In this work, a new technique has been proposed and developed by using hybrid integration of THz QCLs on hetero-substrates, rather than conventional MM bonding on GaAs receptor. The selected hetero substrates are with higher thermal conductivity and lower coefficient of thermal expansion (CTE) mismatch compared with GaAs based THz QCLs, providing superior heat dissipation properties and facilitates photonic integration. The results show that the maximum operating temperature of transfer bonded THz QCLs on AlN is 97 K which is comparable with 100 K by conventional metal-metal (MM) waveguide on GaAs receptor carrier in a short pulse injection (pulse width of 250 ns). In addition, pulse duration dependent L-J-V measurements show the normalized light intensity (light intensity per pulse width) drops much faster for THz QCLs on GaAs compared to THz QCLs on AlN substrate at higher heat sink temperature (e.g., 80 K), and it eventually leads to lasing quenching when the pulse duration above 30 μs at 80 K, which could be attributed to Joule heating. These results indicate that THz QCLs in MM waveguides hetero bonded on AlN perform efficient heat extraction and dissipation, which is promising for breaking the T_{max} towards cw operation.

Acknowledgements

The Ph.D. study is like a long journey. Finally, I am approaching the destination and have this opportunity to share my experiences. First, I would like to sincerely express my gratitude to my supervisor, Professor Dayan Ban, for his guidance and support throughout my Ph.D. study. Although there were lots of difficulties and challenges on the path towards success in research, Prof. Ban enlightened and encouraged me to overcome them to achieve my goals. Moreover, he always provided me with plenty of resources, facilitating access to the research facilities I requested, which were incredibly beneficial for my career.

I want to thank my external committee member Professor Qiying Chen from Memorial University of Newfoundland, and all other internal committee members at University of Waterloo: Professor Bo Cui, Professor Youngki Yoon, and Professor Jonathan Baugh, for their contributions to reviewing my dissertation and making comments on my thesis defence.

I want to express my gratitude to Professor Zbigniew Wasilewski, one of my committee members throughout my Ph.D. study. Although he was unavailable to attend my defence due to a conflicting schedule, professor Zbigniew Wasilewski played a keystone role in my research, who took the lead on the wafer growth by molecular beam epitaxy (MBE). I could not complete this thesis without the collaboration and support of his MBE team.

I want to thank Professor Lan Wei for kindly providing the thermoreflectance imaging system. This tool facilitated me to contribute two journal articles and two conference proceedings enclosed in this thesis. Acknowledgement should also go to Dr. Xuesong Chen for assisting in equipment troubleshooting.

In addition, I would like to acknowledge all my co-authors contributing to journal articles and conference proceedings: Dr. Chao Xu, Dr. Fei Duan, Dr. Boyu Wen, Dr. S. M. Shazzad Rassel, Dr. Man Chun Tam, Dr. Seyed Ghasem Razavipour, Dr. Guocheng Liu, Xiaoliang He, Kaixi Wang, and all the other current and former group members at Professor Dayan Ban's research group. I enjoyed the accompanying and partnership with them. Especially, I want to thank Dr. Chao Xu for his great help, discussion, and advice in my research. We worked closely together, figuring out the technical issues and practical solutions in research. Gratitude should also go to Jian Yin (current Ph.D. student at Ban's group), who is a good companion in my research and daily life.

I want to extend my acknowledgement to the people listed as follows: Kailyn Vaillancourt (undergraduate research assistant student) for assisting me in manuscript editing (May – August 2022), Dr. MD Rejvi Kaysir (Post-Doc Fellow) for reviewing this dissertation, Professor Jean-Pierre Landsman (external collaborator) at McMaster University (Canada) and University of Rennes (France) for providing degree of polarization (DOP) stress measurements on quantum cascade lasers, and Professor Donna Strickland (Nobel Laureate in Physics, 2018) as one of my former committee members for her tough questions in my Ph.D. background exam.

I would like to gratefully acknowledge all the staff and technicians of the Quantum-Nano Fabrication and Characterization Facility (QNFCF) at University of Waterloo for assisting in device fabrication and characterization: Vito Logiudice, Dr. Nathan Nelson-Fitzpatrick, Dr. Lino Eugene, Dr. Greg Holloway, Dr. Sandra Gibson, Rodello (Rod) Salandanan, Matt Scott, Ken Speirs, and others. They are experienced and professional and always give prompt actions for troubleshooting when the FAB tools are malfunctioning. I would also like to thank our building manager Chris Kleven for assisting with the lab issues. In addition, I want to acknowledge Dustin Kendig at Microsanj LLC. for the technical assistance with the thermoreflectance imaging system.

Moreover, I would like to sincerely express my gratitude to some of my friends outside the academic community. A special thanks should be credited to Ms. Mingrui Wang for her consistent encouragement and support, letting me overcome the obstacles and depression in my research.

Finally, I would like to express my deepest and endless love to my parents, who gave me enduring support throughout my Ph.D. study. Though the covid pandemic and the long distance separate us from getting together, the love would never fade away.

Dedication

To My Parents and Grandparents

Table of Contents

Examining Committee Membership ii

Author's Declaration iii

Statement of Contributions iv

Abstract viii

Acknowledgements x

Dedication xii

List of Figures xvii

List of Tables xxix

List of Abbreviations xxxi

List of Symbols xxxiii

Chapter 1 Background 1

1.1 Introduction of Quantum Cascade Lasers (QCLs) 1

1.2 Challenges for Mid-infrared Quantum Cascade Lasers (MIR QCLs): Joule Heating Effect 4

1.3 Challenges for Terahertz Quantum Cascade Lasers (THz QCLs): Higher Operating Temperature Limitation 6

1.4 Motivation and Research Objectives 10

1.5 Thesis Organization 12

Chapter 2 Thermal Dynamics Model and Thermoreflectance Microscopy 14

2.1 Theory of Heat Transfer Model 14

2.1.1 Fourier's Law in General Form 14

2.1.2 Heat Equation in General Form 14

2.1.3 Heat Equation with External Power Injection 15

2.1.4 Fourier's Law in Steady-State with External Power Injection 16

2.1.5 Fourier's Law in Transient State with External Power Injection 16
2.1.6 Fourier's Law with Anisotropic Thermal Conductivity 17
2.1.7 Thermal Resistance Across QCLs' Active Region 18
2.1.8 Thermal Equilibrium Time Constant 21
2.1.9 Temperature Saturation Factor 26
2.2 Principle of Spatially Resolved Time-domain Thermoreflectance Microscopy 27
2.2.1 Introduction 27
2.2.2 Spatial Resolution 29
2.2.3 Temporal and Temperature Resolution: Pulsed Boxcar Averaging Technique 29
2.3 Spatially Resolved Time-Domain Thermoreflectance Microscopy Setup 31
2.3.1 SR-TDTR in Steady-State Mode for thermoreflectance Coefficient Calibration 31
2.3.2 SR-TDTR in Transient State Mode for Thermal Dynamics Measurements 32
2.4 Summary 36
Chapter 3 Thermal Dynamic Imaging of Mid-Infrared Quantum Cascade Lasers with High Temporal–Spatial Resolution 37
3.1 Introduction 37
3.2 Layer Structures and Fabrication Procedures 37
3.3 Thermal Dynamics Imaging of MIR QCLs by SR-TDTR Microscopy 41
3.3.1 Calibration for Thermoreflectance Coefficient in Steady-State Mode 41
3.3.2 Transient Temperature Rising of MIR QCLs in short Pulse Duration with High Current Injection 42
3.3.3 Transient Temperature Rising of MIR QCLs in Long Pulse Duration with Low Current Injection 46
3.3.4 Lasing Quenching Effect Study: Correlation of Temperature-Dependent L-I-V Measurements, TDTR Thermal Imaging, and Thermal Thermodynamics Modelling 51

3.3.5 Thermal Dynamics of MIR QCLs: From Transient State to Thermal Equilibrium 53
3.3.6 Thermal Conductivity and Thermal Resistant 55
3.3.7 Simulation Setting in COMSOL Multiphysics 57
3.4 Summary 57
Chapter 4 Thermal Dynamic Imaging of Mid-Infrared Quantum Cascade Lasers: Analysis of Ridge Width Dependent Effect 58
4.1 Introduction 58
4.2 Device Structure and Experimental Setup 59
4.3 Calibration of Thermoreflectance Coefficient 61
4.4 Results and discussion 62
4.5 Summary 70
Chapter 5 Facet Joule Heating of Mid-Infrared Quantum Cascade Lasers: Optical Degradation and Reliability Test 71
5.1 Introduction 71
5.2 Methodology and Procedures 73
5.3 Results and Discussion 76
5.4 Summary 87
Chapter 6 Heterogeneous Integration of Transfer Bonded Terahertz Quantum Cascade Lasers (THz QCL) for Improved Heat Management and Light Coupling 89
6.1 Introduction 89
6.2 Conventional THz QCLs in Metal-Metal Waveguide on GaAs Receptor Substrate 91
6.2.1 Waveguide Structures of THz QCLs 91
6.2.2 Device Fabrication 93
6.3 Hybrid Integration of THz QCLs in Metal-Metal Waveguide on hetero substrate: Towards Higher Temperature Performance 102

6.3.1 Strategies of Hybrid Integration 102

6.3.2 Material Selection for Hetero-Substrate 104

6.3.3 Fabrication Process of Hybrid Integration of THz QCLs on Si and AlN Substrate 106

6.4 Device Characterization and Optical Performance between THz QCLs on Hetero-substrates and THz QCLs on GaAs substrates 112

6.5 Thermal Dynamics Modeling: Comparison of THz QCLs on Intrinsic GaAs and on Hetero-Substrates 122

6.6 Summary 126

Chapter 7 Conclusion 127

7.1 Summary of This Dissertation 127

7.2 Future Work and Perspectives 129

Bibliography 134

Appendices 145

Appendix A. Fabrication Procedures of THz QCLs 145

Appendix B. Process Flow of THz QCLs Hybrid Bonded on Hetero Substrate 147

Appendix C. Process Flow of THz QCLs Integrated with Si Waveguide on Si Substrate 148

Appendix D. Wafer Growth Sheet 151

List of Figures

Figure 1.1 (a) Mid-infrared range (3 – 50 μm) in electromagnetic spectrum; (b) atmospheric window (3-5 μm and 8-14 μm) with high transmittance in infrared range; (c) photograph of a mounted laser bar with four wire-bonded MIR QCLs in Fabry–Pérot (FP) ridge waveguides; (d) scanning electron microscope (SEM) imaging of one of the MIR QCLs' cleaved facet, showing repeating multiple quantum wells (MQWs) modules in the active region core; (e) simplified conduction band diagram for a MIR QCL, where the lasing transition from the upper lasing level (3) to the lower lasing level (2). [Adapted with permission from Ref. [13] © 2012 Springer Nature Publishing] 5

Figure 1.2 (a) Cross-sectional SEM image of a MIR QCL ridge facet in buried heterostructure (BH); (b) simulated 2D temperature distribution of a buried ridge MIR QCL epi-down bonded on a diamond heatsink for cw operation; (c) The maximum (T_{max}) and average (T_{ave}) temperature of the active region (laser core) of the buried ridge MIR QCL under cw operation as a function of QCL stages; (d) the light-current-voltage (L-I-V) curves and extracted wall-plug efficiency (WPE) for a 5 mm length MIR QCL ridge waveguide. [Adapted with permission from Ref. [12] © 2020 Optica Publishing Group and Ref. [33] © 2007 AIP Publishing].. 6

Figure 1.3 Terahertz gap in the electromagnetic spectrum. [Reprinted with permission from Ref. [3] © 2002 Springer Nature Publishing] 7

Figure 1.4 Simulated 2D temperature distribution on the laser facet of a narrow ridge THz QCL in metal-metal waveguide on GaAs substrate under cw operation (power density at 1.1×10^7 W/cm^3) [Reprinted with permission from Ref. [38] © 2005 Optica Publishing Group] ... 9

Figure 1.5 Temperature-dependent L-I-V curves of the THz QCL under pulse mode (a) and cw mode (b). [Adapted with permission from Ref. [38] © 2005 The Optical Society] 9

Figure 1.6 Objectives and goals for high performance THz QCLs 11

Figure 1.7 Methodology flow for the experiments 12

Figure 2.1 Schematic diagram of heat flux dissipates out from the QCL's active region.................... 18

Figure 2.2 Temperature dependence of thermal conductivity (cross-plane in k_y and in-plane in k_x) and heat capacity of AlGaAs/GaAs superlattices in active region and GaAs substrate. [Adopted with the permission from Ref. [54], IEEE copyright line © 2011 IEEE] 18

Figure 2.3 Transient temperature rise above heatsink with time delay 22

Figure 2.4 Derivative transient temperature rise with time delay 23
Figure 2.5 Transient density of heat power accumulation with time delay 25
Figure 2.6 Transient density of heat power dissipation with time delay 25
Figure 2.7 Density of total energy accumulation with injected pulse width 26
Figure 2.8 SR-TDTR System (Model type NT210 B, images provided by Microsanj User Manual) . 28
Figure 2.9 Typical Time chart and schematic diagram of the setup principle (images provided by Microsanj User Manual) 28
Figure 2.10 Working principle of a boxcar average [62] 30
Figure 2.11 Schematic diagram of the SR-TDTR setup working on steady-state mode for the calibration of thermoreflectance coefficient 31
Figure 2.12 Time chart of SR-TDTR setup working on steady-state mode for the calibration of thermoreflectance coefficient.. 32
Figure 2.13 Schematic diagram of the SR-TDTR setup for QCL's transient temperature measurement 34
Figure 2.14 Time chart of SR-TDTR setup working on transient state for transient temperature profile measurements.. 35
Figure 2.15 Time chart of SR-TDTR setup working on transient state for temperature profile measurements from transient state to quasi-steady state... 35
Figure 2.16 (a) Device ridge bar on a copper package; (b) device under a microscope with ×100 magnification, scale bar is 10 μm; (c) package on the thermal electric stage under the microscope. 36
Figure 3.1 Fabrication Sequence of GaAs/$Al_xGa_{1-x}As$-based MIR QCLs (λ~9 μm).......................... 38
Figure 3.2 (a) L-I/J-V characteristic on pulse mode with heat sink temperature from 50 K to 295 K (modulation frequency of 500 Hz, pulse width of 500 ns, duty cycle of 0.025%); (b) measured (symbols) and fitting (dash line) of threshold current - threshold current density with respect to heat sink temperature from 50 K to 280 K, where T_0 = 50 K is the characteristic temperature; the inset in (b) shows lasing spectrum by FTIR at 100 K (heat sink temperature) when current injection is just above the threshold. 39
Figure 3.3 Schematic diagram of the cross-sectional view of the MIR QCL ridge waveguide 40

Figure 3.4 (a) An image under optical microscope from the top-down view of an area of the fabricated MIR QCL ridge waveguide; (b) an SEM image of the cleaved facet of the fabricated MIR QCL ridge waveguide. 40
Figure 3.5 Calibration results of C_{th} for GaAs/$Al_{0.45}Ga_{0.55}As$ MQWs and n-type GaAs, respectively 41
Figure 3.6 (a) Schematic diagram of the cross-section view of a fabricated QCL mounted on the copper package with epi-side up. (b) Two-dimensional (2D) transient temperature imaging profiles at time delay (τ_d) of 150 ns, 450 ns, and 1250 ns, respectively. The temperature change ΔT along x and z direction across the center of the active region (indicated by white dash line in (b)) at different time delays are plotted in (c) and (d), respectively. (e) The measured transient temperature change ΔT at the center of the active region – red solid line (1), center of the top cladding layer – orange solid line (2), center of the bottom cladding layer – purple solid line (3), the point at 4.5 μm below AR layer inside the substrate – grey solid line (4), at different time delay when pulse width of the electrical injection is fixed to 500 ns and peak injected power (P_{in}) is set to 112.2 W (I = 6 A, V = 18.7 V); LED pulse width is set to 50 ns; T_0 is the heat sink temperature (296.5K). 43
Figure 3.7 (a) 2D transient temperature imaging profiles at different time delay with a short pulse-width current injection (I = 6 A, V= 18.7 V, PW = 500 ns, each image was averaged over 6000 CCD frames); measured transient temperature change ΔT along x direction (b) and z direction (c) across the center of the active region at different time delay. 44
Figure 3.8 Transient state thermal imaging profile at the delay time (τ_d) of 500 ns (the same as device pulse width) when QCL is injected from 1 A to 6 A. 45
Figure 3.9 (a) Transient temperature rises in active region with different time delay under pulsed injection (PW = 500 ns, duty cycle = 0.25%, heatsink at room temperature, current sweep from 0.5 A to 6 A, step = 0.5 A). (b) Black dots: the maximum temperature rises at the end of each pulse with respect to the peak power injection; red dash line: linear fitting curve.. 46
Figure 3.10 2D transient temperature imaging profiles (a) and percentage of heat dissipation rates (b) within the close-to-active-region area at the time delay of 1 μs (beginning of the current-injection pulse), 5 μs (in the middle of the current-injection pulse), and 10 μs (end of the current-injection pulse). (c) Calculated transient heat flow profiles within one period of current-injection pulse when the pulse width is 10 μs and the peak injection power is 20

W (I = 2 A, V = 10 V) within the close-to-active-region area from SR-TDTR measurement. The orange and the blue lines show the vertical heat flow from the active region (AR) towards to the bottom cladding (BCL) and the top cladding layer (TCL), respectively. Two black lines are the lateral heat dissipation from the top cladding and bottom cladding layer towards both lateral sides, respectively. The magenta line is the lateral heat flow inside the active region. (d) Temperature change with respect to time delay at the center of the active region, at the center of the top cladding layer, at the center of the bottom cladding layer, respectively. 48

Figure 3.11 (a) 2D transient temperature imaging profiles at different time delay (in 1 μs step) under pulsed injection (I = 2 A, V= 10 V, PW = 10 μs, duty cycle = 0.2%). (b) Measured transient temperature rises (ΔT) above the heatsink temperature on QCL's facet from top cladding layer to the substrate at different time delay (in 1 μs step)........ 49

Figure 3.12 (a) Measured relationship in pulse widths (symbols) between current-injection pulse and output light pulse at a heat sink temperature of 150 K and a current-injection amplitude of 2.375 A. Saturated value of optical pulse width is shown in black dashed line. (b) Measured (circles) and simulated (solid lines) time dependent temperature changes in active region with different current-injection pulse widths of 1, 2.5, 5, and 10 μs at room temperature (296.5 K). (c) Simulated time dependent temperature in the active region with different current-injection pulse widths of 1, 2.5, 5, and 10 μs at a heat sink temperature of 150 K. (d) Measured temperature at threshold as a function of device injection current, derived from light-current-voltage measurements in pulse mode (pulse width of 500 ns, modulation frequency of 500 Hz). The purple dashed line shows the relationship among the threshold current of 2.375 A in (d), the threshold temperature of 197 K in (c), and the threshold pulse width of ~2 μs in (a). 52

Figure 3.13 (a) Measured the maximum transient temperature rises (ΔT) on QCL's facet above the T_{HS} at RT at different pulse width (time delay is set at the fall edge of each pulse) under 20 W of peak power (I = 2 A, V = 10 V). (b) Mapped 2D thermal imaging profile on QCL's facet under quasi-steady state (thermal equilibrium) when the pulse width and time delay are both at 100 μs. Black arrows illustrate the heat dissipation channels. 54

Figure 3.14 Transient temperature rises with time delay at different current injection (from 0.5 A to 2 A) with pulse width of 100 μs and duty cycle of 2%. 55

Figure 3.15 Linear fitting of correlating measured maximum temperature rises in quasi-steady state (PW = 100 μs) with extrapolated maximum temperature rises (PW = 500 ns) from transient state measurements. 56

Figure 4.1 Calibration of the thermoreflectance coefficient (C_{th}) of EP Au layer, showing C_{th} is linear fitting at $(1.053\pm0.01)\times10^{4}$ K^{-1}. The calibration is conducted under an optical microscope objective magnitude with the magnitude of ×20 (green dots) and ×100 (purple dots), respectively, with the reference heatsink temperature at 25 °C. 62

Figure 4.2 3D thermodynamics of temperature rise above heat sink at room temperature. (a) Spatially resolved temperature profile of a MIR QCL at the laser facet (XZ plane) under ×100 of objective lens; (b) spatially resolved temperature profile of a MIR QCL on the top of ridge waveguide (XY plane) under ×20 of objective lens; (c) spatially resolved temperature profile of a selected area (XY plane) under ×100 of objective lens; (d) average temperature rise above the heatsink temperature on different locations extracted from (a) and (c). (Measurement conditions: pump pulse duration of 80 μs, duty cycle of 4%, time delay of probe signal at 80 μs, peak power injection of 12.58 W, peak injected power density of 2.12×10^{14} W/m^3, heatsink temperature at 25 °C). 64

Figure 4.3 Temperature rise above heatsink at quasi-steady state (with peak power injection) and transient state (with time delay) at different locations. (a) Temperature rise above heatsink at quasi-steady state with the increasing of the peak power injection with 80 μs of pulse injection (4% of duty cycle) at different locations indicated in Figure 4.2, and the temperature rise is acquired at the end of each pulse; (b) transient state of temperature rise above the heatsink with the change of the time delay of 80-μs-long pulse injection (4% of duty cycle) in 12.58 W of peak power injection from different locations. 66

Figure 4.4 Thermal resistance (a) and thermal conductance per unit area (b) analysis in quasi-steady state measurement, in linear fitting with peak power injection and temperature rise above heatsink temperature, respectively. 68

Figure 4.5 Quasi-steady state and transient state thermal analysis: (a) 2D temperature profile under quasi-steady state (100 μs of pulse injection; 20 W of peak power, and 100 μs of time delay); (b) transient temperature profile of the temperature rise above heatsink at active region (red), upper cladding layer (blue), and the lower cladding layer (orange); (c) transient temperature profile of the temperature rise above heatsink at active region with

different peak power injection. (d) line scan of transient temperature rise at different time delay in z direction from upper cladding layer to lower cladding layer. 69

Figure 4.6 SEM image of an MIR QCL (Wafer#: G0241) cleaved facet with 2.5 μm thick EP-Au.... 70

Figure 5.1 (a) Three-dimensional (3D) schematic diagram of the MIR QCL's layer structures as a truncated view close to the laser facet. (b) Scanning electron microscope (SEM) image of the MIR QCL on uncoated cleaved facet (xz-plane). (c-e) Two-dimensional (2D) schematic diagram of the MIR QCL along the laser cavity (yz-plane) before aging, after aging, and after hydrogen plasma treatment. 74

Figure 5.2 Current density – voltage (J-V) curve of pulsed injected MIR QCL when the heatsink temperature at 295 K (a) and 200 K (b); relative light intensity – current density (L-J) curve at 200 K (c). Before aging, after 10 hours of aging, after 20 hours of aging, after 30 hours of aging, and after 10 min of hydrogen plasma treatment are shown in black solid curve, blue dash curve, orange dash curve, red dash curve, and magenta dot curve, respectively. Threshold current density, normalized slope efficiency, and normalized light intensity as increasing of the aging time are shown in (d), (e), and (f), respectively; magenta stars indicated by green arrows show the values after hydrogen plasma treatment. Aging conditions are set on pulse mode with current density (J) of 4 kA/cm^2, dose per pulse of 3.6 J/cm^2, pulse width (PW) of 100 μs, and 2% of duty cycle at 1 atm at ambient room temperature (295 K). 78

Figure 5.3 (a) 2D thermal imaging profiles of the surface temperature rise (ΔT) above the heatsink temperature (295 K) on MIR-QCL's facet before (a), after aging for 30 hours (b), and after hydrogen plasma for 10 min. The averaged ΔT in rectangular regions on the active region (AR), the upper cladding layer (UC), and the lower cladding layer (LC) in (a-c) are indicated by black arrows. (d) Averaged ΔT of AR, UC, and LC on the laser facet extracted from the indicated rectangular regions in (a-c). (e) ΔT above the heatsink before (black solid curve), after aging for 30 hours (red dash curve), and after hydrogen plasma for 10 min (magenta dot curve) in vertical line scan across the middle of the laser facet from the top of the upper cladding layer towards the substrate. The pulsed injection for the thermal measurement is set as the same as the aging condition.. 80

Figure 5.4 (a) 2D thermal imaging profiles of the QCL's ridge top layer before (a), after aging for 30 hours (b), and after 10 min hydrogen plasma (c). An inset figure in (b) shows a CCD image

from a rectangle region with 16 by 70 μm (indicated in white dash frame) close to the laser facet. The top layer on this region is the metal contact layer (Ti/Au: 20/250 nm) without 2.5 μm-thick electroplated gold (EP-Au) capped. (d) ΔT above the heatsink in horizontal line scans along the laser cavity from the laser facet (indicated in white dash lines in (a-c)) before aging (black solid curve), after 30 hours of aging (red dash curve), and after hydrogen plasma for 10 min (magenta dot curve). 81

Figure 5.5 Injected pulse width (PW) dependent threshold current density (a) and PW dependent normalized light intensity (at J = 7.8 kA/cm^2) (b) after thermal imaging test prior to accelerated aging test (green dash curve), after 10 hours of aging (blue dash curve), after 20 hours of aging (orange dash curve), after 30 hours of aging (red dash curve), and the after 10 min of hydrogen plasma treatment (magenta dash curve). $J_{th}(0)$ = 6.93 kA/cm^2 (indicated in black star) is the threshold current density as a benchmark measured under 500 ns of the injected pulse width before the aging test (black star). PW-dependent averaged transient temperature rises at the active region (AR) on the laser facet (in xz-plane) (c) and on the top ridge close to the facet edge (in xy-plane) (d) at 295 K under high current injections (J=18.85 kA/cm^2, f_{rep}= 1 kHz) in short pulse duration (PW = 250 ns – 1000 ns)... 84

Figure 5.6 Injected pulse width (PW) dependent threshold current density (a) and PW dependent normalized light intensity (at J = 7.8 kA/cm^2) (b) after 100 hours of vacuum aging (blue dash curve) and after 10 min of hydrogen plasma treatment (magenta dash curve). $J_{th}(0)$ = 6.93 kA/cm^2 (indicated in black star) is the threshold current density as a benchmark measured under 500 ns of the injected pulse width before the aging test (black star). J-V curve (c) and L-J curve (d) of pulsed injected MIR QCL when the heatsink temperature at 295 K. Vacuum aging conditions are set on pulse mode with current density (J) of 4 kA/cm^2, dose per pulse of 3.6 J/cm^2, pulse width (PW) of 100 μs, and 2% of duty cycle at the pressure of 9 × 10^{-7} mbar at ambient room temperature (295 K). The MIR QCL ridge waveguide is with 16 μm of ridge width and 2 mm of cavity length............................. 85

Figure 5.7 PW dependent threshold current density (a) and PW dependent normalized light intensity (at J = 9 kA/cm^2) (b) after 30 hours exposed on ambient atmosphere (enclosed in chamber without biased) – blue dash curve, and after 10 min of hydrogen plasma treatment – magenta dash curve. J-V curve (c) and L-J curve (d) of pulsed injected MIR QCL when

the heatsink temperature at 295 K. The MIR QCL ridge waveguide is with 12 μm of ridge width and 2 mm of cavity length. 86

Figure 5.8 Thermal dynamics behaviours of MIR QCL's active region temperature rise above the heatsink on laser facet in transient state before aging (black curve) and after 30 hours of accelerated aging in atmosphere (red curve) under a 100 μs pulsed duration................. 87

Figure 6.1 Schematic diagrams of (a) a semi-insulating surface-plasmon (SISP) waveguide and (b) a metal-metal (MM) waveguide used in terahertz (THz) quantum cascade lasers (QCLs). The typical electric field intensity is plotted with blue arrows indicating the electric field polarization. [Adapted from Ref. [84], with the permission of John Wiley and Sons Publishing] 93

Figure 6.2 Thermocompression Au-Au bonding for metal-metal ridge waveguide THz QCLs on GaAs 94

Figure 6.3 (a) An image of the bonding holder and a schematic diagram of the cross-section view of the bonding holder. The graphite plates are employed to uniformly distribute the bonding stress.. 95

Figure 6.4 (a) A piezoelectric force gauge (a) and the calibrated force-resistance diagram (b). The force is measured and read by the resistance between pin 1 and 3. The red round shape in the diagram indicates the reference region of the bonding force. 95

Figure 6.5 (a) An image of a bonded device piece on a GaAs receptor by Au-Au wafer bonding, and (b) a schematic diagram of the layers structure in top-down view and cross-section view. 96

Figure 6.6 Schematic diagram of the bonding mechanism at the interface. A stress gradient forms between the contacted areas (higher gradient) and the voids (lower gradient), with the atoms then driven to diffuse along the interface to "fill" the voids. The high surface diffusivity of the (111) surface is the main contributor to this phenomenon. The plotted voids are exaggerated for explanation. 96

Figure 6.7 SEM cross-section view of the bonding interface of a THz QCL in Au-Au waveguide 97

Figure 6.8 (a) Bonded THz QCLs piece (1 ×1 cm, wafer# G0405) with wax glued on a glass plate (the device substrate side is facing up); (b) lapping machine and the metal chuck with a height gauge (the glass plate is under the bottom of the chuck in vacuum, and the device substrate

side is facing down); (c) bonded piece after substrate lapping; (d) bonded piece immersed into the wet etching solution. 98

Figure 6.9 (a) After substrate wet etch; (b) after etch-stop layer removal; (c) after fabrication completion; (d) image of ridge waveguide in different ridge width under optical microscope. THz QCLs wafer#: G0405. 100

Figure 6.10 (a) wire bond on the top metal of THz QCLs ridge waveguides; (b) cleaved ridge waveguide facet of THz QCL in Au-Au waveguide on GaAs receptor 101

Figure 6.11 Temperature dependent thermal conductivity (k) of different materials (heat sink submount and bonding metal) 106

Figure 6.12 (a) The coefficient of thermal expansion (CTE) and (b) the specific heat capacity (C_p) of different materials (heat sink submount and bonding metal) at 300 K 106

Figure 6.13 Fabrication process of transferred THz QCLs (wafer#: G0312) with dry etched facet bonded on Si Substrate........ 108

Figure 6.14 Fabrication process of THz QCLs (wafer#: G0312) with metal-metal waveguides hetero bonded on AlN substrate. (a) Fabricated THz QCLs in ridge waveguides on GaAs substrate with cleaved facet; (b) as gold deposited AlN substrate; (c) metal-metal thermocompression bonding process by die-bonder; (d) THz QCLs die on AlN substrate after bonding process; (e) exposed THz QCLs laser bars after GaAs substrate liftoff process by dipping in concentrated HF (49%). 110

Figure 6.15 (a) Bonded THz QCLs (wafer#: G0312, cavity length: 2.4 mm, ridge width: 120/90/60 µm) in ridge waveguides on AlN substrate with gold coating; (b) bonded THz QCLs on AlN substrate onto an Au-plated copper package along with a 7-pin PCB board, which are mounted onto a cold finger with a cryostat, and each laser device is connected to a bonding pad on the PCB board via Au-wire-bonding; (c) top side view of THz QCLs with Au-wire bonding under optical microscope (laser bars with ridge width of 120 µm, 90 µm, and 60 µm, respectively); (d) cross-section view under scanning electron microscopy (SEM) of a bonded THz QCL ridge waveguide on AlN substrate. 111

Figure 6.16 (a) Bonded THz QCLs (wafer#: G0226, cavity length: 2.4 mm, ridge width: 80 µm for each) with cleaved facet on Si substrate; (b) facet view under SEM of a bonded THz QCL ridge waveguide on Si substrate in 80 µm of ridge width; (c) bonded THz QCLs with

cleaved facet on AlN substrate; facet view under SEM of a bonded THz QCL ridge waveguide on AlN substrate in 80 μm of ridge width. 112
Figure 6.17 Temperature dependent L-J-V measurements under short pulse injection of THz QCLs bonded on AlN (a), and injected pulse width dependent L-J-V measurements of THz QCLs bonded on AlN when the heat sink temperature is at 10 K, 50 K, and 80 K, respectively (b-d). 114
Figure 6.18 Temperature dependent L-J-V measurements under short pulse injection of THz QCLs bonded on GaAs (a), and injected pulse width dependent L-J-V measurements of THz QCLs bonded on GaAs when the heat sink temperature is at 10 K, 50 K, and 80 K, respectively (b-d). 115
Figure 6.19 Temperature dependent threshold current density (J_{th}) of THz QCLs on AlN and GaAs under short pulse injection (a); pulse duration dependent J_{th} of THz QCLs on AlN (b) and GaAs (c) with various heat sink temperature; the peak light intensity with the change of the pulse duration of THz QCLs on AlN (d) and GaAs (e); normalized light intensity with pulse duration for THz QCLs bonded on AlN and GaAs (f). 116
Figure 6.20 L-I-V characterization of THz QCL (wafer#: G0312) ridge waveguide bonded on Si substrate. The device is with dry etch facet, with 120 μm of width and 1 mm of length. 118
Figure 6.21 L-I-V characterization of THz QCL (wafer#: G0312) ridge waveguide bonded on AlN substrate. The device is with cleaved, with 90 μm of width and 2.4 mm of length. 119
Figure 6.22 L-I-V characterization of THz QCL (wafer#: G0312) ridge waveguide bonded on AlN substrate. The device is with cleaved facet, with 120 μm of width and 2.4 mm of length. 120
Figure 6.23 Threshold current density (J_{th}) vs. the heat sink temperature 121
Figure 6.24 Relative dynamic range (RDR) vs. the heat sink temperature 122
Figure 6.25 Schematic diagram of cross-section view of a typical THz QCL in metal-metal waveguide 123
Figure 6.26 3D (a) and 2D (b) temperature profile by COMSOL simulation for the temperature rise in cw mode operation for Au-Au waveguide THz QCLs on GaAs when the heat sink temperature steady at 100 K. 123

Figure 6.27 Average (blue) and max (orange) temperature rise above heat sink temperature (set to100 K) of THz QCLs (Au-Au bonding) on different heat sink submount of GaAs, Si, AlN, and diamond coated (1 µm) Si, respectively. The power injection density is at 2.56×10^{12} W/m^3 (J = 320 A/cm^2). 124
Figure 6.28 Average temperature rising (a) and peak temperature rising (b) in active region with different heat sink temperature on DC biased (cw mode) 125
Figure 6.29 Simulated maximum temperature rise (left axis) and the temperature rise above heatsink temperature (right axis) in active region when THz QCL is in DC biased (injected power density is 8.00×10^{12} W/m^3) 125
Figure 6.30 Simulated internal active region temperature rises of THz QCL bonded on GaAs (red line) and AlN (blue line) when the pulse injection at 40 µs (a) and 500 µs (b). The heatsink temperature is kept at 80 K and the injected peak power density is 8.00×10^{12} W/m^3... 126
Figure 7.1 Schematic diagram of THz QCL ridge waveguide in near field pattern (a) and far field pattern (b). 130
Figure 7.2 Simulation of far-field pattern of THz QCL coupling with Si Waveguide (Si WG), the lateral gap between THz QCL and Si WG is optimized at 10 µm: (a) Far-field beam pattern of THz QCL with 40 µm of ridge width of and 10 µm of depth without Si waveguide coupling; (b) Far-field beam pattern of THz QCL coupling with Si waveguide with 10 µm depth (without metal coating on Si WG sidewall); (c) Far-field beam pattern of THz QCL coupling with Si waveguide with 20 µm depth (without metal coating on Si WG sidewall); (d) Far-field beam pattern of THz QCL coupling with Si waveguide with 30 µm depth (without metal coating on Si WG sidewall); (e) Far-field beam pattern of THz QCL coupling with Si waveguide with 10 µm depth (Au coating on Si WG sidewall); (f) Far-field beam pattern of THz QCL coupling with Si waveguide with 20 µm depth (Au coating on Si WG sidewall); (g) Far-field beam pattern of THz QCL coupling with Si waveguide with 30 µm depth (Au coating on Si WG sidewall). 131
Figure 7.3 Mode propagation along THz QCL ridge waveguide towards Si Waveguide (Si WG): (a) Mode propagation along THz QCL ridge waveguide towards Si WG with 10 µm depth (without metal coating on Si WG sidewall); (b) Mode propagation along THz QCL ridge waveguide towards Si WG with 20 µm depth (without metal coating on Si WG sidewall); (c) Mode propagation along THz QCL ridge waveguide towards Si WG with 30 µm depth

(without metal coating on Si WG sidewall); (d) Mode propagation along THz QCL ridge waveguide towards Si WG with 10 µm depth (Au metal coating on Si WG sidewall); (e) Mode propagation along THz QCL ridge waveguide towards Si WG with 20 µm depth (Au metal coating on Si WG sidewall); (f) Mode propagation along THz QCL ridge waveguide towards Si WG with 30 µm depth (Au metal coating on Si WG sidewall). 132
Figure 7.4 Top view pattern distribution along THz QCL ridge waveguide towards Si Waveguide (Si WG): (a) without metal coating on Si sidewall; (b) with Au coating on Si sidewall..... 133
Figure B.1 Schematic diagram of the fabrication process flow of THz QCLs in hetero bonding process (1)..... 147
Figure B.2 Schematic diagram of the fabrication process flow of THz QCLs in hetero bonding process (2)..... 147
Figure C.1 Schematic diagram of process flow (1): Si Waveguide on Si 148
Figure C.2 Schematic diagram of process flow (2): Fabrication of THz QCL 148
Figure C.3 Schematic diagram of process flow (3): Transfer THz QCL on Si 149
Figure C.4 Schematic diagram of the cross-section view of the device 149
Figure C.5 Fabrication process for QCL on Si with Si Waveguide 150
Figure C.6 Dry-etched Si ridge waveguide with cleaved facet for integration in different ridge height (etch-depth)..... 150

List of Tables

Table 3.1 Thermal conductivity [W/(m·K)] of different layers of materials 49
Table 3.2 Time-dependent (transient state) heat flow in long-pulse injection (Peak power injection = 20 W, Pulse width = 10 μs, duty cycle = 0.2%) 50
Table 3.3 Time-dependent (transient state) heat flow in short-pulse injection (I = 6 A, V= 18.7 V, Peak power injection = 112.2 W, Pulse width= 500 ns, duty cycle = 0.25%) 50
Table 3.4 Quasi-Steady State Heat Flow (W) in pulse injection (I = 2 A, V= 10 V, PW = 100 μs, duty cycle = 2%, τ_d = 80-100 μs) 54
Table 4.1 Device parameters of three sets of MIR QCL ridge waveguides (w is the ridge width, l is the cavity length, d' is the ridge etched depth, A is the top ridge area in XY plane, T_{EP-Au} is the electroplated Au layer thickness 60
Table 4.2 Thermal properties of three sets of MIR QCL ridge waveguides: R_{th} is the thermal resistance, G_{th} is the thermal conductance per unit area, Γ is the proportion of heat flux in vertical direction, β_1 and β_2 is the coefficient of heat extraction towards upper cladding and lower cladding layer, respectively. 68
Table 5.1 Measurement Conditions on MIR QCL (W = 16 μm, L = 2 mm) 76
Table 6.1 Comparison among conventional flip-chip bonding, direct wafer bonding, and massive transfer printing on chip scale hybrid integration [89-103] 102
Table 6.2 Summary of the advantages and disadvantages among different wafer bonding strategies on wafer scale hybrid integration [89-103] 103
Table 6.3 Comparison of Thermal Conductivity (k), Coefficient of thermal expansion (CTE), Specific Heat Capacity (C_p), and density among different materials (heat sink submount and bonding metal) at 300 K [39-49] 105
Table 6.4 Extracted thermal conductivity (κ) and coefficient of thermal expansion (CTE) of GaAs, Si, and AlN 105
Table A.1 Fabrication procedures of conventional THz QCLs structure in metal-metal waveguide on GaAs 145
Table A.2 Fabrication procedures of hybrid integration of THz QCLs on hetero substrates 146
Table D.1 Wafer# G0241 (MIR QCLs) Growth Sheet 151
Table D.2 Wafer# G0226 (THz QCLs) Growth Sheet 152
Table D.3 Wafer# G0312 (THz QCLs) Growth Sheet 153

Table D.4 Wafer# G0405 (THz QCLs) Growth Sheet 154

List of Abbreviations

AlN: Aluminum Nitride

AR: Active Region

BCL: Bottom Cladding Layer

BH: Buried Heterostructure

CMD: Catastrophic Mirror Damage

CTE: Coefficient of Thermal Expansion

cw: Continuous Wave

DFG: Difference Frequency Generation

EO: Electro-Optical

EP-Au: Electroplated Gold

GaAs: Gallium Arsenide

MIR QCL: Mid-infrared Quantum Cascade Laser

L-I-V: Light-Current-Voltage

LL Level: Lower Lasing Level

LO-phonon: Longitudinal Optical Phonon

MBE: Molecular Beam Epitaxy

MM: Metal-Metal

MOCVD: Metal-Organic Chemical Vapour Deposition

MQWs: Multiple Quantum Wells

PICs: Photonic Integrated Circuits

PW: Pulse Width

QCL: Quantum Cascade Laser

RT: Room Temperature

R_{th}: Thermal Resistance

Si: Silicon

SISP: Semi-Insulating Surface-Plasmon

SNR: Signal-to-noise Ratio

SR-TDTR: Spatially Resolved Time-domain Thermoreflectance

TBR: Thermal Boundary Resistance

TCL: Top Cladding Layer

TEC: Thermoelectric Cooler

T_{HS}: Heatsink Temperature

THz QCL: THz Quantum Cascade Laser

T_{max}: Maximum Operating Temperature

UL Level: Upper Lasing Level

WPE: Wall Plug Efficiency

List of Symbols

λ: Emission Lasing Wavelength

η_{se}: Slope Efficiency

mm: Millimeter

μm: Micrometer

μs: Microsecond

ps: Picosecond

K: Kelvin

W: Watt

$\overrightarrow{\phi_q}$: Heat Flux [$W \cdot m^{-2}$]

P: Injected or Dissipated Power [W]

A: Cross-section Area of Power Injection or Dissipation [m^2]

Δd: A Thin Layer along with Heat Transfer Direction [m]

Q: Injected or Dissipated Energy Density [$J \cdot m^{-3}$]

$\Delta Q(t)$: Time-dependent Heat Density Generation inside the Medium [$J \cdot m^{-3}$]

q: Injected or Dissipated Power Density [$W \cdot m^{-3}$]

$\Delta q(t)$: Time-dependent Rate of Heat Density Generation inside the Medium [$W \cdot m^{-3}$]

k: Material's Thermal Conductivity [$W \cdot m^{-1} \cdot K^{-1}$]

ρ: Material Density [$Kg \cdot m^{-3}$]

C_p: Specific Heat Capacity [$J \cdot Kg^{-1} \cdot K^{-1}$]

ρC_p: Volumetric Heat Capacity [$J \cdot K^{-1} \cdot m^{-3}$]

α: Thermal Diffusivity [$m^2 \cdot s^{-1}$]

L_d: Thermal Diffusion Length [m]

ΔT: Transient Temperature Difference [K]

∇T: Temperature Gradient [K·m^{-1}]

R_{th}: Thermal Resistance [K·W^{-1}]

ΔT_{ss}: Maximum Temperature Rise in Steady-State [K]

t_d: Time Delay [s]

τ_{th}: Thermal Equilibrium Time Constant [s]

t_{pw}: Injection Pulse Width [s]

Γ: Portion of Power Flow in Cross-Plane Direction Channel in Steady-State

β_1: Coefficient of the Heat Extraction towards Upper Cladding Layer

β_2: Coefficient of the Heat Extraction towards Lower Cladding Layer

γ : Temperature Saturation Factor

R_0: Material's Reflectivity at Ambient Temperature

ΔR: Change in Reflectivity

ΔN: Change in Carrier Density

Chapter 1
Background

1.1 Introduction of Quantum Cascade Lasers (QCLs)

Quantum cascade lasers (QCLs) are a unique type of semiconductor lasers which are based on intersubband transitions rather than interband transitions [1][2]. This is different from the conventional semiconductor laser diode, where the electron-hole recombination occurs between the conduction band and the valence band, namely as interband transitions. For QCLs, as shown in Figure 1.1, the population inversion and photon emissions are taken place within the conduction band itself. In the photon emission process, the electrons are injected from an injection energy level to an upper lasing (UL) level by resonant tunnelling or phonon-assisted scattering, followed by phonon or photon-assisted scattering process from the UL level to a lower lasing (LL) level, namely as intersubband transition. There are several characteristics of QCLs as follows. First, QCLs are unipolar photonic devices because only electrons as the injected carriers participate in photon generation. Secondly, since there is a narrow energy level difference within the conduction band, the lasing wavelength can be accurately tuned in a small range by precisely controlling the doping concentration and/or changing the thickness of quantum wells and barriers. Thanks to the small energy gap between the subband energy levels, the lasing wavelength can extend from mid-infrared (3-30 μm) to far-infrared (30-300 μm) range, which makes QCLs the only practical photonic devices covering the broadband infrared spectrum [3][4]. The mid-infrared QCLs (MIR-QCLs) and far-infrared QCLs, so-called terahertz (THz) QCLs are introduced in sections 1.2 and 1.3, respectively. The third characteristic of QCLs is their high threshold current density, typically at kA/cm^2 level for MIR QCLs and hundreds of A/cm^2 for THz QCLs.

The high threshold current density is due to a fast depopulation process, high series resistance, and low anisotropic thermal conductivity along the epitaxially grown direction. First, due to the fast dynamic process of the electrons regarding intersubband transition, the longitudinal optical phonon (LO-phonon) scattering lifetime is in orders of picosecond (ps), which dramatically reduce the carrier lifetime in the UL level for photon emission. As a result, a higher density of the carrier injection is required to maintain the population inversion. Second, varying from a few microns (μm) to 10 μm in thickness, the epitaxially grown multiple quantum wells (MQWs) as the active region (AR) layer of the QCLs contain 30-50 repeating modules (stages) and over one hundred modules (stages) for MIR QCLs and THz QCLs, respectively. [2]. As a result, due to the high series resistance of QCLs, ampere (A)

level current injection and over 10 volts (V) of the biased voltage are required before reaching the lasing threshold, which is one of the major limitations for high power operation on continuous-wave (cw) mode at room temperature (RT). This is because Joule heating is also generated inside the active region due to over 10 watts (W) of power injection. Third, owing to the thermal boundary resistance (TBR), the anisotropic thermal conductivity along the epitaxial layer growth in the active region layer is one order of magnitude lower than the in-plane thermal conductivity and the thermal conductivity in bulk III-V semiconductors. This intrinsic material property further reduces the heat dissipation efficiency as the Joule heating generation inside the active region.

Therefore, due to the high power consumption, the electro-optical power conversion efficiency, so-called wall-plug efficiency (η_w), is still low (up to ~31% for MIR QCLs and up to ~5.5% for THz QCLs) [5][6] compared to the conventional laser diode (~70%) at RT operation [7]. Therefore, thermal management for heat dissipation is crucial for MIR QCLs and THz QCLs, which are also addressed in the sections 1.2 and 1.3, respectively.

The concept of QCLs was firstly proposed by Kazarinov and Suris in 1971 with a superlattice structure design [8]. Thanks to the development in epitaxial layer growth techniques by molecular beam epitaxy (MBE) [9] and metal-organic chemical vapour deposition (MOCVD) [10], in which, sub-nanometer-monolayer-thickness can be precisely controlled. The first QCL was proposed by Faist *et al.* in 1994 based on GaInAs/AlInAs material system epitaxially grown on InP substrate [1]. This QCL performed with a strong and narrow-linewidth emission at a wavelength of 4.2 micrometers (μm) with peak powers over 8 milliwatts (mW) in pulse-mode operation. In 2002, the first working MIR QCL operating on continues-wave (cw) mode at RT was achieved by Beck *et al.* based on the same material system with an optimized active region design and fabricated into buried heterostructure (BH) to improve heat dissipation [11]. This cw mode laser device has an optical output power range from 17 mW at 292 K to 3 mW at 312 K, at an emitting wavelength of 9.1 μm. The cw operation at RT is a milestone for MIR QCLs. In the following two decades, the performance of MIR QCLs has been significantly improved. In 2020, Razeghi's group at Northwestern University reported the world-record-high η_w of MIR QCLs at 31% and 22% on pulse mode and cw mode at RT operation, respectively, with the optical output power of 23 W (peak power on pulse mode) and 5.6 W (on cw mode), respectively [5][12].

One of the most important tuning factors determining the lasing performance of MIR QCLs is the active region design. There are four types of material systems: InP-based GaInAs/AlInAs, GaAs-based GaAs/AlGaAs, antimonide compound (InAs-based InAs/AlSb, InP-based InGaAs/AlAsSb, and InP-based InGaAs/AlGaAsSb), and InAs/GaSb/AlSb based material systems [2][13]. The first three belong to type-I superlattices, and the last one belongs to type-II superlattices.

To date, with the development and maturity of epi-layer growth and device fabrication, the best performing MIR QCLs are based on the techniques stated as follows. The active region layers are firstly grown by MBE, followed by MOCVD re-growth for the cladding layers forming buried heterostructure. The laser cavities are processed standard Micro-fabrication technique into Fabry–Pérot (FP) ridge waveguides or distributed feedback (DFB) waveguides. After electroplating, wafer thinning, bar cleaving, and facet coating, the laser device is with epi-layer down mounting on a high thermal conductive heatsink to accomplish a high heat dissipation efficiency.

Although there are significant achievements in research regarding MIR QCLs, for THz QCls, the progress is far more behind. One of the main challenges for THz QCLs is to achieve RT operation [14][15][16]. Due to the even narrow energy gap for electron transitions towards lasing emission in THz range (4-40 meV), which is comparable to the LO phonon energy of GaAs (36 meV at 300 K), the population inversion is suppressed by thermal-activated phonon scattering. Therefore, it is extremely difficult to achieve RT operating THz QCLs. Although non-linear effect strategies by difference frequency generation (DFG) - QCLs are employed to realize RT operation in THz range, the peak output power is relatively low: up to 1.9 mW with ~0.1-1m W/W^2 power conversion efficiency on pulsed mode [17][18], compared to up to Watt-level output power of a single THz QCL (peak power in cryogenic temperature) [19].

In 2002, when the first RT cw mode MIR QCL was demonstrated, the first working THz QCL was invented by Köhler *et al.* [4]. A novel active region design was presented by employing chirped superlattice for QCLs fabricated as semi-insulating surface-plasmon (SI-SP) waveguides. The device lases at a frequency of 4.4 THz with maximum optical power of ~2 mW up to 50 K. In the following two decades, novel design schemes in active region structures were proposed for a single and ultimate goal: towards RT operation [14][15][16]. These design schemes include chirped superlattice [4], bound-to-continuum [20], resonant-phonon [21], scattering-assisted [22], phonon-photon-phonon [23], and two-well direct phonon [24]. In 2012, Fathololoumi *et al.* of Ban's group at University of Waterloo

reported a maximum temperature (T_{max}) at 200 K on pulsed mode operating THz QCL by optimizing the resonant-phonon scheme [25], a milestone for THz QCLs. In the following seven years, none of the new design schemes broke this record until 2019, where Faist's group at ETH reported the first thermal electrical cooled (TEC) THz QCL operating at T_{max} of 210 K by introducing a two-well direct-phonon scheme [24]. One years later in 2020, Hu's group at MIT further pushed T_{max} up to 250 K by optimizing the two-well direct-phonon scheme [26]. This result demonstrates a promising and practical application for portable THz QCLs system by only applying a single stage TEC module.

1.2 Challenges for Mid-infrared Quantum Cascade Lasers (MIR QCLs): Joule Heating Effect

MIR QCLs operating at an atmospheric transparent window of 8–14 μm have multiple applications in various fields such as remote sensing, chemical and trace gas analysis, industrial process control, biomedical application, infrared countermeasures, and free space optical communications [13][27][28][29]. As mentioned in section 1.1, MIR QCLs are power-hungry devices which consume over 10 W before reaching the lasing threshold, leading to a low electro-optical power conversion efficiency (wall-plug efficiency). In other words, they emit more heat than light [27][29]. Consequently, as the pulse width injection increases (from pulse mode to quasi-cw mode), the Joule heating gradually increases, where the average temperature in the active region core is much larger than the heatsink temperature, as shown in Figure 1.2. This effect decreases the device's maximum operating temperature and reduces the optical output power.

RT cw mode lasing operation of MIR QCLs has been achieved since 2002 [11]; nonetheless, the maximum wall-plug efficiency (η_w) of MIR QCLs operating at RT is still limited: up to 31% and 22% under pulse-mode and cw mode operation, respectively [5][12]. Due to large electrical power consumption and low anisotropic thermal conductivity of the multilayer heterostructures, the excess Joule heating localized inside the active region is still an obstacle to optimizing lasing performance [29][30][31]. As the increase of the pulse width injection, this Joule heating accumulated in the device active region drastically raises the device's internal temperature [31]. It lowers wall-plug efficiency and optical output power, eventually leading to long-term device degradation or even catastrophic failure [32]. Clearly, as the Joule heating increases, the heat dissipation plays a critical role in MIR QCLs lasing performance. Indeed, it is crucial to understand the internal heat dynamics of a laser from the

perspective of designing the active region and developing a better heat management technique. Real-time two-dimensional (2D) internal temperature profiling directly reveals where heat is generated and how heat is dissipated, providing insights based on where the best strategy for MIR QCLs thermal management can be found.

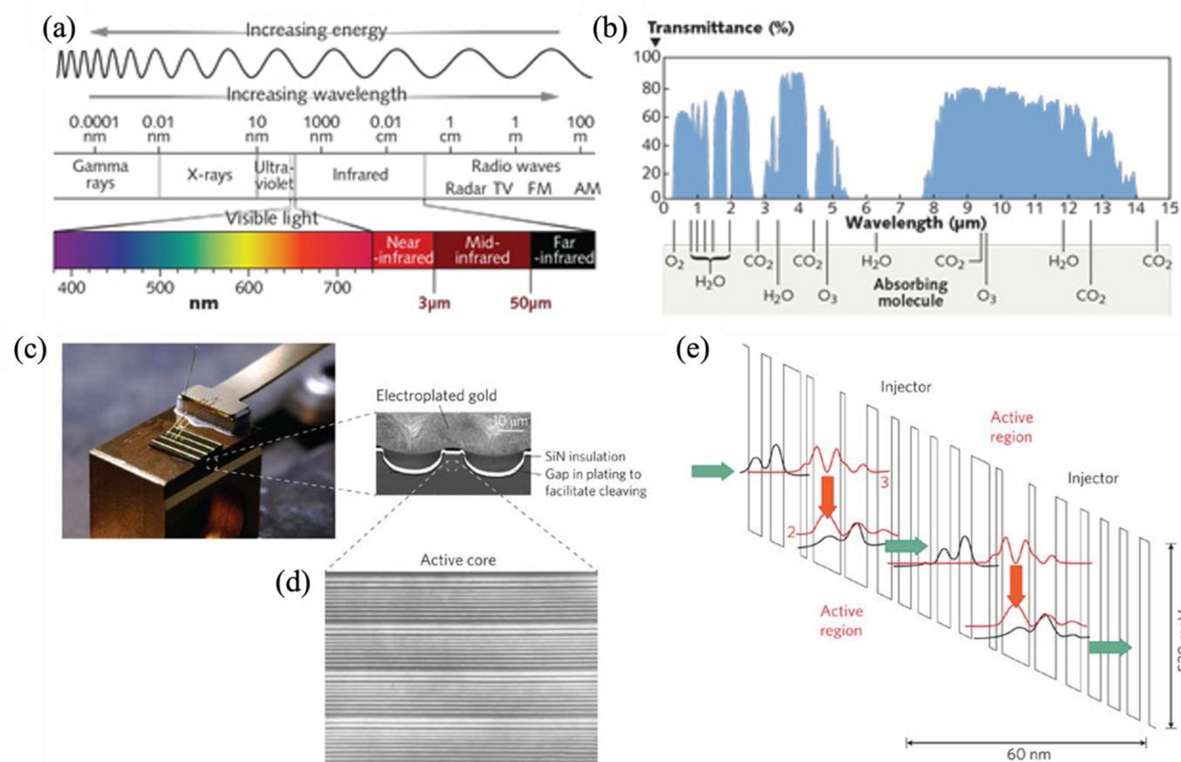

Figure 1.1 (a) Mid-infrared range (3 – 50 μm) in electromagnetic spectrum; (b) atmospheric window (3-5 μm and 8-14 μm) with high transmittance in infrared range; (c) photograph of a mounted laser bar with four wire-bonded MIR QCLs in Fabry–Pérot (FP) ridge waveguides; (d) scanning electron microscope (SEM) imaging of one of the MIR QCLs' cleaved facet, showing repeating multiple quantum wells (MQWs) modules in the active region core; (e) simplified conduction band diagram for a MIR QCL, where the lasing transition from the upper lasing level (3) to the lower lasing level (2). [Adapted with permission from Ref. [13] © 2012 Springer Nature Publishing]

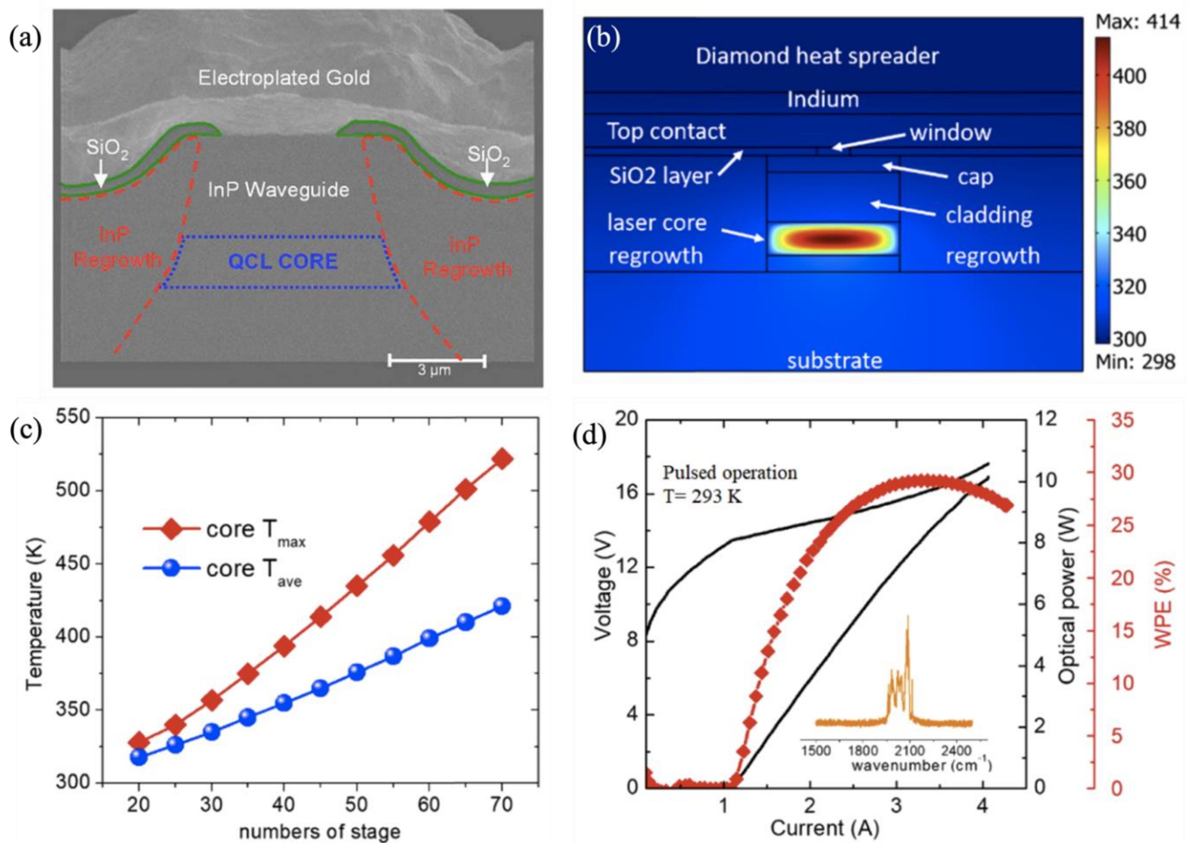

Figure 1.2 (a) Cross-sectional SEM image of a MIR QCL ridge facet in buried heterostructure (BH); (b) simulated 2D temperature distribution of a buried ridge MIR QCL epi-down bonded on a diamond heatsink for cw operation; (c) The maximum (T_{max}) and average (T_{ave}) temperature of the active region (laser core) of the buried ridge MIR QCL under cw operation as a function of QCL stages; (d) the light-current-voltage (L-I-V) curves and extracted wall-plug efficiency (WPE) for a 5 mm length MIR QCL ridge waveguide. [Adapted with permission from Ref. [12] © 2020 Optica Publishing Group and Ref. [33] © 2007 AIP Publishing]

1.3 Challenges for Terahertz Quantum Cascade Lasers (THz QCLs): Higher Operating Temperature Limitation

The far-infrared radiation region, also known as terahertz region or terahertz gap (1-10 THz/ 30-300 μm/ 4-40 meV) has unique properties with "fingerprint region" for molecular rotational and vibrational band, as shown in Figure 1.3. It can penetrate non-conduction materials such as paper, wood, and cloth, showing promising applications in spectroscopy, remote sensing, trace-gas analysis, biomolecule

detection, real-time imaging, and free space communication [34][35]. Terahertz applications are developing rapidly; nevertheless, the terahertz region's laser sources are still limited. The narrow energy gap between the UL level and the LL level in the terahertz range (4-40 meV) makes it inaccessible for conventional semiconductor laser diodes which are based on interband transitions. Other approaches, such as solid-state device and optically pumped gas lasers, are also limited by low optical output power, poor tuning range of lasing frequency, and low conversion efficiency [34][36].

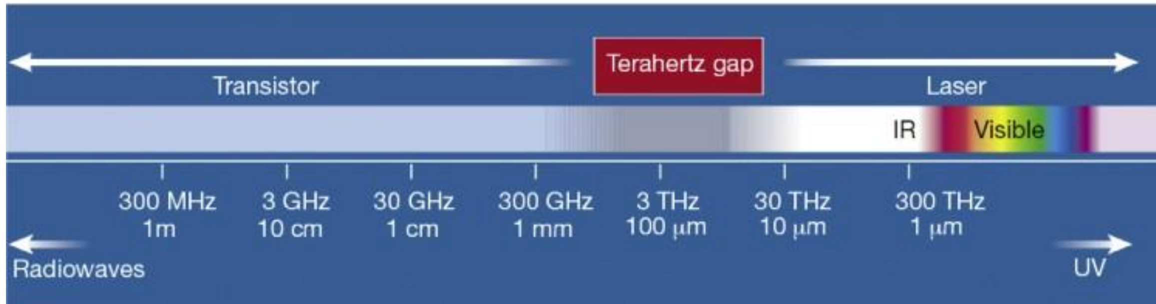

Figure 1.3 Terahertz gap in the electromagnetic spectrum. [Reprinted with permission from Ref. [3] © 2002 Springer Nature Publishing]

On the other hand, THz QCLs are based on intersubband transitions, which are compatible with terahertz emissions. However, the thermal activated LO-phonon scattering (36 meV for GaAs at RT) dramatically reduces the population inversion. It deteriorates the lasing performance, making it extremely difficult to achieve room temperature operation. Therefore, developing high-performance THz QCLs for covering the entire terahertz range is highly demanded.

To date, high-temperature, high-power, and continuous-wave (cw) operating terahertz quantum cascade lasers (THz QCLs) are of great interest, as cw operation can provide frequency stabilization and phase locking for broadband frequency comb [15]. However, the requirement of cryogenic cooling is still an obstacle to the practical applications of THz QCLs. Due to the limitations of the physical properties (e.g., low electro-optical power conversion efficiency and high series resistance before reaching the threshold), THz QCLs are subject to a great deal of power consumption (e.g., several watts in DC biased) and Joule heating issues, leading to impediments for optical performances. So far, the maximum operating temperature (T_{max}) of pulsed mode THz QCL has been pushed up to 250 K in a single-stage thermal electrical cooler (TEC) system [26]. On the other hand, the record-high operating temperature on cw mode THz QCL is still limited to 129 K with a low optical output power of less than

0.1 mW [37]. Therefore, there is a large T_{max} gap between pulsed and cw modes, mainly due to the Joule heating and insufficient heat extraction. In the past two decades since the initiation of THz QCLs in 2002 [4], a large majority of the research activities in this field focused on active region design and optimized waveguide structure to push up THz QCLs T_{max} on pulse mode. The thermal management structure towards cw mode operation has also been increasingly demanding.

On pulsed mode, the active region temperature is almost the same as the heat sink temperature. However, when the device operates on cw mode, the Joule heating effect leads the active region temperature to be much higher than the heatsink temperature. For example, as illustrated in Figure 1.4, the active region temperature on the laser facet is 20-30 K above the heatsink temperature when the device is biased under cw mode from a thermal modeling, reported by B. Williams in [38]. In this case, the main issue is the inefficient heat extraction and dissipation towards the heat sink, leading to a degradation of lasing performance. The T_{max} on pulsed and cw mode are 164 K and 117 K, respectively, with 47 K of difference, as shown in Figure 1.5 [38]. Nevertheless, the threshold current density (J_{th}) at its T_{max} is relatively close: 810 A/cm^2 on pulsed mode and 835 A/cm^2 on cw mode. This phenomenon indicates a considerable temperature rise inside the active region core with poor heat extraction from the heatsink materials. This restrains the optical performance under cw operation towards higher operating temperature.

Therefore, it becomes requisite for heat removal engineering to lower the thermal resistance for THz QCLs. Typically, bulk gallium arsenide (GaAs) is employed as the receptor substrate for the heatsink submount on THz QCLs in metal-metal (MM) waveguides. However, GaAs is a poor material with low thermal conductivity, producing only 55 W/(m·K) at 300 K compared with other massive used bulk semiconductor materials, such as silicon (Si) and aluminum nitride (AlN). In this case, the high thermal conductivity heatsink submount with hybrid integration is a promising strategy for improving heat dissipation efficiency.

There are three requirements for submount heatsink materials: high thermal conductivity; low mismatch of the coefficient of thermal expansion (CTE) between THz QCLs and the heatsink; and the availability of materials and processing techniques. Among these materials, Si and AlN are good candidates, especially for AlN, which gives high thermal conductivity (180 – 230 W/(m·K)) and low CTE mismatch compared with GaAs (AlN: 4.5×10-6 K-1, GaAs: 5.9×10-6 K-1) [39-49]. The low CTE mismatch can minimize the undesired stress on laser structure induced by thermocompression bonding

process. In order to form gold-gold (Au-Au) ridge waveguides of THz QCLs on hetero substrate, THz QCLs are fabricated on its intrinsic GaAs substrate first, followed by thermocompression bonding on hetero substrate and substrate liftoff process. This process technique reduces the bonding contact areas, and it facilitates the minimization of the thermal-induced bonding stress between THz QCLs and the heatsink submount materials resulting from the CTE mismatch.

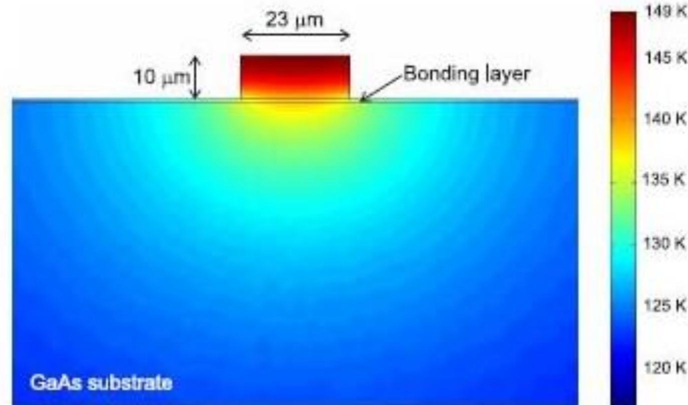

Figure 1.4 Simulated 2D temperature distribution on the laser facet of a narrow ridge THz QCL in metal-metal waveguide on GaAs substrate under cw operation (power density at 1.1×10^7 W/cm^3) [Reprinted with permission from Ref. [38] © 2005 Optica Publishing Group]

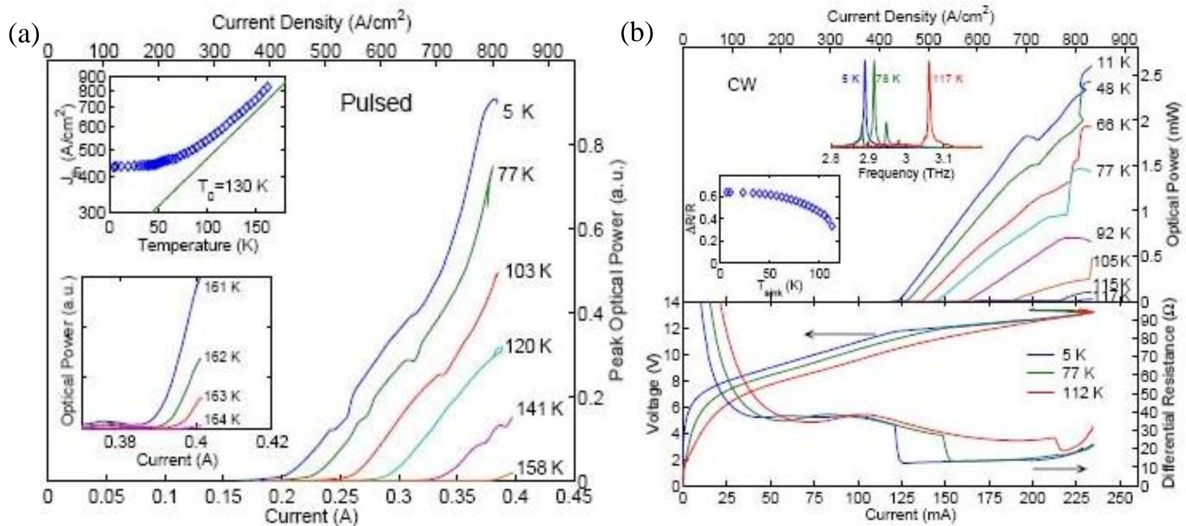

Figure 1.5 Temperature-dependent L-I-V curves of the THz QCL under pulse mode (a) and cw mode (b). [Adapted with permission from Ref. [38] © 2005 The Optical Society]

1.4 Motivation and Research Objectives

The first primary objective is to investigate the thermal dynamics of MIR QCLs. Joule heating is detrimental, suppressing QCL's lasing performance with increased pulse width injection. However, there is still a lack of direct evidence for understanding the thermal dynamics of the device, especially in a high temporal and spatial resolution. Therefore, a systematic study is implemented by employing spatially resolved time-domain thermoreflectance (SR-TDTR) microscopy as a tool for imaging the thermal dynamic behaviours of an actively-biased QCL down to tens-of-nanoseconds (temporal resolution) and hundreds of nanometers (spatial resolution). The experimental results reveal that the heat accumulation in device active region starts even within less than 1 μs upon the application of electric current injection. It is found that within 1-2 μs, the heat dissipation to the top cladding is substantially reduced, and most of the heat is drained to the substrate through the bottom cladding layer, which eventually leads to thermal quenching of lasing operation. These results are also confirmed by combining light-current-voltage (L-I-V) measurements and theoretical thermal modelling. Thus, the SR-TDTR provides direct evidence of thermally-induced lasing quenching of QCLs, and it is an enabling tool to probe the internal dynamics of operating actively-biased devices.

The second major objective is to investigate the thermal behaviours of THz QCLs on different thermal management schemes (transfer bonding THz QCLs on hetero substrate in metal-metal waveguides compared with the conventional THz QCLs in metal-metal waveguides bonded on GaAs receptor) in long pulse injection from pulse mode towards quasi-cw mode operation. The optimized thermal management by hybrid integration is to achieve higher T_{max} for THz QCLs towards cw operation. This strategy reduces the internal temperature rise in active region and boosts a higher thermal dissipation efficiency. A diagram of the goals and objectives is shown in Figure 1.6.

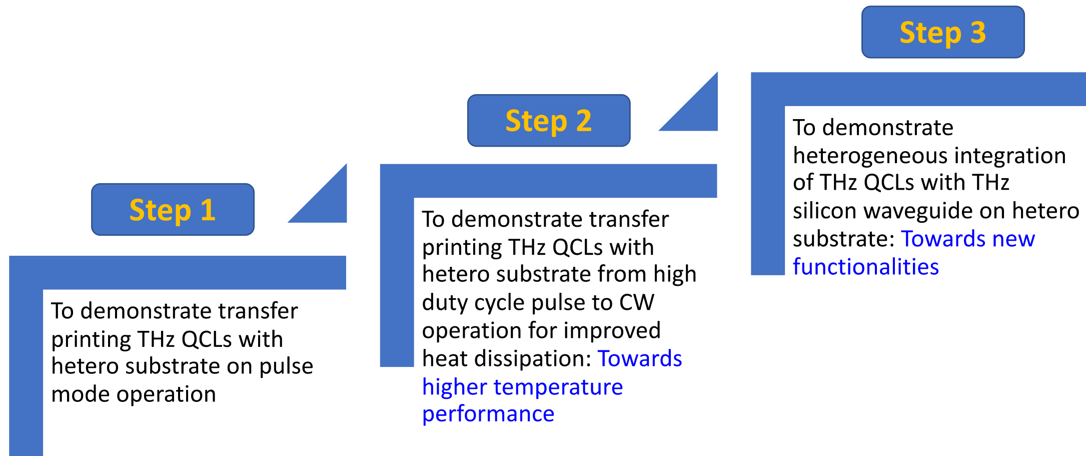

Figure 1.6 Objectives and goals for high performance THz QCLs

This study demonstrates a hybrid integration of THz QCLs on hetero substrates with higher thermal conductivity materials (e.g., Si and AlN), showing a comparable T_{max} operation on pulse mode with the conventional bonding strategies on GaAs. With the increase of the pulse width injection up to 40 μs, the THz QCL bonded on AlN shows a higher operating temperature compared to the THz QCL bonded on GaAs receptor substrate. In this study, THz QCLs are fabricated into ridge waveguides on the intrinsic as-grown GaAs substrate first, followed by metal-metal (MM) thermocompression bonding on hetero substrates. After device fabrication, temperature dependent L-I-V is characterized the electrical and optical properties on each device on pulse mode. At different heatsink temperature, the pulse width injection along with the duty cycle is tuned from pulse mode to quasi-cw mode. The thermal effect strongly suppresses the device lasing performance, as the internal temperature rise in active region increases with the pulse width injection. This study shows a higher heat dissipation efficiency of THz QCL bonded AlN compared with on its intrinsic GaAs receptor substrate. The Methodology flow chart is shown in Figure 1.7.

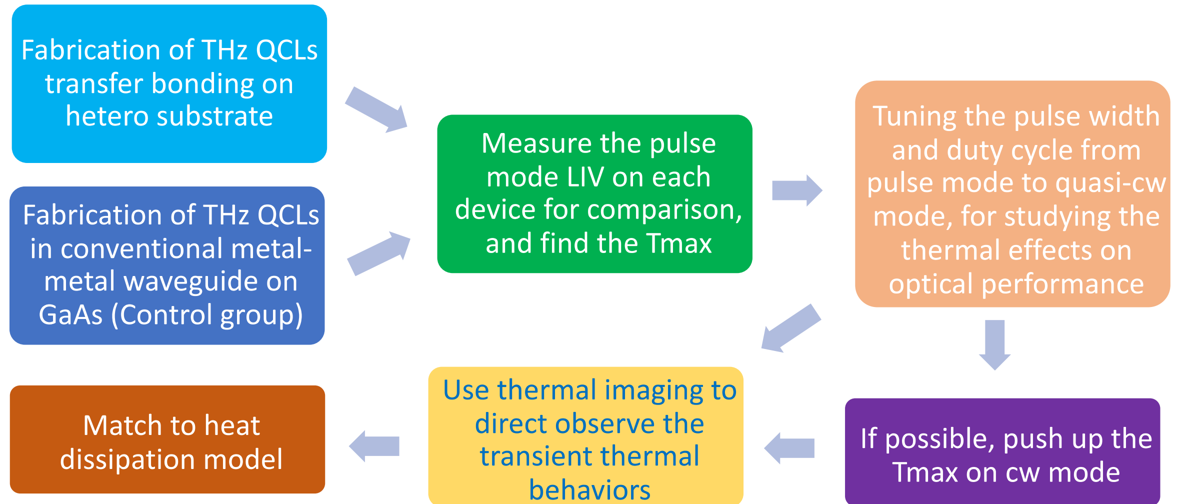

Figure 1.7 Methodology flow for the experiments

1.5 Thesis Organization

This dissertation is organized as follows.

Chapter 1 briefly introduces the current challenges for MIR QCLs and THz QCLs, towards higher optical performance and efficient thermal management. Also, the research objectives and the thesis organization are elaborated.

Chapter 2 discusses the basic theory of the heat transfer model. A series of equations are derived based on Fourier's Law and the heat equation. Also, a brief introduction of the Thermoreflectance Microscopy is enclosed.

Chapter 3 studies and demonstrates the thermal dynamics imaging on MIR QCLs from transient state to thermal equilibrium by SR-TDTR microscopy, showing high spatial resolution (390 nm), temporal resolution (50 ns), temperature resolution (0.1 K), simultaneously. The results show a thermal surge up to 100 degrees higher in the active region above the heatsink temperature in a 500 ns pulse injection (I = 6 A), and the lasing quenching occurs when the pulse width injection is above 2 μs (I = 2.375 A) when the internal temperature rises above the threshold operating temperature.

Chapter 4 investigate the thermal properties and optical performance of MIR QCLs with different ridge width. In this chapter, ridge width-dependent thermal and optical properties of MIR QCL are characterized by SR-TDTR microscopy and L-I-V measurements. The results show a trade-off between the optical performance and the thermal effect. The narrow ridge-width device has a lower Joule heating on the facet due to the higher thermal conductance. On the other hand, it has a higher threshold current density due to the higher optical loss.

Chapter 5 discusses the facet Joule heating of MIR QCLs. This chapter investigates reversible lasing performance degradation on an actively-biased facet-uncoated $GaAs/Al_{0.45}Ga_{0.55}As$ mid-infrared quantum cascade laser (MIR-QCL), when the device is undergone an accelerated aging burn-in test, followed by hydrogen plasma treatment. It is found that thermal-induced facet oxidation is the primary reason for the rapid degradation of the lasing performance in the early aging stage.

Chapter 6 compares two strategies for fabricating THz QCLs in metal-metal waveguides toward high thermal dissipation efficiency. The first one is a conventional methodology by bonding THz QCLs on its intrinsic GaAs receptor substrate. The second is a novel strategy by hybrid-integrating THz QCLs on hetero substrates such as AlN and Si as high thermal conductivity materials to improve the heat dissipation efficiency. The results show that at a long pulse duration (e.g., 4% of duty cycle), the THz QCL on AlN substrate has more than 10 degrees of maximum operation temperature (T_{max}) than THz QCL on GaAs. Also, the hybrid integration of AlGaAs/GaAs-based THz QCL on Si waveguides is discussed towards near-field and far-field beam pattern improvement and higher efficiency light coupling.

Chapter 7 outlines the conclusions and contributions of this thesis and discusses future work.

Chapter 2
Thermal Dynamics Model and Thermoreflectance Microscopy

2.1 Theory of Heat Transfer Model

2.1.1 Fourier's Law in General Form

Fourier's law is an empirical relationship between the conduction rate in a material and the temperature gradient in the direction of energy flow, firstly proposed and formulated by Joseph Fourier in 1822. It states the rate of heat transfer (heat flux) is proportional to the magnitude of the temperature gradient in negative sign. For an isotropic medium, Fourier's law is given by [50]

$$\overrightarrow{\phi_q} = -k\nabla T \qquad (eq. 2.1)$$

where, $\overrightarrow{\phi_q}$ in positive sign is defined as the net heat flux out from the medium, ∇T is the temperature gradient in three dimensions (3D), and k is the material's thermal conductivity.

2.1.2 Heat Equation in General Form

Consider the internal heat is transferring inside a uniform and isotropic layer. Let $Q = Q\ (x, y, z, t)$ be the time-dependent internal heat energy per unit volume, $T = T\ (x, y, z, t)$ is the time-dependent temperature distribution, and $\overrightarrow{\phi_q} = \overrightarrow{\phi_q}(x, y, z, t)$ is the time-dependent heat flux given by

$$\overrightarrow{\phi_q}(x, y, z, t) = -k\nabla T \qquad (eq. 2.2)$$

In absence of any heat energy generation from external or internal source, the rate of change in internal heat energy per volume in the material, $\partial\Delta Q(t)/\partial t$, is proportional to the rate of change of its temperature, that is

$$\frac{\partial\Delta Q(t)}{\partial t} = \rho C_p \frac{\partial T}{\partial t} \qquad (eq. 2.3)$$

where ρC_p is the volumetric heat capacity.

As the law of conservation of energy, for a small element in linear space, the rate of heat change at a given point is equal to a negative rate of the net energy dissipation (the derivative of the heat flux at that point in negative sign), that is,

$$\frac{\partial \Delta Q(t)}{\partial t} = -\frac{\partial Q_{out}(t)}{\partial t} = -\nabla\overrightarrow{\phi_q} \qquad (eq. 2.4)$$

Therefore,

$$\frac{\partial \Delta Q(t)}{\partial t} = -\nabla\overrightarrow{\phi_q} = -\nabla \cdot (-k\nabla T) = k\nabla^2 T \qquad (eq. 2.5)$$

Take (eq. 2.3) and (eq. 2.5) together, then,

$$\frac{\partial T}{\partial t} = \frac{k}{\rho C_p}\nabla^2 T \qquad (eq. 2.6)$$

(eq. 2.6) can be also written as

$$\frac{\partial T}{\partial t} = \alpha \cdot \nabla^2 T \qquad (eq. 2.7)$$

where α is the thermal diffusivity, measuring the rate of transfer of heat of a material from the hot end to the cold end, given by

$$\alpha = \frac{k}{\rho C_P} \qquad (eq. 2.8)$$

Hence, (eq. 2.7) is the heat equation in general form.

2.1.3 Heat Equation with External Power Injection

Considering there is an external energy injection Q_{in} to a medium, in this case, the internal rate of energy density change with time is equal to the net power flow out from the medium, negated, where is

$$\frac{\partial \Delta Q(t)}{\partial t} = -\left(\frac{\partial Q_{out}(t)}{\partial t} - \frac{\partial Q_{in}}{\partial t}\right) \qquad (eq. 2.9)$$

Let $q_{in} = \partial Q_{in}/\partial t$ be the injection power density. From (eq. 2.3) and (eq. 2.5), we can get

$$q_{in} = \rho C_p \frac{\partial T}{\partial t} - \nabla \cdot (k\nabla T) \qquad (eq. 2.10)$$

Therefore, (2.10) is the heat equation with external power injection.

2.1.4 Fourier's Law in Steady-State with External Power Injection

Equation (2.10) describes the heat transfer in transient state with external power injection. In thermal equilibrium (steady-state), however, the internal temperature of the medium does not change with the time ($\partial T/\partial t=0$). In this case, the density of power injection is equal to the density of power dissipating out from the medium, where is

$$q_{in} = q_{out} = -\nabla \cdot (k\nabla T) \qquad (eq. 2.11)$$

The heat flux injection and dissipation are also the same, where is

$$\overrightarrow{\phi_q}(in) = \overrightarrow{\phi_q}(out) = -k\nabla T \qquad (eq. 2.12)$$

(2.12) is the Fourier's law in steady-state, which can be used to determine and calibrate the thermal conductivity, k, and the thermal resistance, R_{th}.

2.1.5 Fourier's Law in Transient State with External Power Injection

In some cases, we are interested in the thermal dynamics of QCL devices in transient state on pulsed mode in high current injection, and the heat transfer equation is given by (eq. 2.10). Before thermal equilibrium condition is reached ($\partial T/\partial t=0$), the heat flux out of the medium is always smaller than the heat flux injection, given that

$$\overrightarrow{\phi_q}(out) = \overrightarrow{\phi_q}(in) - \int_0^d \rho C_p \frac{\partial T}{\partial t} dl = -k\nabla T \qquad (eq. 2.13)$$

where dl is the small linear element in heat flow direction.

Also, the amount of power dissipating out from the active region can be written as

$$P_{out} = P_{in} - \rho C_p \frac{\partial}{\partial t} \iiint_V T(x, y, z, t) \cdot dv = -k \oiint_S \nabla T \cdot dS \qquad (eq. 2.14)$$

where *dS* and *dv* are the small elements of area and volume, respectively. Therefore, in transient state with external power injection, (2.13) and (2.14) are the derivative and integral forms of Fourier's law, respectively.

2.1.6 Fourier's Law with Anisotropic Thermal Conductivity

Other than the isotropic thermal conductivity of bulk GaAs, the thermal conductivity of GaAs/AlGaAs based MIR QCLs and THz QCLs is anisotropic, which can be split into two orthogonal components: in-plane thermal conductivity ($k_{\parallel}$) and cross-plane thermal conductivity ($k_{\perp}$). A schematic diagram is shown in Figure 2.1 Schematic diagram of heat flux dissipates out from the QCL's active region. The value of $k_{\parallel}$ is comparable to the bulk GaAs, but $k_{\perp}$ is typically one order of magnitude lower than $k_{\parallel}$ or k_{bulk} due to the thermal boundary resistance (TBR) [51]. Therefore, the 3D time-dependent heat flux out from the active region can be written as

$$\overrightarrow{\phi_q}(out) = -\{k_{\parallel}[\nabla T(x) + \nabla T(y)] + k_{\perp}\nabla T(z)\} \qquad (eq. 2.15)$$

Different from phonon-phonon interaction scattering processes in bulk GaAs, the cross-plane thermal conductivity ($k_{\perp}$) of GaAs/AlGaAs superlattices (SLs) is dominated by TBR, which is originating from phonon scattering/reflection at the SLs interfaces. There are two mechanisms regarding. First is the Al fraction induced (from the barrier layers at well/barrier interface) interface roughness phonon scattering [52]. The second is the layer thickness of barrier/well is much thinner than the phonon mean free path [53]. For the first mechanism, even in the best-quality lattice matched SLs, atomic scale interface roughness still exists, which breaks the phonon phase coherence (phonons suffer from phase-breaking scattering in rough-interface SLs). For the second one, a phonon will be reflected or transmitted at multiple interfaces before it is scattered within a layer of the SLs. Considering these two mechanisms, therefore, the $k_{\perp}$ of GaAs/AlGaAs SLs is much lower than the thermal conductivity of bulk GaAs. For example, at room temperature (295 K), $k_{\perp}$ of GaAs/AlGaAs is one order of magnitude (4-6 $W \cdot m^{-1} \cdot K^{-1}$) lower than k of bulk GaAs (55 $W \cdot m^{-1} \cdot K^{-1}$). Also, $k_{\perp}$ of GaAs/AlGaAs SLs varies very little as the temperature changes (temperature-independent), indicating that TBR indeed dominates the thermal transport across SLs layers [51]. Simulations of the temperature dependent thermal conductivity and heat capacity are shown in Figure 2.2 Temperature dependence of thermal conductivity (cross-plane in k_y and in-plane in k_x) and heat capacity of AlGaAs/GaAs superlattices in active region

and GaAs substrate. [Adopted with the permission from Ref. **[54]**, IEEE copyright line © 2011 IEEE], adopted from Ref. [54].

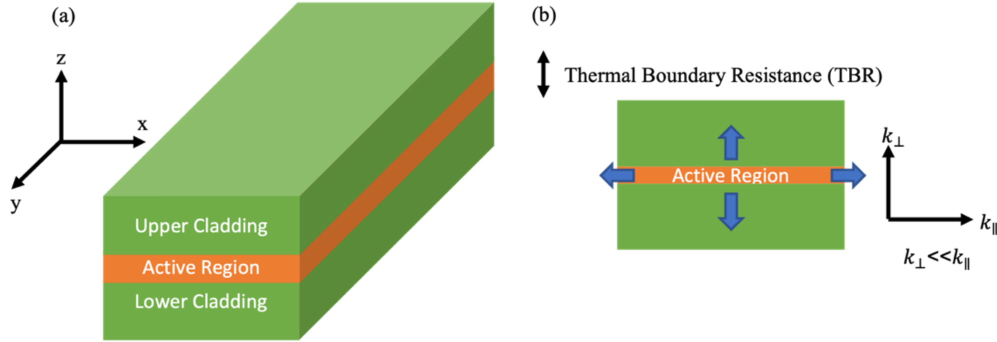

Figure 2.1 Schematic diagram of heat flux dissipates out from the QCL's active region

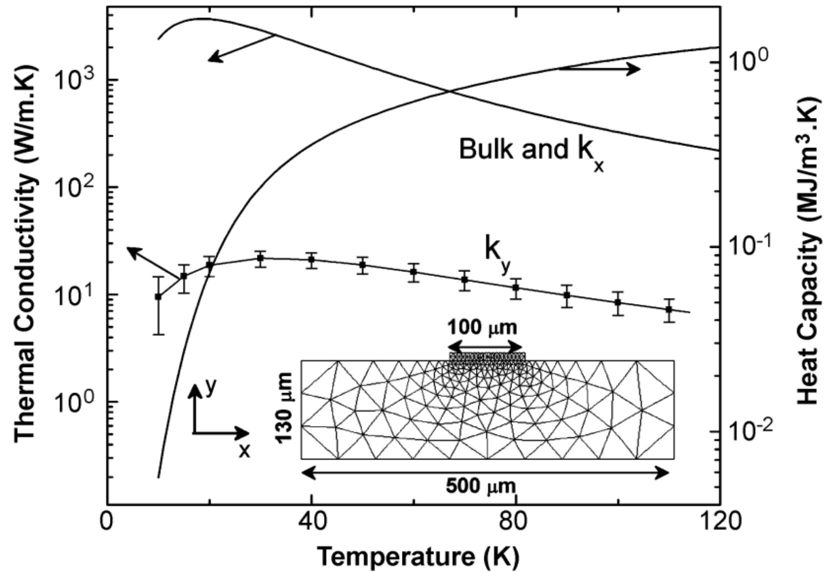

Figure 2.2 Temperature dependence of thermal conductivity (cross-plane in k_y and in-plane in k_x) and heat capacity of AlGaAs/GaAs superlattices in active region and GaAs substrate. [Adopted with the permission from Ref. [54], IEEE copyright line © 2011 IEEE]

2.1.7 Thermal Resistance Across QCLs' Active Region

In most cases, the total thermal resistance, R_{th}, is typically used to characterize the thermal properties of the QCLs devices, which equals to the series resistances of TBR in the active region and the bulk resistance of GaAs in the substrate and the cladding layers, given by

$$R_{th} = TBR + R_{bulk} \quad (eq. 2.16)$$

where $TBR \gg R_{bulk}$.

In thermal equilibrium (steady-state), the total thermal resistance (R_{th}) of the QCLs devices can be simply determined by

$$R_{th} = \frac{\Delta T_{SS}}{P_{diss}} = \frac{\Delta T_{SS}}{P_{in} - P_{out}} \quad (eq. 2.17)$$

where $\Delta T_{SS} = T_{AR} - T_{HS}$ is the maximum temperature rise at the active region layer above the heatsink temperature in steady-state, and P_{diss} is the dissipated power consumption, which equals to the electrical injected power (P_{in}) minus the optical output power (P_{out}). If the optical output power is much smaller comparable with the injection driven power, the total thermal resistance of the QCL can also be written as

$$R_{th} \approx \frac{\Delta T_{SS}}{P_{in}} \quad (eq. 2.18)$$

As discussed in section 2.1.6, due to the TBR (resulting from the phonon reflection at interface roughness scattering by a large aluminum fraction in SLs) is dominant across the epitaxial layers of the QCLs, the thermal conductivity of the active region layer is anisotropic, and $k_{\perp}$ is typically one order of magnitude smaller (~5.5 $W \cdot m^{-1} \cdot K^{-1}$ for AlGaAs/GaAs superlattice structure at room temperature) than $k_{\parallel}$ as well as the bulk III-V material's substrate (55 $W \cdot m^{-1} \cdot K^{-1}$ for GaAs bulk material at room temperature).

From equation (2.15), net heat flow out from the active region core can be grouped in lateral (in-plane) and vertical (cross-plane) channels, given that

$$\overrightarrow{\phi_q}(out) = -\left[\overrightarrow{\phi_q}(out)_{\parallel} + \overrightarrow{\phi_q}(out)_{\perp}\right] \quad (eq. 2.19)$$

where

$$\overrightarrow{\phi_q}(out)_{\parallel} = -k_{\parallel}[\nabla T(x) + \nabla T(y)] \quad (eq. 2.20)$$

$$\overrightarrow{\phi_q}(out)_{\perp} = -k_{\perp}\nabla T(z) \quad (eq. 2.21)$$

Let Γ is the portion of the heat flow in cross-plane direction channel to the total heat flow in steady-state, then,

$$\overrightarrow{\phi_q}(out)_\perp = \Gamma \cdot \overrightarrow{\phi_q}(out) \qquad (eq.\,2.22)$$

$$\overrightarrow{\phi_q}(out)_\parallel = (1-\Gamma) \cdot \overrightarrow{\phi_q}(out) = \frac{1-\Gamma}{\Gamma}\overrightarrow{\phi_q}(out)_\perp \qquad (eq.\,2.23)$$

Considering the heat flow is propagating along the z-axis (cross-plane), and the heat is extracted from the active region towards upper cladding layer and the bottom cladding layer. Then, the cross-plane temperature gradient at the active region – cladding layers interfaces can be written as

$$\nabla T(z) = \nabla T(z)_{up} + \nabla T(z)_{down} \qquad (eq.\,2.24)$$

$$\nabla T(z)_{up} = \left(\frac{\partial T}{\partial z}\right)_{up} = -\beta_1 \cdot \frac{\Delta T_{SS}}{d} \qquad (eq.\,2.25)$$

$$\nabla T(z)_{down} = \left(\frac{\partial T}{\partial z}\right)_{down} = -\beta_2 \cdot \frac{\Delta T_{SS}}{d} \qquad (eq.\,2.26)$$

where d is the active region layer thickness; β_1 and β_2 is the coefficient of the heat extraction towards upper cladding layer and the lower cladding layer, respectively. The higher the β, the higher the heat extraction efficiency. Therefore, the cross-plane heat flow is

$$\overrightarrow{\phi_q}(out)_\perp = -k_\perp\left(\nabla T(z)_{up} + \nabla T(z)_{down}\right) = k_\perp \cdot \frac{\Delta T_{SS}}{d} \cdot (\beta_1 + \beta_2) \qquad (eq.\,2.27)$$

As $TBR \gg R_{bulk}$, we can assume that most of the heat is generated at the active region layer; in thermal equilibrium, the heat flux flowing in is equivalent to the heat flux flowing out, as $\overrightarrow{\phi_q}(in) = \overrightarrow{\phi_q}(out)$. Hence, the total injection power is the sum of the heat flow multiplied by the flowing cross-section area, given that

$$P_{in} = \overrightarrow{\phi_q}(out)_\perp \cdot wl + \overrightarrow{\phi_q}(out)_\parallel \cdot (wd + ld) \qquad (eq.\,2.28)$$

where w is ridge width and l is the cavity length. As $l \gg w$, equation (2.28) can also be written as

$$P_{in} = \overrightarrow{\phi_q}(out)_\perp \left(wl + dl \cdot \frac{1-\Gamma}{\Gamma}\right) = k_\perp \cdot \frac{\Delta T_{SS}}{d} \cdot (\beta_1 + \beta_2) \cdot A\left(1 + \frac{d}{w} \cdot \frac{1-\Gamma}{\Gamma}\right) \qquad (eq.\,2.29)$$

where $A=wl$ is the ridge area in xy plane. Therefore, the total thermal resistance of the QCL ridge waveguide is

$$R_{th} = \frac{d}{k_\perp \cdot A \cdot (\beta_1 + \beta_2)} \cdot \left(1 + \frac{d}{w} \cdot \frac{1-\Gamma}{\Gamma}\right)^{-1} \qquad (eq.\,2.30)$$

Also, the thermal conductance per unit area is

$$G_{th} = \frac{1}{R_{th} \cdot A} = (\beta_1 + \beta_2) \cdot \frac{k_\perp}{d} \cdot \left(1 + \frac{d}{w} \cdot \frac{1 - \Gamma}{\Gamma}\right) \qquad (eq. 2.31)$$

From equation (2.31), clearly, to achieve higher G_{th} of QCLs requires higher across-plane thermal conductivity ($k_\perp$), smaller device dimension (thinner d and narrower w), and efficient thermal dissipation draining to the surrounding medium. For example, epi-side down mounted buried heterostructure (BH) MIR QCLs has efficient heat extraction both in in-plane and cross-plane channels, which can lower Γ, In addition, epi-side down mounting can give higher heat extraction efficiency (higher β_1 and β_2). Therefore, the total thermal resistance R_{th} is reduced.

Also, (2.32) can be used to determined and calibrate the cross-plane thermal conductivity $k_\perp$, given that

$$k_\perp = \frac{P_{in} \cdot d}{\Delta T_{SS} \cdot A \cdot (\beta_1 + \beta_2)} \cdot \left(1 + \frac{d}{w} \cdot \frac{1 - \Gamma}{\Gamma}\right)^{-1} \qquad (eq. 2.32)$$

2.1.8 Thermal Equilibrium Time Constant

In transient state, during the power injection in a single pulse ($t_d < t_{pw}$, where t_d is the time delay and t_{pw} is the pulse width duration), transient temperature change (ΔT) with the time delay (t_d) for MIR QCL's active region can be described in an empirical function, as shown in equation (2.33).

If the pulse duration is long enough, the transient temperature change will reach to a thermal equilibrium (steady-state), where ΔT_{ss} is the maximum temperature rise in steady-state, given by

$$\Delta T(t_d) = \Delta T_{ss} \cdot \left(1 - \exp\left(-\frac{t_d}{\tau_{th}}\right)\right), \qquad where\ t_d < t_{pw} \qquad (eq. 2.33)$$

as plotted in Figure 2.3 Transient temperature rise above heatsink with time delay, where τ_{th} is the thermal equilibrium time constant ("time constant" in short).

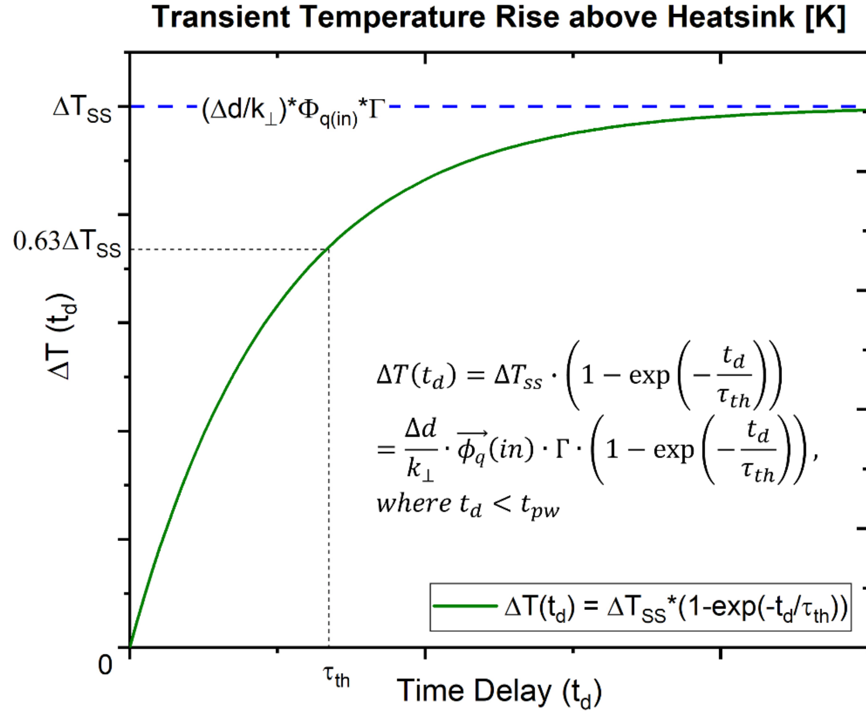

Figure 2.3 Transient temperature rise above heatsink with time delay

The rate the temperature change with time delay is

$$\frac{\partial \Delta T(t_d)}{\partial t_d} = \frac{\Delta T_{ss}}{\tau_{th}} \cdot \exp\left(-\frac{t_d}{\tau_{th}}\right), \qquad where\ t_d < t_{pw} \qquad (eq. 2.34)$$

as plotted in Figure 2.4 Derivative transient temperature rise with time delay

From the heat equation with external heat injection in equation (eq. 2.10), the time-dependent density of the heat power accumulated inside the medium is the difference of the density of the injected power minus the density of power flowing out of the medium in transient state, where,

$$\Delta q(t) = q_{in} - q_{out} \qquad (eq. 2.35)$$

then

$$\frac{\partial T}{\partial t} = \frac{q_{in} - q_{out}}{\rho C_p} \qquad (eq. 2.36)$$

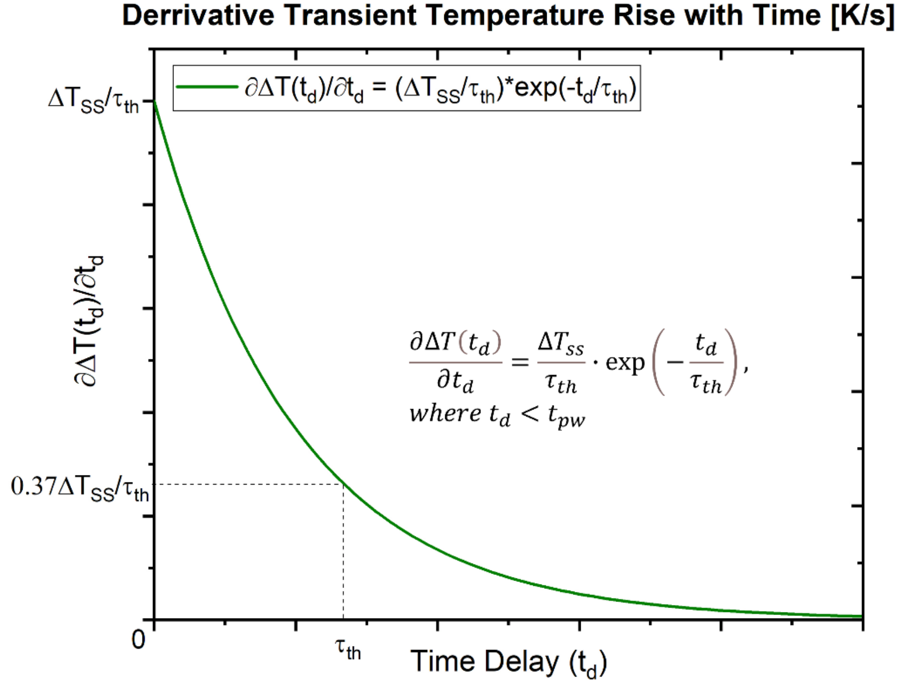

Figure 2.4 Derivative transient temperature rise with time delay

From (2.34) and (2.36), the time-dependent density of the heat power accumulation is

$$\Delta q(t_d) = \frac{\rho C_p}{\tau_{th}} \cdot \Delta T_{ss} \cdot \exp\left(-\frac{t_d}{\tau_{th}}\right) \qquad (eq. 2.37)$$

From (2.17), the maximum temperature rise in steady-state is the injection power flux $\overrightarrow{\phi_q}(in)$ multiplied by the thermal resistance R_T. Therefore, (2.37) can be written as

$$\Delta q(t_d) = \frac{\rho C_p}{\tau_{th}} \cdot \frac{\Delta d}{k_\perp} \cdot \overrightarrow{\phi_q}(in) \cdot \Gamma \cdot \exp\left(-\frac{t_d}{\tau_{th}}\right) \qquad (eq. 2.38)$$

In the duration of thermal equilibrium time constant, the thermal diffusion length L_d in cross-plane is defined as

$$L_d = (\tau_{th} \cdot \alpha_\perp)^{1/2} \qquad (eq. 2.39)$$

where $\alpha_\perp$ is the thermal diffusivity in cross-plane.

Therefore, (2.38) can be written as

$$\Delta q(t_d) = \left(\frac{\Delta d}{L_d}\right)^2 \cdot q_{in} \cdot \Gamma \cdot \exp\left(-\frac{t_d}{\tau_{th}}\right) \qquad (eq.2.40)$$

Equation (2.40) is plotted in Figure 2.5 Transient density of heat power accumulation with time delay, showing the transient density of heat power accumulation exponentially increases with the time delay.

The transient density of heat power dissipation is

$$q_{out}(t_d) = q_{in} - \Delta q(t_d) = q_{in}\left(1 - \left(\frac{\Delta d}{L_d}\right)^2 \cdot \Gamma \cdot \exp\left(-\frac{t_d}{\tau_{th}}\right)\right) \qquad (eq.2.41)$$

as plotted in Figure 2.6 Transient density of heat power dissipation with time delay showing the transient density of heat power dissipation saturates with the increase of the time delay.

From (2.40), by integrating $\Delta q(t_d)$ with time delay, the density of total energy accumulation within a pulse duration is

$$\Delta Q(t_{pw}) = \int_0^{t_{pw}} \Delta q(t_d) \cdot d(t_d) = \left(\frac{\Delta d}{L_d}\right)^2 \cdot \tau_{th} \cdot q_{in} \cdot \Gamma \cdot \left(1 - \exp\left(-\frac{t_{pw}}{\tau_{th}}\right)\right) \qquad (eq.2.42)$$

which contribute to the transient temperature rise. From (2.42), the total energy accumulation can be saturated in a long pulse injection when $t_{pw} >> \tau_{th}$, given that

$$\Delta Q_{max} = \left(\frac{\Delta d}{L_d}\right)^2 \cdot \tau_{th} \cdot q_{in} \cdot \Gamma \qquad (eq.2.43)$$

Equation (2.42) and (2.43) are plotted in Figure 2.7. It shows the energy density accumulation saturates in a thin layer when the pulse width increases towards thermal equilibrium state (quasi-steady state).

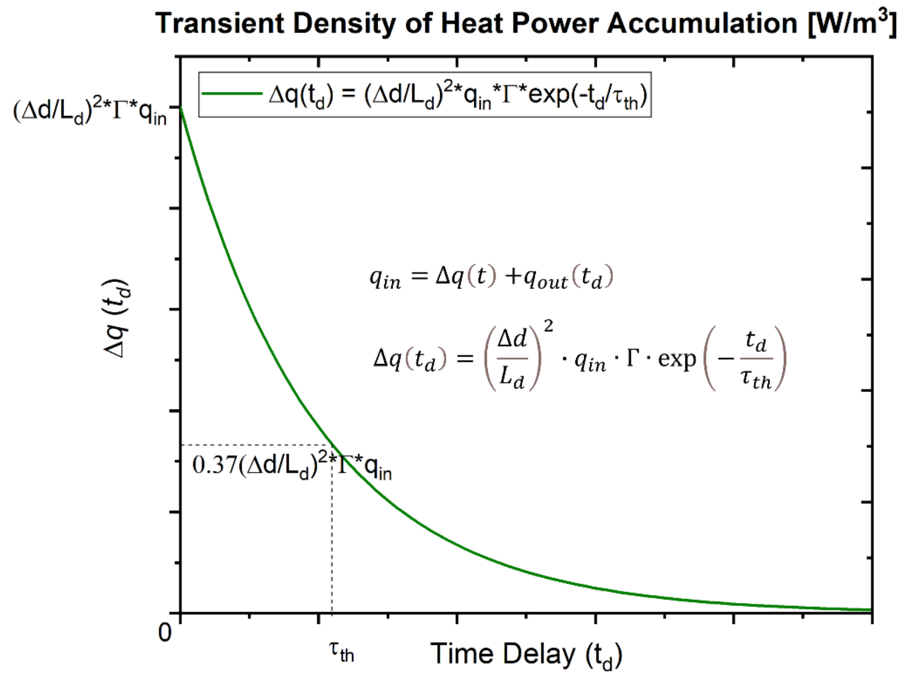

Figure 2.5 Transient density of heat power accumulation with time delay

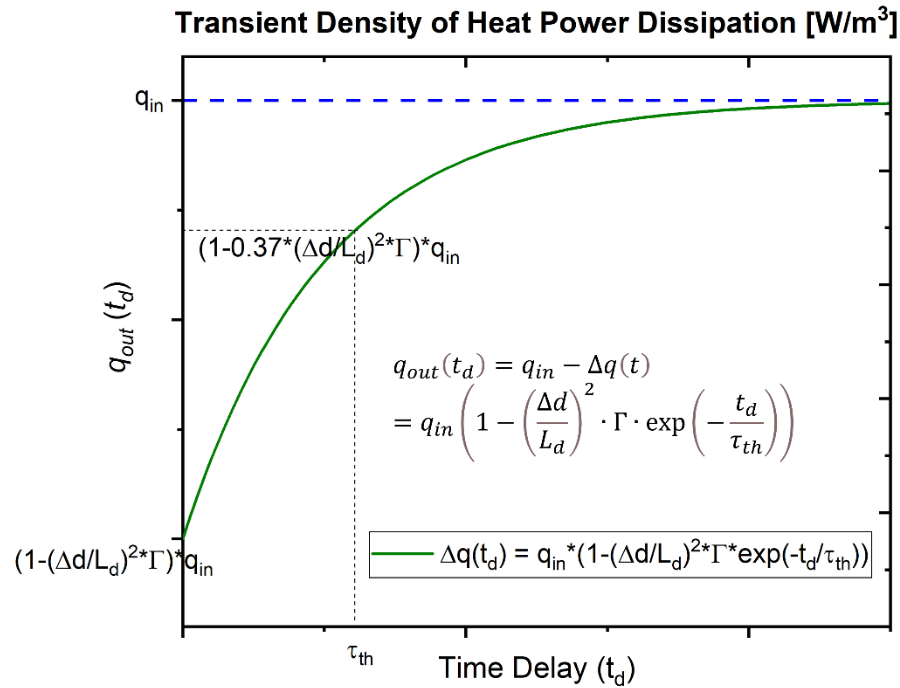

Figure 2.6 Transient density of heat power dissipation with time delay

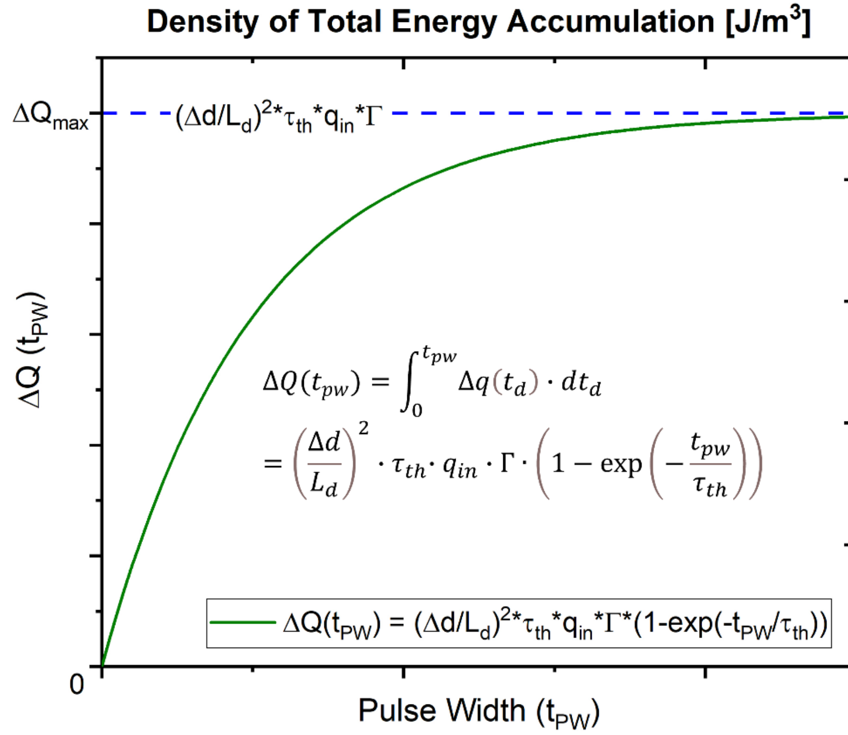

Figure 2.7 Density of total energy accumulation with injected pulse width

2.1.9 Temperature Saturation Factor

As shown in (2.43), the energy accumulation will reach to a saturated point when the pulse duration t_{pw} is far beyond the thermal time constant (τ_{th}), which explains the temperature rise can reach to its maximum in the thermal equilibrium. In transient state (in a short pulse injection), however, the temperature rise is strongly dependent on the pulse duration (i.e., the pulse injection energy) before reaching to thermal equilibrium state. From (2.33), we can define a temperature saturation factor, γ, given that

$$\gamma = \frac{\Delta T(t_d)}{\Delta T_{ss}} = \left(1 - \exp\left(-\frac{t_d}{\tau_{th}}\right)\right), \qquad where\ t_d < t_{pw} \qquad (eq. 2.44)$$

γ is the temperature saturation factor in transient state, which can be used to extrapolate the maximum temperature rise in thermal equilibrium by transient state temperature measurement.

2.2 Principle of Spatially Resolved Time-domain Thermoreflectance Microscopy

2.2.1 Introduction

In principle, the change in reflectivity (ΔR) of a given material (device under test) is related to both the change in temperature of the material (ΔT) and the change of the carrier density from the pump excitation (ΔN), given by the equation (2.45) [56],

$$\Delta R = \frac{\partial R}{\partial T}\Delta T + \frac{\partial R}{\partial N}\Delta N \qquad (eq. 2.45)$$

where $\partial R/\partial T$ is the temperature reflectance coefficient, $\partial R/\partial T$ is the free-carrier reflectance coefficient. The first term is the change of the reflectivity due to the temperature variation, and the second term is the change of the reflectivity due to the carrier density variation. Typically, the carrier-induced reflectivity change is much lower than the temperature-induced reflectivity change. Therefore, the second term can be neglected in practice [57].

As a result, thermoreflectance microscopy is based on measuring the relative change in reflectivity as a function of the change in temperature, given by the equation (2.46) [58][59]:

$$\frac{\Delta R}{R_0} = \left(\frac{1}{R_0}\cdot\frac{\partial R}{\partial T}\right)\cdot \Delta T = C_{th}\cdot \Delta T \qquad (eq. 2.46)$$

where R_0 is the reflectivity at ambient temperature (e.g., heatsink temperature) and C_{th} is the thermoreflectance coefficient. Equation (2.46) shows the change of the sample surface temperature is in a relation to the change of the reflectivity, which is determined by C_{th}. Indeed, C_{th} may vary nonlinearly (temperature dependent) over a large temperature range. For example, it has approximately 20% variation per 100 K [60][61]. But in a certain temperature range in practice, C_{th} can be treated as steady, which make it in a linear relation between ΔT and R/R0 in practice. It should be noted that C_{th} is depending on measurement conditions, for example, the sample materials, illuminating wavelength, and numerical aperture (NA). In order to acquire ΔT accurately, C_{th} must be precisely calibrated before test. This part which will be discussed in section 2.3.1.

The spatially resolved time-domain thermoreflectance (SR-TDTR) microscopy is based on a basic module of Microsanj NT210B (model type). The setup elements and the typical time chart are shown in Figure 2.8 and Figure 2.9, respectively.

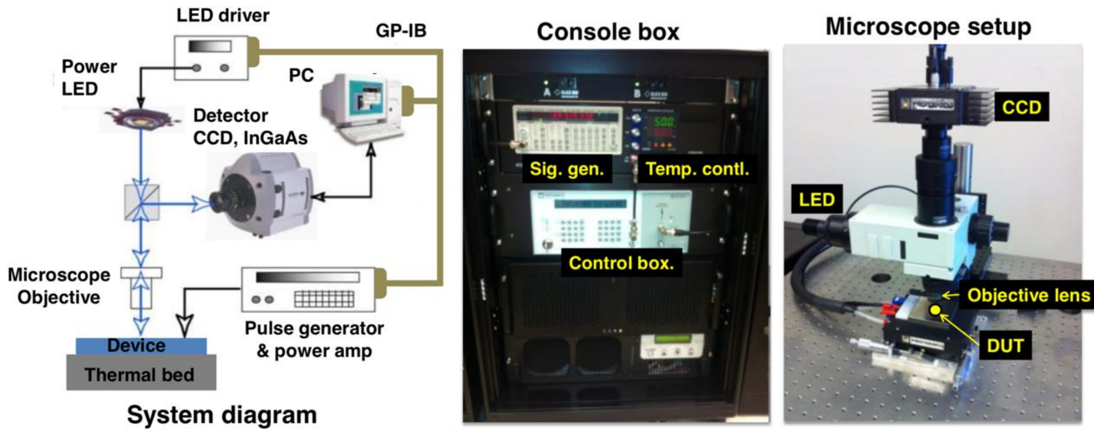

Figure 2.8 SR-TDTR System (Model type NT210 B, images provided by Microsanj User Manual)

SR-TDTR is based on pump-probe technique. In this measurement setup, a built-in pulse generator gives a short pulse (pump signal) to a device under test. A modulated pulsed LED light (probe signal) shines onto the device's surface, and the reflected light is collected by the CCD. The built-in pulse generator, LED, and CCD are synchronized together and controlled via GPIP by the main computer.

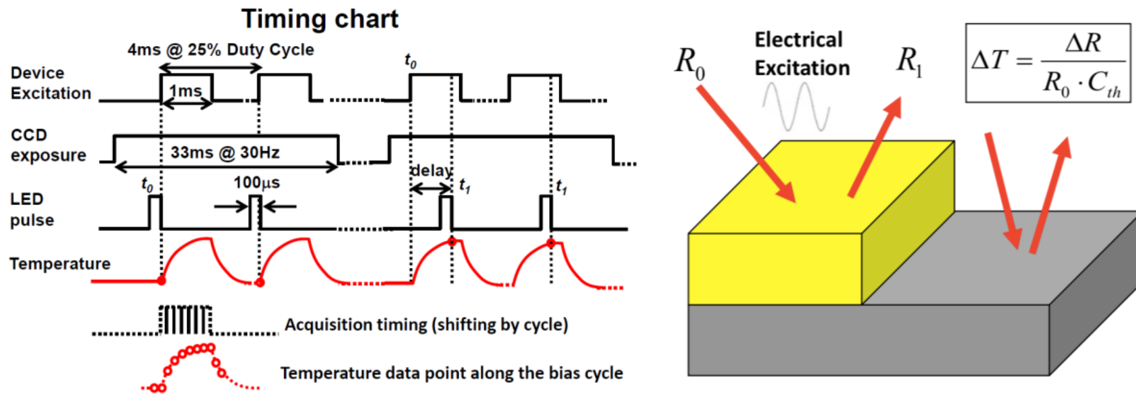

Figure 2.9 Typical Time chart and schematic diagram of the setup principle (images provided by Microsanj User Manual)

In this mode, the built-in pulse generator injects a pules to a device directly, which has a limitation of maximum 5V output and 50Ω impedance. On the other hand, an actively-biased QCL requires 10 to 20 V of biased voltage and ampere level of current injection. In this case, an external pulse generator (e.g., Avtech), which is trigged and synchronized by a built-in pulse generator, is employed to give an injection pulse to the QCL. This will be discussed in the section 2.3.2.

2.2.2 Spatial Resolution

The spatial resolution is based on Abbe diffraction limit:

$$d = \frac{0.61 \cdot \lambda}{n \cdot \sin\theta} = \frac{0.61 \cdot \lambda}{N_A} \qquad (eq. 2.47)$$

where λ is the wavelength of the LEDs, and NA is numerical aperture of the microscope's objectives. The system is equipped with four different LEDs: blue (470 nm), green (530 nm), NIR (780 nm), and broadband white LED. The microscope has X5, X20, X100 magnification of objectives. When blue (470 nm) LED and X100 objective (NA=0.6) are employed, the diffraction limit is around 400 nm.

2.2.3 Temporal and Temperature Resolution: Pulsed Boxcar Averaging Technique

High resolution in temporal and temperature domains are achieved based on pulsed boxcar averaging technique. Pulsed boxcar averaging is a data treatment method that enhances the signal-to-noise ratio (SNR) of an analytical signal by replacing a group of consecutive data points with its average [62][63][64]. It captures the signal during a well-defined temporal window that matches the pulses duration and position. The signal is integrated inside the boxcar window and ignored outside of it. To increase the SNR, the result can be averaged over many periods. The two main measurement parameters are the boxcar window width and the number of averaging periods. Consequently, this treatment smooths and filters out rapidly changing signals by averaging over a relatively long time but has a negligible effect on slowly changing signals.

Figure 2.10 shows the working principle of a pulsed boxcar average. A boxcar average captures a raw pulsed signal (Figure 2.10(a)) from a well-defined temporal window (Figure 2.10(b)) in each period, and all the signal components outside of that window are filtered out. By repeating averaging the pulse over a large number of periods (N), the noise signal is filtered out, and high SNR is acquired, as shown in Figure 2.10(c) and Figure 2.10(d). For N boxcar periods after averaging, the resulting SNR is given by the equation (2.48) [62].

$$SNR = \frac{\sum_{i=1}^{N} S_{box}}{\sqrt{\sum_{i=1}^{N} N_{box}^2}} = \frac{N \cdot S_{box}}{\sqrt{N \cdot N_{box}^2}} = \frac{S_{box}}{N_{box}}\sqrt{N} \qquad (eq. 2.48)$$

where S_{box} and N_{box} are the amplitudes of the signal and noise, respectively.

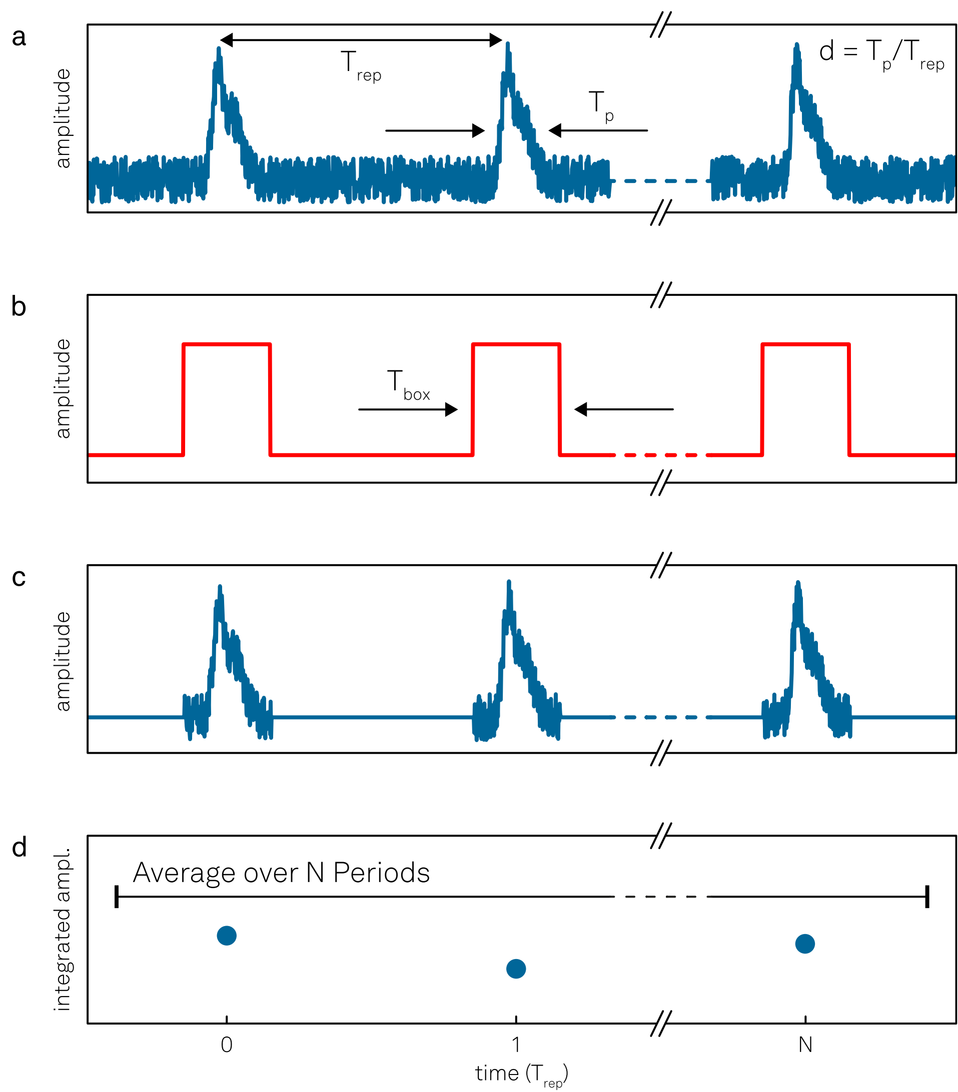

Figure 2.10 Working principle of a boxcar average [62]

In SR-TDTR measurement, pulsed boxcar average is employed for the probe signal (short LED pulse) to obtain a high-resolution transient thermal imaging profile. As the CCD frame rate is limited (20 Hz in module NT210B), repeatedly averaging a large number of CCD frames is required. The more CCD frames (longer averaging time), the higher SNR. As a result, by pulsed boxcar averaging technique, high temperature and temporal resolution can be achieved down to 0.1 K and 50 ns, respectively.

2.3 Spatially Resolved Time-Domain Thermoreflectance Microscopy Setup

2.3.1 SR-TDTR in Steady-State Mode for thermoreflectance Coefficient Calibration

The thermoreflectance coefficient (C_{th}) is highly sensitive to the test condition, which should be precisely calibrated before test. C_{th} of semiconductor materials is typically of the order of 10^{-2} to 10^{-5} K^{-1}, and it depends on measurement conditions such as constituent material, wavelength of operation, numerical aperture, and surface roughness. The detailed calibration procedures for MIR QCLs are discussed in 3.3.1.

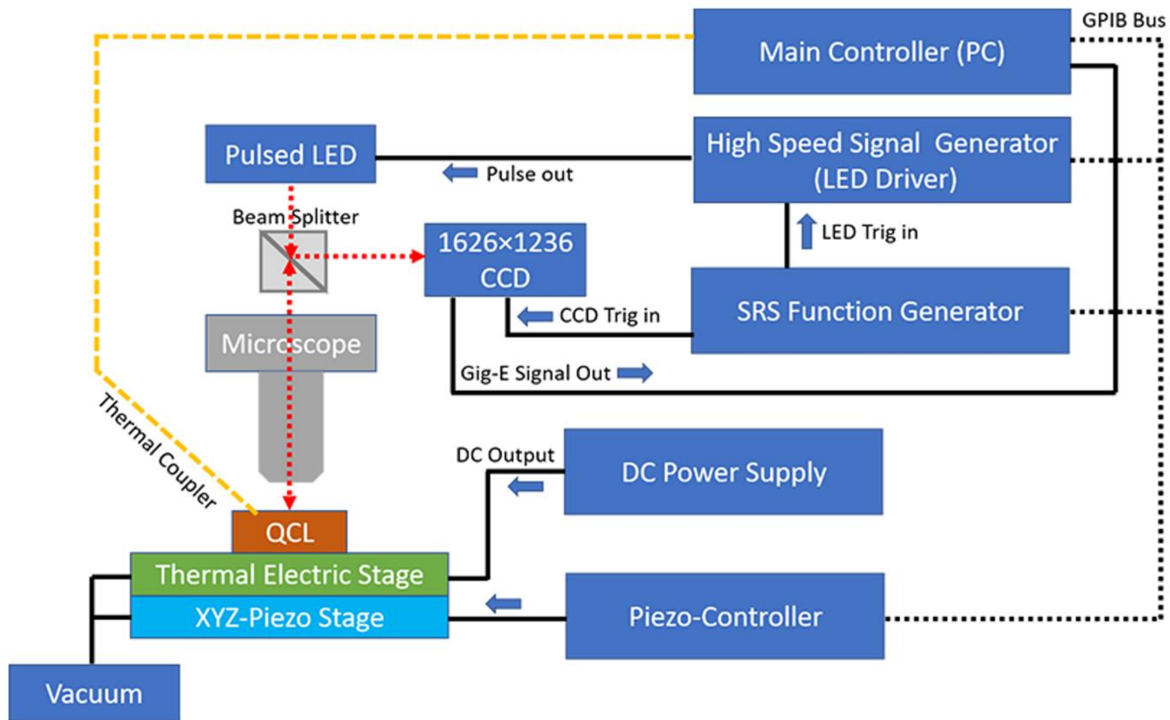

Figure 2.11 Schematic diagram of the SR-TDTR setup working on steady-state mode for the calibration of thermoreflectance coefficient

A Schematic diagram of the calibration setup is shown in Figure 2.11 Schematic diagram of the SR-TDTR setup working on steady-state mode for the calibration of thermoreflectance coefficient, which is working on steady state. As discussed earlier, C_{th} is determined by equation (2.49), in a linear relation between the change of the reflectivity ($\Delta R/R$) and the change of the surface temperature (ΔT) on the

device. As shown in a schematic diagram in Figure 2.11 Schematic diagram of the SR-TDTR setup working on steady-state mode for the calibration of thermoreflectance coefficient, A DC power supply is applied to globally heat up the heatsink chunk, the temperature rise on the device is directly read by a calibrated thermal coupler. The maximum temperature rise is collected on steady state, as shown in a time chart in Figure 2.12. DC on and off should be long enough to make sure the temperature is stable. Multiple cycles should be run for averaging at a certain injected current amplitude. C_{th} can be fit in a linear relation between $\Delta R/R$ and ΔT in a certain temperature range by modulating the amplitude of the DC power supply.

$$\frac{\Delta R}{R} = C_{th} \cdot \Delta T \qquad (eq. 2.49)$$

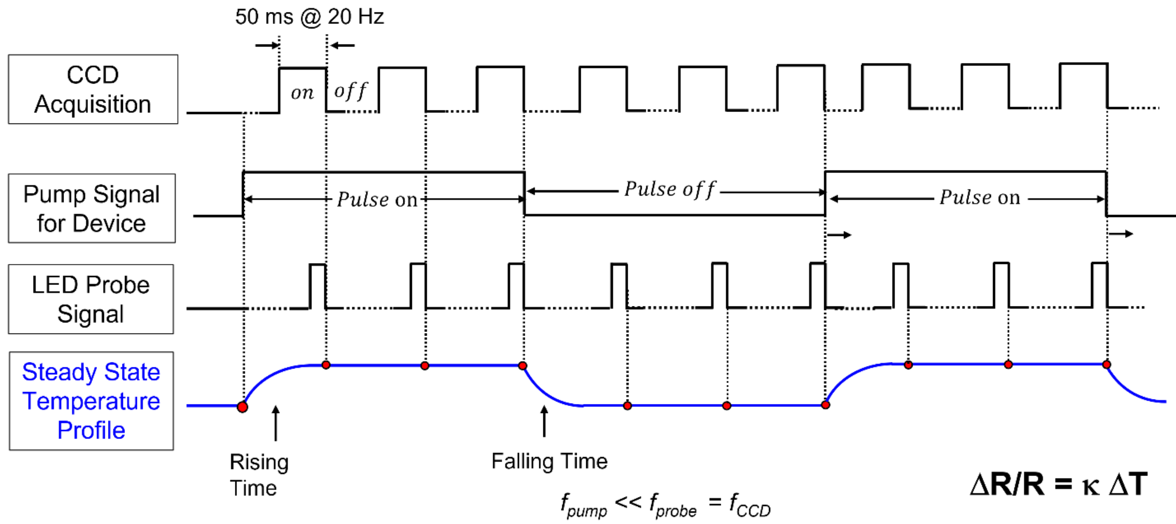

Figure 2.12 Time chart of SR-TDTR setup working on steady-state mode for the calibration of thermoreflectance coefficient

2.3.2 SR-TDTR in Transient State Mode for Thermal Dynamics Measurements

The experimental setup of the SR-TDTR is based on an integrated transient imaging module (Microsanj: NT210B). As shown in Figure 2.13, an ultrafast blue LED (THORLABS: M470L4) is used as a pulsed light source to shine on the QCL's lasing facet, and a high-resolution CCD sensor (1626×1236 pixels, 20 Hz, 12 bits) is employed to collect the spatial surface reflection signals. The LED was modulated to provide a light at wavelength of 470 nm and pulse width down to 50 ns. An as-

fabricated QCL ridge waveguide was mounted on a copper heat sink with laser facet facing up towards the microscope's objective, and the copper heat sink was placed on a thermal electric stage which was precisely controlled by a piezo controller to compensate any vibration or thermal expansion. The piezo stage moved in XYZ directions driven by a 3-axis piezo controller (THORLABS: MDT693B), giving voltage output to control the piezo stage in three dimensions in a range of 0 to 150 V. The piezo step size (minimum incremental movement) depends on the magnification, but the minimum value is 20 nm. The position was corrected roughly every 300 ms. The input signal was calculated with machine vision algorithm. Vibrations were controlled mainly with a vibration isolation table and filtered out through lock-in acquisition. Without the compensation, high magnification measurements are unobtainable for most of the cased because of the thermal expansion, which results in the images being blurry and inaccurate. The QCL and the LED were both electrically pumped by a high-power pulse generator (AVTECH: AVR-3HF-B) and a high-speed signal generator (Microsanj: NT200T-PG/202H), respectively, and then synchronized by a synthesized function generator (SRS DS345).

By precisely adjusting the time delay relationship between the pulsed LED and the pulse of device excitation, a series of high-resolution transient thermal imaging profiles are obtained, which is called "pulsed boxcar averaging" technique [63][64]. As shown in Figure 2.13, a 50 ns pulsed LED light shines onto the facet of a QCL device, and the LED light is reflected and acquired by a CCD sensor. The LED was pulsed as the same modulation frequency as the QCL's excitation pulse but swept with controllable different time delay (τ_d) with respect to the pulse of the QCL. For the reflectivity at ambient temperature (R_0), an image was captured at zero time delay ($\tau_d = t_0$) when the falling edge of the LED pulse was just before the rising edge of the QCL's pulse. When the QCL's excitation pulse was on, a series of images were captured at non-zero time delays for changed reflectivity (e.g., reflectivity is R_1 when $\tau_d = t_1$). Therefore, the change of reflectivity can be calculated by the equation (2.50).

$$\frac{\Delta R}{R_0} = \frac{R_1 - R_0}{R_0} \qquad (eq. 2.50)$$

The transient temperature profile of the laser facet was mapped by measuring the intensity of the reflected light from the CCD. To improve the signal-to-noise ratio (SNR), each image was captured for 30 seconds at each time delay (600 CCD frames averaging with 150,000 heating and cooling cycles). As the calibration for thermoreflectance coefficient (C_{th}) of different materials has been done before this thermal imaging measurement, pseudo-colors on different regions were automatically shown on

the screen based on built-in machine vision algorithm [64][65]. Finally, the data of images were post-processed by *SanjANALYZER-PLUS™* software provided by Microsanj LLC. In this technique, the thermal, the temporal, and the spatial resolution are down to 0.1 K, 50 ns, and 390 nm, respectively.

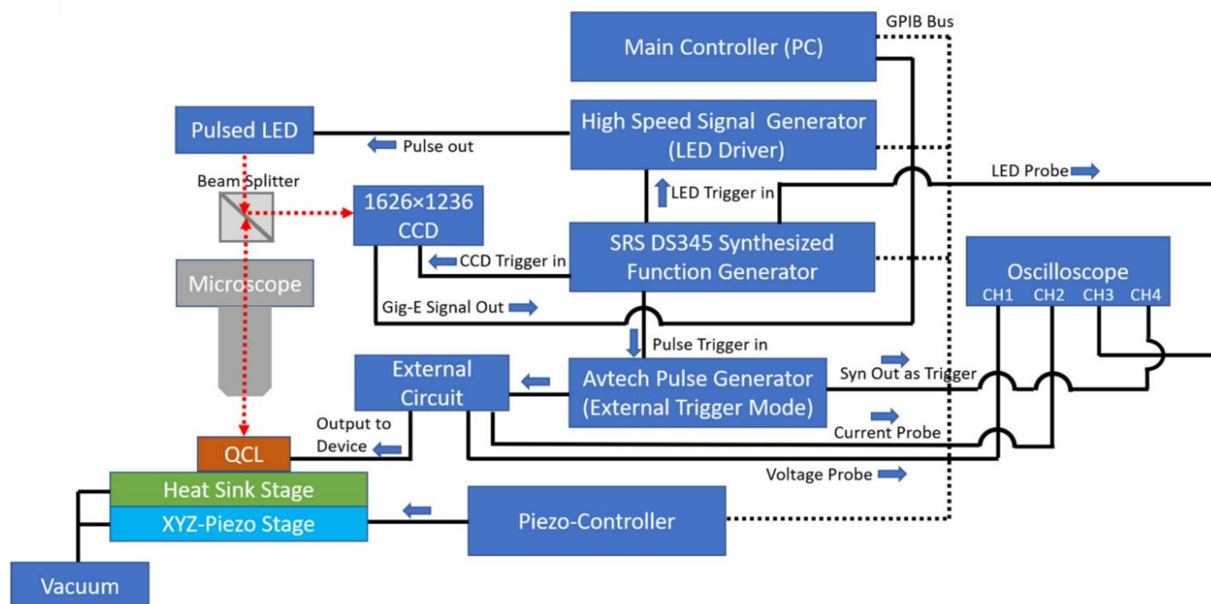

Figure 2.13 Schematic diagram of the SR-TDTR setup for QCL's transient temperature measurement

Figure 2.14 shows the time chart of SR-TDTR imaging setup working on transient mode, where a pumped pulse duration is lower or comparable to the temperature rising rise. For example, A short pulse injection on QCL (device excitation) is set at 500 ns. The width of the LED pulse is set at 50 ns shining onto the QCL facet with a synchronized modulation frequency at 5 kHz as the same as the QCL excitation pulse. The LED light has an average optical power of 3.75 μW (duty cycle of 0.025%) and ~200-250 μm in diameter of spot size focused on QCL facet surface under 100× objective lens (NA = 0.6). The reflected light from the QCL is collected from CCD sensor and mapped showing the temperature change at different positions on the facet. The transient temperature is acquired by sweeping the LED pulse at different time delays (τ_d). For example, t_0 is the time delay just before the device pulse is on, t_1 is the time delay at a certain time when device pulse is on, and t_2 is the time delay at a certain time when device pulse is off. As the increase of the injected pulse width until it is much

longer than the temperature rising time, the transient temperature rise on the device surface gradually becomes stable. This is so called quasi-steady state, and the time chart is shown in Figure 2.15.

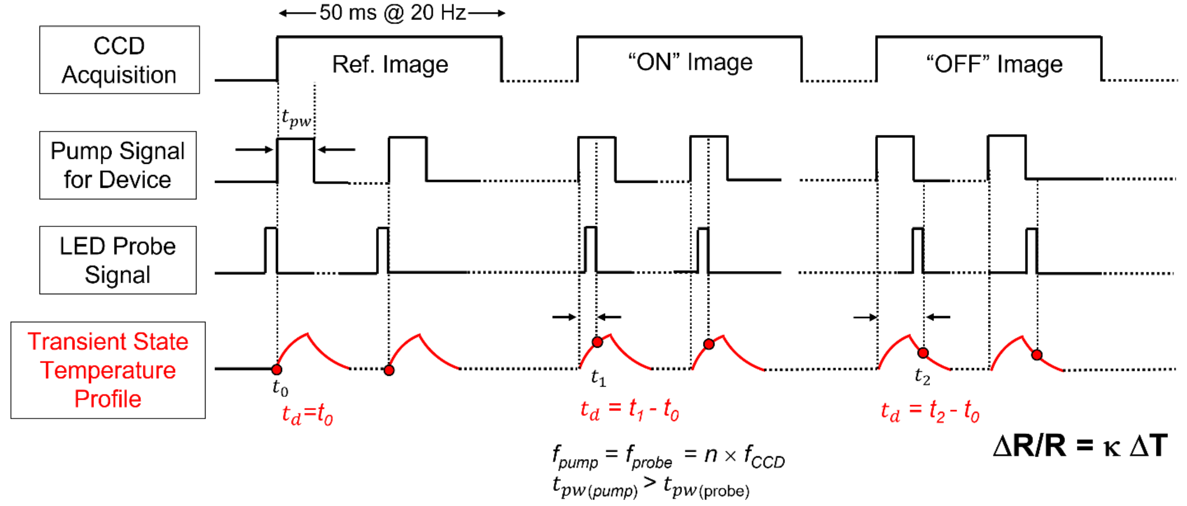

Figure 2.14 Time chart of SR-TDTR setup working on transient state for transient temperature profile measurements.

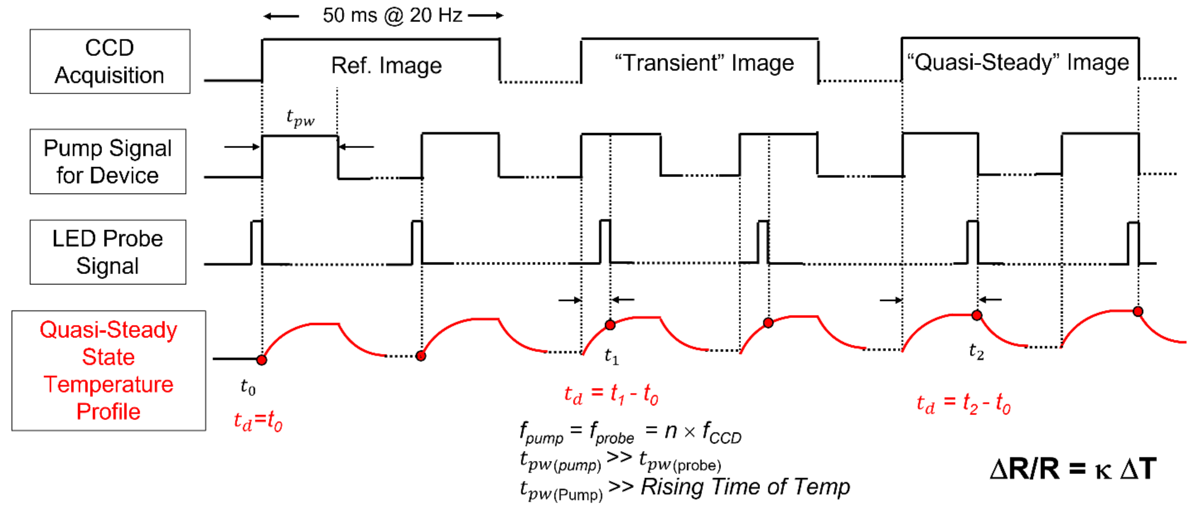

Figure 2.15 Time chart of SR-TDTR setup working on transient state for temperature profile measurements from transient state to quasi-steady state.

Under measurement on SR-TDTR system, the as-cleaved QCL laser bar is mounted on a specially designed copper heatsink, as shown in Figure 2.16(a). The laser facet is facing up towards the microscope lens, for measuring the surface temperature change when the device is actively-biased. Figure 2.16(b) shows the QCL laser facet under an optical microscope in ×100 of magnitude. The red rectangular region indicates the area of the device's active region (AR) on the cleaved facet. Figure 2.16(c) shows the device attached the whole package sitting on the thermal electric under the microscope for SR-TDTR measurement.

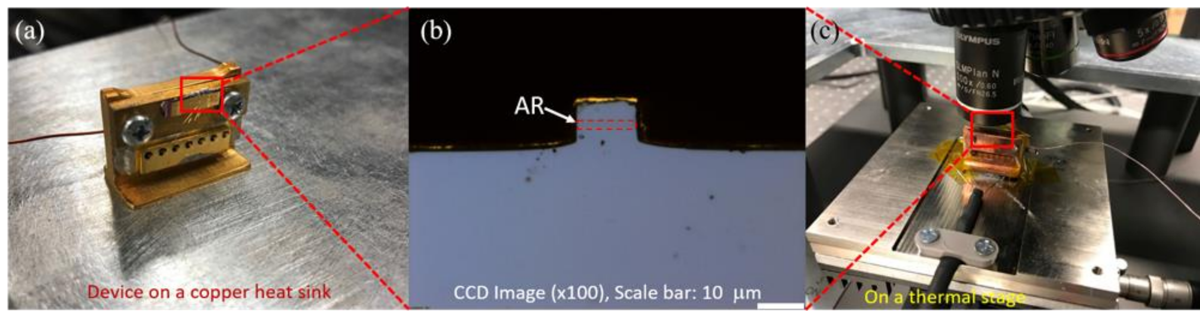

Figure 2.16 (a) Device ridge bar on a copper package; (b) device under a microscope with ×100 magnification, scale bar is 10 μm; (c) package on the thermal electric stage under the microscope.

2.4 Summary

This chapter introduces a fundamental heat equation theory derived from Fourier's Law, followed by an introduction to the thermal imaging measurement setup. Section 2.1 in this chapter consists of heat transfer model derivation on quantum cascade lasers (QCLs) based on Fourier's Law with anisotropic thermal conductivity. This model is applied in thermal simulations in the chapter 3, chapter 4, chapter 5, and chapter 6. Section 2.2 and 2.3 in this chapter introduce the principle and the measurement setup of spatially resolved time-domain thermoreflectance microscopy (SR-TDTR) microscopy, respectively. This chapter is the theoretical foundation for the following chapters.

Chapter 3
Thermal Dynamic Imaging of Mid-Infrared Quantum Cascade Lasers with High Temporal–Spatial Resolution

3.1 Introduction

Joule heating is an adverse factor which suppresses QCL's lasing performance at room temperature. However, there is still lack of direct evidence for understanding the thermal dynamics of the device, especially in a high temporal and spatial resolution. In this chapter, systematic study on thermal dynamics of an actively-biased MIR QCLs was presented by employing spatially-resolved time domain thermoreflectance (SR-TDTR) microscopy down to tens-of-nanoseconds (temporal resolution) and hundreds of nanometers (spatial resolution). The experimental results reveal that the heat accumulation in device active region starts even within less than 1 µs upon the application of electric current injection. It is found that within 1-2 µs, the heat dissipation to the top cladding is substantially reduced and most of the heat is drained to the substrate through the bottom cladding layer, which eventually leads to thermal quenching of lasing operation. These results are also confirmed by combining light-current-voltage measurements and theoretical thermal modeling. Thus, the SR-TDTR microscopy provides direct evidence of thermally-induced lasing quenching of QCLs, and it is an enabling tool to probe internal dynamics of operating actively-biased devices.

3.2 Layer Structures and Fabrication Procedures

The QCL was grown by an in-house molecular beam epitaxy (MBE) at University of Waterloo (Wafer #: G0241), and the designed emitting wavelength is around ~9 µm on pulse mode. The epitaxial layer growth was followed by the design in a reference paper by Page *et al.* [66], which contains 36 periods of GaAs/$Al_{0.45}Ga_{0.55}As$ multiple quantum wells (MWQs). The layer sequence starting from injection barrier is as follows: **46**, 19, **11**, 54, **11**, 48, **28**, 34, **17**, 30, **<u>18</u>**, <u>28</u>, **<u>20</u>**, <u>30</u>, **26**, 30 Å. The denoted bold scripts are $Al_{0.45}Ga_{0.55}As$ as barrier layer; the normal scripts are GaAs wells; and the underlined layers are the Si doping region (n=3.96 × 10^{17} cm^{-3}). The total thickness of MWQs is 1.65 µm, which is sandwiched by n-type GaAs (n_{Si}=4.0 × 10^{16} cm^{-3}) top cladding and bottom cladding layer with 3.5 µm of thickness on each side. Also, both cladding layers are terminated by 1 µm thick of high doped n-type

GaAs (n_{Si}=6.0 × 10^{18} cm^{-3}) for electrical contact, and the substrate wafer (purchased from AXT Inc.) is high doped n-type GaAs which coated by gold on its backside as bottom contact. The total thickness of grown epitaxial layers is 10.65 μm.

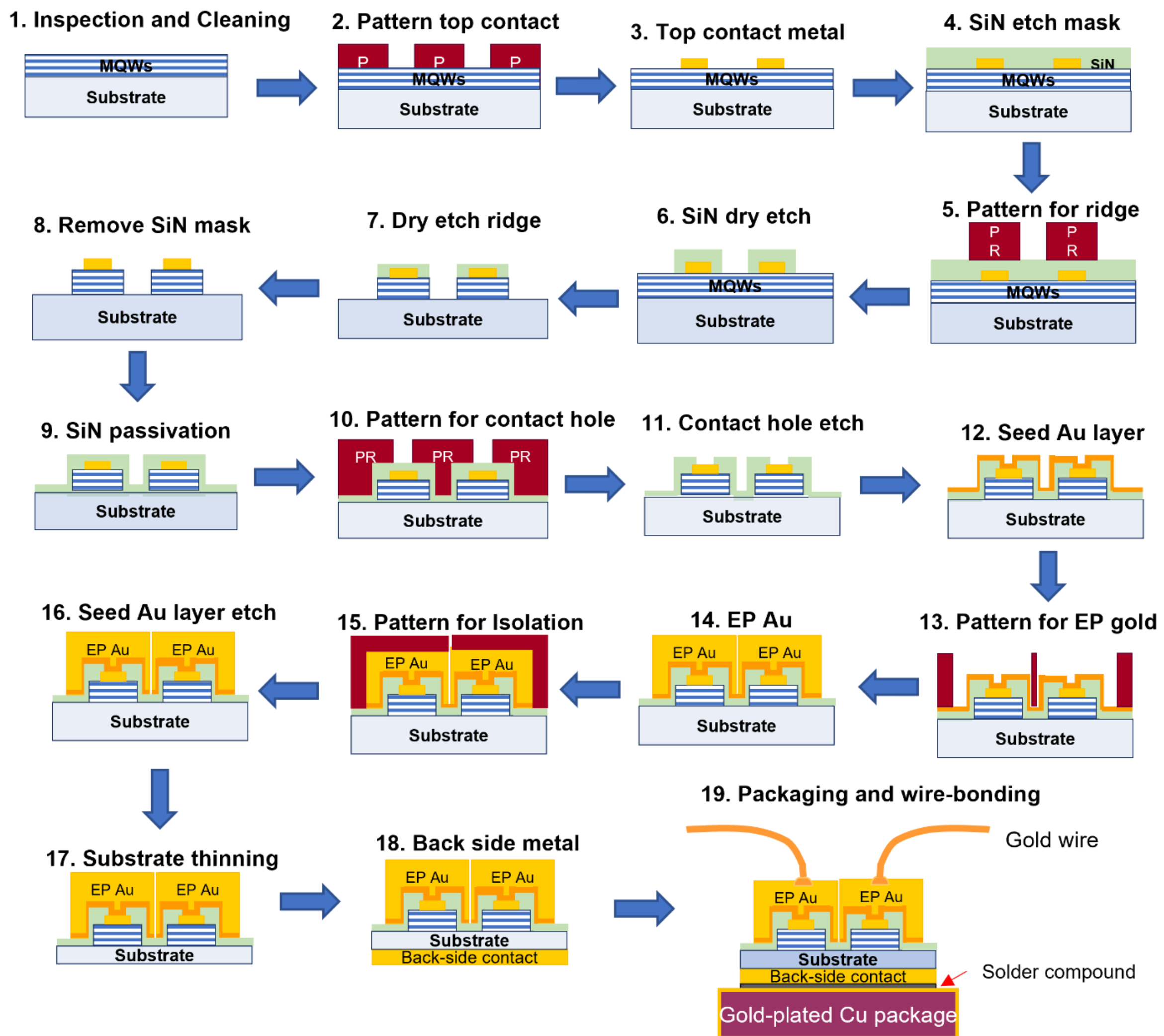

Figure 3.1 Fabrication Sequence of GaAs/Al_xGa_{1-x}As-based MIR QCLs (λ~9 μm)

A process flow for fabricating MIR QCLs is shown in Figure 3.1 Fabrication Sequence of GaAs/Al_xGa_{1-x}As-based MIR QCLs (λ~9 μm). The laser devices are fabricated into Fabry–Pérot ridge waveguides by standard microfabrication technique with a series of steps including photolithography, metal deposition, plasma-enhanced chemical vapor deposition (PECVD), inductively coupled plasma

- reactive ion etching (ICP-RIE), and gold electroplating. The MIR QCLs are etched down to 11 μm of depth and 14 μm of width. Finally, the fabricated devices are cleaved into laser bars with 2.5 mm in cavity length for each, followed by epi-side-up mounting on a copper heatsink. The MIR QCL devices with copper heatsink is placed into a liquid helium cooling cryostat chamber, attached onto a gold-plated copper cold finger. The MIR QCL devices are characterized by temperature-dependent light-current/current density-voltage (L-I/J-V) measurements with heatsink temperature from 50 K to 295 K, followed by Fourier-transform infrared spectroscopy (FTIR) measurement successively. The measurement results show that MIR QCL has a maximum operating temperature at 280 K on pulsed mode with emitting wavelength at 9.05 μm (measured under 100 K), which are shown in Figure 3.2(a) and Figure 3.2(b), respectively.

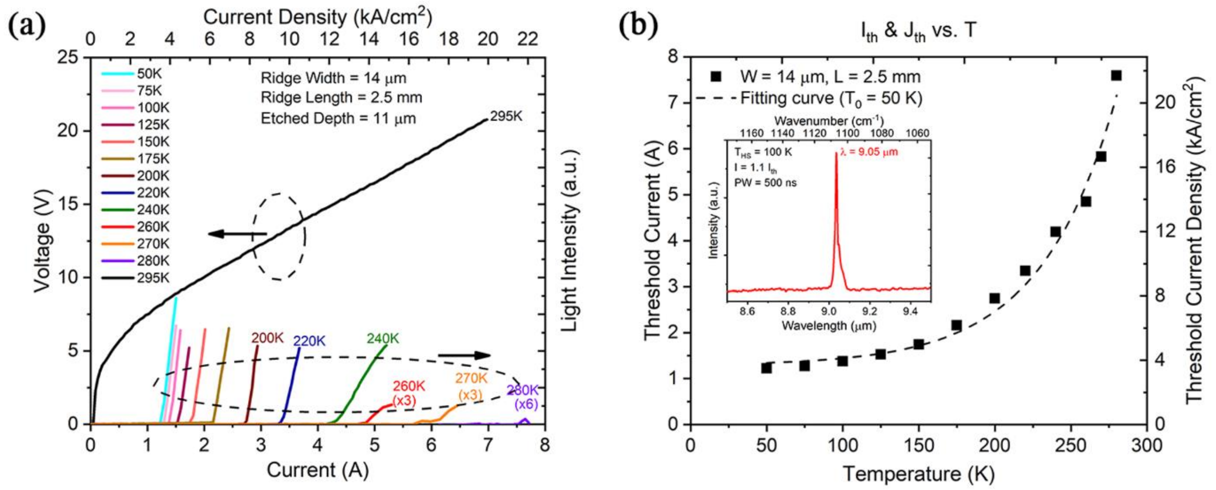

Figure 3.2 (a) L-I/J-V characteristic on pulse mode with heat sink temperature from 50 K to 295 K (modulation frequency of 500 Hz, pulse width of 500 ns, duty cycle of 0.025%); (b) measured (symbols) and fitting (dash line) of threshold current - threshold current density with respect to heat sink temperature from 50 K to 280 K, where T_0 = 50 K is the characteristic temperature; the inset in (b) shows lasing spectrum by FTIR at 100 K (heat sink temperature) when current injection is just above the threshold.

Figure 3.3 shows a schematic diagram of the cross-sectional view of the MIR QCL ridge waveguide, illustrating the layer structure and dimensions. Figure 3.4(a) shows an optical microscope image of the MIR QCL fabricated in ridge waveguide from the top-down view, indicating the areas of the ridge waveguide, electroplated gold (EP-Au), and the isolation. Figure 3.4(b) shows at SEM image on the MIR QCL's cleaved facet. The area between two white dash lines is the active region.

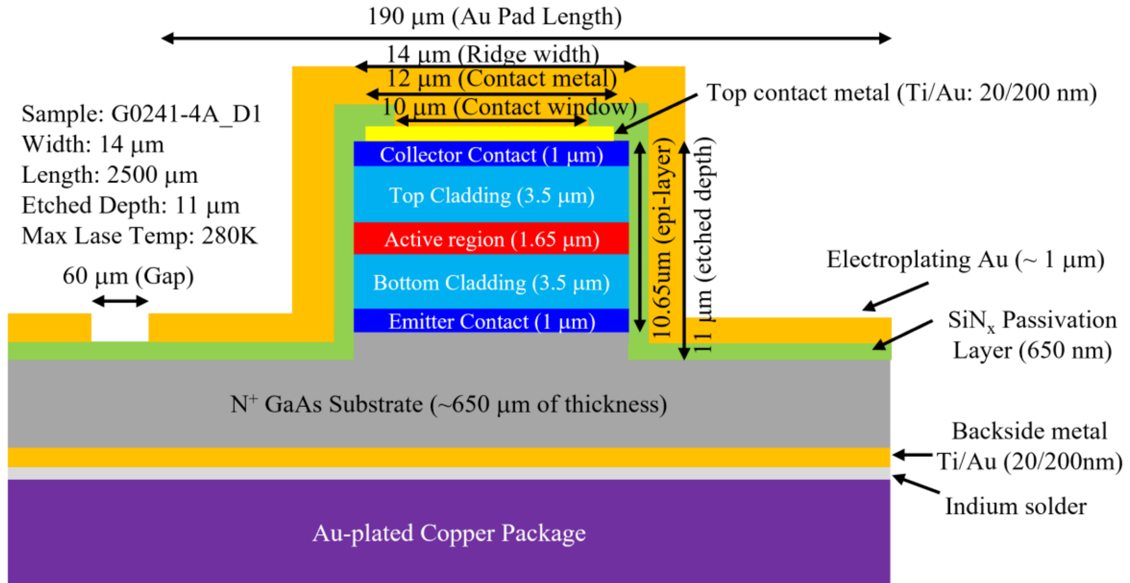

Figure 3.3 Schematic diagram of the cross-sectional view of the MIR QCL ridge waveguide

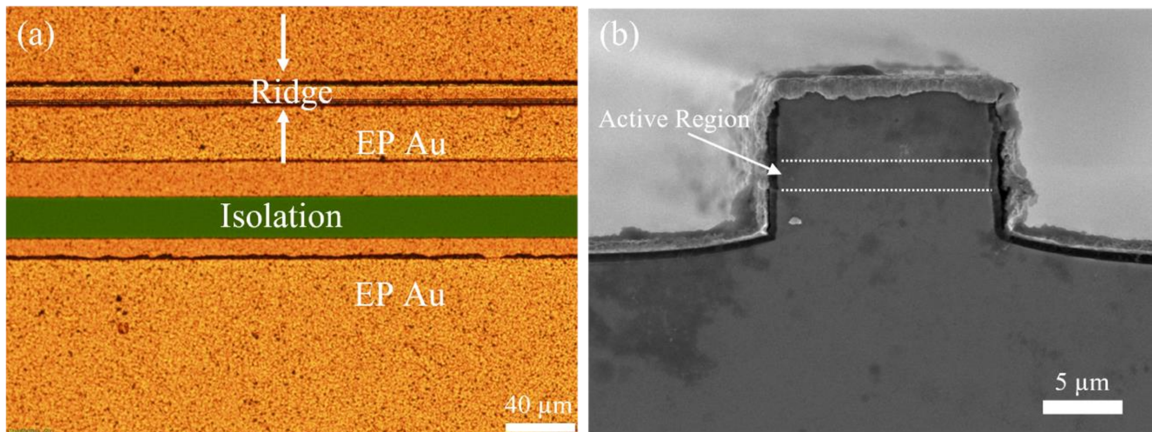

Figure 3.4 (a) An image under optical microscope from the top-down view of an area of the fabricated MIR QCL ridge waveguide; (b) an SEM image of the cleaved facet of the fabricated MIR QCL ridge waveguide.

3.3 Thermal Dynamics Imaging of MIR QCLs by SR-TDTR Microscopy

3.3.1 Calibration for Thermoreflectance Coefficient in Steady-State Mode

The value of the C_{th} on III-V semiconductor materials is typically of the order of 10^{-2} to 10^{-5} K^{-1} and depends on measurement conditions such as constituent material, wavelength of operation, numerical aperture, and surface roughness. Therefore, in order to obtain precise temperature change on QCL's laser fact, a careful calibration of C_{th} is performed considering the LED wavelength of 470 nm and numerical aperture of 0.6 (100× objective lens) at heat sink temperature of 296.5 K. A thermal electric stage under the copper heat sink is modulated by a DC power supply for power injection, and two thermocouples are placed between the heat sink and the laser facet to directly measure the temperature difference. The change in both the reflectivity and the temperature are plotted in Figure 3.5 and the thermoreflectance coefficient C_{th} is extracted from the linear slope. The extracted value of C_{th} is found as ~1.525×10^{-4} K^{-1} in the active region (GaAs/$Al_{0.45}Ga_{0.55}As$ multiple quantum wells) and ~2.431×10^{-4} K^{-1} in other region (together with the cladding, the contact, and the GaAs substrate) of the laser. It is reported that C_{th} is in linear relationship to $\Delta R/R_0$ to a broad temperature range (77-500 K) for GaAs-based materials [67]. Therefore, C_{th} is independent of the temperature change, which means in a larger temperature range (ΔT ~100 K) the change of C_{th} can be negligible.

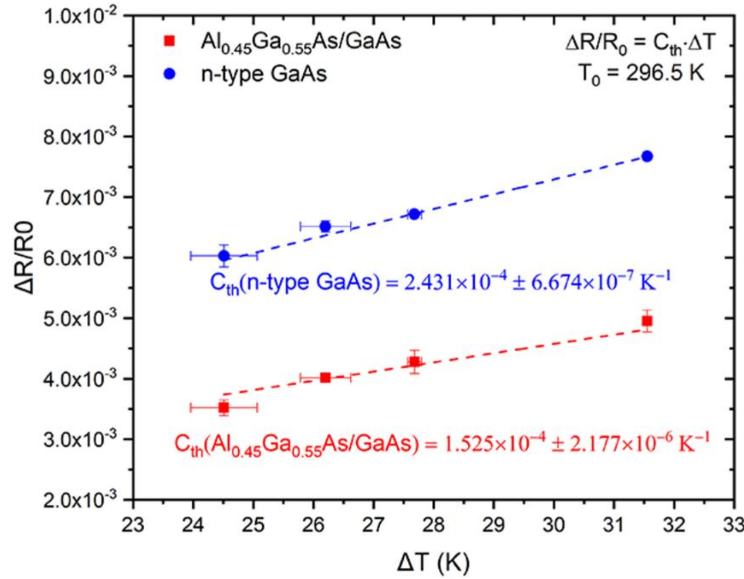

Figure 3.5 Calibration results of C_{th} for GaAs/$Al_{0.45}Ga_{0.55}As$ MQWs and n-type GaAs, respectively

3.3.2 Transient Temperature Rising of MIR QCLs in short Pulse Duration with High Current Injection

The schematic diagram of the cross-section of the QCL laser is shown in Figure 3.6(a). This device was grown by molecular beam epitaxy with an active region consists of $Al_{0.45}Ga_{0.55}As/GaAs$ multiple quantum wells (1.65 μm) sandwiched by n-type GaAs cladding layers (3.5 μm) then terminated by electrical contact layers (1 μm). The laser was fabricated with a ridge waveguide width of 14 μm and isolated by a 600 nm thick SiN_x insulating layer. Titanium/gold (20/250 nm) was deposited by e-beam evaporation on top of the ridge to provide top electrical contact followed by a thick electroplated gold (1 μm). The QCL is lased up to 280 K at center wavelength of ~9 μm. When the experiment was conducted at room temperature (296.5 K), the QCL was operated below threshold current condition and electrically pumped in square pulse mode with a peak current of 6 A (with a bias voltage of 18.7 V), a pulse width of 500 ns, and a modulation frequency of 5 kHz.

Figure 3.6(b) shows 2D transient temperature profiles of a QCL facet with time delays of 150 ns, 450 ns, and 1250 ns at 6 A injection current, which reveal the temperature evolution on the laser facet at the beginning, near the end, and beyond the electrical pulse, respectively. It is evident from the contour color plot that most of the heat is generated inside the active region which gradually dissipated to surrounding regions. Figure 3.6(c) and Figure 3.6(d) are one-dimensional (1D) temperature profiles along the active region (line AA') and across the active region (line BB') at different time delays extracted from Figure 3.6(b). Along the active region, a relatively uniform temperature distribution is observed as expected, indicating a low rate of heat flow (heat flow, for short) through the lateral direction of the active region to the side walls. On the contrary, a substantial temperature rise is observed across the active region which denotes that most of the heat from active region is likely to be dissipated vertically through cladding layers and eventually to the substrate. In Figure 3.6(e), the time dependent increase of temperatures at four different positions on the facet of a QCL are plotted: at the centers of the active region (position 1), the top cladding (position 2), the bottom cladding (position 3), and the top edge of the substrate (position 4). At the end of the electrical pumping pulse (τ_d =450 ns), the active region temperature rises to 101 K (ΔT_{max}) above room temperature, while the ΔT_{max} of the top (43.4 K) and bottom (35.4 K) cladding layer is observed at τ_d =600 ns – an additional time delay of 150 ns, which is attributed to the finite speed of heat transferring. The substrate reaches its maximum ΔT of 14.1 K at even a later time of τ_d =1250 ns (the inset of Figure 3.6(e)). A more detailed 2D transient temperature profiles are also shown in Figure 3.7.

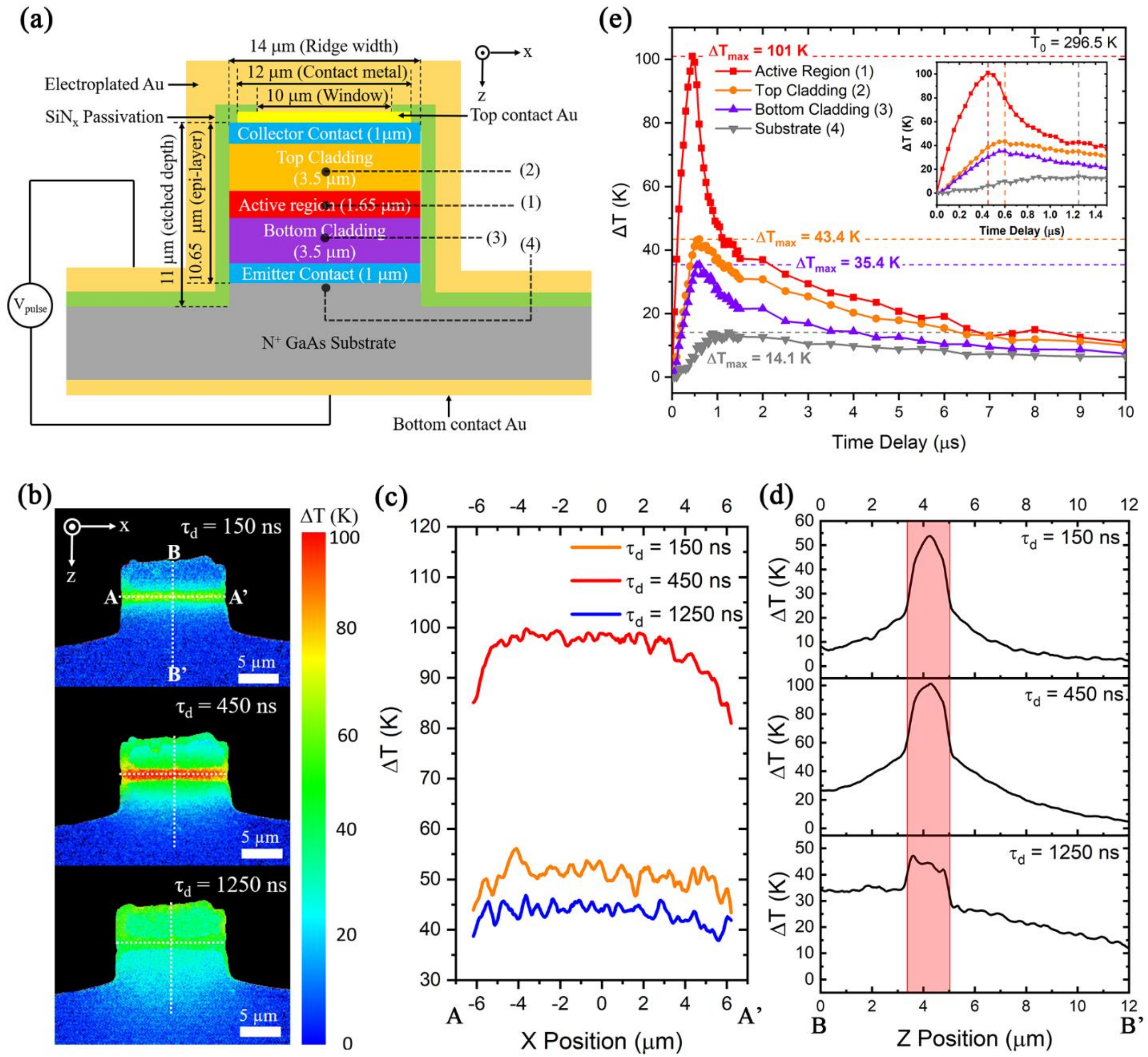

Figure 3.6 (a) Schematic diagram of the cross-section view of a fabricated QCL mounted on the copper package with epi-side up. (b) Two-dimensional (2D) transient temperature imaging profiles at time delay (τ_d) of 150 ns, 450 ns, and 1250 ns, respectively. The temperature change ΔT along x and z direction across the center of the active region (indicated by white dash line in (b)) at different time delays are plotted in (c) and (d), respectively. (e) The measured transient temperature change ΔT at the center of the active region – red solid line (1), center of the top cladding layer – orange solid line (2), center of the bottom cladding layer – purple solid line (3), the point at 4.5 μm below AR layer inside the substrate – grey solid line (4), at different time delay when pulse width of the electrical injection is fixed to 500 ns and peak injected power (P_{in}) is set to 112.2 W (I = 6 A, V = 18.7 V); LED pulse width is set to 50 ns; T_0 is the heat sink temperature (296.5K).

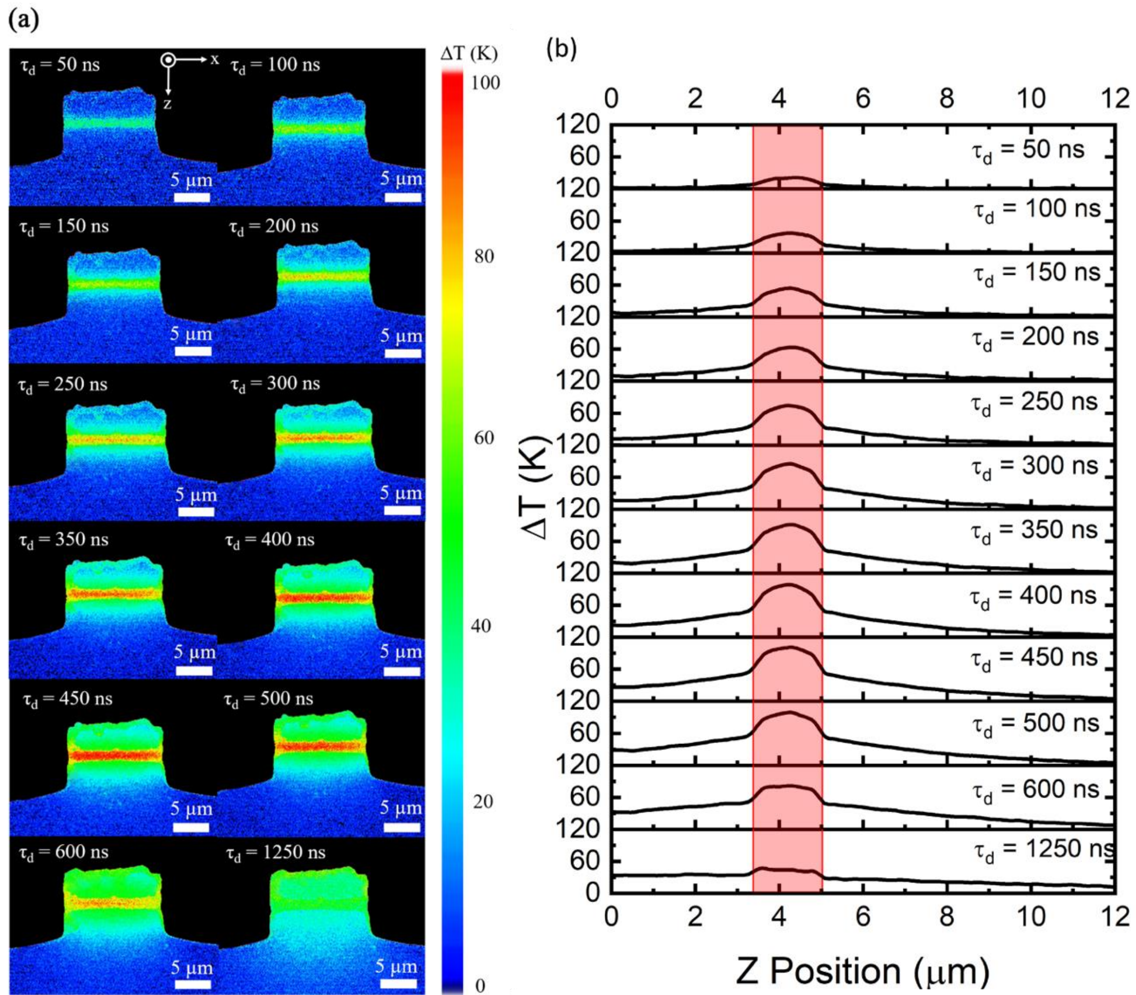

Figure 3.7 (a) 2D transient temperature imaging profiles at different time delay with a short pulse-width current injection (I = 6 A, V= 18.7 V, PW = 500 ns, each image was averaged over 6000 CCD frames); measured transient temperature change ΔT along x direction (b) and z direction (c) across the center of the active region at different time delay.

In addition, Figure 3.8 show transient temperature imaging profiles under injection current from 1 A to 6 A when the time delay at 500 ns (aligned with the fall edge of the pumped pulse). These images show the maximum temperature rises at the end of each pulse injection with different current value. The temperature rises dynamics with the time delay at different current injection (from 0.5 A to 6 A) and the maximum temperature rises at the end of each pulse (set time delay at 500 ns) with respect to

the peak power injection (I·V) are shown in Figure 3.9(a) and Figure 3.9(b), respectively. Figure 3.9(b) shows a well-fitted linear relation between the maximum temperature rises and the peak power injection in pulsed current injection.

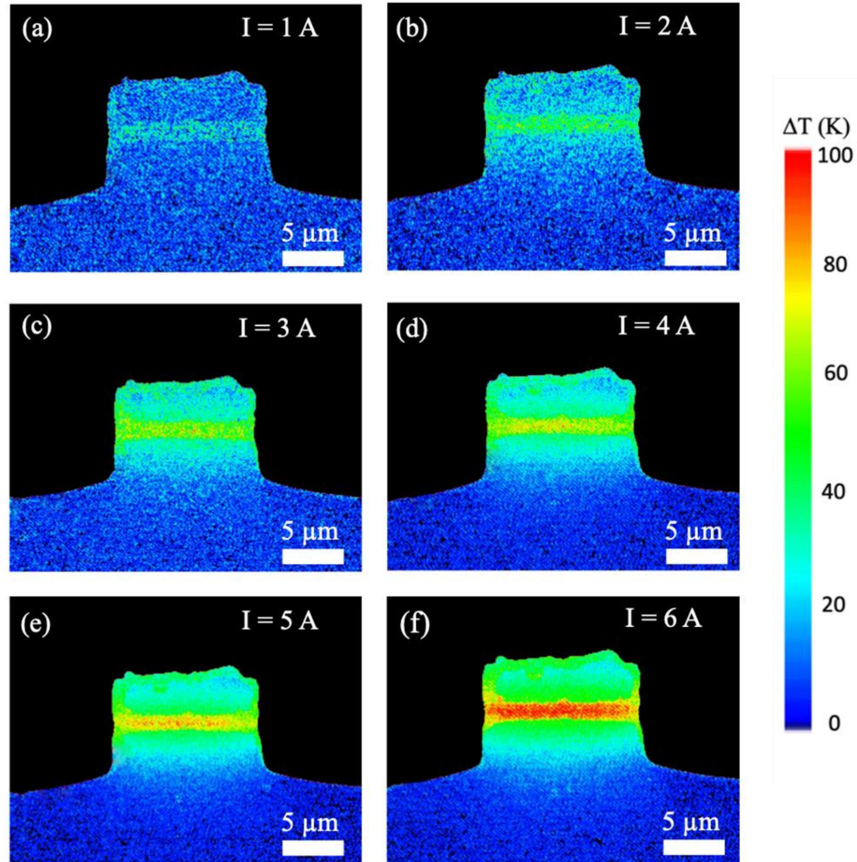

Figure 3.8 Transient state thermal imaging profile at the delay time (τ_d) of 500 ns (the same as device pulse width) when QCL is injected from 1 A to 6 A.

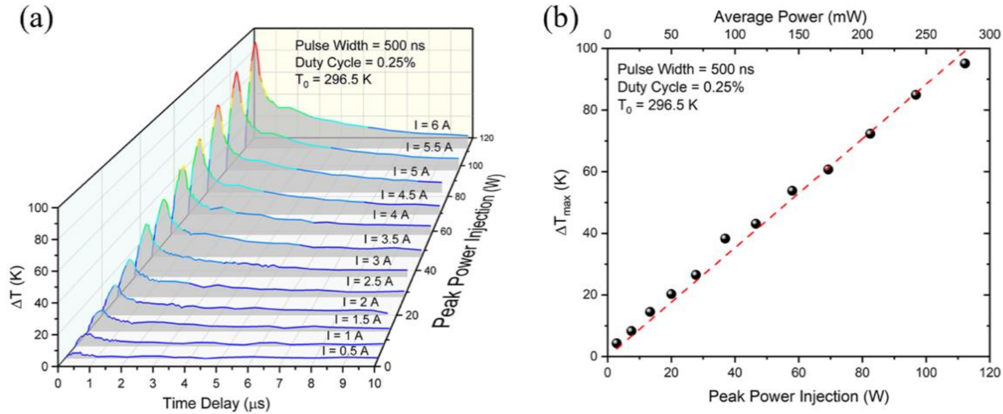

Figure 3.9 (a) Transient temperature rises in active region with different time delay under pulsed injection (PW = 500 ns, duty cycle = 0.25%, heatsink at room temperature, current sweep from 0.5 A to 6 A, step = 0.5 A). (b) Black dots: the maximum temperature rises at the end of each pulse with respect to the peak power injection; red dash line: linear fitting curve.

3.3.3 Transient Temperature Rising of MIR QCLs in Long Pulse Duration with Low Current Injection

The high temporal and spatial resolution of the SR-TDTR enables quantitatively inferring 2D mapping of the heat flow from the active region to the surrounding regions in actively-biased QCLs. Figure 3.10(a) shows a series of transient 2D thermal imaging profiles of the QCL under 2 A injection current (10 V bias) at a pulse width of 10 μs at room temperature. The profiles from left to right in the Figure 3.10(a) are acquired at $\tau_d = 1, 5, 10$ μs after the leading edge of the injection pulse, respectively. More details can be found in Figure 3.11. As the device does not emit light at room temperature, all the injected electrical power is likely to be converted into heat mostly inside the active region because of the presence of thermal boundary resistance (TBR) [51]. The heat of the active region eventually dissipates to the surrounding regions along all directions and can be calculated by Fourier's law of heat conduction model (eq. 2.1 and eq. 2.15), where Δq_{out} is time-dependent net heat flux out from the active region, ∇T is the two-dimensional temperature gradient, and k is the thermal conductivity tensor of the material determined by the steady-state temperature profile measurements [56][60]. The calibrated values of thermal conductivity are shown in Table 3.1 Thermal conductivity [W/(m·K)] of different layers of materials. The calculated heat dissipation towards different directions is shown in Figure 3.10(b). As an example, at $\tau_d = 5$ μs, only 0.25% of the Joule heat is dissipated laterally in the active region to the

left (or right). Around 18.37% of the heat flows to the top of the ridge, and most of the heat (52.3%) goes down to the substrate. These ratios are changing with delay time.

Figure 3.10(c) shows the corresponding heat flow along different directions (channels) in the active region as a function of time delay (more details can be found in Table 3.2). The heat flow to the bottom cladding vertical channel (to the substrate) increases from 6.38 W (31.89%) at $\tau_d = 1$ μs to 12.57 W (62.86%) at $\tau_d = 10$ μs. In contrast, the heat flow to the top cladding vertical channel decreases from 5.16 W (25.8%) at $\tau_d = 1$ μs to 0.54 W (2.7%) at $\tau_d = 10$ μs. This can be explained as follows. As shown in Figure 3.10(d), the initial temperature rise of the top cladding layer is much lower than that of the active region at the beginning (when $\tau_d = 1$ μs) of the electrical pulse. This large temperature gradient yields a higher rate of heat flow. As it is surrounded by air from all sides except the bottom, heat dissipation from the top cladding layer to surrounding air is much slowed down and thus heat starts to accumulate in this layer. As a result, the temperature of the top cladding layer increases quickly, resulting a drop in the temperature gradient. The rate of heat flow through the top cladding vertical channel thus decreases with time and become almost insignificant at the end of the 10 μs injection electric pulse.

The heat flow along the lateral directions (channels), such as the active-region lateral channel, the top cladding lateral channel, the bottom cladding lateral channel, remains relatively low (in the range of 0.24 to 1.3 W out of the total 20 W injected electrical power) throughout the whole pulse duration (Figure 3.10(a)). This can also be attributed to the impeded heat dissipation through the air/semiconductor interface in the ridge-waveguide QCL. It was proposed to employ buried-heterostructures (BH), in which the active region is surrounded by solid-state/semiconductor materials, to mitigate this problem [68][69]. The SR-TDTR technique could provide direct experimental evidence to show how much the BH structures can help in heat dissipation process.

Similarly, heat flow analysis towards different channels is also conducted for QCL under high current injection (I = 6 A) with short pulse duration (pulse width at 500 ns). The detailed data can be found in Table 3.3. At the end of the pulse (time delay at 500 ns), less than half of the injected power (47.03%) is dissipated out from the active region, and the rest of power is contributing on heat accumulation (Joule heating) inside the active region. Also, there is only slightly differences between the heat flow towards top cladding layer (20.92%) and towards bottom cladding layer (24.62%). These results indicate that heat management is not a significant issue for short pulse injection.

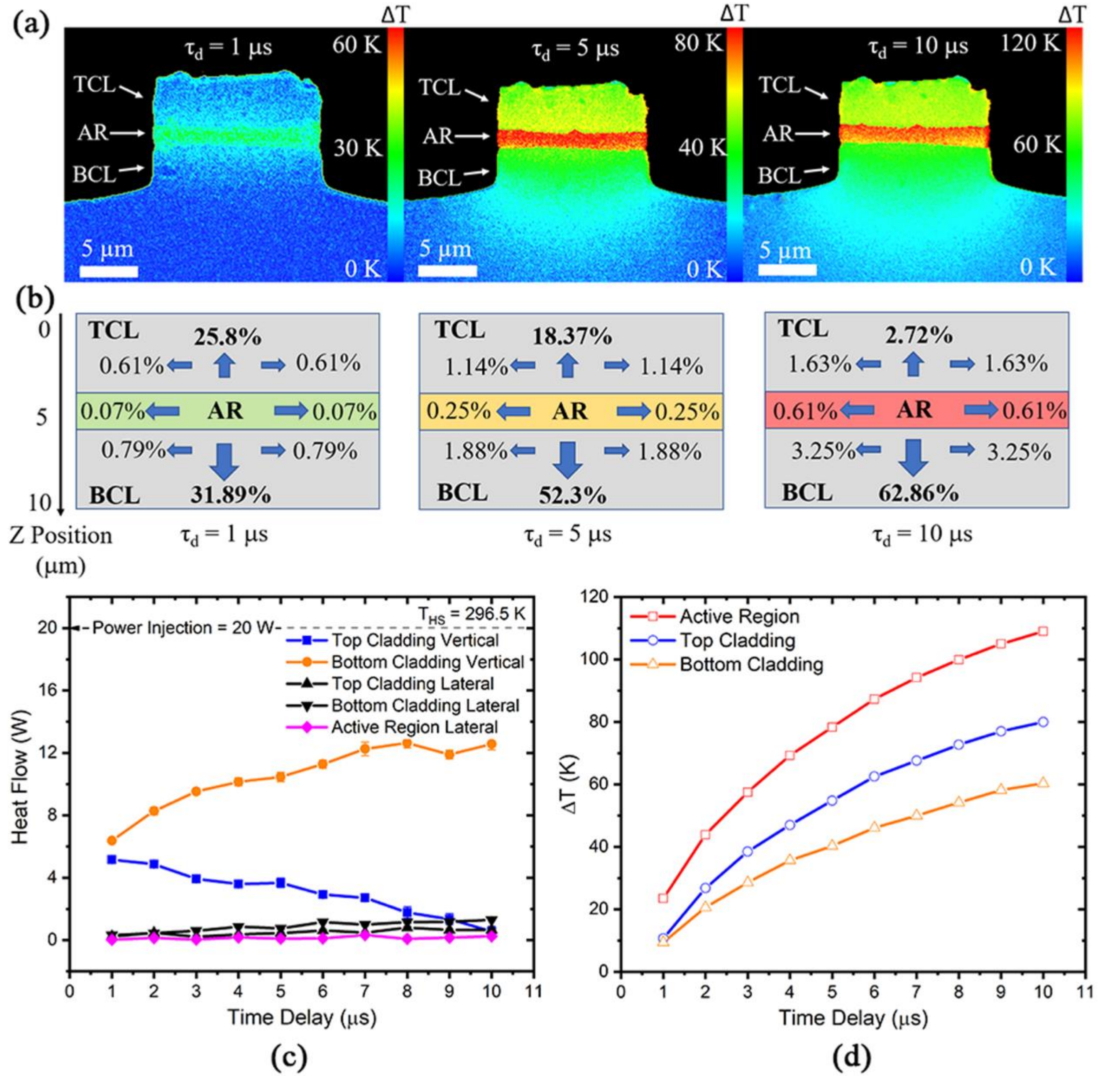

Figure 3.10 2D transient temperature imaging profiles (a) and percentage of heat dissipation rates (b) within the close-to-active-region area at the time delay of 1 μs (beginning of the current-injection pulse), 5 μs (in the middle of the current-injection pulse), and 10 μs (end of the current-injection pulse). (c) Calculated transient heat flow profiles within one period of current-injection pulse when the pulse width is 10 μs and the peak injection power is 20 W (I = 2 A, V = 10 V) within the close-to-active-region area from SR-TDTR measurement. The orange and the blue lines show the vertical heat flow from the active region (AR) towards to the bottom cladding (BCL) and the top cladding layer (TCL), respectively. Two black lines are the lateral heat dissipation from the top cladding and bottom cladding layer towards both lateral sides, respectively. The magenta line is the lateral heat flow inside the active region. (d) Temperature change with respect to time delay at the center of the active region, at the center of the top cladding layer, at the center of the bottom cladding layer, respectively.

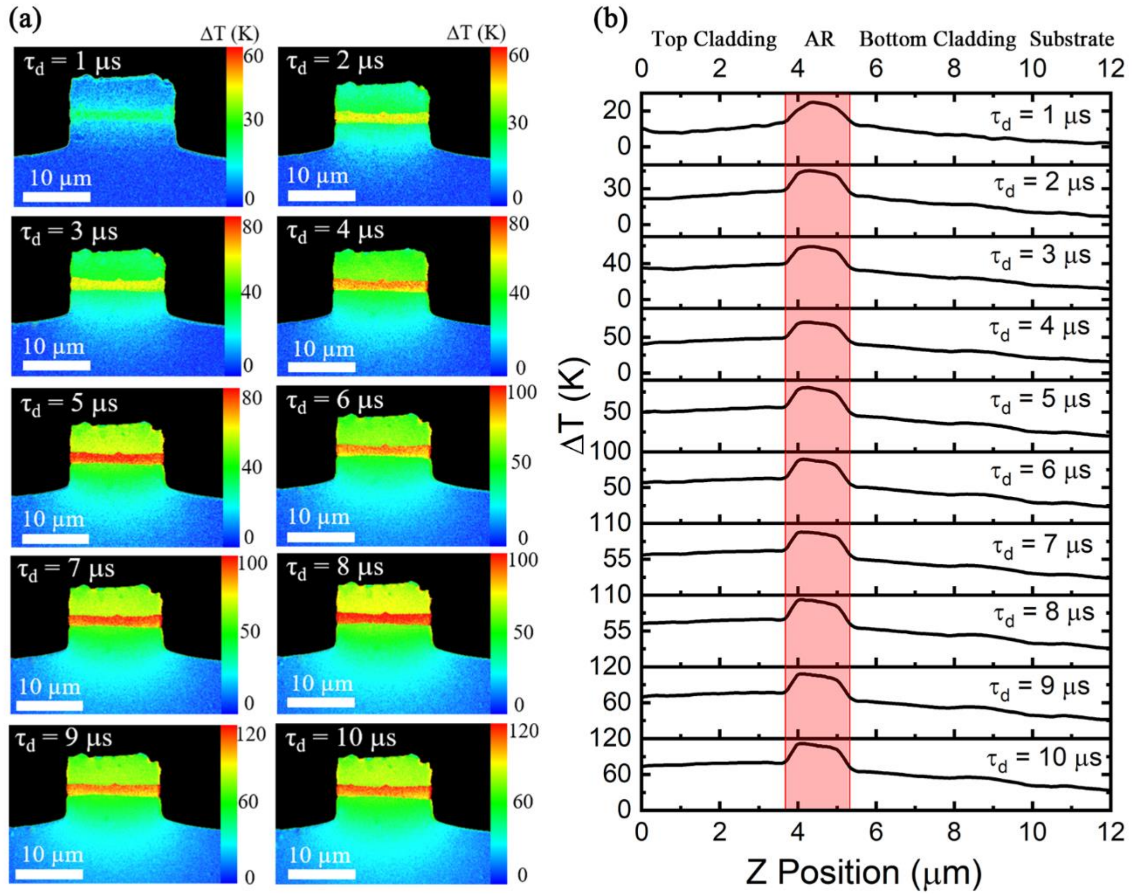

Figure 3.11 (a) 2D transient temperature imaging profiles at different time delay (in 1 μs step) under pulsed injection (I = 2 A, V= 10 V, PW = 10 μs, duty cycle = 0.2%). (b) Measured transient temperature rises (ΔT) above the heatsink temperature on QCL's facet from top cladding layer to the substrate at different time delay (in 1 μs step).

Table 3.1 Thermal conductivity [W/(m·K)] of different layers of materials

	Active Region (Cross-plane)	Active Region (In-plane)	Cladding Layer – Contact Layer – Substrate
Exp. in this work (296.5 K)	5.33±0.8		65.44±2.68
Sim. in this work (296.5 K)	5.33	22 [52]	65.44
Sim. in this work (150 K)	5.33	22 [52]	180 [42][53]

Table 3.2 Time-dependent (transient state) heat flow in long-pulse injection (Peak power injection = 20 W, Pulse width = 10 μs, duty cycle = 0.2%)

Time Delay (τ_d)	1 μs	2 μs	3 μs	4 μs	5 μs	6 μs	7 μs	8 μs	9 μs	10 μs
Top Cladding Vertical	5.16 W (25.80%)	4.87 W (24.35%)	3.92 W (19.61%)	3.60 W (17.99%)	3.67 W (18.37%)	2.93 W (14.63%)	2.71 W (13.55%)	1.77 W (8.85%)	1.34 W (6.72%)	0.54 W (2.72%)
Bottom Cladding Vertical	6.38 W (31.89%)	8.27 W (41.36%)	9.53 W (47.63%)	10.14 W (50.72%)	10.46 W (52.30%)	11.28 W (56.41%)	12.26 W (61.29%)	12.64 W (63.18%)	11.90 W (59.49%)	12.57 W (62.86%)
Top Cladding Lateral	0.24 W (1.21%)	0.46 W (2.30%)	0.22 W (1.09%)	0.37 W (1.85%)	0.45 W (2.27%)	0.62 W (3.08%)	0.48 W (2.38%)	0.80 W (4.00%)	0.65 W (3.25%)	0.65 W (3.25%)
Bottom Cladding Lateral	0.31 W (1.57%)	0.45 W (2.24%)	0.60 W (3.00%)	0.86 W (4.30%)	0.75 W (3.76%)	1.16 W (5.78%)	0.99 W (4.97%)	1.16 W (5.79%)	1.17 W (5.86%)	1.30 W (6.50%)
Active Region Lateral	0.03 W (0.14%)	0.14 W (0.69%)	0.04 W (0.22%)	0.17 W (0.85%)	0.10 W (0.51%)	0.11 W (0.56%)	0.32 W (1.61%)	0.09 W (0.43%)	0.16 W (0.81%)	0.24 W (1.21%)
Total	12.12 W (60.62%)	14.19 W (71.93%)	14.31 W (71.55%)	15.14 W (75.71%)	15.43 W (77.22%)	16.10 W (80.46%)	16.76 W (83.80%)	16.46 W (82.25%)	15.22 W (76.13%)	15.30 W (76.55%)

Table 3.3 Time-dependent (transient state) heat flow in short-pulse injection (I = 6 A, V= 18.7 V, Peak power injection = 112.2 W, Pulse width= 500 ns, duty cycle = 0.25%)

Time Delay (τ_d)	50 ns	100 ns	150 ns	200 ns	250 ns	300 ns	350 ns	400 ns	450 ns	500 ns	600 ns	1250ns
Top Cladding Vertical	9.87W 8.80%	15.35W 13.68%	16.54W 14.74%	20.50W 18.27%	23.55W 20.99%	23.71W 21.13%	24.99W 22.27%	25.74W 22.95%	26.43W 23.56%	23.48W 20.92%	13.81W	0.73W
Bottom Cladding Vertical	7.54W 6.72%	13.90W 12.39%	20.34W 18.13%	20.20W 18.01%	25.86W 23.05%	25.91W 23.09%	26.94W 24.01%	31.56W 28.13%	29.04W 25.89%	27.62W 24.62%	18.44W	2.77W
Top Cladding Lateral	0.03W 0.03%	0.14W 0.12%	0.10W 0.09%	0.22W 0.19%	0.18W 0.16%	0.40W 0.35%	0.41W 0.37%	0.58W 0.52%	0.72W 0.64%	0.66W 0.59%	0.58W	0.25W
Bottom Cladding Lateral	0.25W 0.22%	0.13W 0.12%	0.29W 0.26%	0.35W 0.31%	0.49W 0.43%	0.68W 0.61%	0.69W 0.61%	0.67W 0.60%	0.69W 0.62%	0.87W 0.78%	0.82W	0.44W
Active Region Lateral	0.00W 0.00%	0.01W 0.01%	0.03W 0.03%	0.05W 0.04%	0.09W 0.08%	0.11W 0.10%	0.10W 0.09%	0.11W 0.10%	0.11W 0.10%	0.14W 0.13%	0.12W	0.05W
Total	17.69W 15.76%	29.54W 26.32%	37.30W 33.24%	41.32W 36.82%	50.16W 44.71%	50.80W 45.28%	53.13W 47.35%	58.67W 52.29%	57.00W 50.80%	52.77W 47.03%	33.77W	4.24W

3.3.4 Lasing Quenching Effect Study: Correlation of Temperature-Dependent L-I-V Measurements, TDTR Thermal Imaging, and Thermal Thermodynamics Modelling

The SR-TDTR imaging can be used individually or in combined with thermal modeling to reveal other dynamics in device operation. One such example is thermally-induced lasing quench. Figure 3.12(a) shows the measured pulse width of an emitted optical output from the QCL under test biased at 2.375 A in current (above threshold) and cooled down to 150 K (heat sink temperature). The pulse width of the injected electrical pulse is increased from 1 μs to 10 μs. As expected, the corresponding optical pulse width increases linearly with the electrical pulse width, but only up to ~2.1 μs (vertical dash line) of the electrical pulse. Beyond that, the optical pulse becomes saturated at ~1.9 μs (horizontal dash line) regardless of further increase of the electrical pulse width. This can be attributed to the thermal quenching of lasing operation [54]. As the device under test does not lase at room temperature, while the current version of the SR-TDTR cannot be operated at lower temperatures, thermal modeling has to be employed in addition to experimental measurements to reveal the underline dynamics of device operation.

Figure 3.12(b) compares the temperature of the active region measured by SR-TDTR technique as a function of time delay with simulated results. The QCL is injected 2 A of current (biased voltage: 10 V) in pulse mode at room temperature (not lasing). A series of measurements are conducted for pulse widths of 1 μs, 2.5 μs, 5 μs, and 10 μs, respectively. As shown in Figure 3.12(b), the rising temperature of the active region (ΔT) increases quickly when the current is injected, and it drops to zero when the current is switched off. This rise and drop of the laser temperature of the active region with the injected current are simulated using COMSOL Multiphysics. The simulated results (solid lines) are found in good agreement with the experimental data (symbols) as shown in Figure 3.12(b).

Following the same approach, the active region temperature of the QCL biased at current injection of 2.375 A in pulse mode at a heat sink temperature of 150 K is simulated. As shown in Figure 3.12(c), the simulation result shows that the peak temperature of the active region increases quickly as the pulse width increases from 1, 2.5, 5 to 10 μs. In particular, the temperature increases to 197 K (47 K above the heatsink temperature) at an injected pulse width of ~2.0 μs (denoted by the vertical dashed line in purple).

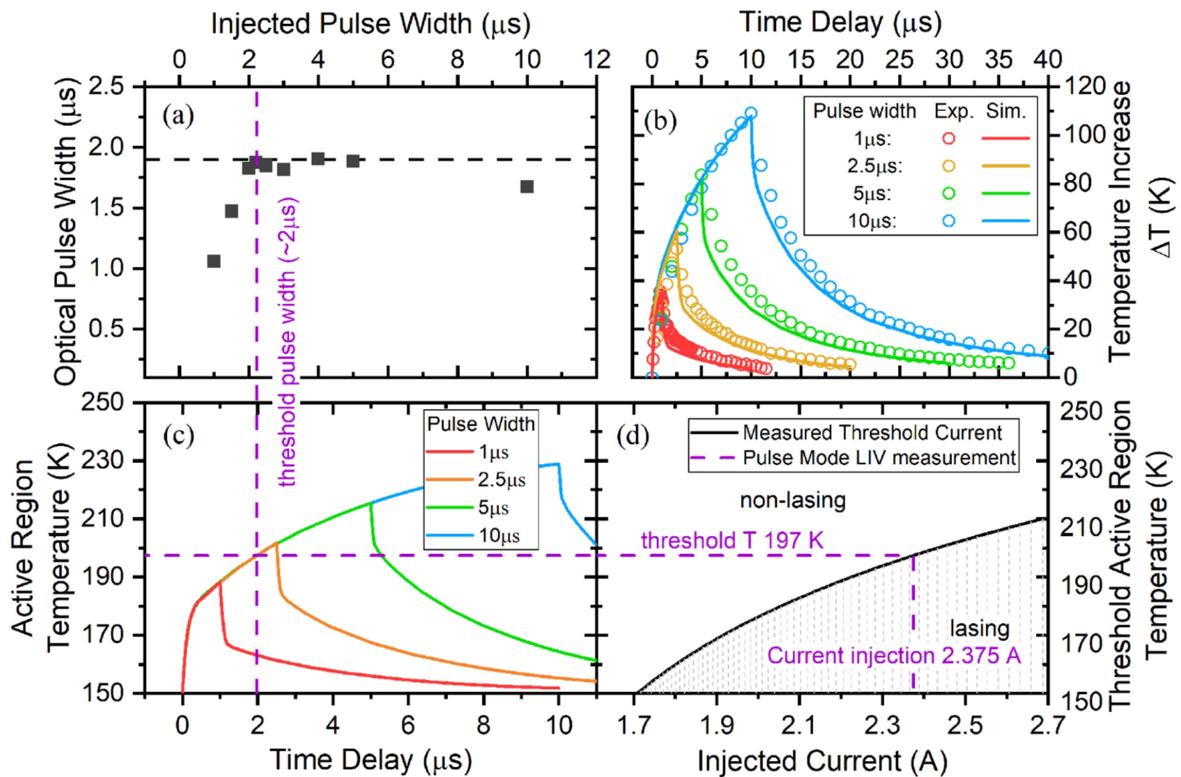

Figure 3.12 (a) Measured relationship in pulse widths (symbols) between current-injection pulse and output light pulse at a heat sink temperature of 150 K and a current-injection amplitude of 2.375 A. Saturated value of optical pulse width is shown in black dashed line. (b) Measured (circles) and simulated (solid lines) time dependent temperature changes in active region with different current-injection pulse widths of 1, 2.5, 5, and 10 μs at room temperature (296.5 K). (c) Simulated time dependent temperature in the active region with different current-injection pulse widths of 1, 2.5, 5, and 10 μs at a heat sink temperature of 150 K. (d) Measured temperature at threshold as a function of device injection current, derived from light-current-voltage measurements in pulse mode (pulse width of 500 ns, modulation frequency of 500 Hz). The purple dashed line shows the relationship among the threshold current of 2.375 A in (d), the threshold temperature of 197 K in (c), and the threshold pulse width of ~2 μs in (a).

Figure 3.12(d) shows measured threshold current with respect to the threshold active region temperature, derived from light-current-voltage (L-I-V) measurements in pulse mode (pulse width of 500 ns, modulation frequency of 500 Hz). Due to the ultra-low duty cycle (0.025%), Joule heating is minimum, and the active region temperature of the device is in equilibrium with the heat sink

temperature. The threshold temperature for a fixed injection current of 2.375 A is measured as 197 K (Figure 3.12(d)). Beyond this temperature, the lasing stops. The simulation results in Figure 3.12(c) thus clearly reveal the observation in Figure 3.12(a) which is attributed to thermally-induced lasing quench. The purple dashed line shows a relationship among the threshold current of 2.375A in Figure 3.12(d), the threshold temperature of 197 K in Figure 3.12(c), and the threshold pulse width of ~2 μs in Figure 3.12(a).

3.3.5 Thermal Dynamics of MIR QCLs: From Transient State to Thermal Equilibrium

As discussed in section 2.1.8 and section 2.1.9, the transient temperature rise in active region above the heatsink temperature will be steady (reach on a maximum temperature) when the injected pulse duration is long enough. In this case, with the pulse width increasing, the QCL is transiting from transient state to quasi-steady state under thermal equilibrium. As shown in Figure 3.13(a), under 20 W of peak power ($I = 2$ A, $V = 20$ V), the maximum temperature rises are characterized at various pulse width from 500 ns to 100 μs when the time delay is aligned with the falling edge of each pulse injection. The red dash line indicates the fitting curve by equation (2.33). The time constant is calculated at 10.87 ± 0.37 μs. Figure 3.13(b) shows the 2D temperature profile at thermal equilibrium (quasi-steady state) when the pulse width and the time delay are both at 100 μs. Black arrows illustrate the heat dissipation channels.

The quasi-steady state heat flow values in different channels extracted from Figure 3.13(b) are shown in Table 3.4. The heat flow is averaged when the time delay from 80 μs to 100 μs. The results further confirm that most of the heat drains to the bottom cladding layer towards the substrate and finally to the heatsink. These results illustrate clear evidence and quantitative guidance for thermal management on QCLs.

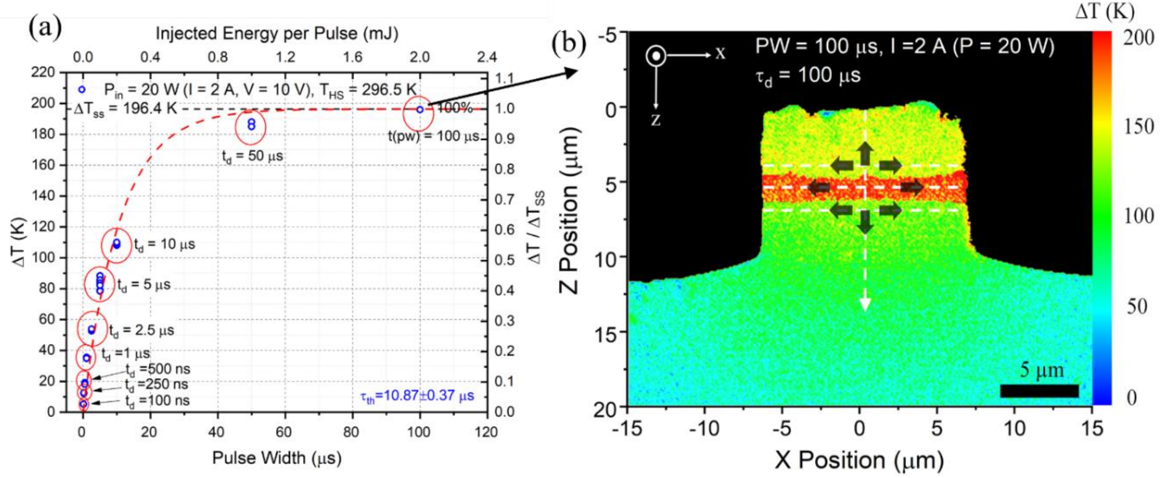

Figure 3.13 (a) Measured the maximum transient temperature rises (ΔT) on QCL's facet above the T_{HS} at RT at different pulse width (time delay is set at the fall edge of each pulse) under 20 W of peak power (I = 2 A, V = 10 V). (b) Mapped 2D thermal imaging profile on QCL's facet under quasi-steady state (thermal equilibrium) when the pulse width and time delay are both at 100 μs. Black arrows illustrate the heat dissipation channels.

Table 3.4 Quasi-Steady State Heat Flow (W) in pulse injection (I = 2 A, V= 10 V, PW = 100 μs, duty cycle = 2%, τ_d = 80-100 μs)

	Heat Flow (W)	Percentage of Pulse Injection Power
Top Cladding Vertical	2.84±0.27	14.21%±1.36%
Bottom Cladding Vertical	13.64±0.16	68.21%±0.78
Top Cladding Lateral	1.07±0.18	5.34%±0.89%
Bottom Cladding Lateral	2.04±0.10	10.19%±0.49%
Active Region Lateral	0.41±0.01	2.04%±0.05%
Total	20	100%

In addition, Figure 3.14 shows transient temperature rises with time delay at different current injection (from 0.5 A to 2 A) with pulse width of 100 μs and duty cycle of 2%. The results indicate that the temperature rises almost reach to maximum points when the pulse duration at 100 μs. As the time constant (τ) is calculated at ~10 μs from Figure 3.13, it could be a good point to lower τ by more efficient thermal management, especially when the QCL is biased under cw mode.

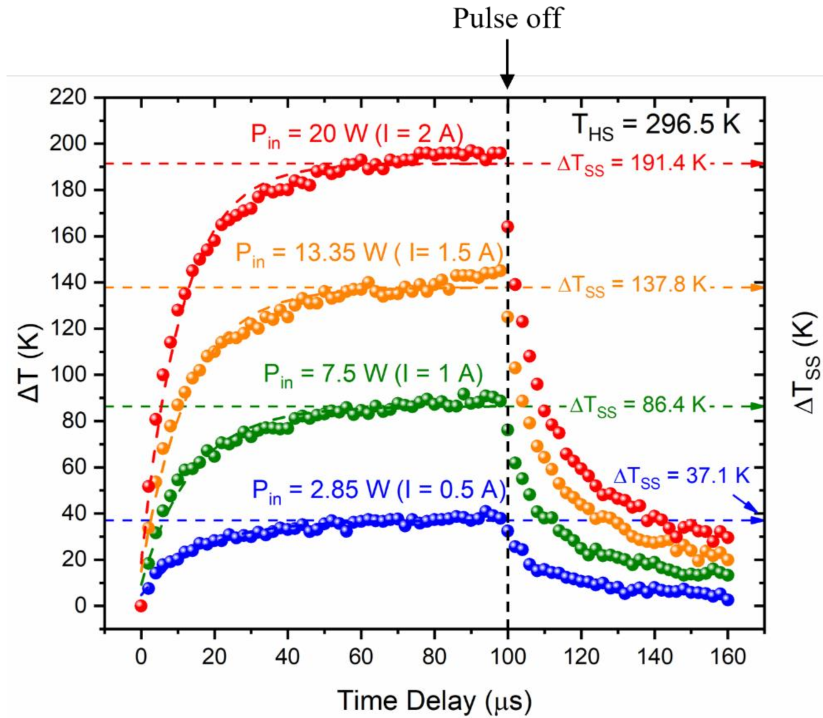

Figure 3.14 Transient temperature rises with time delay at different current injection (from 0.5 A to 2 A) with pulse width of 100 μs and duty cycle of 2%.

3.3.6 Thermal Conductivity and Thermal Resistant

It was proposed by employing steady-state thermoreflectance (SSTR) technique to calibrate the thermal conductivity of the materials [56][60]. Table 3.1 shows the calibrated results of the cross-plane thermal conductivity of the active region ($k_{\perp(AR)}$) and the thermal conductivity of cladding layers as well as the substrate. In addition, the in-plane thermal conductivity of the active region ($k_{\parallel(AR)}$) was directly extracted from the reference paper [52]. Since the temperature gradient in lateral direction within the active region is very small, the value of $k_{\parallel(AR)}$ has negligible impact on the calculation accuracy of other measured values.

In transient state, as discussed in chapter 2, Fourier's law can be written as 2D time-dependent heat conduction equation [54][68], given by

$$Q = -\nabla \cdot (k\nabla T) + \rho C_p(\partial T/\partial t) \qquad (eq. 3.1)$$

where Q is the injected power density [W/m^3] and ρC_p is the volumetric heat capacity of the material [J/(m^3·K)]. From the right-hand side of the equation (3.1), the first term determines the time-dependent net heat flow density out from the active region (heat dissipation), and the second term represents the ability of time-dependent heat accumulation. Therefore, the time-dependent net heat flux [W/m^2] out from the active region (Δq_{out}) can be written as

$$\Delta q_{out} = -k\nabla T \qquad (eq. 3.2)$$

which is the as the same as the equation (2.12) in chapter 2.

As mentioned in Figure 3.10 in the section 3.3.3, the transient temperature gradients in lateral and vertical directions are extracted from 2D transient temperature imaging profiles. Detailed values of time-dependent (transient state) rate of heat flow [W] are shown in Table 3.2 and Table 3.3.

The thermal resistant (R_{th}) of the QCL can be linearly fitted under steady state measurement. However, under high current injection on cw mode, the device could be possibly burnt out. Therefore, combining quasi-steady state measurements and extrapolation from transient state measurements can be applied for linear fitting, where R_{th} is determined by the maximum temperature rise (ΔT_{SS}) divided by the peak injection power (P_{in}). As shown in Figure 3.15, the thermal resistant and thermal conductivity of the active region are 8.84 ± 0.14 K/W and 5.33 ± 0.8 W/(m·K), respectively.

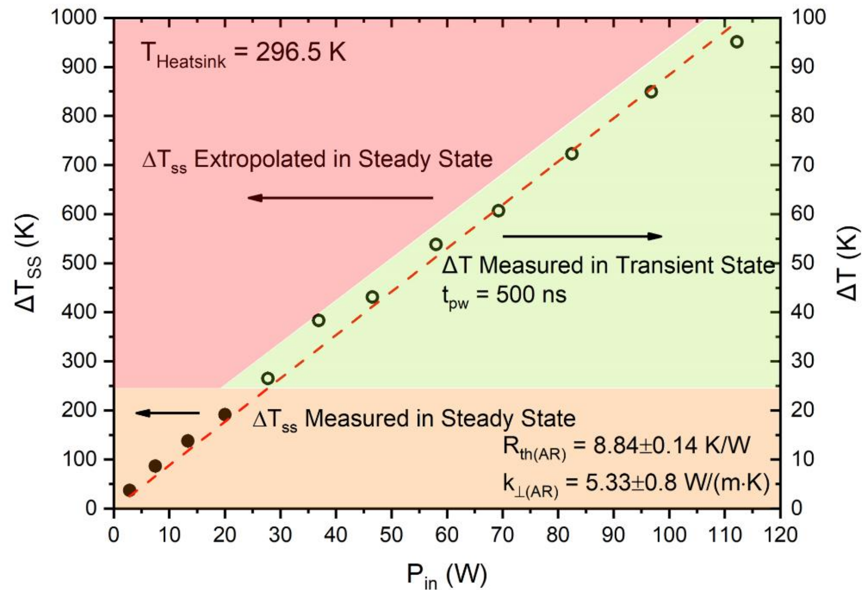

Figure 3.15 Linear fitting of correlating measured maximum temperature rises in quasi-steady state (PW = 100 µs) with extrapolated maximum temperature rises (PW = 500 ns) from transient state measurements.

3.3.7 Simulation Setting in COMSOL Multiphysics

The simulation by COMSOL Multiphysics is based on heat conduction module by solving 2D time-dependent heat conduction equation (3.1) at room temperature (296.5 K) and at cryogenic temperature of 150 K, respectively.

The values of thermal conductivity (k) used for simulation are also shown in Table 3.1. The cross-plane thermal conductivity value of the active region $k_{(AR\perp)}$ and the thermal conductivity of the cladding layers are extracted from our calibration results. It is noticed that the same value was employed both at room temperature and cryogenic temperature for $k_{(AR\perp)}$, since $k_{(AR\perp)}$ is much less sensitive to temperature change due to a large thermal boundary resistance (TBR) [51][70][71]. This is because that TBR in active region is dominant due to the enhanced phonon reflection at interfaces (interface roughness scattering) by a large Aluminum fraction (45%) [70][72]; on the contrary, thermal resistance in cladding layers and substrate (bulk material) is dominated by temperature-dependent phonon-phonon scattering, which has much higher sensitivity to the temperature change, resulting in a much lower thermal resistance (higher thermal conductivity) in cryogenic temperature [42][53]. Therefore, the same $k_{(AR\perp)}$ value from the temperature profile measurement was used in COMSOL Multiphysics simulation applying in low temperature conditions.

3.4 Summary

In summary, time-resolved CCD-based spatially-resolved time-domain thermoreflectance microscopy (SR-TDTR) technique is applied to map two-dimensional temperature profiles of actively-biased MIR QCLs with high resolution down to 50 ns (temporal) and 390 nm (spatial). Experimental results clearly show that the heat accumulation in device active region starts even within less than 1 μs upon the application of electric current injection. Detailed data analysis discloses in such ridge-waveguide QCLs that, even though heat can be dissipated toward the top surface at the beginning of the process, most heat is dissipated down to the substrate. The SR-TDTR provides direct evidence of thermally-induced lasing quench of QCLs, and it is an enabling tool to probe internal dynamics of operating actively-biased devices.

Chapter 4
Thermal Dynamic Imaging of Mid-Infrared Quantum Cascade Lasers: Analysis of Ridge Width Dependent Effect

Self-heating or so-called Joule heating effect is detrimental for mid-infrared quantum cascade laser (MIR QCL) especially in high power electrical injection. In this chapter, by employing spatially resolved time-domain thermoreflectance (TDTR) spectroscopy, a strong localized heat confinement is observed on the laser facet within a small region of the electroplated gold (EP-Au) layer – air interface on the top of the ridge waveguide. Also, hot spots are clearly observed on the facet EP-Au layer due to the imperfect facet cleaving. In addition, a simplified 3D-thermodynamics heat transport model based on the experimental results was built-up for thermal properties investigation. It is found that ridge width, etched depth, vertical heat extraction coefficients (Γ, β_1, β_2) have strong effects on the thermal resistance (R_{th}) and thermal conductance per unit area (G_{th}), though thicker EP-Au from 1 μm to 2.5 μm does not have strong contribution.

4.1 Introduction

MIR QCLs are power-hungry devices; due to the fast dynamic process of carriers between intersubband transitions (orders of picosecond), it is required to consume a large amount of power before reaching the lasing threshold, and a high threshold current density is needed to maintain population inversion, leading to emits more heat than light. In this case, a large amount of energy injection towards the QCL is consumed and wasted which converts to Joule heating. To date, the highest wall-plug efficiency (WPE) of MIR QCLs is 22% on cw mode and 31% on pulsed mode at room temperature respectively, leading to emitting more heat than light. More importantly, when the QCLs are biased from long pulsed duration (high duty cycle) to cw mode current injection, the temperature rise inside the active region core is becoming significantly prominent. Not only it leads to a large temperature difference above the heatsink temperature, but also does it cause a large temperature gradient both in temporal and spatial, resulting in nonuniform temperature distribution and thermal instability in three dimensions (3D), which deteriorates the device lasing performances, reduces device reliability, and eventually leads to device failure in long-term. Therefore, it is requisite to characterize the 3D thermodynamics in transient state for MIR QCLs.

To date, several tools have been developed to characterize the thermal behaviours of QCLs, including micro-thermocouples, infrared (IR) thermometers, liquid crystal thermography (LCT) technique, scanning thermal microscopy (SThM), Raman spectroscopy, time-resolved microprobe photoluminescence (μ-PL), and CCD-based time-domain thermoflectance (TDTR) microscopy. Among of them, CCD-based TDTR microscopy provides non-invasive real-time monitoring in high resolutions, which is capable of probing down to 50 ns of temporal resolution, sub-micron of spatial resolution (probing wavelength dependent), and 0.1 K of temperature resolution. Nevertheless, most of the studies are focusing on the temperature distribution on laser facet in two-dimension (2D), which assume the Joule heating is uniformly distributed along the ridge cavity. However, there is lack of sufficient studies on 3D thermodynamics, especially for how the Joule heating is uniformly distributed along the ridge cavity.

In this chapter, transient state and quasi-steady state (thermal equivalent) of 3D thermodynamics of MIR QCLs was investigated on MIR QCLs. The temperature distribution was acquired both from the laser facet and on the top ridge waveguide. It is observed that there are strong localized Joule heating spots (hot spots) at the outer EP Au layer on the top of the laser ridge close to the laser facet, which show much higher than the. In addition, the spatial temperature profiles shows that there is the surface roughness of the EP Au layer generate hot spots.

4.2 Device Structure and Experimental Setup

MIR QCLs devices (lasing wavelength at ~ 9 μm) are from the same as-grown wafer (wafer#: G0241) by molecular beam epitaxy (MBE), the same wafer in Ref. [55]. The epitaxial layer thickness is 9.65 μm, with an active region consisting of $Al_{0.45}Ga_{0.55}As/GaAs$ multiple quantum wells (1.65 μm) sandwiched by n-type GaAs cladding layers (3.5 μm) on each side then terminated by electrical contact layers (1 μm). The QCL devices were fabricated into Fabry–Pérot ridge waveguides by standard microfabrication technique with a series of steps including photolithography, metal deposition, plasma-enhanced chemical vapor deposition (PECVD), inductively coupled plasma – reactive ion etching (ICP-RIE), and gold electroplating. There are three sets of devices, as shown in Table 4.1. Devices 1 and 2 are both in 2 mm of cavity length and 2.5 μm of thick Au electroplating, whereas ridge width is 18 μm

and 14 μm of device 1 and 2 respectively. Device 3 is as a refence device with the ridge width of 14 μm, cavity length of 2.5 mm, and 1 μm of cavity length, as the same as in Ref. [55].

Table 4.1 Device parameters of three sets of MIR QCL ridge waveguides (w is the ridge width, l is the cavity length, d' is the ridge etched depth, A is the top ridge area in XY plane, $T_{EP\text{-}Au}$ is the electroplated Au layer thickness

	w [mm]	l [mm]	d' [mm]	A [cm^2]	$T_{EP\text{-}Au}$ [μm]
QCL Ridge 1	18	2	9.5	0.00036	2.5
QCL Ridge 2	14	2	9.5	0.00036	2.5
QCL Ridge 3	14	2.5	11	0.00035	1

The experimental setup is as the same as the one mentioned earlier in chapter 2 and chapter 3, based on an integrated transient imaging module from Microsanj (Model: NT210B). In brief, the principle of the CCD-based TDTR microscopy is based on a pump-probe technique. As the device is actively-biased by an external electrical current injection (pump signal) by a high-power pulse generator (Avtech: AVR-3HF-B), a modulated blue LED pulse in tens of ns to μs (probe signal) is shinned on the device surface, and the spatial reflection signals from the device surface are collected by high-resolution CCD sensor (1626×1236 pixels, 20 Hz, 12 bits). The pump signal, probe signal, and CCD sensor are all synchronized together. The probe signals are modulated at different time delay (τ_d) as respect to the pump signals. As the relative change in optical reflectivity is proportional to the surface temperature change, the device surface temperature rise can be determined. By pulsed boxcar averaging technique, the temperature profile can be acquired both in spatially and temporally in high-resolution simultaneously. A more detailed setup description can be found in section 2.3.

The fabricated QCL ridge waveguides were mounted on a T-shaped copper heat sink, placed on a piezo-controlled thermal electric stage. The QCL devices (with facet plane or top ridge plane) are facing up towards the microscope's objective in different magnifications (×5, ×20, and ×100) for mapping the temperature profile. According to the equation (2.46) in section 2.2, the temperature variation is proportional to the change of the optical reflectivity on sample surface. As the thermoreflectance coefficient (C_{th}) is highly sensitive, it should be carefully calibrated. C_{th} is highly depending on

materials property, probing wavelength, as well as the surface roughness, typically on the order of 10^{-5} to 10^{-3} per degree. Although C_{th} is dependent on material temperature, in a certain temperature range, this correlation between $\Delta R/R$ and ΔT can be approximately assumed in first order relationship, which means the temperature dependence of C_{th} is relatively small and negligible.

4.3 Calibration of Thermoreflectance Coefficient

In chapter 3, thermoreflectance coefficient (C_{th}) is calibrated to be 1.525×10^{4} K^{-1} for the AlGaAs/GaAs-based MQWs active region layer on the laser facet, and 2.431×10^{4} K^{-1} for the n-type GaAs-based cladding layer and the n+ GaAs substrate region. Nevertheless, when measuring the temperature from the top side of the MIR QCL ridge waveguide, electroplating gold (EP-Au) layer should still be carefully calibrated. Different from the facet temperature measurements, the EP Au layer on the top ridge waveguide is facing towards the optical microscope, where the change of reflectivity is employed to collect. A DC power supply is modulated to heat up the entire thermal electric stage under the copper heatsink of the MIR QCLs. When the thermal equivalent is reached (takes appx 2-3 min), the temperature rise on device surface is directly read by a thermocouple, and the change the optical reflectivity on the metal surface from the blue LED probing pulse (wavelength of 470 nm) is acquired by the CCD sensor. The power of the DC power supply is continuously tuned to produce a series of temperature rise for the whole stage in a range of 15-50 K above the room temperature (25 °C). After repeating and averaging of data acquisition, the change of the reflectivity of the EP Au as respect to the temperature rise is plot in Figure 4.1. The green dots are the data acquired under ×20 of the objective lens with the numerical aperture (NA) of 0.4, and the purple dots are the data acquired under ×100 of the objective lens (NA=0.6). By linear regression fitting, it is found that the optical reflectivity change ($\Delta R/R$) with respect to the temperature change (ΔT) has the same trend for both magnifications of ×20 and ×100 of the objective lens, which turns out that the C_{th} is $(1.053\pm0.01)\times10^{4}$ K^{-1}. This C_{th} number is almost 60% lower than the PVD evaporated Au thin layer (2.59×10^{4} K^{-1}) report in Ref. [61], which is probably due to the surface roughness of EP Au in lower reflectivity.

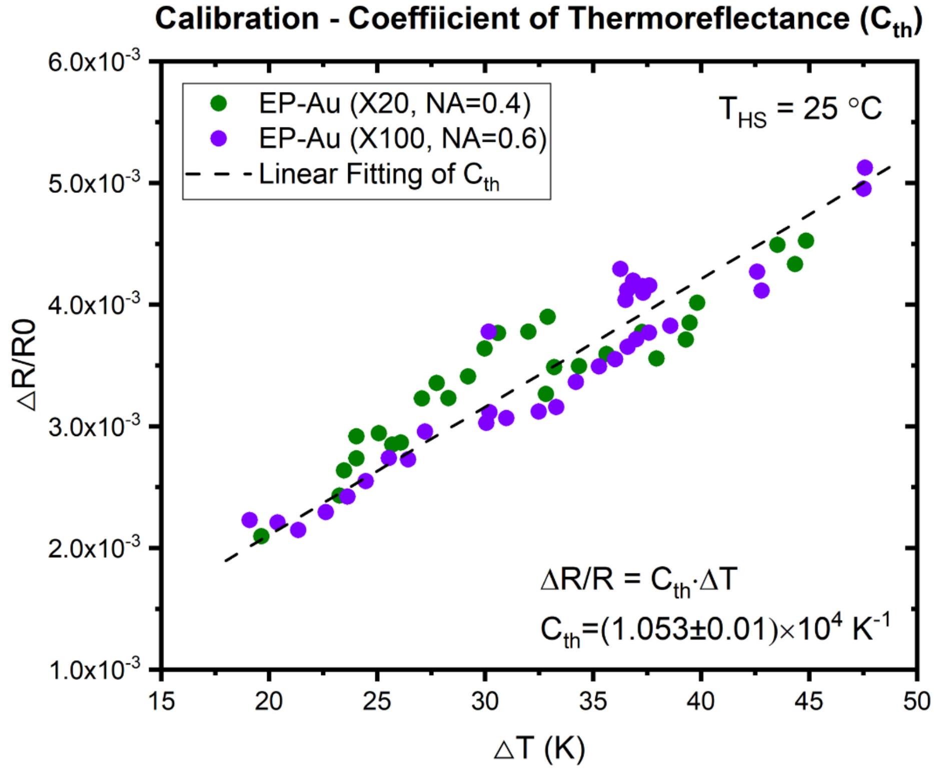

Figure 4.1 Calibration of the thermoreflectance coefficient (C_{th}) of EP Au layer, showing C_{th} is linear fitting at $(1.053\pm0.01)\times10^4$ K^{-1}. The calibration is conducted under an optical microscope objective magnitude with the magnitude of ×20 (green dots) and ×100 (purple dots), respectively, with the reference heatsink temperature at 25 °C.

4.4 Results and discussion

Figure 4.2 shows the spatial temperature profiles of MIR QCL device 1 in XZ plane (facet view) and XY plane (top ridge view) when the time delay (μs) is at 80 μs. The spatial resolved temperature rise above heat sink is mapped in pseudocolors. The MIR QCL device 1 was electrical pumped below threshold current in square pulse mode condition (pulse width of 80 μs, repetitive frequency of 500 Hz, and the duty cycle of 4%) with a peak current density of 3.92 kA/cm^2 (bias voltage of 8.9 V, current of 1.4 A, peak injected power of 12.58 W, and injected power density of 2.12×10^{14} W/m^3). Figure 4.2(a) shows the spatial resolved transient temperature profile from the ridge waveguide facet (XZ plane). The measurement is conducted under ×100 of the objective lens. The heat sink temperature is kept at

25 °C. The time delay of the pulsed LED probe signal (pulse width of 2 μs) with respect to the electric pump signal is set the same at 80 μs when the falling edge for both pulses are synchronized, in order to collect the transient temperature rise at the end of the electric pulse injection. As the Joule heating generates from the active region core, it is not surprising that the highest temperature rise (red color region) appears at active region area. But it is also observed that there is strong temperature rise at the electroplated Au layer from the sidewall the top (EP-Au to air interface). As discussed in Ref. [55], the heat dissipation channel from active region towards top cladding layers is blocked and slowed down due to the low thermal diffusion at the EP-Au to air interface compared with the high compared with the high thermal conductivity of the semiconductor. Thus, most of heat drains towards the heatsink through the bottom cladding layer – substrate. As a result, the temperature rise on top cladding layer is much higher than the bottom cladding, which leads to the localized high temperature rise at the outer EP-Au layer.

Figure 4.2(b) maps the transient temperature profile from the ridge waveguide top layer (XY plane) where the top layer of ridge waveguide is facing towards ×20 of the objective lens, and the other measurement conditions are kept the same. The top ridge waveguide from the device is covered by 2.5-μm-thick EP-Au which connects to the bonding pad (the whole blue rectangle area). It is clearly seen that the temperature rise gradient disperses from the top ridge towards the bonding pad, which shows the lateral heat dissipation flow channels. It is also observed that there is a strong localized temperature rise (hot spots) close to the laser facet (indicated by the arrows). A selected area close to the QCL facet (frame in white dash line) indicated in Figure 4.2(b) is further remeasured under ×100 of the objective lens, which is shown in Figure 4.2(c). The reddish area (hot spots) surrounding the laser facet indicates the Joule heating is strongly localized at the laser facet – air interface. Also, from the temperature profile of the EP-Au layer on the top of ridge waveguide, it can be seen that the hot spots nonuniformly distribute on the ridge top surface, which suggests that the EP-Au layer surface is quite rough. To further investigate the temperature distribution from the top EP-Au layer along the laser cavity, five different regions are selected from the laser facet towards the inner cavity, which are denoted in white dash frames (from Location 1 to Location 5). The average surface temperature in the five locations from Figure 4.2(c) together with the average temperature of three selected areas on the laser facet (active region, top cladding layer, and bottom cladding layer) from Figure 4.2(c) are plotted in a bar diagram shown in Figure 4.2(d). The facet temperature rise (ΔT) above the heat sink temperature of the active region, top cladding layer, and bottom cladding layer is 159.92 K, 114.77 K, 98.25 K,

respectively; and ΔT at the location from 1 to 5 of the EP-Au on the top ridge waveguide is 156.66 K, 103.1 K, 98.25 K, 93.7 K, 87.14 K, respectively. It is noticeable that ΔT of location 1 (156.66 K) is standing out, which is much higher than other locations, even higher than the top cladding layer, and only slightly lower than ΔT of the active region on the laser facet. This phenomenon indicates that the Joule heating is localized and accumulated at the device ridge facet.

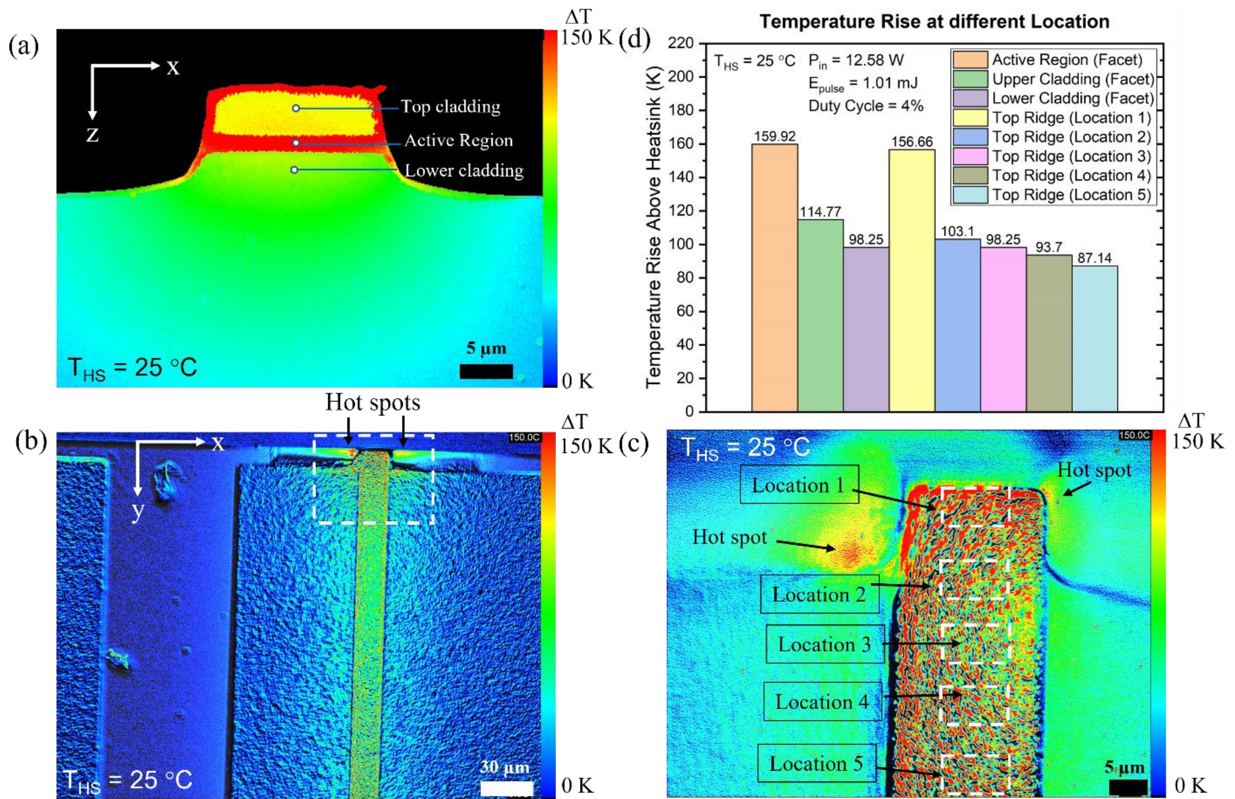

Figure 4.2 3D thermodynamics of temperature rise above heat sink at room temperature. (a) Spatially resolved temperature profile of a MIR QCL at the laser facet (XZ plane) under ×100 of objective lens; (b) spatially resolved temperature profile of a MIR QCL on the top of ridge waveguide (XY plane) under ×20 of objective lens; (c) spatially resolved temperature profile of a selected area (XY plane) under ×100 of objective lens; (d) average temperature rise above the heatsink temperature on different locations extracted from (a) and (c). (Measurement conditions: pump pulse duration of 80 µs, duty cycle of 4%, time delay of probe signal at 80 µs, peak power injection of 12.58 W, peak injected power density of 2.12×10^{14} W/m^3, heatsink temperature at 25 °C).

To further investigate 3D thermodynamics from the selected locations of the MIR QCL device 1, spatially resolved thermal imaging were conducted with injection power dependent and temporal dependent, respectively. Figure 4.3(a) and (b) show the temperature rise above the heatsink at quasi-steady state (with peak power injection) and transient state (with time delay) at different locations, respectively. The same MIR QCL ridge waveguide was pumped on pulse mode (80 μs of pulse width and 4% of the duty cycle) under difference peak power injection from 0.57 W to 12.58 W (current density from 0.43 A/cm^2 to 3.92 A/cm^2) at room temperature before reaching the threshold. The time delay τ_d was kept at the 80 μs, where the falling edge of probe signal was synchronized with the pump's one, in order to acquire the highest temperature rise within the electrical pulse injection. ΔT at difference locations from the QCL are plotted in scatter diagram, as shown in Figure 4.3(a). Inarguably, ΔT from different locations is almost linear increasing with the injected power. Although the active region temperature marks the highest one (red solid dots), it is also noticeable that the at the location 1 (close to the laser facet) of the EP-Au layer is comparable with the ΔT at the active region (purple hollow dots), much higher than the other ones. In comparison, ΔT from location 2 to location 4 are all below ΔT at the top cladding layer, which is understandable. To further investigate how the temperature change with the time delay within a pulse injection, a series of transient temperature rise was measured when τ_d was tuned from 0 to 80 μs with a step at 2 μs, as the peak injected power is kept at 12.58 W, shown in Figure 4.3(b). Remarkably, although the higher temperature rise occurs at the active region (red solid dots), the ΔT at location 1 is surpass ΔT of top cladding layer when the τ_d over 4 μs, and it gradually increases to close to the maximum temperature rise situated at the active region. In addition, within such long pulse duration (80 μs), ΔT at each follow the same trend of increase then go to saturation. At such long pulse injection (80 μs), the temperature rise is in exponential increase and gradually goes to saturation, which indicate that it close to thermal equilibrium, this can infer that it goes to quasi-steady state. It is clearly revealed from this figure that the transient temperature quickly rise on the laser facet.

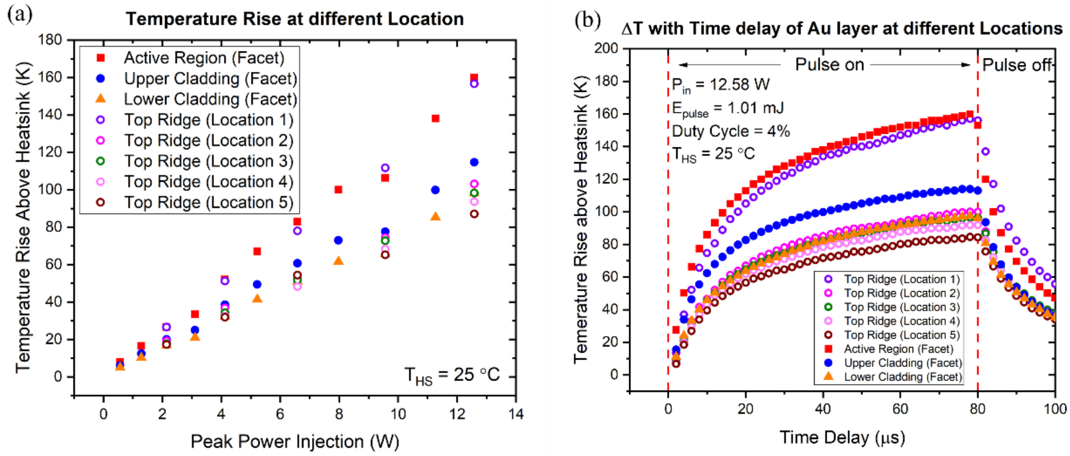

Figure 4.3 Temperature rise above heatsink at quasi-steady state (with peak power injection) and transient state (with time delay) at different locations. (a) Temperature rise above heatsink at quasi-steady state with the increasing of the peak power injection with 80 μs of pulse injection (4% of duty cycle) at different locations indicated in Figure 4.2, and the temperature rise is acquired at the end of each pulse; (b) transient state of temperature rise above the heatsink with the change of the time delay of 80-μs-long pulse injection (4% of duty cycle) in 12.58 W of peak power injection from different locations.

To compare and investigate how the layer structure and the dimensions of the ridge waveguides affects the thermal behaviours to the devices (e.g., width ridge, cavity length, and thickness of EP-Au), thermal resistance (R_{th}) and thermal conductance per unit area (G_{th}) were employed for the device 1, 2 and 3. The measurements were conducted in the same working conditions, which was in quasi-steady state, where the thermal performance is in thermal equilibrium. The temperature rise was acquired from the active region facet when the time delay of the pulsed probe signal synchronized with the electric pump signal at 80 μs, with respect to tuning of the peak power injection, as shown in Figure 4.4(a). As a results, the Data were linear fitted, which shows the R_{th} is 12.28±0.19 K/W, 13.07±0.19 K/W, and 10.91±0.23 K/W for MIR QCLs ridge device 1, 2, and 3, respectively. Figure 4.4(b) shows the thermal conductance per unit area, which evaluates the ability of the thermal dissipation per area among different devices. By linear fitting, the results shows that the G_{th} is 225.9±3.5 W/(K·cm^2), 272.7±4.1 W/(K·cm^2), and 280.8±5.5 W/(K·cm^2) for device 1, 2, and 3, respectively. The results shows that narrower ridge width superior higher thermal dissipation capability, compared device 2 (ridge width of 14 μm) with device 1 (ridge width of 18 μm). However, surprisingly, there no improvement by a thicker

EP-Au layer, compared device 2 (EP-Au thickness of 2.5 μm) and device 3 (EP-Au thickness of 1 μm), which shows the comparable G_{th} of 272.7±4.1 W/(K·cm^2) and 280.8±5.5 W/(K·cm^2).

Since the ridge dimensions and packaging strategies can strongly affect the heat extraction/dissipation efficiency from the active region towards the heatsink, herein, we introduce three sets of parameters for the thermal behaviours of these devices. Γ, β_1 and β_2, is the proportion of heat flux in vertical direction, the coefficient of heat extraction towards upper cladding, and the coefficient of heat extraction towards lower cladding layer, respectively. The algorithm of the calculation is described in chapter 2, and the results are shown in Table 4.2. It is shown that Γ of device 1, 2, and 3 is 86.3%, 90.28%, and 63.96%, indicating that there is much higher portion of heat extraction/dissipation in vertically for the thicker EP-Au (device 1 and 2), compared with reference thinner EP-Au layer one (device 1). It also shows that β_1 for device 1, 2, and 3 is 0.0075, 0.0046, and 0.0104, respectively; β_2 for device 1, 2, and 3 is 0.0530, 0.0579, and 0.0501, respectively. As a results, compared with the reference device 3, both devices 1 and 2 have a much higher vertical heat extraction channel. Compared with heat extraction towards upper cladding (β_1) and lower cladding (β_2), β_2 /β_1 is 7.07, 12.52, and 4.81 for device 1, 2, and 3, respectively, indicating there are there are much higher portion of heat dissipation towards the heatsink through bottom cladding layer – substrate channel. In other word, thicker EP-Au does not act as a strong heat dissipation channel in this epi-layer up mounting strategy.

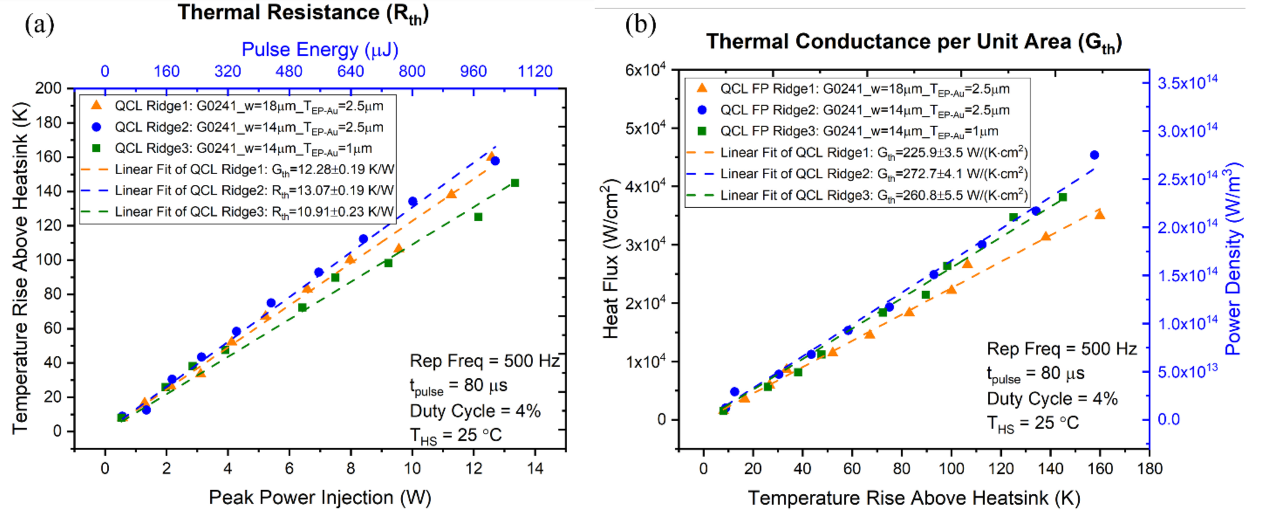

Figure 4.4 Thermal resistance (a) and thermal conductance per unit area (b) analysis in quasi-steady state measurement, in linear fitting with peak power injection and temperature rise above heatsink temperature, respectively.

Table 4.2 Thermal properties of three sets of MIR QCL ridge waveguides: R_{th} is the thermal resistance, G_{th} is the thermal conductance per unit area, Γ is the proportion of heat flux in vertical direction, β_1 and β_2 is the coefficient of heat extraction towards upper cladding and lower cladding layer, respectively.

	R_{th} [K/W]	G_{th} [W/(K·cm^2)]	Γ	β_1	β_2	β_2/β_1
QCL Ridge 1	12.28±0.19	225.9±3.5	0.863	0.0075	0.0530	7.07
QCL Ridge 2	13.07±0.19	272.7±4.1	0.9028	0.0046	0.0579	12.52
QCL Ridge 3	10.91±0.23	260.8±5.5	0.6396	0.0104	0.0501	4.81

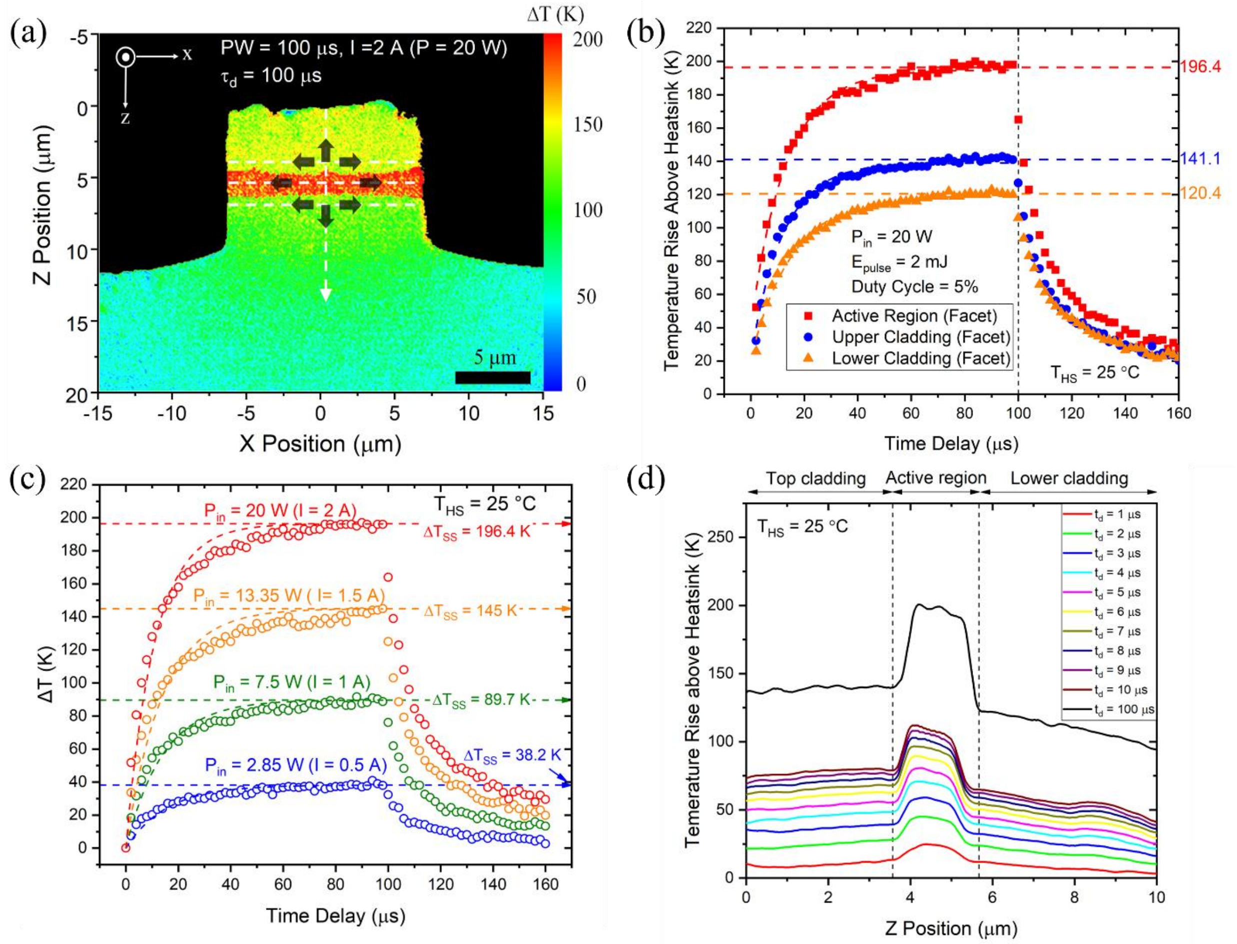

Figure 4.5 Quasi-steady state and transient state thermal analysis: (a) 2D temperature profile under quasi-steady state (100 μs of pulse injection; 20 W of peak power, and 100 μs of time delay); (b) transient temperature profile of the temperature rise above heatsink at active region (red), upper cladding layer (blue), and the lower cladding layer (orange); (c) transient temperature profile of the temperature rise above heatsink at active region with different peak power injection. (d) line scan of transient temperature rise at different time delay in z direction from upper cladding layer to lower cladding layer.

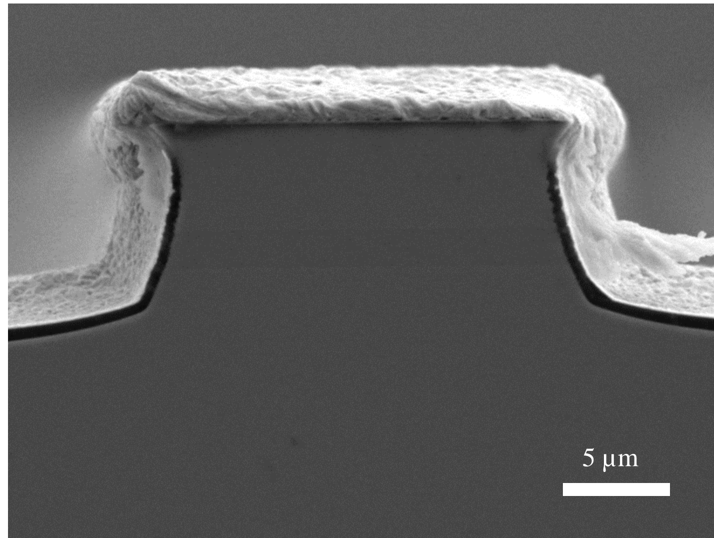

Figure 4.6 SEM image of an MIR QCL (Wafer#: G0241) cleaved facet with 2.5 μm thick EP-Au

4.5 Summary

In summary, spatially resolved time-domain thermoreflectance (SR-TDTR) microscopy has been applied to observe 3D thermodynamics of MIR QCLs. It is clearly observed that there is strong localized Joule heating occurring on the laser facet, especially on the edge of EP-Au layer on the top of the top cladding layer close to the facet. It is also observed that stronger Joule heating situates on the rough surface of EP-Au, leading to higher temperature rise (hot spots). Three sets of devices were characterized for the thermal properties (thermal resistance and thermal conductance per unit area). Comparing to the dissipation channel towards top EP-Au layer through the top cladding layer, it is found that most of heat is dissipating towards to the heatsink through bottom cladding layer – substrate channel. Thicker EP-Au layer does not have strong effects on enhancing the thermal dissipation efficiency based on the epi-layer up mounting. In comparison, narrow ridge waveguide could have a more efficient way for thermal dissipation. This evidence leads a guidance for improving thermal management on MIR QCLs based on packaging strategies.

Chapter 5

Facet Joule Heating of Mid-Infrared Quantum Cascade Lasers: Optical Degradation and Reliability Test

Localized Joule heating on the laser facet is detrimental to mid-infrared quantum cascade lasers (MIR QCLs) when long-term operation and reliability are requisite in high output power applications. However, the thermal stress-induced degradation process on MIR QCLs is still under discussion, and limited evidence is reported by real-time monitoring of thermal dynamics properties change in the early aging stage. In this chapter, reversible lasing performance degradation of an actively-biased MIR QCL is investigated under an accelerated aging burn-in test for 30 hours in an ambient atmosphere, followed by 10 minutes of hydrogen plasma treatment. The surface temperature rises (ΔT) of the MIR QCL are visualized by spatially resolved time-domain thermoreflectance (SR-TDTR) microscopy. The author found that ΔT on the laser facet decreases after 30 hours of the aging test, along with the lasing performance degradation; whereas ΔT increases after 10 minutes of post hydrogen plasma treatment, with the lasing performance resumption. In the meantime, the thermal property change along the laser cavity is negligible before and after the aging test, independent of the optical performance change. These results verify that thermal-induced facet oxidation is the main reason for the rapid degradation of the lasing performance in the early aging stage.

5.1 Introduction

28 years after the invention, mid-infrared quantum cascade lasers (MIR-QCLs) have developed from research to products [1][13][27][28]. For high output power requirements in applications, Joule heating is the detrimental factor causing reliability issues [29][30][32]. Unlike diode lasers, MIR-QCLs are power-hungry devices, exhibiting high series resistance, high threshold current density, and low electro-optical conversion efficiency. In general, >10 W of the electrical power is consumed to trigger the population inversion before reaching the lasing threshold (>1 A of current and >10 V of biased voltage typically) [2]. On the other hand, relatively low wall-plug efficiency (WPE) is achieved: up to 22% WPE and 31% WPE at room temperature on continuous-wave (cw) mode and on pulsed mode, respectively [5][12]. Due to high power consumption, most of the electrical current injection converts to Joule heating inside the active region, heating up the active region core temperature (T_{AR}). For

example, T_{AR} can rise 150 - 200 Kelvin (K) degrees above the heatsink temperature (T_{HS}) on the laser facet at ambient room temperature in cw mode operation when the injected power density is at 10^{14} W/m^3 level [31]. As a result, the localized Joule heating effect on the laser facet is detrimental to MIR QCLs, leading to lasing performance degradation, lifetime shortening, and thermally triggered catastrophic mirror damage (CMD) [32][73].

On the other hand, for MIR QCLs, thermal stress induced degradation mechanisms are still under discussion, and it is requisite to fully understand the change of the thermal dynamics properties from the laser active region with the change of the optical performance degradation during the aging process [73-77]. Recently, non-invasive tools such as micro-Raman (MR) and thermoreflectance (TR) microscopy are employed for thermal dynamics monitoring [58][77]. However, limited evidence is reported for the simultaneous visualization of the thermal dynamics in spatial and time-domain during the degradation process for an actively-biased MIR QCL. In the MR technique, indirect characterization of the thermal properties is extracted from the temperature-dependent Raman-shift but gives less accuracy and with one order of magnitude lower in the temperature resolution (~5-10 K) compared to the TR microscopy (~0.1-0.5 K) [55][58][59][68][77]. On the other hand, TR microscopy has been widely employed on monitoring surface temperature change on an actively-biased QCLs on both transient state and steady state [55][68][74]. In addition, previous findings indicated that facet Joule heating may cause facet damage and optical degradation when the QCLs are under high power density injection [73-77]. For example, in Ref. [77], facet oxidation and higher temperature rises are simultaneously observed on an uncoated long wave infrared QCL's emitting facet ($\lambda \sim 8.5$ μm) when the QCL is operating under high power injection. However, it is still unclear that if the facet Joule heating itself or the high-optical-power-density (HOPD) is the triggering mechanism for observed the facet damage/degradation in QCLs, even at the long wavelength mid-infrared (LW-MIR) range of 8-15 μm.

In this chapter, a reversible lasing performance degradation of an actively-biased $GaAs/Al_{0.45}Ga_{0.55}As$ multiple quantum wells (MQWs) based MIR-QCLs is investigated before and after an accelerated aging burn-in test ("aging" in short), followed by hydrogen plasma treatment. The aging is conducted under pre-lasing conditions (below threshold) to block the potential effect from HOPD triggered facet degradation. The electro-optical (EO) properties are characterized by light-current-voltage (L-I-V) measurements, and the thermal dynamic properties are visualized via spatially resolved time-domain thermoreflectance (SR-TDTR) microscopy on the laser facet and along the laser cavity.

Based on the results, the threshold current density (J_{th}) increases from 6.93 kA/cm^2 to 7.82 kA/cm^2, and the normalized slope efficiency (η_{se}) drops by 76% when T_{HS} at 200 K after 30 hours of aging. In the meanwhile, the average ΔT of the active region (AR) on the laser facet reduces from 234 K to 182 K above the T_{HS} after 30 hours of aging. By employing 10 minutes of hydrogen plasma treatment after the aging test, the lasing performance resumes while the average ΔT of AR on the laser facet also returns to 206 K. Along the laser cavity, ΔT does not change with the various stages (before aging, after 30 hours of aging, and after hydrogen plasma treatment).

This chapter gives direct evidence on the thermally triggered optical degradation by facet Joule heating since the aging is conducted under pre-lasing conditions. The findings in this chapter indicate that the Joule heating induced optical degradation is localizing on the uncoated laser facet of the lattice-matched GaAs/$Al_{0.45}Ga_{0.55}As$ based MIR QCLs in the early aging stage within the first 30 hours, with no significant degradation inside the bulk of the laser. The rapid optical degradation is attributed to facet oxidation during thermal-induced aging process. High aluminum (Al) fraction of the active region (45% of the Al composition in the barrier layer within the GaAs/$Al_{0.45}Ga_{0.55}As$ MQWs) is easily oxidized in high-temperature aging burn-in process. This oxidized layer on the facet surface has a strong absorption at the laser emitting wavelength ($\lambda \sim 9$ μm). Also, the oxidized layer on the laser facet serves as a passivation layer on the facet surface, isolating the current flow. As a result, it reduces the Joule heating on the laser facet while the device is biased under pre-lasing conditions. After hydrogen plasma treatment removes the oxidized layer, optical performance resumes while the localized facet Joule heating intensifies.

5.2 Methodology and Procedures

A three-dimensional (3D) schematic diagram of the MIR QCL layer structure is shown in Figure 5.1(a). The GaAs/$Al_{0.45}Ga_{0.55}As$ MQWs based MIR-QCL (emission lasing wavelength at ~9 μm) is fabricated from the as-grown wafer reported in our earlier work [55], and the epi-layers are grown following the same structures from the reference paper [66]. The MIR-QCL is fabricated into Fabry–Pérot (FP) ridge waveguides with a ridge width of 16 μm, etched depth of 9 μm, and cavity length of 2 mm with uncoated cleaved facets. The MIR-QCL cleaved laser bar is with 20/250 nm of the electron-beam evaporated Titanium/Gold (Ti/Au) layers as the top contact metals capped with a 2.5 μm-thick electroplated (EP)

Au on its top, facilitating heat dissipation and wire-bonding, except for a 70 μm-length region close to the cleaved facets (only with the thin contact metals, assisted for cleaving). The MIR-QCL laser bar is mounted epi-side up on an Au-plated copper heatsink package with electrical connection via Au-wire bonding. Figure 5.1(b) shows the scanning electron microscope (SEM) image of the uncoated cleaved laser facet. The as-fabricated MIR-QCL is characterized by L-I-V measurements for the EO properties in a short-pulsed injection at continuously tuned heatsink temperatures (from 200 K to 295 K) inside a vacuum pumped cryostat. The MIR-QCL is biased under pulsed mode electrical injection by Avtech pulse generator (model: AVR-3HF-B). A short-pulsed current injection with pulse width (PW) of 500 ns and repetitive frequency (f_{rep}) of 1 kHz is kept minimizing self-heating effect. The heatsink temperature is tuned by a PID temperature controller. After the EO test, thermal properties of the MIR-QCL are characterized by SR-TDTR imaging system (Microsanj, model: NT210B) in both quasi-steady state (by a 100 μs-long pulse injection) and transient state (short pulse injections varying from 250 ns to 1000 ns) at ambient room temperature (295 K, the same as T_{HS}).

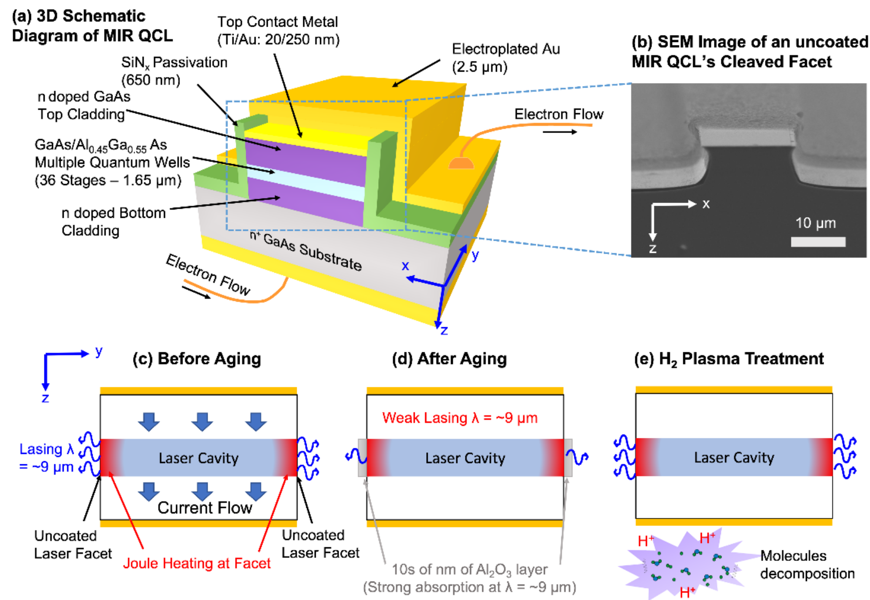

Figure 5.1 (a) Three-dimensional (3D) schematic diagram of the MIR QCL's layer structures as a truncated view close to the laser facet. (b) Scanning electron microscope (SEM) image of the MIR QCL on uncoated cleaved facet (xz-plane). (c-e) Two-dimensional (2D) schematic diagram of the MIR QCL along the laser cavity (yz-plane) before aging, after aging, and after hydrogen plasma treatment.

In the measurement, ΔT above T_{HS} is spatially resolved in a time domain both on MIR-QCL's cleaved facet and on the top of the ridge waveguide along the laser cavity. Subsequently, an accelerated aging burn-in test ("aging" in short) is applied for the same MIR-QCL mounted on a copper heatsink enclosing the unvacuumed cryostat chamber at ambient room temperature while keeping T_{HS} at 295 K. The MIR-QCL is biased under pulsed mode pre-lasing condition, with a current density (J) of 4 kA/cm^2, which is below the lasing threshold. A long pulse duration at 100 μs is kept while maintaining sufficient Joule heating within the pulse injection (PW: 100 μs, f_{rep}: 200 Hz, duty cycle: 2%, dose/pulse: 3.6 J/cm^2, injected peak power density: 2.18×10^{14} W/m^3).

The aging test successively runs for 10 hours, 20 hours and 30 hours. After every 10 hours during the aging test, the EO properties of the MIR-QCL are characterized by L-I-V measurement again in a short-pulsed current injection (PW = 500 ns) in-situ in the cryostat chamber at 200 K, followed by thermal properties measurement by SR-TDTR imaging system at ambient room temperature. After completing the aging test and L-I-V measurements, the as-measured MIR-QCL attached to the copper package is transferred to hydrogen plasma cleaner (model: UCP LFC150 G) for 10 min. A mixed flow of Argon (introduced at filament) and Hydrogen (serving as reactive gas) in the composition of 20/20 standard cubic centimeters per minute (sccm) flows into the chamber with the filament and the arc current values at 190 A and 40 A, respectively, and the DC biased voltage of 10 V. The reactive hydrogen plasma burns out the organic contamination and the metallic oxide layer on the device surface [78]. After the 10 min hydrogen plasma treatment, EO properties and thermal properties of the same MIR-QCL device are characterized instantly by a L-I-V measurement and a SR-TDTR imaging system. Figure 5.1(c), (d), and (e) show the schematic process before aging, after aging, and after post hydrogen plasma treatment, respectively. The measurement conditions for all the process are summarized in Table 5.1 below.

Table 5.1 Measurement Conditions on MIR QCL (W = 16 μm, L = 2 mm)

	P (mbar)	T_{HS} (K)	PW (μs)	f_{rep} (Hz)	DC (%)	J (kA/cm^2)	V (V)	Max E_{Pulse} (mJ/cm^2)
Accelerated Aging Test for 10 hours, 20 hours, 30 hours*	1 x 10^3	295	100	200	2	4	9	3.6
Accelerated Aging Test in Vacuum for 100 hours	9 x 10^{-7}	295	100	200	2	4	9	3.6
Natural Aging Test in atmosphere for 30 days**	1 x 10^3	295	Non-biased					
Thermal Test in Quasi-steady State	1 x 10^3	295	100	200	2	4	9	3.6
Thermal Test in Transient State	1 x 10^3	295	0.25 – 1 (sweeping)	1000	0.025 – 0.1	18.85	22	414.7
J-V Test at Room Temperature	9 x 10^{-7}	295	0.5	1000	0.05	Sweeping up to 18.85	Sweeping up to 22	207.35
J-V Test at Cryogenic Temperature	9 x 10^{-7}	200	0.5	1000	0.05	Sweeping up to 8.3	Sweeping up to 13.8	229.08
L-J Test at Cryogenic Temperature	9 x 10^{-7}	200	0.25 – 2 (sweeping)	1000	0.025 – 0.2	Sweeping up to 8.3	Sweeping up to 13.8	229.08

W = Ridge Width, L = Cavity Length, P = Pressure, T_{HS} = Heatsink Temperature, PW = Pulse Width, f_{rep} = Repetitive Frequency, DC = Duty Cycle, J = Current Density, V = Voltage, Max E_{pulse} = Maximum Dose per Pulse per unit area

*The MIR QCL is kept enclosed in the chamber without vacuuming

** Measured MIR QCL ridge waveguide is with ridge width of 12 um and cavity length of 2 mm under this condiction, enclosed in chamber at for 30 days

5.3 Results and Discussion

The L-I-V measurement results for EO testing are shown in Figure 5.2. Figure 5.2(a) and Figure 5.2(b) shows the injected current density – voltage (J-V) curve of the MIR-QCL before and after 30 hours of aging when the heatsink temperature (T_{HS}) is kept at 295 K and 200 K. The results show there is negligible change in the J-V curves before and after aging, indicating the leakage current is not dominant after aging. However, relative light intensity – current density (L-J) curves (Figure 5.2(c)) show the threshold current density (J_{th}) increases with the aging duration (black solid curve – before

aging, blue dash curve – 10 hours of aging, orange dash curve – 20 hours of aging, red dash curve – 30 hours of aging), and the relative light intensity is diminishing.

After 10 minutes of hydrogen plasma treatment, the optical performance degradation reverses, and the L-J curve (magenta dot) is almost recovered, compared to the curve (solid black) before aging. The threshold current density (J_{th}), normalized slope efficiency (η_{se}), and normalized light intensity (P_o) with the aging time are plotted in Figure 5.2(d), Figure 5.2(e), and Figure 5.2(f), respectively. In Figure 5.2(d), J_{th} increases by 13% from 6.93 kA/cm^2 to 7.82 kA/cm^2 after 30 hours of aging, while after 10 min of hydrogen plasma treatment J_{th} drops to 6.99 kA/cm^2 (magenta star, indicated in a green arrow) with only 1% of increase compared to the J_{th} (the benchmark black dash line) before aging. In Figure 5.2(e), ηse drops by 76% after 30 hours of aging, resuming to 100% (magenta star, indicated in a green arrow) after 10 minutes of hydrogen plasma treatment compared to the ηse before aging. Figure 5.2(f) shows that the Po decreases to zero (lasing quenching) after 30 hours of aging when the injected current density is at 7.8 kA/cm^2. While after 10 min of hydrogen plasma treatment, P_o resumes to 92% (magenta star, indicated in a green arrow) compared to the P_o before aging. The results are direct evidence of the lasing performance degradation after aging, but the degradation is reversible after hydrogen plasma treatment. The J-V curves show negligible leakage current increase after aging (Figure 5.2(a) and Figure 5.2(b)), but with significant lasing performance degradation (Figure 5.2(c-f)). These results indicate that facet degradation rather than the bulk region degradation inside the laser cavity could be the dominant reason for the rapid degradation of lasing performance in the early aging stage.

To understand the mechanism of this reversible optical degradation of the MIR-QCL, SR-TDTR imaging system is employed to characterize two-dimensional (2D) thermal imaging profiles from two orthogonal planes: the cross-sectional plane on the cleaved laser facet and the plane on the top of the ridge waveguide along the laser cavity. The SR-TDTR is based on a linear relationship of the relative reflectivity change (ΔR/R) from the material's surface with respect to the transient surface temperature change (ΔT), which is linked by the thermoreflectance coefficient (C_{th}) based on the linear equation $\Delta R/R = C_{th} \cdot \Delta T$ [55][58][59]. C_{th} is calibrated under a blue LED probe ($\lambda = 470$ nm), showing 1.053×10^4 K^{-1}, 1.525×10^4 K^{-1}, and 2.431×10^4 K^{-1} from the Au layer on the top of the ridge, from the MQWs active region, and from the n^+ GaAs bulk layer on the laser facet, respectively [55].

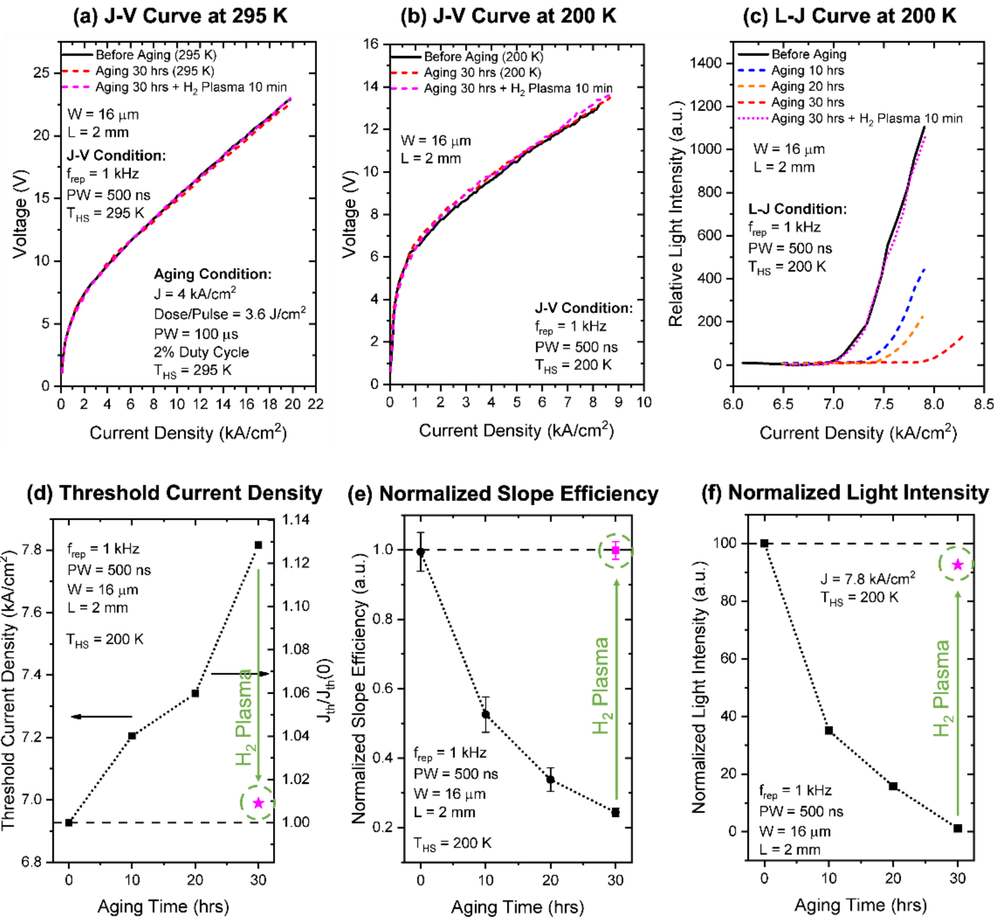

Figure 5.2 Current density – voltage (J-V) curve of pulsed injected MIR QCL when the heatsink temperature at 295 K (a) and 200 K (b); relative light intensity – current density (L-J) curve at 200 K (c). Before aging, after 10 hours of aging, after 20 hours of aging, after 30 hours of aging, and after 10 min of hydrogen plasma treatment are shown in black solid curve, blue dash curve, orange dash curve, red dash curve, and magenta dot curve, respectively. Threshold current density, normalized slope efficiency, and normalized light intensity as increasing of the aging time are shown in (d), (e), and (f), respectively; magenta stars indicated by green arrows show the values after hydrogen plasma treatment. Aging conditions are set on pulse mode with current density (J) of 4 kA/cm^2, dose per pulse of 3.6 J/cm^2, pulse width (PW) of 100 μs, and 2% of duty cycle at 1 atm at ambient room temperature (295 K).

2D thermal imaging profiles are acquired by SR-TDTR system from the MIR-QCL's facet before aging (Figure 5.3(a)), after 30 hours of aging (Figure 5.3(b)), and after post-aging hydrogen plasma treatment for 10 minutes (Figure 5.3(c)). The MIR-QCL is biased under pulse mode in 2% of the duty

cycle (PW = 100 μs, J = 4 kA/cm^2, f_{rep} = 200 Hz, T_{HS} = 295 K), which are as the same as in the aging process. The contour pseudo colours from blue to red display the ΔT above the T_{HS} (T_{HS} is kept at the ambient room temperature at 295 K). The average ΔT from the indicated rectangular regions in Figure 5.3(a-c) are plotted in Figure 5.3(d), showing the change of ΔT before aging, after 30 hours of aging, and after hydrogen plasma treatment. It is shown that the active region (AR), the upper cladding layer (UC), and the lower cladding layer (LC) indicated in the rectangular regions are 234 K, 173 K, and 128 K, respectively before aging (Figure 5.3(a)); 182 K, 140 K, and 112 K, respectively after 30 hours of aging (Figure 5.3(b)); 206 K, 155 K, and 122 K, respectively after 10 min of hydrogen plasma treatment (Figure 5.3(c)). It is noticeable that the ΔT at all regions (AR, UC, and LC) on the laser facet decrease after 30 hours of aging, then they increase after 10 minutes of hydrogen plasma treatment. Vertical line scans of ΔT are also show the same trend. ΔT across the middle line of the laser facet (indicated in black dot lines in Figure 5.3(a-c)) from the top of the upper cladding layer towards the substrate are plotted in stack, as shown in Figure 5.3(e). The active region marks the highest temperature rise (in the middle region of the vertical line scans at the position from 4.35 μm to 6 μm), and temperatures gradient shows most of heat drains towards the lower cladding layer to the substrate.

To verify there is no damage inside the laser cavity and the optical degradation localizes on the laser facet, 2D thermal imaging profiles from the top of the laser ridge plane close to one of the cleaved facets are acquired before aging (Figure 5.4(a)), after 30 hours of aging (Figure 5.4(b)), and after post-aging hydrogen plasma treatment for 10 minutes (Figure 5.4(c)). The "red" region close to the cleaved facet (70 μm in length without EP Au, a CCD image is shown in the inset figure in Figure 5.4(b) from the indicated rectangular region) shows the ΔT is much higher than the EP Au region, indicating less efficient heat dissipation without thick Au-plated. To quantitatively visualize the temperature change along the surface of the laser cavity, horizontal line scans along the laser cavity (white dash lines in Figure 5.4(a-c)) are plotted in Figure 5.4(d). It shows that the ΔT on the top of the ridge waveguide close to the cleaved laser facet (position at 0-2 μm) marks the highest temperature rise of ~250 K above T_{HS}, higher than the ΔT of AR on facet (Figure 5.3) by tens of Kelvins. This additional heating could be generating from the Schottky barrier junction (electrical properties shown in Figure 5.2(a)) at the interface between Ti/Au contact metals and the lower semiconductor materials. ΔT dramatically decreases by ~200 K along with the 70 μm-long thin Ti/Au contact layer towards the thick Au-plated layer. The large temperature gradient from the edge of the facet towards the inner cavity suggests a

large Joule heating from the facet is extracted towards the EP Au layer, followed by draining to the heatsink. The fluctuation of ΔT in the EP Au layer region is due to the relatively low signal-to-noise ratio (SNR) from the reflected light scattering on the rough EP Au layer surface. These results verify that the change of ΔT is negligible before and after the aging test along the laser cavity, while the optical performance dramatically degrades.

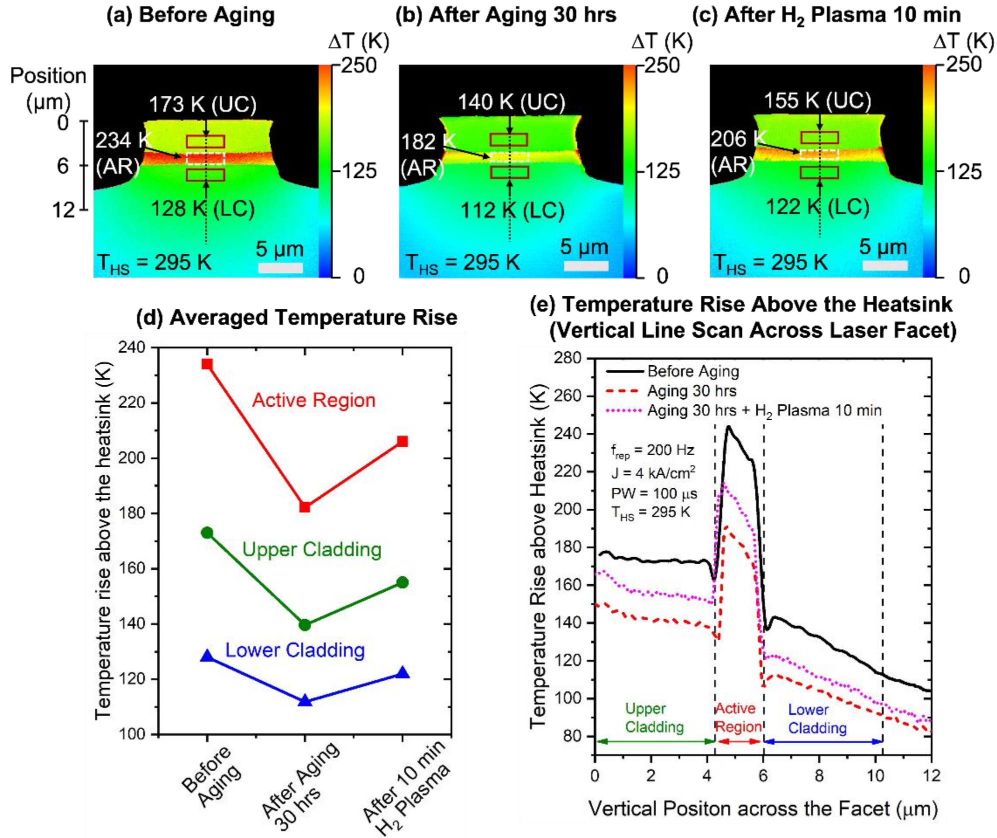

Figure 5.3 (a) 2D thermal imaging profiles of the surface temperature rise (ΔT) above the heatsink temperature (295 K) on MIR-QCL's facet before (a), after aging for 30 hours (b), and after hydrogen plasma for 10 min. The averaged ΔT in rectangular regions on the active region (AR), the upper cladding layer (UC), and the lower cladding layer (LC) in (a-c) are indicated by black arrows. (d) Averaged ΔT of AR, UC, and LC on the laser facet extracted from the indicated rectangular regions in (a-c). (e) ΔT above the heatsink before (black solid curve), after aging for 30 hours (red dash curve), and after hydrogen plasma for 10 min (magenta dot curve) in vertical line scan across the middle of the laser facet from the top of the upper cladding layer towards the substrate. The pulsed injection for the thermal measurement is set as the same as the aging condition.

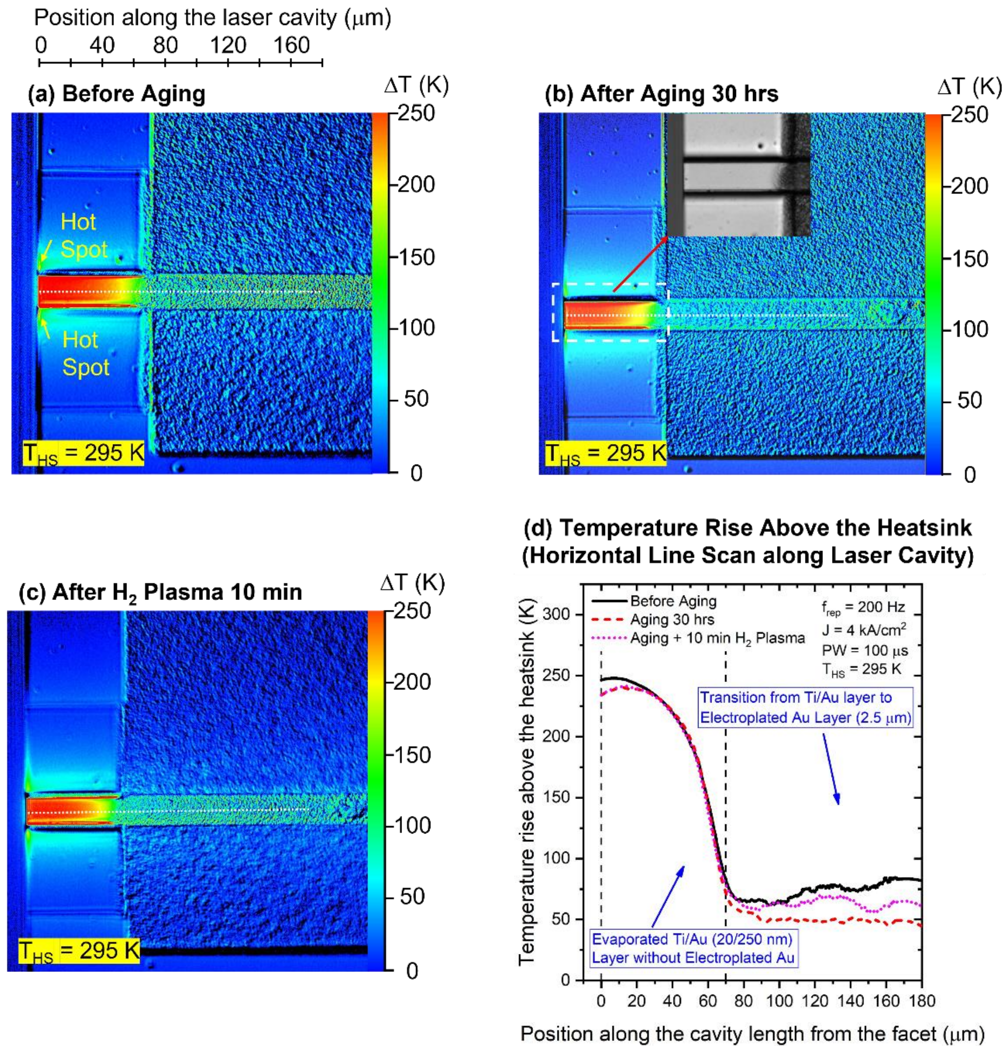

Figure 5.4 (a) 2D thermal imaging profiles of the QCL's ridge top layer before (a), after aging for 30 hours (b), and after 10 min hydrogen plasma (c). An inset figure in (b) shows a CCD image from a rectangle region with 16 by 70 μm (indicated in white dash frame) close to the laser facet. The top layer on this region is the metal contact layer (Ti/Au: 20/250 nm) without 2.5 μm-thick electroplated gold (EP-Au) capped. (d) ΔT above the heatsink in horizontal line scans along the laser cavity from the laser facet (indicated in white dash lines in (a-c)) before aging (black solid curve), after 30 hours of aging (red dash curve), and after hydrogen plasma for 10 min (magenta dot curve).

Furthermore, transient state EO properties and thermal properties are characterized under a tunable short pulsed injection. L-I-V for this MIR-QCL is measured under various injected pulse durations

from 250 ns to 2000 ns at 200 K. Reported by *Wang et al.* in 2020 [55], the Joule heating becomes prominent with the increasing of the injected pulse width leading to the lasing quenching. Figure 5.5(a) clearly demonstrates the J_{th} increases with the injected pulse width. Not only J_{th} is increasing at a certain injected pulse duration after thermal imaging test and the aging test, but has a faster increasing slope. J_{th} increases from 7.08 kA/cm^2 (PW = 250 ns) to 7.83 kA/cm^2 (PW = 1750 ns) after thermal imaging test prior to the accelerated aging test, and J_{th} increases from 7.65 kA/cm^2 (PW = 250 ns) to 8.14 kA/cm^2 (PW = 750 ns) after 30 hours of aging. The increase of J_{th} after thermal imaging test is because of the thermal-induced facet oxidation in ambient atmosphere measurement condition. In comparison, after post-aging hydrogen plasma treatment, J_{th} only increases from 6.90 kA/cm^2 (PW = 250 ns) to 7.13 kA/cm^2 (PW = 2000 ns), only 2.5% of increase compared to J_{th} (0) = 6.93 kA/cm^2 before aging (a benchmark of J_{th} under 500 ns of PW). Also, the normalized light intensity (P_o) is plotted under J = 7.8 kA/cm^2 at 200 K, as shown in Figure 5.5(b). As the aging duration increases, P_o becomes weaker. For example, under 500 ns of PW, P_o drops to 35.1%, 15.7%, and 1.1% (lasing quenching) after aging for 10 hours, 20 hours, and 30 hours, respectively compared to P_o before aging (indicated in a black star as a benchmark). In addition, with the aging duration increases, the lasing is quickly quenching when increasing the pulse duration. On the other hand, after the post-aging hydrogen plasma treatment, P_o marks the highest intensity (92.5%) under 500 ns of PW, and it gradually drops to 73.6% under 2000 ns of PW.

In addition, this effect is further verified by the transient state thermal imaging measurement at ambient room temperature (295 K) on both cross-sectional plane on laser facet and the plane along the top of the ridge waveguide. Transient temperature rises of the AR on the uncoated cleaved facet are plotted in Figure 5.5(c), under the conditions of short pulse width in high current injection (PW = 250 to 1000 ns, J = 18.85 kA/cm^2). With the increase of the injected pulse width, not only does the transient ΔT of the AR increase, but also the ΔT difference between the two curves (in black solid – before aging and in red dash – after aging) are also expanding. Figure 5.5(c) shows that ΔT difference increases from 14 K (38 K before aging and 24 K after aging) to 57 K (187 K before aging and 130 K after aging) when the PW increases from 250 to 1000 ns. On the other hand, after the post-aging hydrogen plasma treatment for 10 minutes, the transient ΔT of the AR bounces back (magenta dash curve), higher than the ΔT after 30 hours of aging. In addition, thermal dynamics behaviours of transient temperature rise on the top of ridge waveguide close to the laser facet (position at 0-2 μm) are plotted in Figure 5.5(d), under the same measurement conditions. The results show insignificant change of ΔT before aging,

after 30 hours of aging, and after post-aging hydrogen plasma treatment for 10 minutes. The results from Figure 5.5(c) and Figure 5.5(d) further verify that the optical degradation mainly localizes on the cleaved facet. It indicates no leakage-current induced Joule heating inside the cavity (matching the J-V results from Figure 5.2(a)), which is typically from the defects-assisted non-radiative recombination. These results also show inner cavity degradation is negligible because there is no significant temperature rise changes with the optical degradation before and after aging within a short-pulsed high current injection.

The reversible rapid optical degradation process can be explained by facet oxidation "coating" mechanism [76][77]. In the thermal stress accelerated aging process, having a high Al concentration (45%) in the barrier layer within the MQWs can be easily oxidized in the long- duration aging process to form unexpected aluminum oxide (Al_2O_3) layer "coating" on the facet. It should be noted that Al_2O_3 has a relatively high degree of absorption coefficient for LW-MIR range over 8 μm [77][79]. Therefore, the facet oxidized layer strongly absorbed the emitted lasing wavelength at ~9 μm, which blocks the lasing output. As the increase of the aging duration, the Al_2O_3 layer grows thicker. During the lasing operation, the light reabsorption within the thin Al_2O_3 layer on the laser facet leads to higher mirror loss and lower slope efficiency. As the injected pulse width increases, the thicker oxidized layer further reduces the optical light intensity, which converts to additional localized Joule heating on the facet, leading to higher threshold current density and lower output power (lasing performance degradation). On the other hand, from the thermal imaging, a decrease of ΔT on the facet is acquired under a pre-lasing condition after aging test because the unexpected Al_2O_3 layer serves as a passivation layer on the facet surface, isolating the current flow. Therefore, facet surface temperature rise reduces. When the post-aging hydrogen plasma treatment is applied, the unexpected Al_2O_3 "coating" layer is eliminated, accompanying with the lasing performance resumption and an increase of the surface temperature rise on the laser facet.

In addition, further investigations are conducted for QCLs under burn-in test under vacuum system for further 100 hours or long-term natural degradation for 30 days. These results are shown in Figure 5.6 and Figure 5.7.

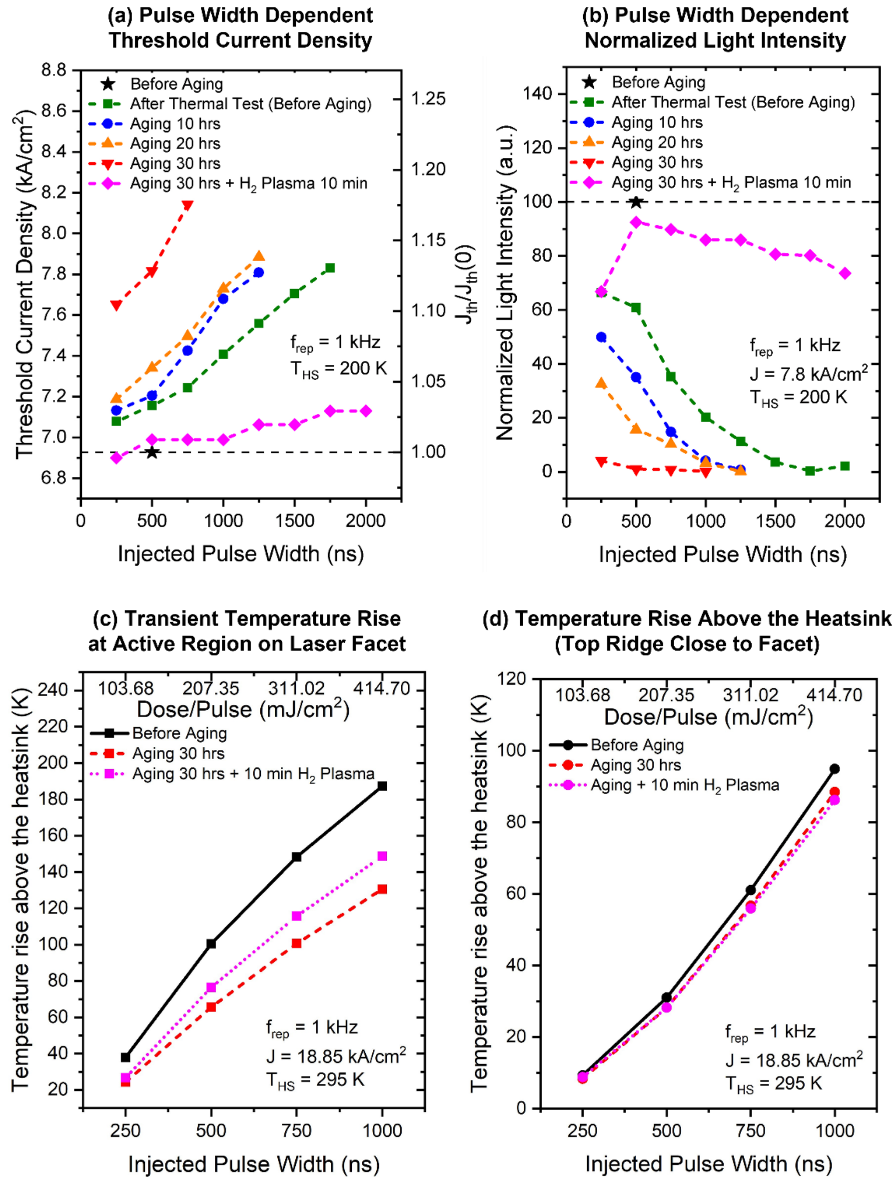

Figure 5.5 Injected pulse width (PW) dependent threshold current density (a) and PW dependent normalized light intensity (at J = 7.8 kA/cm^2) (b) after thermal imaging test prior to accelerated aging test (green dash curve), after 10 hours of aging (blue dash curve), after 20 hours of aging (orange dash curve), after 30 hours of aging (red dash curve), and the after 10 min of hydrogen plasma treatment (magenta dash curve). $J_{th}(0)$ = 6.93 kA/cm^2 (indicated in black star) is the threshold current density as a benchmark measured under 500 ns of the injected pulse width before the aging test (black star). PW-dependent averaged transient temperature rises at the active region (AR) on the laser facet (in xz-plane) (c) and on the top ridge close to the facet edge (in xy-plane) (d) at 295 K under high current injections (J=18.85 kA/cm^2, f_{rep}= 1 kHz) in short pulse duration (PW = 250 ns – 1000 ns).

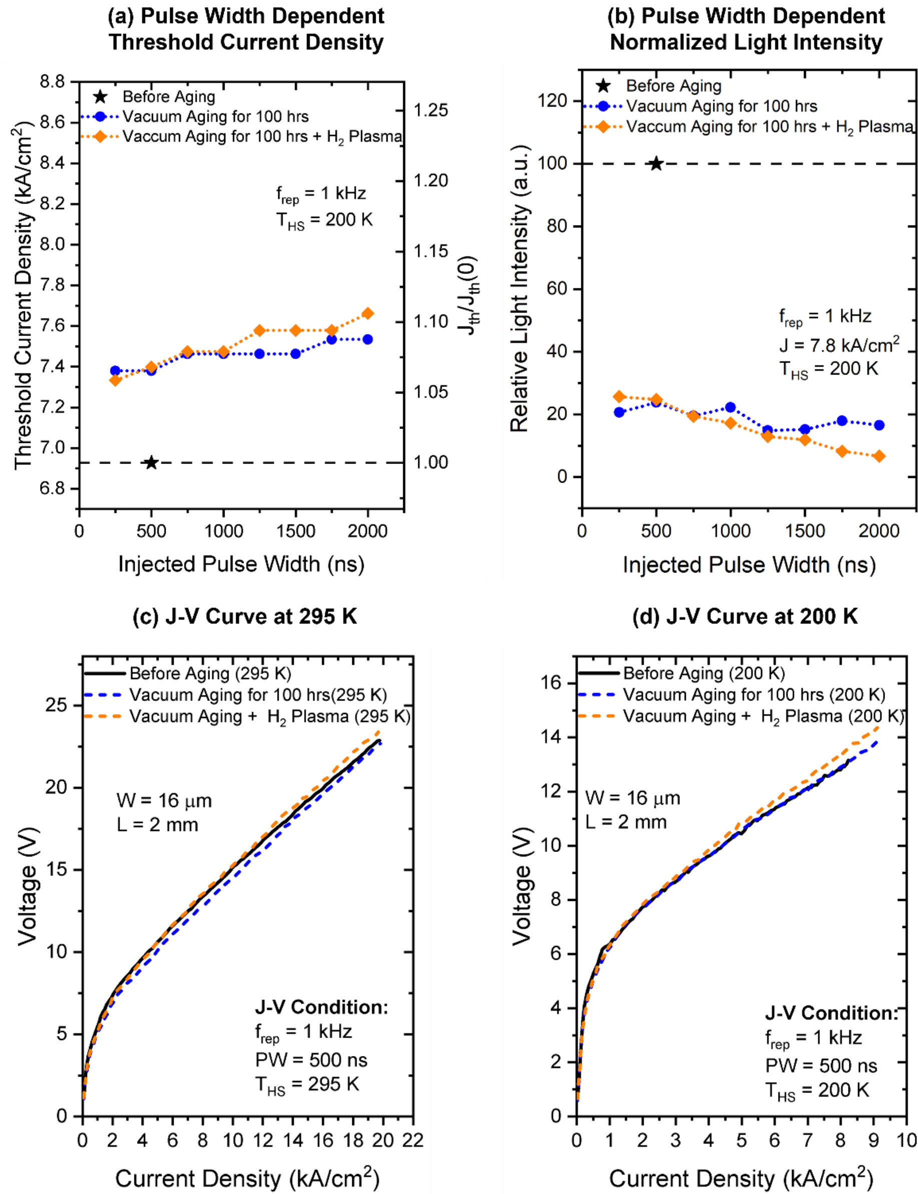

Figure 5.6 Injected pulse width (PW) dependent threshold current density (a) and PW dependent normalized light intensity (at J = 7.8 kA/cm^2) (b) after 100 hours of vacuum aging (blue dash curve) and after 10 min of hydrogen plasma treatment (magenta dash curve). J_{th} (0) = 6.93 kA/cm^2 (indicated in black star) is the threshold current density as a benchmark measured under 500 ns of the injected pulse width before the aging test (black star). J-V curve (c) and L-J curve (d) of pulsed injected MIR QCL when the heatsink temperature at 295 K. Vacuum aging conditions are set on pulse mode with current density (J) of 4 kA/cm^2, dose per pulse of 3.6 J/cm^2, pulse width (PW) of 100 μs, and 2% of duty cycle at the pressure of 9×10^{-7} mbar at ambient room temperature (295 K). The MIR QCL ridge waveguide is with 16 μm of ridge width and 2 mm of cavity length.

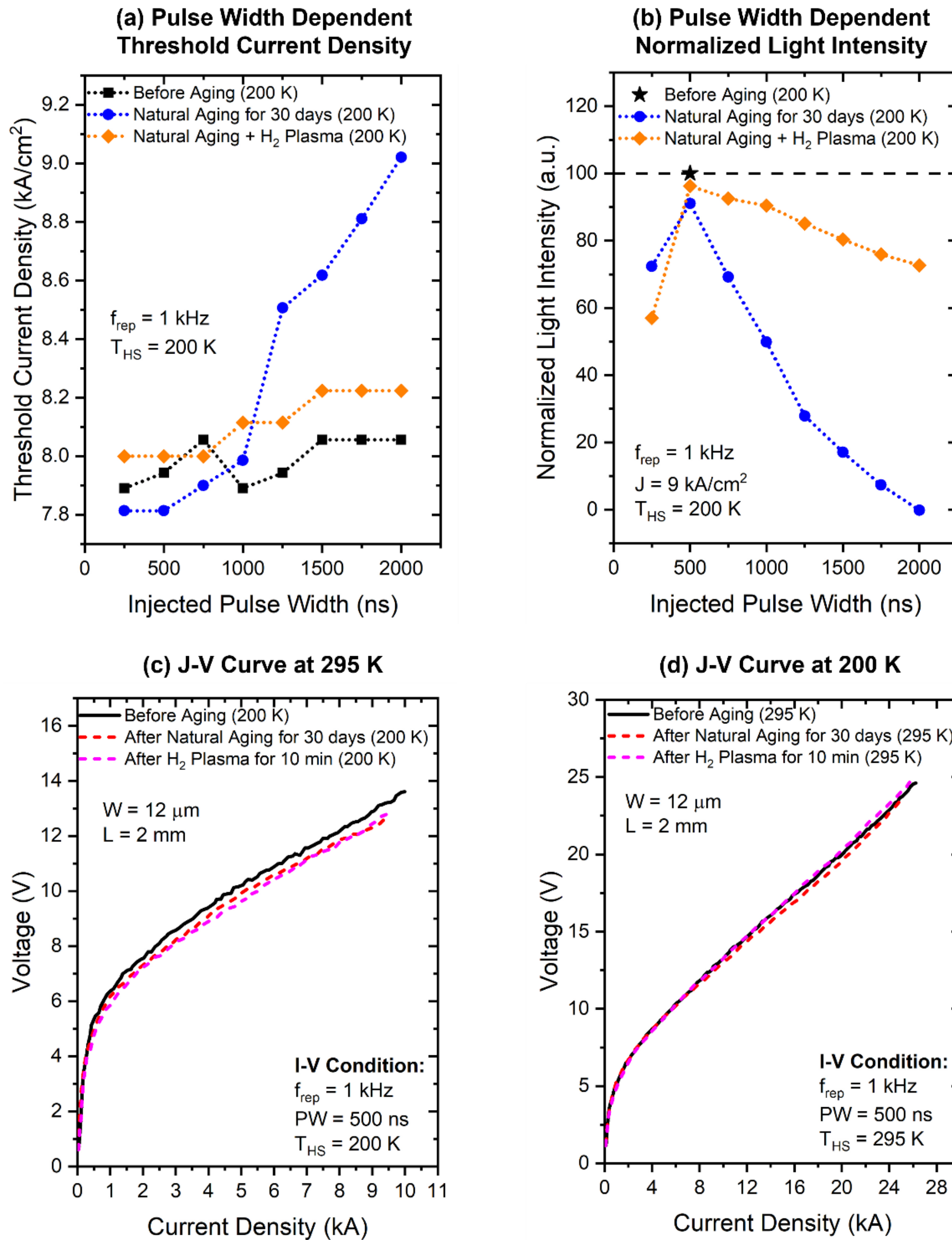

Figure 5.7 PW dependent threshold current density (a) and PW dependent normalized light intensity (at J = 9 kA/cm^2) (b) after 30 hours exposed on ambient atmosphere (enclosed in chamber without biased) – blue dash curve, and after 10 min of hydrogen plasma treatment – magenta dash curve. J-V curve (c) and L-J curve (d) of pulsed injected MIR QCL when the heatsink temperature at 295 K. The MIR QCL ridge waveguide is with 12 µm of ridge width and 2 mm of cavity length.

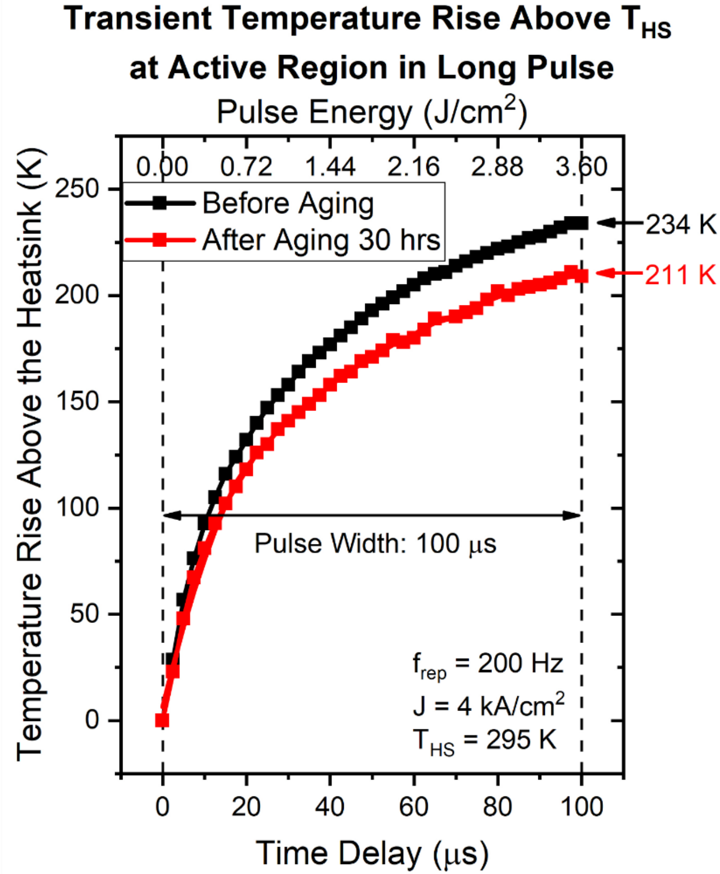

Figure 5.8 Thermal dynamics behaviours of MIR QCL's active region temperature rise above the heatsink on laser facet in transient state before aging (black curve) and after 30 hours of accelerated aging in atmosphere (red curve) under a 100 μs pulsed duration.

5.4 Summary

In conclusion, reversible lasing performance degradation of an actively-biased mid-infrared quantum cascade laser (MIR-QCL) is investigated under an accelerated aging burn-in test for 30 hours in ambient atmosphere, followed by 10 minutes of hydrogen plasma treatment. The thermal dynamics of the localized facet Joule heating from the facet-uncoated $GaAs/Al_{0.45}Ga_{0.55}As$ MIR-QCL is visualized by spatially resolved time-domain thermoreflectance (SR-TDTR) imaging system. It is found that the thermal-induced facet oxidation is the main reason for the rapid optical degradation. The high aluminum compound within the active region can easily be oxidized on the uncoated facet in a thermal-

stress aging process. This oxidized layer attaches on the laser facet, having a strong light absorption at the MIR-QCL's lasing wavelength ($\lambda \sim 9$ μm). The temperature rises on the laser facet reduce after 30 hours of an accelerated aging burn-in test, along with a degradation of the optical performance. On the contrary, the facet temperature rise increases after 10 minutes of hydrogen plasma treatment, along with the resuming of the lasing performance. On the other hand, the temperature rises along the laser cavity is negligible before and after aging test, indicating insignificant degradation inside the laser cavity. The optical degradation localizes on the device facet, and the lasing performance degrades from the additional localized facet Joule heating due to the oxidation layer reabsorption on the facet. These results verify that thermal-induced facet oxidation is the main reason for the rapid degradation of the lasing performance in the early aging stage.

Chapter 6
Heterogeneous Integration of Transfer Bonded Terahertz Quantum Cascade Lasers (THz QCL) for Improved Heat Management and Light Coupling

Terahertz quantum cascade lasers (THz QCLs) in metal-metal (MM) ridge waveguides have been fabricated and hetero bonded on aluminum nitride (AlN) substrate as heat sink submount. Compared with the conventional structure of THz QCLs in MM waveguides on gallium arsenide (GaAs) as receptor substrate, AlN performs superior heat dissipation properties for thermal management due to its much higher thermal conductivity. The light–current density–voltage (L-J-V) characterization shows comparable maximum operating temperature (T_{max}) at 93-95 K for both THz QCLs bonded on AlN and GaAs under short pulse injection (250 ns). However, as the injected pulse duration increases for THz QCLs on GaAs, the light intensity drops quickly, eventually leading to lasing quenching when the pulse duration is above 30 μs at 80 K (heat sink temperature). On the other hand, THz QCL on AlN shows much stronger light intensity and slower decrease with the increase of the pulse duration; for example, the light intensity is 100 times higher for the THz QCL on AlN (pulse duration of 40 μs) than THz QCL on GaAs (pulse duration of 30 μs) at the same measurement conditions at 80 K. This study shows Joule heating plays a great role on THz QCLs operating from long duty cycle towards continuous-wave (cw) mode, indicating AlN substrate as a high thermal conductivity material produces superior thermal management for heat extraction and dissipation.

6.1 Introduction

High-temperature, high-power, and continuous-wave (cw) operating terahertz quantum cascade lasers (THz QCLs) are of great interest, as cw operation can provide frequency stabilization and phase locking for broadband frequency comb [15][80][81][82]. However, the requirement of cryogenic cooling is still an obstacle for practical application of THz QCLs. Due to the limitations of the physical properties (e.g., low electro-optical power conversion efficiency, and high series resistance before reaching the threshold), THz QCLs are subject to a great deal of power consumption (e.g., several watts in DC biased) and Joule heating issues, leading to undermining the lasing performance towards higher

operating temperature. So far, although the maximum operating temperature (T_{max}) for THz QCLs on pulsed mode has been recently pushed up to 250 K in a single-stage thermal electrical cooler (TEC) system [26], the record high T_{max} for THz QCLs operating on cw mode is still limited to 129 K with low optical output power less than 0.1 mW [37]. In the past two decades, although some progress has been achieved mainly targeting on active region design to push up the pulsed mode T_{max} of THz QCLs [24][25][26], the thermal management structure design towards cw operation is with less attention but cannot be ignored.

On pulsed mode, it can be assumed that the active region temperature is kept the same as the heat sink temperature. However, when the device is operating within longer pulse injection towards quasi-cw mode, the main issue is the inefficient heat extraction and dissipation towards the heat sink, leading to Joule heating effect in active region. As a result, there are significant temperature rises and temperature nonuniformity in active region core with respect to the heat sink temperature, which are detrimental for the device's optical performance. For example, reported by B. Williams in [38], the T_{max} on pulsed mode and cw mode are 164 K and 117 K, respectively, with 47 K of difference. Nevertheless, the threshold current density (J_{th}) at its T_{max} is relatively close: 810 A/cm^2 on pulsed mode and 835 A/cm^2 on cw mode, respectively. This phenomenon indicates that there must be a huge temperature rise inside the active region core during cw operation compared with the stabilized heat sink temperature, which restrains the optical performance under cw mode at higher operating temperature.

Therefore, it becomes requisite towards heat removal engineering to lower the thermal resistance for THz QCLs, similar as epitaxial-side mounting assembly for high-power diode laser or mid-infrared (MIR) QCLs. It is known that bulk gallium arsenide (GaAs) is typically employed as receptor substrate for heat sink submount for THz QCLs in metal-metal (MM) waveguides. However, GaAs itself is a poor material with low thermal conductivity, which only produces 337 W/(m·K) of thermal conductivity at 100 K compared with other commonly used bulk materials in semiconductor industries, for example silicon (Si) or aluminum nitride (AlN). In this case, thermal management towards hetero submount materials for the heatsink are crucial for improving heat dissipation.

There are three requirements for submount heatsink materials: high thermal conductivity, low mismatch of the coefficient of thermal expansion (CTE) between THz QCLs (based on GaAs/AlGaAs material system) and the substrate/heat sink submount, and the availability of materials and processing techniques. Among these materials, Si and AlN are good candidates, especially for AlN, which gives

high thermal conductivity (e.g., 1750 W/(m·K) at 100 K) and low mismatch (24%) of CTE compared with GaAs (AlN: 4.5×10^{-6} K^{-1}, GaAs: 5.9×10^{-6} K^{-1} at 300 K). The low mismatch of CTE minimizes the undesired stress on laser structure induced by thermocompression bonding process. In order to fabricate gold-gold (Au-Au) ridge waveguides of THz QCLs on hetero substrate, THz QCLs are fabricated on the GaAs-based device substrate first, followed by thermocompression bonding on hetero substrate and substrate liftoff process. This process technique reduces the bonding contact areas, and it facilitates the minimization of the thermal-induced bonding stress between THz QCLs and the heatsink submount materials resulting from the CTE mismatch. The preliminary results show that AlN substrate as heat sink submount performs superior heat dissipation properties and lasing performance during long pulse injection (e.g., 40 μs), which could be a potential application for THz QCLs lasing on cw mode towards higher operating temperature.

Main Points and Significance in This Chapter

- The first demonstration of THz QCLs with metal-metal waveguide transfer bonding on hetero substrate
- Preliminary results show the pulse mode T_{max} of THz QCLs on hetero substrate is comparable with conventional metal-metal waveguide on GaAs substrate
- Pulse-width dependent LIV characterization demonstrates that hybrid bonded THz QCLs-on-AlN has superior thermal management properties towards cw operation
- Instead of breaking the T_{max} on pulse mode, the goal for this study is to reduce the Joule heating effect by lowering temperature rising in active region with respect to the heat sink temperature towards cw operation

6.2 Conventional THz QCLs in Metal-Metal Waveguide on GaAs Receptor Substrate

6.2.1 Waveguide Structures of THz QCLs

It is known that in conventional diode lasers or mid-infrared (MIR) QCLs, lower refractive index semiconductor materials are implemented as cladding layers to confine the optical wave. On the other hand, at THz region (1-10 THz), metallic waveguides are typically employed similar as in radiative

frequency range. This is because that in THz range, due to the strong optical absorption and high waveguide loss with III-V semiconductor materials, the electromagnetic waves should be confined by metallic claddings to minimize the free carrier loss [15][83]. Since the initiation of THz QCLs in 2002, two types of waveguide structures have been developed for THz QCLs: semi-insulating surface-plasmon (SISP) waveguide (Figure 6.1(a)) and metal-metal (MM) waveguide (Figure 6.1(b)) [84]. SISP waveguide uses metal layer as the top cladding layer and 0.2-0.8 μm n-type highly doped (~10^{18} cm^{-3}) GaAs layer as bottom cladding layer, which serves as "quasi-metal" for surface plasmon mode at the layer interface. SISP waveguide produces high optical output power (> 1 Watt on pulsed mode) and near Gaussian shape beam pattern profile, but it also has shortcoming with low optical confinement in active region and lower temperature performance. MM waveguide, on the other hand, has much higher operating temperature performance (up to 250 K by single stage TEC cooling on pulse mode operation), and high optical confinement in active region, though the output power is lower, and the far-field beam pattern is divergent compared with SISP waveguide. In order to acquire higher operating temperature performance, MM waveguide is preferable, which has lower optical loss and lower threshold gain.

In the following section, fabrication processes will be discussed for comparing the conventional metal-metal waveguide on GaAs receptors, and the novel strategy of hetero bonding of THz QCLs on Si and AlN as receptor substrate (heat sink submount).

Background: Waveguide Structure of THz QCLs: SISP and MM waveguide

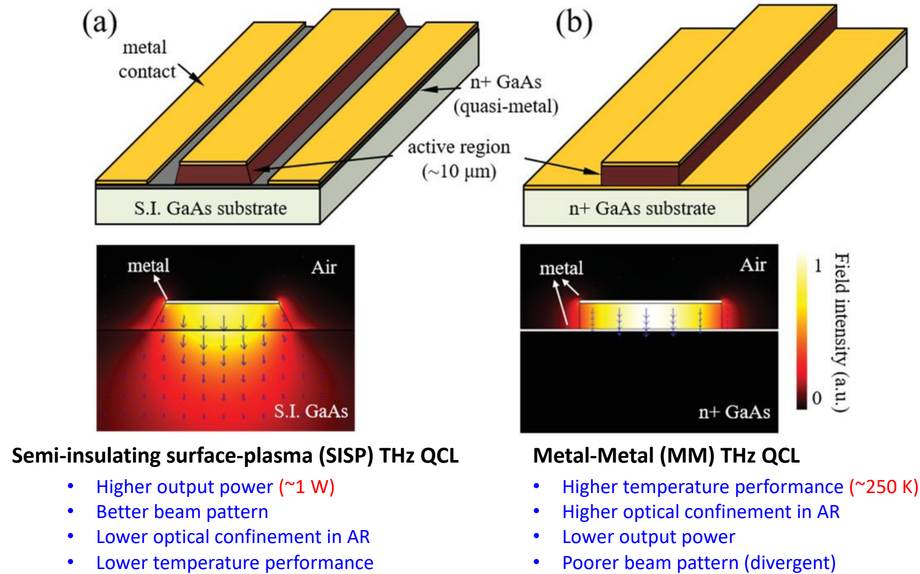

Zeng, Yongquan, Bo Qiang, and Qi Jie Wang. "Photonic engineering technology for the development of terahertz quantum cascade lasers." *Advanced Optical Materials* 8.3 (2020): 1900573.

Figure 6.1 Schematic diagrams of (a) a semi-insulating surface-plasmon (SISP) waveguide and (b) a metal-metal (MM) waveguide used in terahertz (THz) quantum cascade lasers (QCLs). The typical electric field intensity is plotted with blue arrows indicating the electric field polarization. [Adapted from Ref. [84], with the permission of John Wiley and Sons Publishing]

6.2.2 Device Fabrication

Typically, In-Au, Au-Au, Cu-Cu thermocompression bonding are usually applied in metal-metal waveguide. Though it is reported that the Cu-Cu waveguide exhibits lower optical loss and higher operating temperature in pulse mode compared to the Au-Au waveguide, it is highly demanding for the fabrication of the Cu-based waveguide owing to the adhesion and oxidation issue [83]. Therefore, in the following section, Au-Au waveguides are employed for the fabrication both in conventional bonding and novel hetero bonding strategies for the thermal issue study.

A schematic diagram of fabrication process of THz QCLs in Au-Au Fabry–Pérot (F-P) ridge waveguide on GaAs receptor is shown in Figure 6.2.

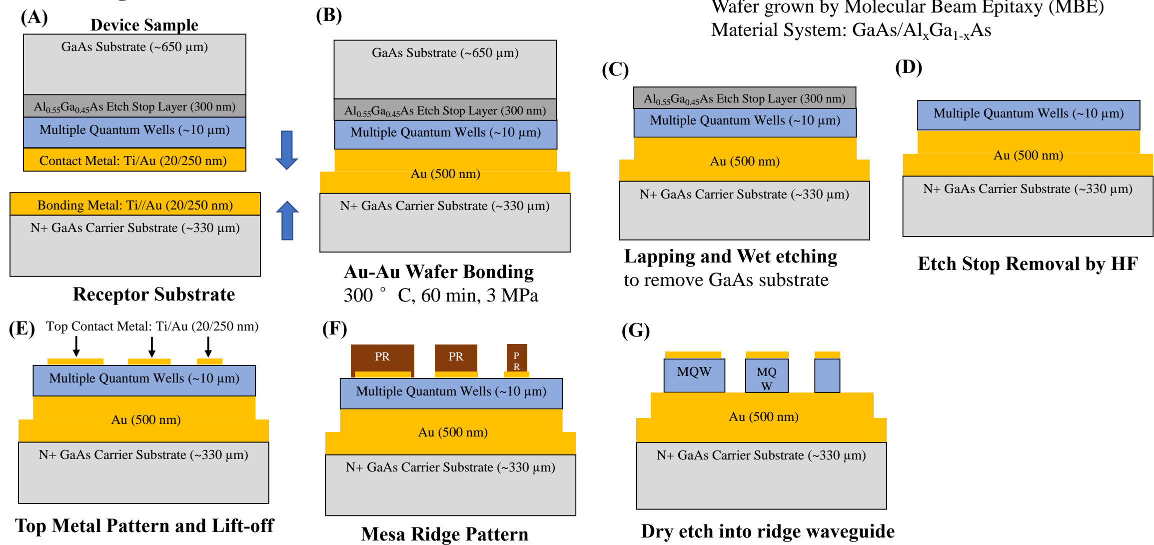

Figure 6.2 Thermocompression Au-Au bonding for metal-metal ridge waveguide THz QCLs on GaAs

The thermocompression bonding process can be stated as follows. The as growth device wafer and the n+ GaAs receptor wafer are cleaved into 10 × 10 mm and 11 × 11 mm small pieces, respectively. After a thorough cleaning, both the pieces are dipped into the diluted hydrogen chloride acid (HCl: H_2O, 1: 10) to remove any natural oxidation layer before metal deposition for bonding. Then, stacks of metal layers [Ti/Au (20/250 nm)] are deposited by electron beam evaporator (Angstrom Engineering Inc.) both on the surface of epitaxial layer of the device piece and the on the surface of n+ GaAs receptor. After the metal deposition, bonding process is taking place.

As shown in Figure 6.3, the pre-bond pieces are placed face to face with van der Waals bond, sandwiched by two graphite slices onto a specially designed holder, which is fastened with metal screws to apply pressure. The applied pressure is measured to be approximately 3 MPa, acquired from a force gauge, shown in Figure 6.4. The holder is then placed into a vacuum oven, with a vacuum degree of 100 mTorr. The oven is heated to 300 °C steady for 1 hr, then naturally cooled down. Figure 6.5 shows the post-bonded device piece on a GaAs receptor.

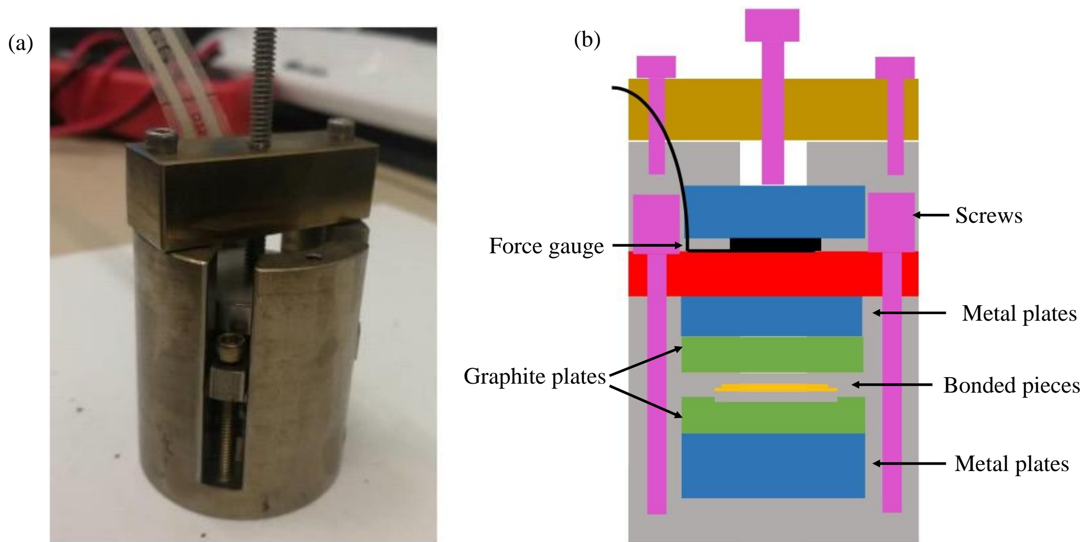

Figure 6.3 (a) An image of the bonding holder and a schematic diagram of the cross-section view of the bonding holder. The graphite plates are employed to uniformly distribute the bonding stress.

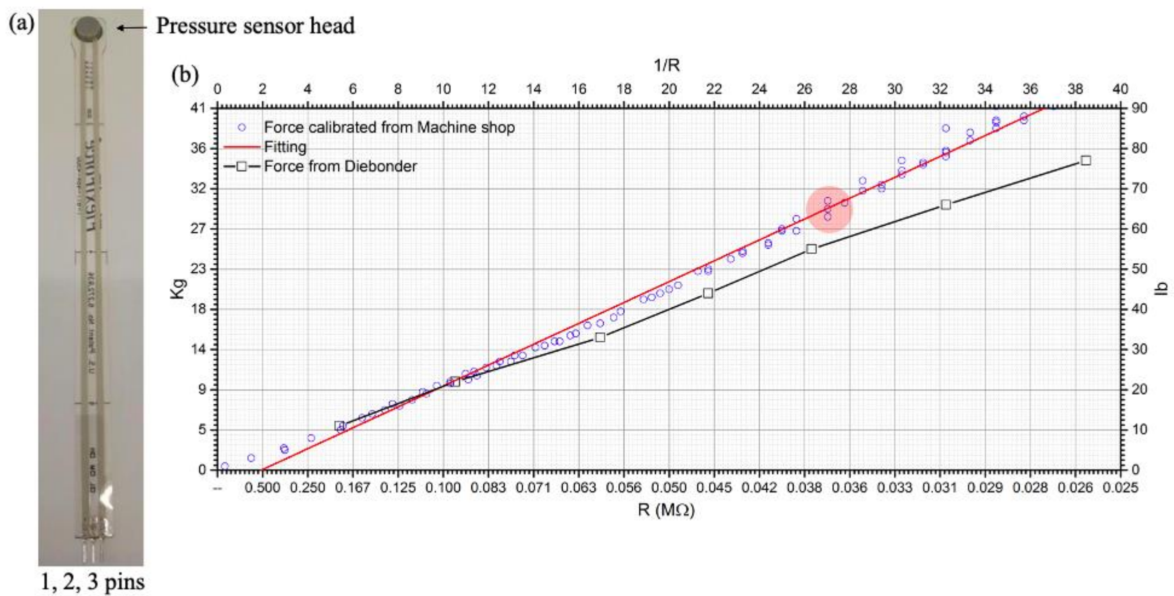

Figure 6.4 (a) A piezoelectric force gauge (a) and the calibrated force-resistance diagram (b). The force is measured and read by the resistance between pin 1 and 3. The red round shape in the diagram indicates the reference region of the bonding force.

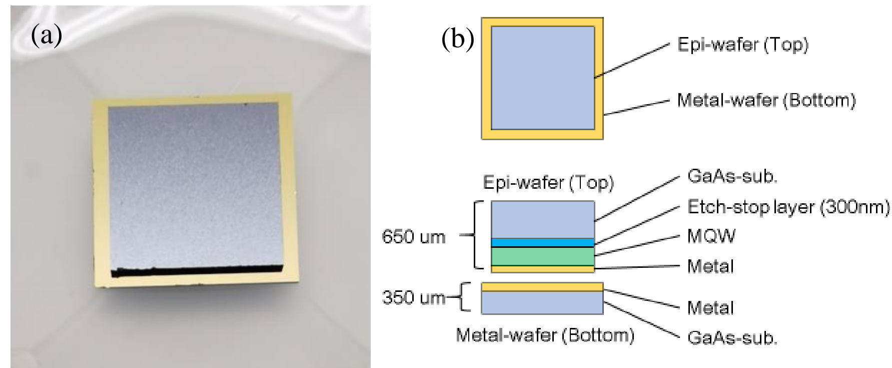

Figure 6.5 (a) An image of a bonded device piece on a GaAs receptor by Au-Au wafer bonding, and (b) a schematic diagram of the layers structure in top-down view and cross-section view.

The principle of bonding process can be stated as follows. Instead of perfectly flat on the metal surface, there is in nanometer (nm)-scale roughness in practical. When the compression is applied, the metal films will first undergo a plastic deformation from the applied force. The force will first cause the surfaces to deform and fill in larger areas of the cavities on the interface caused by surface roughness. After the temperature rises to the higher bonding temperature, the film will undergo the creep transformation (creep model proposed by Liu *et al.* in Ref. [85]). With the stress gradient present, gold atoms would then fill the voids amongst the interface due the nature of its fast surface diffusion on the (111) gold surface [86]. A schematic diagram of the bonding process and a scanning electron microscopy (SEM) image of the cross-section view of the bonding interface are shown in Figure 6.6 and Figure 6.7, respectively.

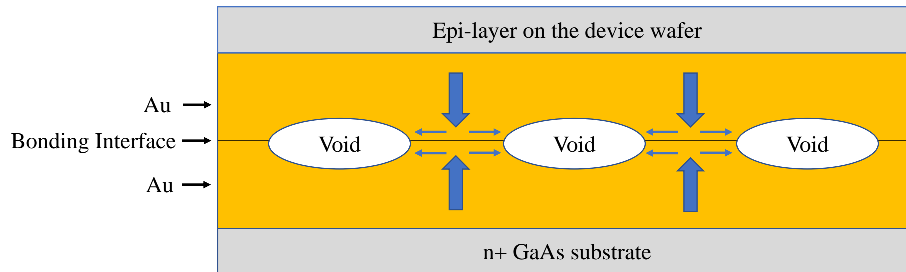

Figure 6.6 Schematic diagram of the bonding mechanism at the interface. A stress gradient forms between the contacted areas (higher gradient) and the voids (lower gradient), with the atoms then driven to diffuse along the interface to "fill" the voids. The high surface diffusivity of the (111) surface is the main contributor to this phenomenon. The plotted voids are exaggerated for explanation.

Figure 6.7 shows a SEM image of the cross-section view of the bonding interface. It is clearly seen that the metal layers from both sides have been successfully fused together, and no voids are observed, though there is observable original bonding interface line across the middle of the bonding layer.

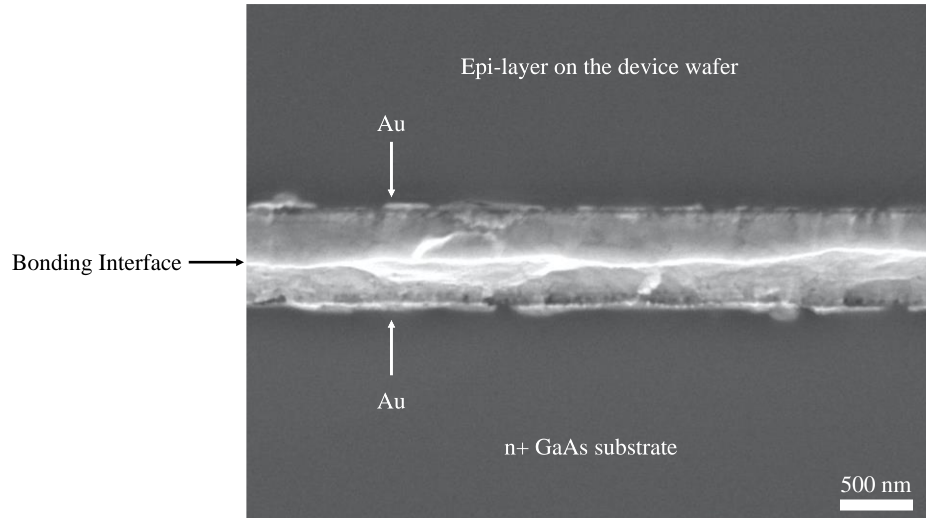

Figure 6.7 SEM cross-section view of the bonding interface of a THz QCL in Au-Au waveguide

After the metal-assisted thermocompression wafer bonding, the bonded piece is undergoing the substrate lapping and wet etching process to remove the ~650 μm thick GaAs substrate from the epitaxial grown device piece. The bonded piece is then placed onto a glass plate with wax glued on its backside, and the device substrate side is facing up (Figure 6.8(a)). The sidewall of the device substrate is also carefully secured by wax glued (by using a toothpick) in case of any unexpected damage during lapping process. Then, the glass plate is mounted under a metal chuck of the lapping machine in vacuum, while the device substrate side is facing down. The lapped substrate thickness is read by the relative value changes on a height gauge on the metal chunk (Figure 6.8(b)). General speaking, the gauge indicates less than 1 μm accuracy. The rotation speed of the chunk is set on 8 rpm, and the whole lapping process takes around 50 min.

The substrate thickness is thinned down to approximately 100 μm to 120 μm left. Figure 6.8(c) shows the thinned down bonded piece after the lapping process. Then the piece is undergoing selective wet etching process to entirely remove the GaAs substrate from the epi-layer side. To protect the device sidewall during the wet etching process, the bonded piece is deliberately mounted with a photoresist

pasted Si piece, and the device sidewall (100 μm ~ 120 μm thick) is manually painted by photoresist (S1811 preferred) as well. To avoid any air bubbles trapped or porous structure from the photoresist on its sidewall, it is preferable to naturally drying for a few hours instead of baking the photoresist. At the same time, a wet etching chemical solution is prepared. 100 g of citric acid powder is fully dissolved into 100 ml deionized (DI) water with the help of magnetic stirring. Then 33 ml of hydrogen peroxide (30%) is added to the as prepared solution, with volume ratio close to 4:1 of citric acid to hydrogen peroxide in the solution. Then, the sample is immersed into the solution for wet etching (Figure 6.8(d)). The etch rate of the solution to GaAs is approximately 22-25 μm per hour. After around 4-5 hours, the etch stop layer ($Al_xGa_{1-x}As$, x=0.55 or 0.97) will start to expose, showing in shiny color in contrast with the remaining grey areas. The grown thickness of the etch stop layer is 300 nm, and the etching selectivity of GaAs to $Al_xGa_{1-x}As$ is more than 20:1. It will take approximate additional 20-30 min until the etch stop layer fully exposes.

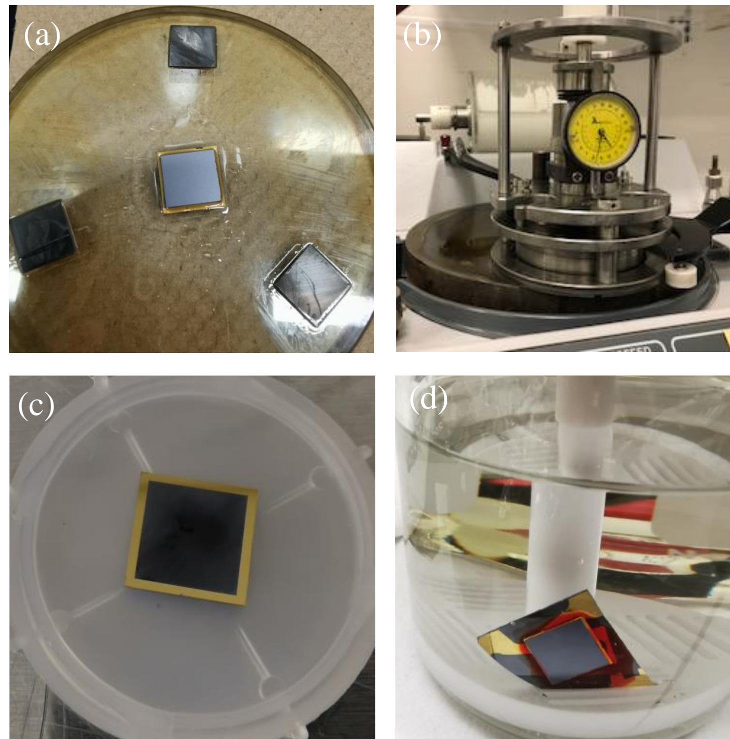

Figure 6.8 (a) Bonded THz QCLs piece (1 ×1 cm, wafer# G0405) with wax glued on a glass plate (the device substrate side is facing up); (b) lapping machine and the metal chuck with a height gauge (the glass plate is under the bottom of the chuck in vacuum, and the device substrate side is facing down); (c) bonded piece after substrate lapping; (d) bonded piece immersed into the wet etching solution.

Figure 6.9(a) shows the etch stop layer ($Al_xGa_{1-x}As$) with 55% of Al fraction on THz QCL device piece. It can be clearly seen that the surface is shinny in rainbow color, which indicates variant thickness of etch stop layer in different areas after wet etching process. Figure 6.9(b) shows the epi-layer in pure shiny color after the etch stop layer is removed by concentrated hydrogen fluoride acid (HF, 49%). In the following steps, the F-P ridge waveguide is fabricated on the device epi-layer via standard micro-fabrication process. The detailed steps can be found in Appendix A. First, the top metal of the ridge waveguide is defined by photoresist patterning, while negative photoresist nLof 2035 is employed with layer thickness of ~3.5 μm at spinning speed of 3000 rpm. The top metal ridge waveguide patterns are five repeating groups, and each group contains variant pattern width of 40, 60, 80, 120, 150 μm, respectively. The next step is top metal deposition with Ti/Au (20/250 nm in stack layer thickness) and liftoff process. Before that, in order to partially etch off the 100 nm top n+ contact layer (doping concentration: 5×10^{18} cm^{-3}) to minimize the optical loss, the sample piece is dipped into a mix of wet etching solution in sulfuric acid (H_2SO_4, 98%), hydrogen peroxide (H_2O_2, 30%), and DI water, by volume ration of 1:8:160, for 15 sec. Then the sample piece is quickly loaded into the e-beam evaporator (Angstrom Engineering Inc.) vacuum chamber for deposition. After the metal deposition and liftoff process, the sample piece is patterned with thick photoresist (AZP 4620) with ~5 μm thick as dry etch mask. The dry etch process is taking place by inductively coupled plasma - reactive ion etching (ICP-RIE) to etch off the remaining ~10 μm thick epi-layer forming mesas. The reactive gas is mixed with chlorine (Cl_2), boron trichloride (BCl_3), and argon (Ar), which mainly act as chemical etching, sidewall passivation, and physical bombardment, respectively [87][88]. After dry etch and cleaning, the sample piece is dipped into buffer hydrogen fluoride acid (BHF, 1:10 to DI water by volume ratio) for 30 seconds to remove any sidewall residues and 20 nm thin Titanium (Ti) layer on the bottom contact metal, facilitating the wire-bonding in the following steps. Before doing the packaging and wire-bonding process, the sample piece is flipped over, and thin film metal layer (Ti/Au: 20/50 nm) is deposited on the backside of the GaAs receptor substrate for indium soldering.

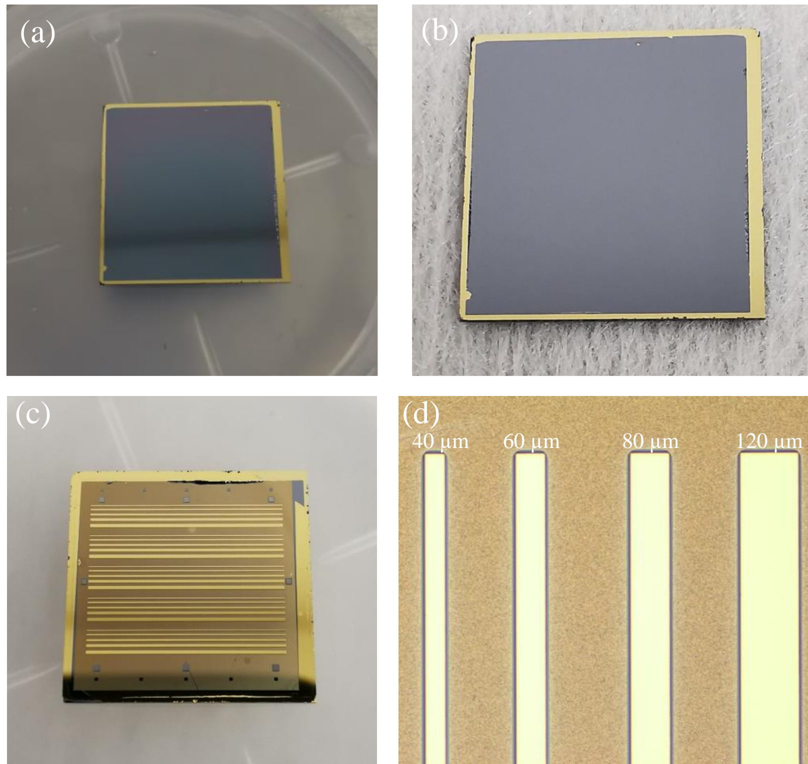

Figure 6.9 (a) After substrate wet etch; (b) after etch-stop layer removal; (c) after fabrication completion; (d) image of ridge waveguide in different ridge width under optical microscope. THz QCLs wafer#: G0405.

Figure 6.9(c) shows an image of the fabricated THz QCLs wafer piece on GaAs receptor substrate. It can be clearly seen that both the top and bottom metal gold is fully exposed. An optical image of the ridge waveguides in different ridge width under optical microscope is also shown in Figure 6.9(d). The shiny gold color and the darker gold color indicate the top metal and bottom metal areas, respectively.

After the fabrication, the THz QCLs is cleaved in ridge waveguide bars with ~2 µm in cavity length. Then the cleaved bars are mounted onto an Au-coated copper package via indium (In) soldering. The THz QCLs ridge waveguides are directly connected from the top contact metal to the bonding pads on a PCB board via Au-wire ball/wedge wire-bonding. Figure 6.10(a) shows the wedge bond on the top metal of ridge waveguides. The white arrows also indicate mild bonding tip damage on the top metal from the wire-bonding process. This could be resulting from the thin capped gold layer thickness (250 nm). Figure 6.10(b) shows an example of a SEM image of a cleaved fabricated THz QCL ridge

facet. It can be clearly seen that the THz QCL is sandwiched by Au-Au waveguide on the GaAs receptor substrate.

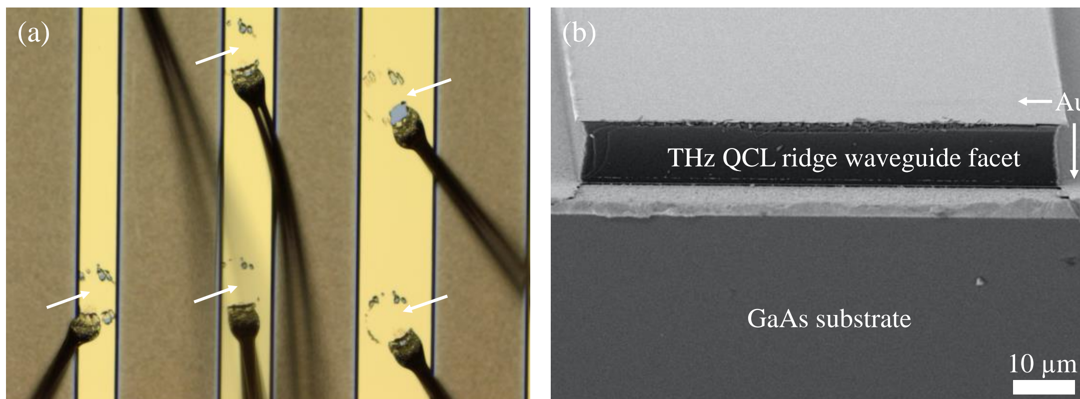

Figure 6.10 (a) wire bond on the top metal of THz QCLs ridge waveguides; (b) cleaved ridge waveguide facet of THz QCL in Au-Au waveguide on GaAs receptor

6.3 Hybrid Integration of THz QCLs in Metal-Metal Waveguide on hetero substrate: Towards Higher Temperature Performance

6.3.1 Strategies of Hybrid Integration

The intrinsic properties of III-V materials have the limitations to achieve improved heat dissipation and efficient light transmission due to the low thermal conductivity and the high waveguide loss. A solution to overcome these limitations is to integrate different materials to achieve desired functionalities. Monolithic integration [89-92], heterogenous integration [92-96], and hybrid integration [96-103] are widely employed for photonic integrated circuits (PICs). THz QCLs in MM waveguides requires 100s of nm thick metal layers for both top and bottom cladding layers. To achieve higher heat dissipation by thermocompression bonding THz QCLs on hetero-substrates as heatsink submount, hybrid integration with flip-chip bonding could be a candidate strategy. The pros and cons of different hybrid integration strategies on chip scale and wafer scale are summarized in Table 6.3 and Table 6.4, respectively.

Table 6.1 Comparison among conventional flip-chip bonding, direct wafer bonding, and massive transfer printing on chip scale hybrid integration [89-103]

	Advantages	Disadvantages
Conventional Flip-chip bonding (die-bonding)	1) Easy, convenient, and self-align	1) Optical loss due to insufficient resolution (1 μm) 2) Unfavorable for light coupling due to the bonding gap 3) Costly and time-consuming (repetitive use solders and dies per die process
Direct Wafer bonding	1) Full-wafer together (fast and efficient)	1) Inefficiently use of III-V materials 2) Extreme tolerance for perfectly clean 3) III-V wafer bowing due to thermal expansion mismatch 4) Not suitable for buried-heterostructure lasers
Massive transfer printing	1) Multiple dies bonding together 2) Save time compared with die-bonding 3) No diced but etched before bonding 4) Use elastomeric stamp to pattern the dies	(1) Not suitable for heat involved bonding process, since photoresist is employed as anchor, which can be solidified as residue being hard to be moved; (2) Low yield during bonding process; (3) Elastomeric stamp process is not compatible with semiconductor process

Table 6.2 Summary of the advantages and disadvantages among different wafer bonding strategies on wafer scale hybrid integration [89-103]

	Advantages	Disadvantages
Wafer Bonding - molecular assisted (O_2 plasma assisted hydrophilic)	1) Efficiently clean the surface 2) Very thin oxide layer at interface with hydrophilic properties 3) Lowering the annealing temperature (<300 C) due to the high surface energy and high bonding strength *Etching out-gassing channels or grooves to minimize bubbles	1) Electrical insulation due to thin oxide layer at interface
Wafer Bonding - molecular assisted (SiO_2 assisted hydrophilic)	1) SiO_2 can absorb gas by-products 2) Less sensitive to surface roughness and defects *Etching out-gassing channels or grooves to minimize bubbles	1) Electrical insulation due to thin oxide layer at interface 2) Degradation of thermal properties and light coupling
Wafer Bonding - molecular assisted (hydrophobic surface)	1) Oxide free at bonding interface *Etching out-gassing channels or grooves to minimize bubbles	1) Highly sensitive to surface roughness and defects 2) Bubbles generation at bonding interface due to gas by-product (H_2) 3) Need very high annealing temperature (1000 °C) which degrades III-V materials
Wafer Bonding - polymer assisted (BCB at interface)	1) Lower bonding temperature 2) No gas by-products generation 3) Easy to be planarized 4) Less stringency for pre-clean 5) BCB is compatible with annealing and wet-etching	1) Very low thermal conductivity of BCB 2) Higher refractive index than SiO_2 (higher optical reflection at bonding interface)
Wafer Bonding - metal assisted	1) Strong bonding at interface from solidification of metal alloy (higher eutectic point than bonding temperature) 2) Fill the voids at bonding interface by melt metal	1) Unfavorable for light coupling due to light absorption by metal layer 2) Cracks may appear due to thermal expansion mismatch at high bonding temperature
Transfer printing - epitaxial lift-off	1) Efficient use of III-V materials	1) Require mechanical support
Transfer printing - massive transfer printing	1) Efficient use of III-V materials 2) Kinetic-dependent adhesion of PDMS, easy to control 3) Optical transparency of PDMS, allowing high resolution alignment (<1 μm)	1) Require mechanical support (PDMS, inconvenient to remove) 2) Residue remained when high temperature is applied (unfavorable for thermocompression bonding)

6.3.2 Material Selection for Hetero-Substrate

There are three requirements for submount heatsink materials: (1) high thermal conductivity; (2) low mismatch of the coefficient of thermal expansion (CTE) between THz QCLs (based on GaAs/AlGaAs material system) and the substrate/heatsink submount; and (3) the availability of materials and processing techniques. Conventionally, bulk GaAs is typically used as the bonding receptor for GaAs/AlGaAs-based material system THz QCLs in metal-metal waveguide. The benefit of GaAs is that there is no CTE mismatch issue between the two bonding materials because both the device and the receptor share the same material system. Therefore, the thermal-induced stress during the metal-metal thermocompression bonding is negligible. Also, this conventional strategy has high production yield in easy-handled fabrication process. However, GaAs receptor substrate itself (typically in hundreds of micrometers thick) as a material has relatively low thermal conductivity (e.g., 55 W/(m·K) at 300 K) compared with other widely used heatsink submout materials such as Si (e.g., 130 W/(m·K) at 300 K), AlN (e.g., 285 W/(m·K) at 300 K), and diamond (e.g., 1000 W/(m·K) at 300 K). As a result, the poor thermal property of GaAs could be the main reason for the inefficient thermal dissipation, which can be an obstacle for THz QCLs under cw operation especially in high power injection and higher operating temperature.

The thermal properties of various materials have been shown in Table 6.3, Table 6.4, Figure 6.11, and Figure 6.12. Among of these materials, diamond has the prominent thermal conductivity, but it does not satisfy requirement (3) since bulk diamond is not easily accessible, and only thin layer coated diamond is available. Sapphire has almost the same CTE with GaAs with only 1.7% CTE mismatch, which can possibly lower the thermal-induced bonding stress, but the thermal conductivity is not superior to GaAs's one. Among these materials, only AlN and Si are the potential candidates. In particular, AlN has relatively high thermal conductivity (e.g., 1750 W/(m·K) at 100 K and 285 W/(m·K) at 300 K) compared with GaAs, and it has relatively low CTE mismatch (23.7%, at 300 K) to GaAs. It should be noticed that AlN as heatsink submount materials has been widely used in high power laser diode and mid-infrared (MIR) QCLs; however, in THz QCLs, especially for metal-metal waveguide, hetero substrate bonding has not been reported since strict bonding conditions (high bonding temperature and high bonding force) is required for THz QCLs in metal-metal waveguide. The fabrication process of hybrid bonding THz QCLs on Si and AlN will be introduced in section 6.3.3.

Table 6.3 Comparison of Thermal Conductivity (k), Coefficient of thermal expansion (CTE), Specific Heat Capacity (C_p), and density among different materials (heat sink submount and bonding metal) at 300 K [39-49]

	Thermal Conductivity [W/(m·K)] at 300 K	Thermal Conductivity [W/(m·K)] at 100 K	Coefficient of thermal expansion (CTE) [K^{-1}] at 300 K	CTE mismatch compared with GaAs at 300 K	Specific Heat Capacity [J/(kg·K)] at 300 K	Density [kg/m^^{3}]
GaAs	55	337	5.9×10^{-6}	0	330	5320
Silicon	130	900	2.6×10^{-6}	55.9%	700	2329
AlN	285	1750	4.5×10^{-6}	23.7%	730	3260
Sapphire	40	380	5.8×10^{-6}	1.7%	782	3980
Diamond	1000	9000	2.3×10^{-6}	61.0%	6192	3510
Cu	401	482	17×10^{-6}	188.1%	384	8960
Au	317	327	14×10^{-6}	137.3%	129	19300

Table 6.4 Extracted thermal conductivity (κ) and coefficient of thermal expansion (CTE) of GaAs, Si, and AlN

	GaAs	Si	AlN
Coefficient of Thermal Expansion (CTE) [10^{-6} K^{-1}] at 300 K	5.9	2.6	4.5
CTE mismatch with GaAs (%)	0	56	24
Thermal Conductivity (κ) [W/(m·K)] at 100 K	337	1000	1750
Thermal Conductivity difference with GaAs (%)	0	197	419
Specific Heat Capacity [J/kg K] at 100 K	199	250	146
Density [kg/m^3]	5320	2329	3260
Thermal diffusivity [m^2/s] at 100 K	3.183E-04	1.717E-03	3.667E-03

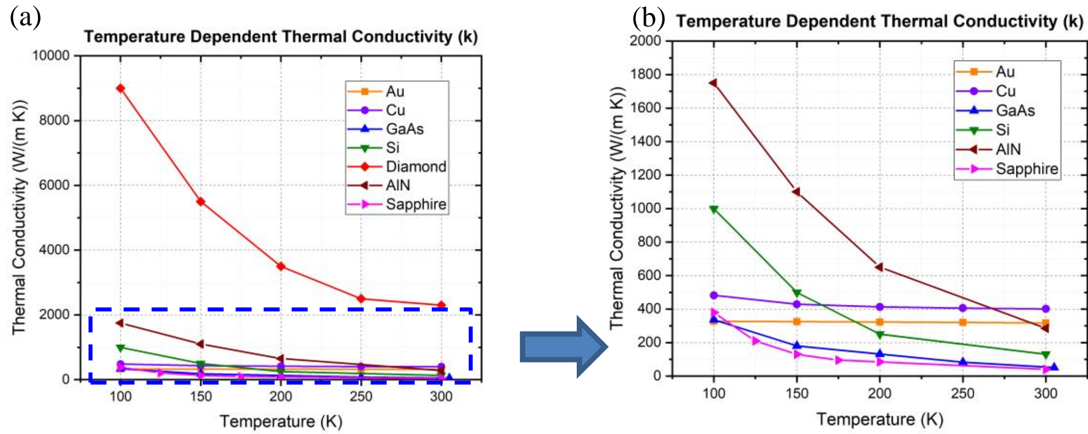

Figure 6.11 Temperature dependent thermal conductivity (k) of different materials (heat sink submount and bonding metal)

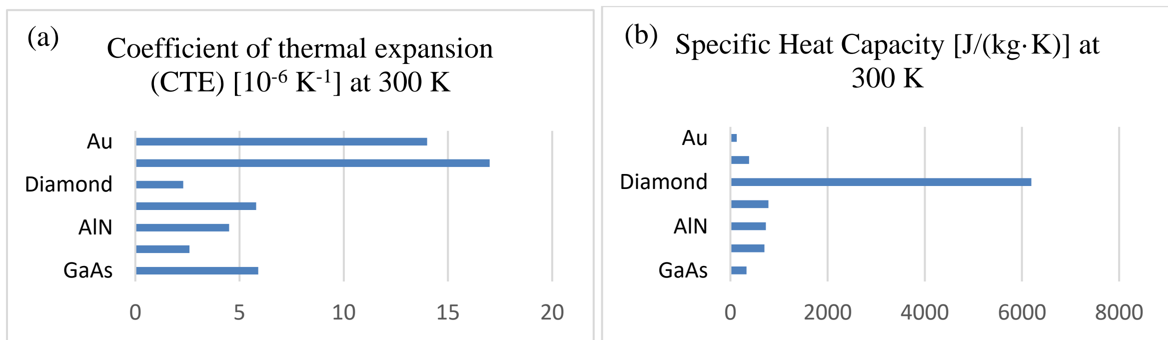

Figure 6.12 (a) The coefficient of thermal expansion (CTE) and (b) the specific heat capacity (C_p) of different materials (heat sink submount and bonding metal) at 300 K

6.3.3 Fabrication Process of Hybrid Integration of THz QCLs on Si and AlN Substrate

Instead of wafer bonding at the beginning of the steps, hetero bonding may suffer much higher thermal stress due to the CTE mismatch (refer to Table 6.4) during the thermocompression bonding process, which can lead to device damage and failure. In this case, the whole fabrication process should be substantially modified. Due to the coefficient of liner thermal expansion (CLTE) mismatch between different materials, the contact areas should be minimized during the hybrid integration on hetero substrates. In this section, I will briefly introduce the whole process for fabricating the THz QCLs in

Au-Au waveguide bonded on silicon (Si) and aluminum nitride (AlN) substrate as high thermal conductivity materials for higher heat dissipation efficiency.

On the other hand, although there is only 23.7% of CTE mismatch of AlN to GaAs, the CTE mismatch is still a serious side effect during the hetero bonding process which should be carefully considered. To simplify, CTE can be considered as coefficient of liner thermal expansion (CLTE). It is the fractional change in length per degree of temperature change, which can be written as:

$$\alpha_L = \frac{1}{L} \cdot \frac{dL}{dT} \qquad (eq. 6.1)$$

where α_L is the CLTE (unit: K^{-1}), L is a particular length measurement, and dL/dT is the rate of change of that linear dimension per unit change in temperature. Thus, the change in the linear dimension can be estimated to be:

$$\frac{\Delta L}{L} = \alpha_L \cdot \Delta T \qquad (eq. 6.2)$$

For example, in a certain length at 2 mm (a typical cavity length of THz QCL ridge waveguide), the change of linear dimension of GaAs from 25 °C to 300 °C (a typical bonding temperature for Au-Au waveguide) is 3.25 μm, while there is 2.48 μm and 1.43 μm for AlN and Si, respectively. As a result, the thermal induced stress during thermocompression bonding between the different bonding layers may cause the device epi-layer cracks, broken, or detached. In this case, the bonding areas should be carefully designed to minimize the contact areas.

Fabrication process diagrams of bonding THz QCLs on Si and AlN are shown in Figure 6.13 and Figure 6.14, respectively. Due to the thermal stress issue, the epi-layer on device substrate will be firstly fabricated into ridge waveguides then bonded to hetero substrate individually, rather than wafer bonding process on the whole area at the beginning. This is because that smaller bonding area can reduce the change of the dimension due to the thermal expansion. In this case, only three ridge waveguides in a group are bonded on hetero substrate at once. After the ridge waveguides are successfully completed on device substrate, the device pieces can be diced (for dry etched facet) or cleaved (cleaved facet is preferred due to the less mirror loss) into many small dies, and each die will be flipped chip thermocompression bonding via TRESKY die-bonder (T-3000-FC3) under 3 MPa pressure at 300 °C for 1 hour into Au-Au waveguides on hetero substrate. After bonding process, the

device substrate will be removed by substrate liftoff process in concentrated HF (49%). The successfully bonded THz QCLs on AlN and Si substrates are shown in Figure 6.15 and Figure 6.16, respectively. Detailed process steps can be found in Appendix A and Appendix B.

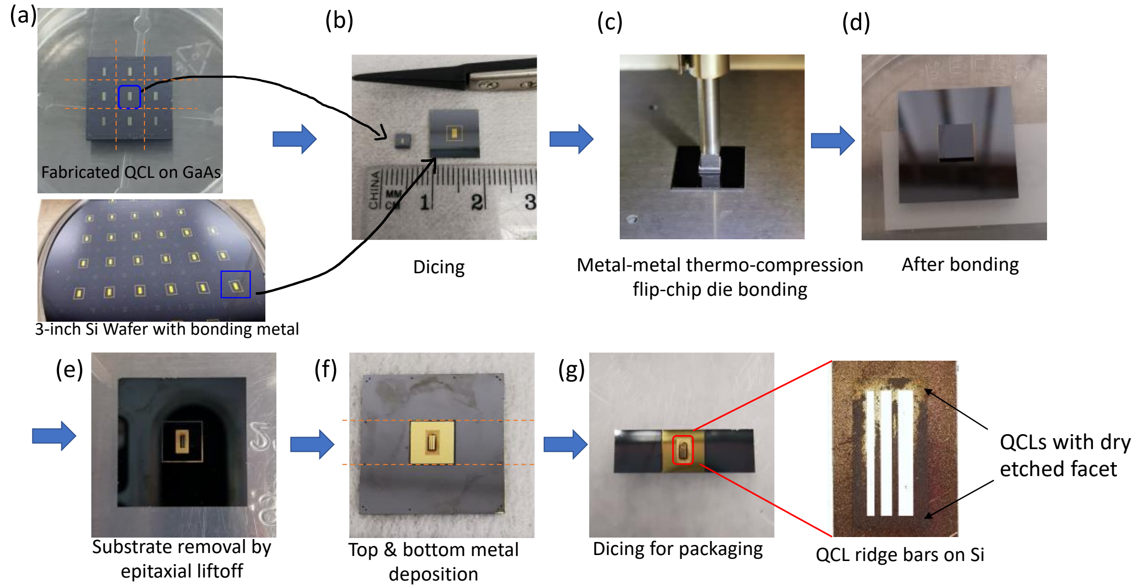

Figure 6.13 Fabrication process of transferred THz QCLs (wafer#: G0312) with dry etched facet bonded on Si Substrate

The growth structure of the THz QCLs wafer (G0312) is similar as the f-series design which can be found in the previous reported paper [25][104]. As CTE mismatch of 24% between GaAs (5.9×10^{-6} K^{-1} at 300 K) and AlN (4.5×10^{-6} K^{-1} at 300 K) during the thermocompression hetero bonding process, the thermal-induced stress issue can potentially lead to device cracking, damage, or failure of lasing. Therefore, preventing from this issue, the fabrication process should be modified and redesigned, which is different from the conventional metal-metal waveguides of THz QCLs bonded on GaAs receptor substrate.

Figure 6.14 shows several critical steps of the fabrication process of THz QCLs hetero bonded on AlN substrate. Due to the thermal stress issue, the epi-layer on the device substrate (GaAs) is firstly fabricated into ridge waveguides, followed by hetero bonded onto AlN substrate, rather than wafer

bonding process of the whole epi-layer surface with metal coating on GaAs receptor substrate at the very beginning. This is because that the contact areas during the bonding process should be minimized in order to reduce the change of the deformation due to the thermal expansion while the bonding temperature is rising up and cooling down. In this regard, only three ridge waveguides in a group (ridge width of 120 μm, 90 μm, and 60 μm, respectively) are hetero bonded on AlN substrate at once. After the ridge waveguides are successfully completed on device substrate, the device pieces are diced and cleaved (cleaved facet is highly preferred due to the much less mirror loss) into many small dies. Figure 6.14(a) shows one die with three laser bars in ridge waveguides fabricated on GaAs substrate, and Figure 6.14(b) shows an AlN substrate piece with patterned electroplated Au on its top. After the fabrication completion, each laser die is flipped chip thermocompression bonding via TRESKY die-bonder (T-3000-FC3) under 3 MPa pressure at 300 °C holding for 1 hour into Au-Au waveguides on as-prepared substrate (Figure 6.14(c)). After bonding process, the GaAs device substrate will be removed by substrate liftoff process dipping in concentrated HF (49%) for dissolving the $Al_xGa_{1-x}As$ ($x>0.55$) etch stop layer. Then, the THz QCLs ridge waveguides are exposed. The THz QCLs hetero bonded on AlN substrate before and after substrate liftoff process are shown in Figure 6.14(d) and Figure 6.14(e), respectively. The indicated areas in rectangular region from Figure 6.14(e) shows the zoomed-in parts of the top side view of three individual THz QCLs bonded on Au-deposited AlN substrate. Finally, after patterning and precise alignment, the top side of the THz QCLs are e-beam evaporated with Au (250 nm of thick) into Au-Au ridge waveguide.

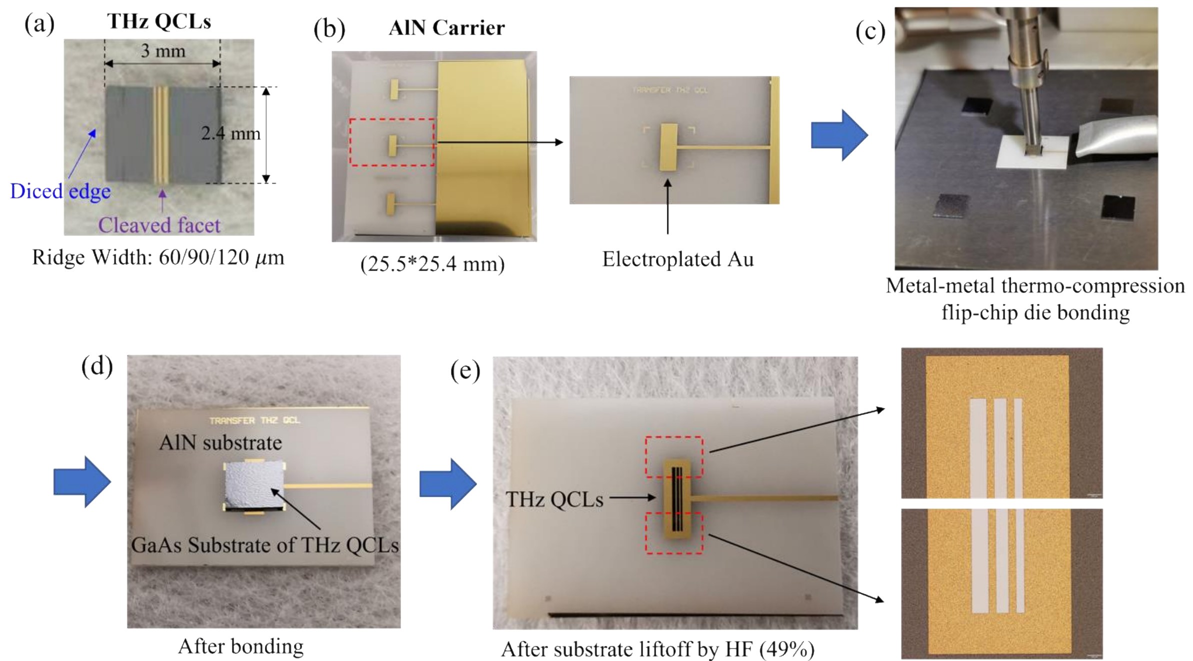

Figure 6.14 Fabrication process of THz QCLs (wafer#: G0312) with metal-metal waveguides hetero bonded on AlN substrate. (a) Fabricated THz QCLs in ridge waveguides on GaAs substrate with cleaved facet; (b) as gold deposited AlN substrate; (c) metal-metal thermocompression bonding process by die-bonder; (d) THz QCLs die on AlN substrate after bonding process; (e) exposed THz QCLs laser bars after GaAs substrate liftoff process by dipping in concentrated HF (49%).

Figure 6.15(a) shows three individual THz QCLs (wafer#: G0312) successfully bonded on AlN substrate. The as-processed AlN piece with devices is diced to facilitate packaging process. The cavity length of each laser bar is 2.4 mm, and the width of the diced AlN piece is slightly wider than the cavity length of the devices preventing from damaging the laser facet during the dicing process. Figure 6.15(b) shows the hetero bonded THz QCLs die on Au-plated copper package. The backside of the AlN is deposited with Au followed by soldering with Indium onto the as-prepared copper package. A 7-pin printed circuit board (PCB) is also fastened with screws onto the package, and each of the laser device is wire-bonded to an Au-plated bonding pad on the PCB board. The whole package is mounted onto a cold finger with a cryostat. Figure 6.15(c) shows the top side view of THz QCLs with Au-wire bonding under optical microscope, and the white shinning color areas show the three ridge waveguides in the width of 120 μm, 90 μm, and 60 μm, respectively. Figure 6.15(d) shows the cross-section view of the

laser cleaved facet under scanning electron microscopy (SEM). It is clearly shown that THz QCL is successfully bonded on AlN substrate in Au-Au ridge waveguide.

Similar results are also shown in Figure 6.16, where THz QCLs (wafer#: G0226, heterogenous broadband gain design [105]) are successfully bonded on Si (Figure 6.16(a) and Figure 6.16(b)) and AlN substrates (Figure 6.16(c) and Figure 6.16(d)).

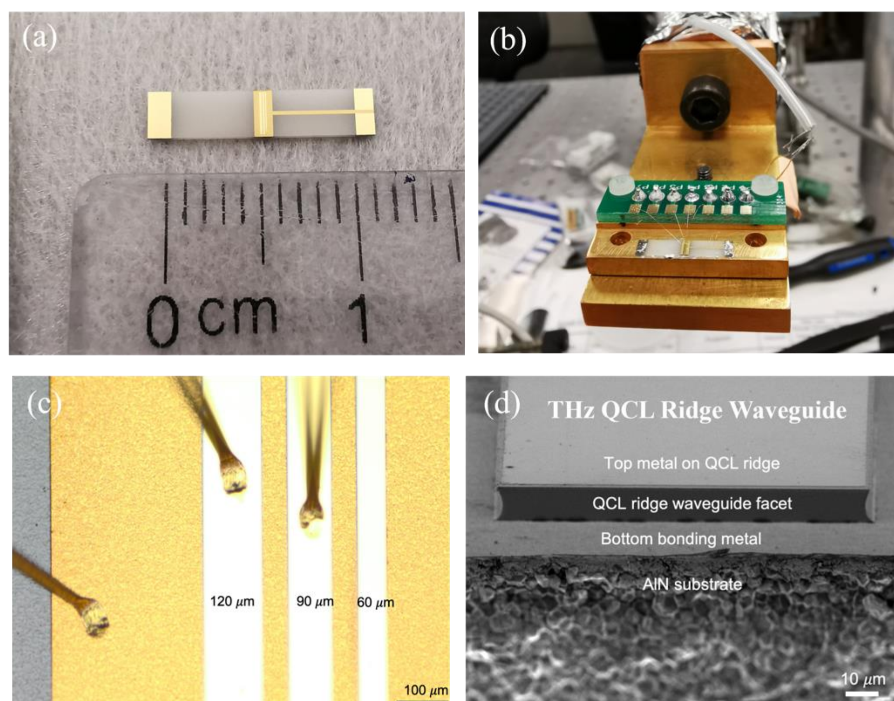

Figure 6.15 (a) Bonded THz QCLs (wafer#: G0312, cavity length: 2.4 mm, ridge width: 120/90/60 μm) in ridge waveguides on AlN substrate with gold coating; (b) bonded THz QCLs on AlN substrate onto an Au-plated copper package along with a 7-pin PCB board, which are mounted onto a cold finger with a cryostat, and each laser device is connected to a bonding pad on the PCB board via Au-wire-bonding; (c) top side view of THz QCLs with Au-wire bonding under optical microscope (laser bars with ridge width of 120 μm, 90 μm, and 60 μm, respectively); (d) cross-section view under scanning electron microscopy (SEM) of a bonded THz QCL ridge waveguide on AlN substrate.

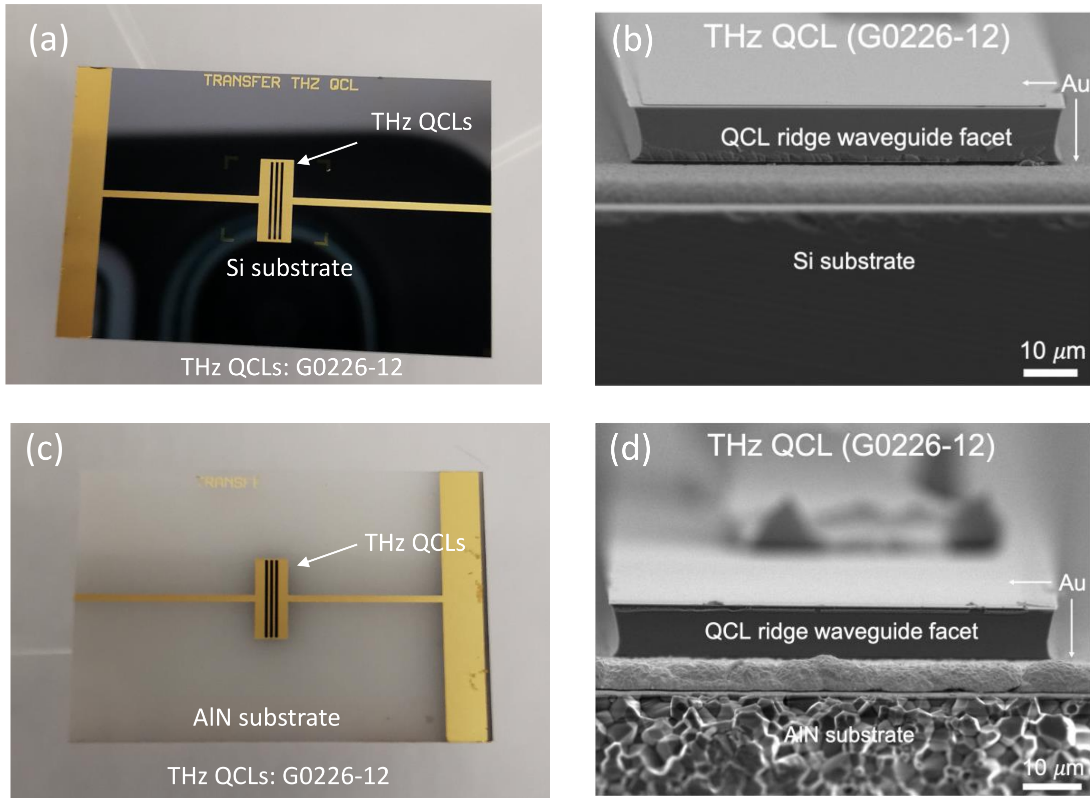

Figure 6.16 (a) Bonded THz QCLs (wafer#: G0226, cavity length: 2.4 mm, ridge width: 80 μm for each) with cleaved facet on Si substrate; (b) facet view under SEM of a bonded THz QCL ridge waveguide on Si substrate in 80 μm of ridge width; (c) bonded THz QCLs with cleaved facet on AlN substrate; facet view under SEM of a bonded THz QCL ridge waveguide on AlN substrate in 80 μm of ridge width.

6.4 Device Characterization and Optical Performance between THz QCLs on Hetero-substrates and THz QCLs on GaAs substrates

The light–current density–voltage (L-J-V) measurements results of hybrid bonded THz QCLs on AlN substrate compared with THz QCLs on GaAs are shown in the Figure 6.17. In comparison, THz QCLs from the same as-grown wafer are fabricated into conventional Au-Au ridge waveguides on GaAs receptor substrate, and the L-J-V measurements results are shown in Figure 6.18. The temperature dependent L-J-V measurements in a short pulse injection (pulse width at 250 ns) for a THz QCL bonded on AlN (QCL ridge width of 120 μm and cavity length of 2.4 mm) and on GaAs substrate (QCL ridge

width of 120 μm and cavity length of 1.66 mm) are shown in Figure 6.17(a) and Figure 6.18(a), respectively, while the heat sink temperature varies from 10 K to 95 K/93 K. The results show the same trend that the QCL device has a relatively close T_{max} in a short pulse injection either bonded on AlN or GaAs substrate. In addition, the pulse duration dependent (pulse width from 250 ns to 40 μm or duty cycle from 0.025% to 4%) L-J-V measurements with various heat sink temperature (10 K, 50 K, and 80 K) for THz QCL bonded on AlN and GaAs are shown in Figure 6.17(b-d) and Figure 6.18(b-d), respectively. It can be clearly observed from the results that the light intensity is increasing with the increase of the injected pulse duration, and the J_{th} is independent with the pulse duration when the heat sink temperature at 10 K or 50 K. However, when the heat sink temperature at 80 K, the light intensity firstly increases then it gradually decreases with the increase of the pulse duration due to the thermal effect. As shown in Figure 6.18(d), the lasing is quenching for the THz QCL on GaAs when the pulse duration is above 30 μs, and the negative differential resistance (NDR) is almost invisible when the pulse duration is above 5 μs. On the contrary, as shown in Figure 6.17(d), though the J_{th} slightly increases with the pulse duration, the NDR is still clearly observed, and the light intensity is still strong enough even when the pulse duration at 40 μs. These results suggested that AlN as substrate performing superior heat dissipation property towards better thermal management. A detailed data analysis is shown in Figure 6.19.

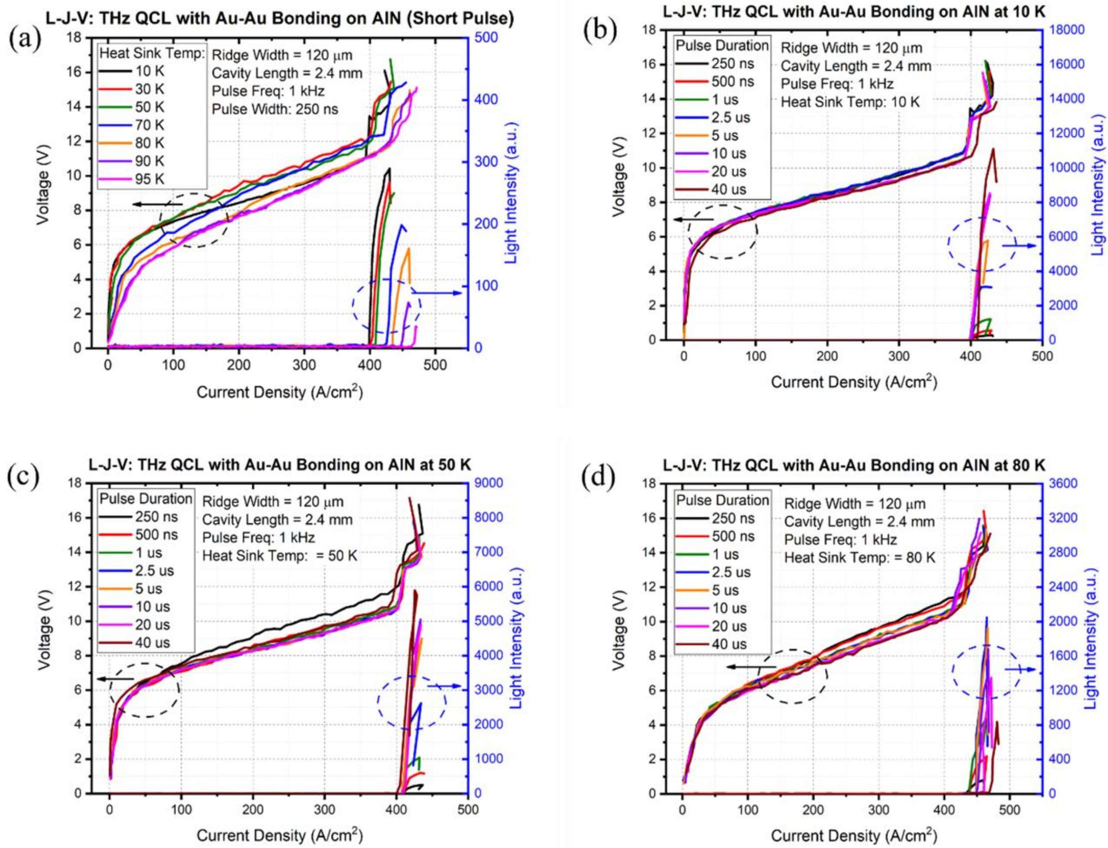

Figure 6.17 Temperature dependent L-J-V measurements under short pulse injection of THz QCLs bonded on AlN (a), and injected pulse width dependent L-J-V measurements of THz QCLs bonded on AlN when the heat sink temperature is at 10 K, 50 K, and 80 K, respectively (b-d).

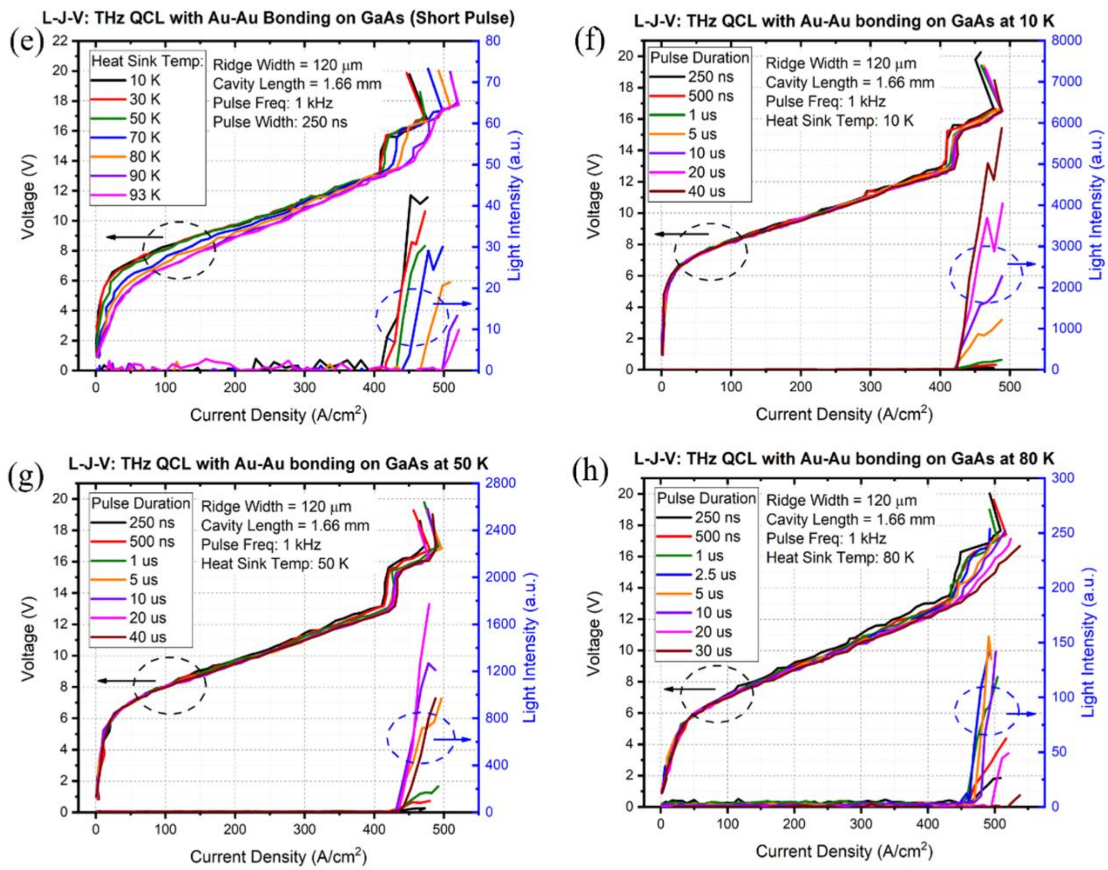

Figure 6.18 Temperature dependent L-J-V measurements under short pulse injection of THz QCLs bonded on GaAs (a), and injected pulse width dependent L-J-V measurements of THz QCLs bonded on GaAs when the heat sink temperature is at 10 K, 50 K, and 80 K, respectively (b-d).

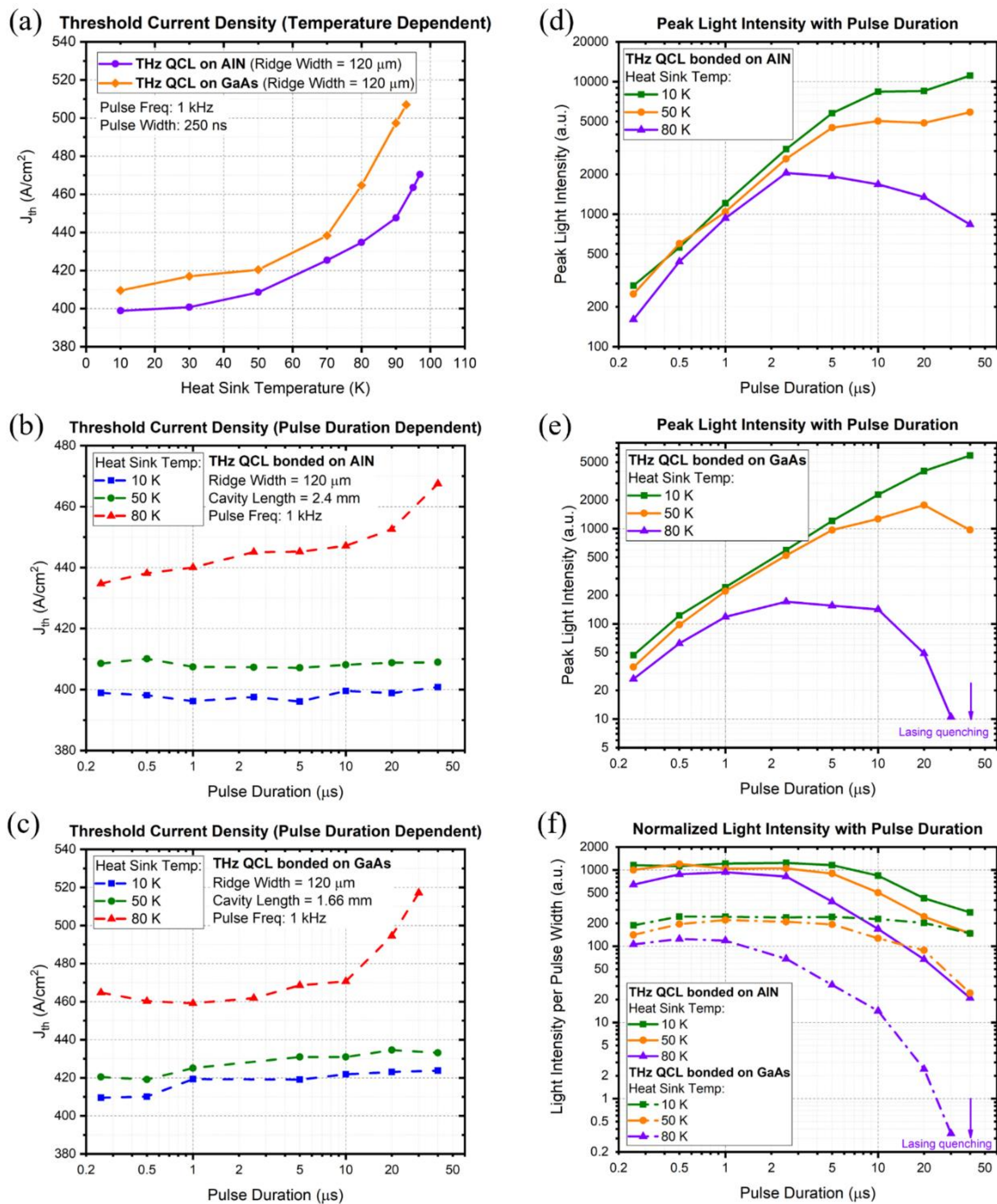

Figure 6.19 Temperature dependent threshold current density (J_{th}) of THz QCLs on AlN and GaAs under short pulse injection (a); pulse duration dependent J_{th} of THz QCLs on AlN (b) and GaAs (c) with various heat sink temperature; the peak light intensity with the change of the pulse duration of THz QCLs on AlN (d) and GaAs (e); normalized light intensity with pulse duration for THz QCLs bonded on AlN and GaAs (f).

The temperature dependent J_{th} for THz QCLs on AlN and GaAs extracted from Figure 6.17(a) and Figure 6.18(a) is shown in Figure 6.19(a). The J_{th} is gradually increasing with the heat sink temperature changing from 10 K to 95 K/93 K. The J_{th} of THz QCL on AlN is slightly lower than the J_{th} of THz QCL on GaAs, which is probably resulting from the lower mirror loss due to the longer cavity length. Figure 6.19(b) and Figure 6.19(c) show that the pulse duration dependent J_{th} for the THz QCL bonded on AlN and GaAs, respectively, when the heat sink temperature is kept at 10 K, 50 K, and 80 K. At 10 K and 50 K, with the change of the pulse duration, the J_{th} is almost at the same for THz QCL bonded on AlN. In comparison, with the pulse duration increasing from 250 ns to 40 μs, the J_{th} for THz QCL bonded on GaAs slightly increases from 410 to 423 A/cm^2 (heat sink temperature at 10 K) or from 420 to 433 A/cm^2 (heat sink temperature at 50 K), which is expected due to the Joule heating effect. In stark contrast, when the heat sink temperature at 80 K, the J_{th} increases by 47 A/cm^2 (from 470 to 517 A/cm^2) for THz QCL on GaAs when the injected pulse duration from 10 μs to 30 μs (Figure 6.19(c)), while the J_{th} only increases by 20 A/cm^2 (from 447 to 467 A/cm^2) when the injected pulse duration from 10 μs to 40 μs (Figure 6.19(b)). This phenomenon suggests that Joule heating effect deteriorate the lasing performance towards cw mode operation when GaAs as the device receptor substrate, and AlN as substrate (heatsink submount) performs superior heat dissipation properties.

Thermal-induced lasing quenching is observed for THz QCL on GaAs substrate in long pulse injection. The peak light intensity with different pulse duration of THz QCL on AlN and GaAs are shown in Figure 6.19(d) and Figure 6.19(e). At 80 K, it is clearly observed that the light intensity dramatically decreases more than 90% when the injected pulse duration above 10 μs for the THz QCL on GaAs, and the lasing is quenching when the pulse duration above 30 μs (Figure 6.19(e)). On the contrary, the same at 80 K, the peak light intensity for the THz QCL on GaAs decreases by approximately 50% when the pulse duration changes from 10 μs to 40 μs or decreases by approximately 60% from 2.5 μs to 40 μs (Figure 6.19(d)). This suggests that AlN as substrate has much less Joule heating effect than the GaAs substrate. As shown in Figure 6.19(f), the normalized light intensity with pulse duration (light intensity per pulse width) for both THz QCL on AlN and GaAs are plotted in the same figure. At 80 K, it is clearly observed that the normalized light intensity for THz QCL on GaAs starts to decrease when the injected pulse duration above 1 μs, and it is close to zero when the pulse duration above 30 μs (normalized light intensity decreasing by 99.7%). On the other hand, for THz QCL on AlN at 80 K, though the normalized light intensity drops by 98% when the injected pulse

duration from 1 μs to 40 μs, the light is still strong enough during lasing operation. These preliminary results show that thermal-induced lasing quenching (Joule heating effect) plays an adverse effect on the lasing performance towards cw mode operation based on GaAs substrate. Instead, due to much higher thermal conductivity for more efficient heat dissipation in cryogenic temperature, hetero bonded THz QCLs on AlN as a heat sink submount could be a promising platform towards cw lasing operation at higher temperature performance.

In addition, the comparison of L-I-V results of the hetero bonded THz QCLs on Si and AlN are showing in Figure 6.20, Figure 6.21, and Figure 6.22 below. Figure 6.20 shows the characterized L-I-V results of THz QCLs (wafer#: G0312) in ridge waveguides with dry etch facet bonded on Si substrate (fabrication process was shown in Figure 6.13). The device is with 120 μm of ridge width and 1 mm of cavity length. The device is characterized on pulse mode (pulse repetitive frequency at 1 kHz and pulse width of 250 ns). The heat sink temperature is changing from 20 K to 90 K. It is shown that the maximum lasing temperature is at 80 K.

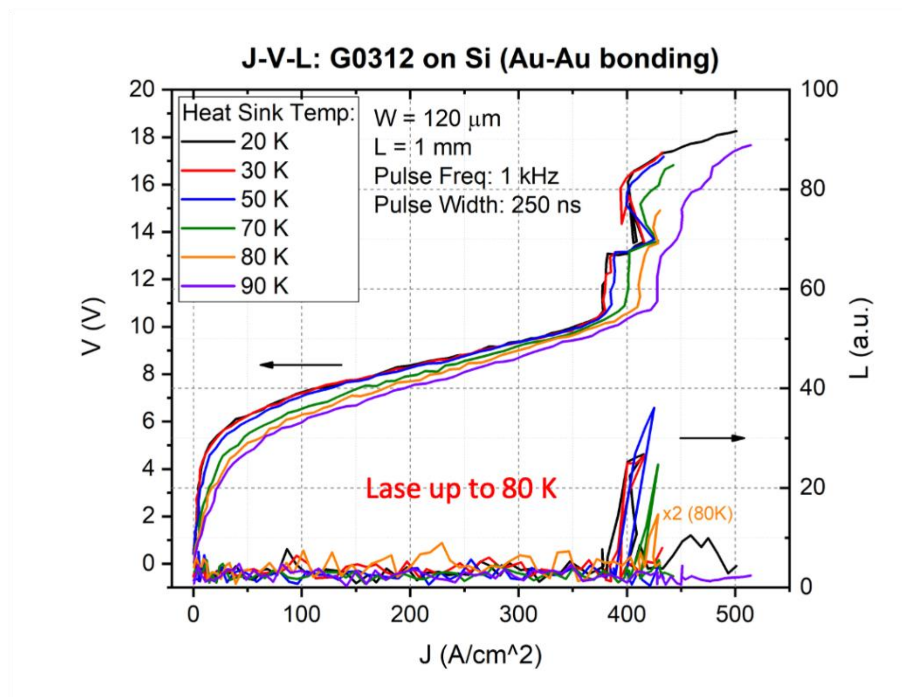

Figure 6.20 L-I-V characterization of THz QCL (wafer#: G0312) ridge waveguide bonded on Si substrate. The device is with dry etch facet, with 120 μm of width and 1 mm of length.

Figure 6.21 and Figure 6.22 show the characterized L-I-V results of THz QCLs (Wafer#: G0312) in ridge waveguides with cleaved facet bonded on AlN substrates (fabrication process was shown in Figure 6.14). In Figure 6.21, the device is with 90 μm of ridge width and 2.4 mm of cavity length. The device is characterized on pulse mode (pulse repetitive frequency at 1 kHz and pulse width of 250 ns). The heat sink temperature is changing from 10 K to 90 K. It is shown that the maximum lasing temperature is at 90 K.

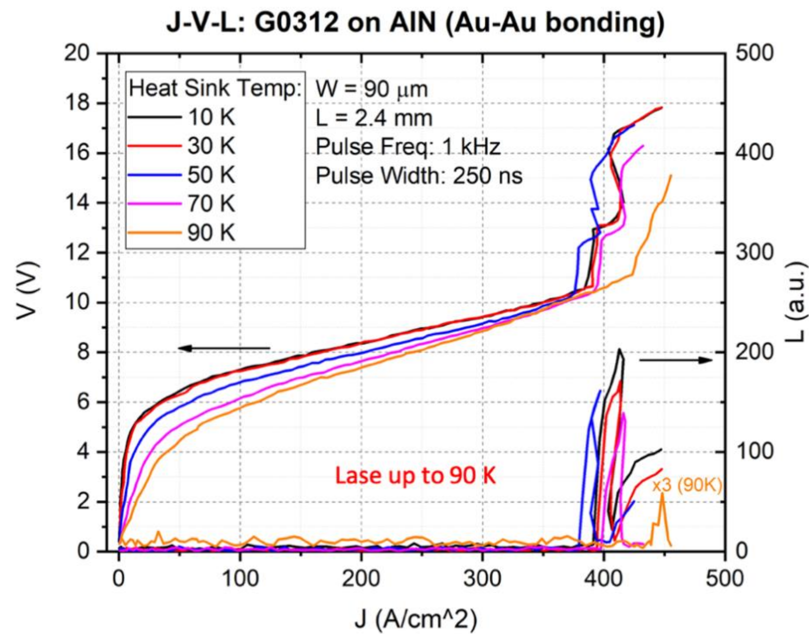

Figure 6.21 L-I-V characterization of THz QCL (wafer#: G0312) ridge waveguide bonded on AlN substrate. The device is with cleaved, with 90 μm of width and 2.4 mm of length.

In Figure 6.22, the device is with 120 μm of ridge width and 2.4 mm of cavity length. The device is characterized on pulse mode (pulse repetitive frequency at 1 kHz and pulse width of 250 ns). The heat sink temperature is changing from 10 K to 97 K. It is shown that the maximum lasing temperature is at 97 K. The slightly higher maximum lasing temperature probably due to the lower optical loss from the wider ridge waveguide. The T_{max} at 97 K is also close to the T_{max} at 100 K for the conventional oven bonding G0312 on GaAs receptor substrate (see section 6.1 for the discussion).

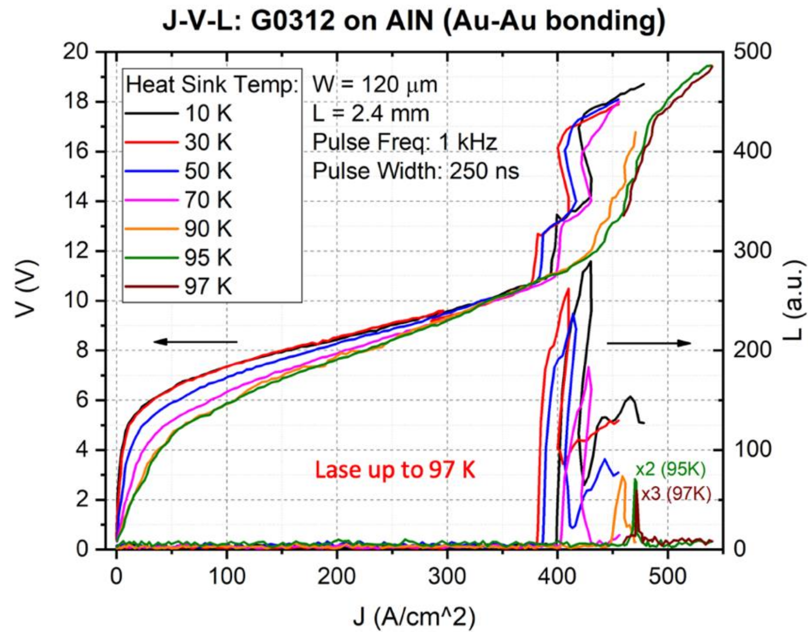

Figure 6.22 L-I-V characterization of THz QCL (wafer#: G0312) ridge waveguide bonded on AlN substrate. The device is with cleaved facet, with 120 μm of width and 2.4 mm of length.

Figure 6.23 shows the curve of the threshold current density changing with the heat sink temperature on pulse mode operation for G0312 hetero bonded on AlN and Si substrate. J_{th} is from ~380 to 470 A/cm^2 when the heat sink temperature changes from 10 K to 97 K. The devices (on AlN and Si) give the similar J_{th} values with the change of the heat sink temperature, which are similar as on conventional oven bonding on GaAs receptor substrate. These results demonstrate that the hetero bonding strategies are successful, and there is no such significant side effect from the thermal stress induced damage towards the optical performance.

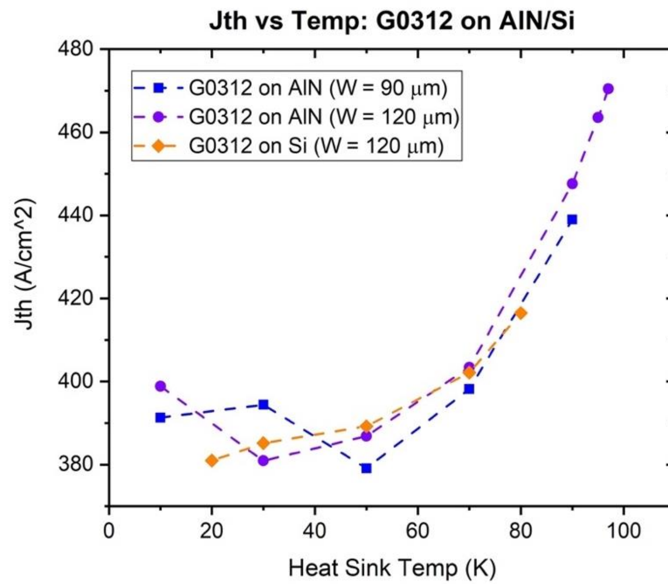

Figure 6.23 Threshold current density (J_{th}) vs. the heat sink temperature

Relative dynamic range (RDR) is defined by $(J_{max}-J_{th})/J_{max}$ [104], which is plotted in Figure 6.24. The RDR of all the three devices show similar temperature dependence, which drop with the increasing heat sink temperature. However, at low-temperature value when the heatsink temperature at 10 K, the RDR of all the devices are below 10%, which is much narrower compared with 34% in Au-Au bonded f30-series device in reference paper [104].

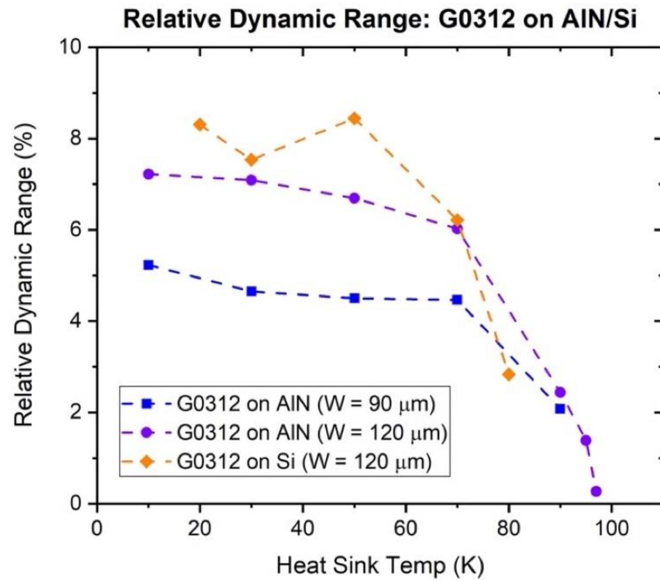

Figure 6.24 Relative dynamic range (RDR) vs. the heat sink temperature

6.5 Thermal Dynamics Modeling: Comparison of THz QCLs on Intrinsic GaAs and on Hetero-Substrates

A schematic diagram of a classical THz QCL in Au-Au waveguide structure on a heatsink submount is plotted in the Figure 6.25 below. The current is injected from the top contact layer flowing through the whole active region towards the bottom contact layer. A typical three-dimension (3D) and two-dimension (2D) temperature profile by COMSOL Multiphysics® simulation (Heat Transfer Module) for THz QCLs operated in cw mode in plotted in Figure 6.26, when the heat sink temperature is steady at 100 K. It is noticed that the maximum temperature inside the active region is more than 40 K above the heat sink temperature, and there is a large temperature gradience from the active region to the substrate. This simulation suggests that most of the heat generated inside the active region inefficiently dissipate towards the heat sink submount, which significantly limit the lasing performance. Therefore, high thermal conductivity hetero substrate for heat sink submount is requisite in cw operation.

THz QCL on GaAs in Au-Au waveguide (Not to scale)
Mesa Width: 120 μm
Mesa Depth: 10 μm

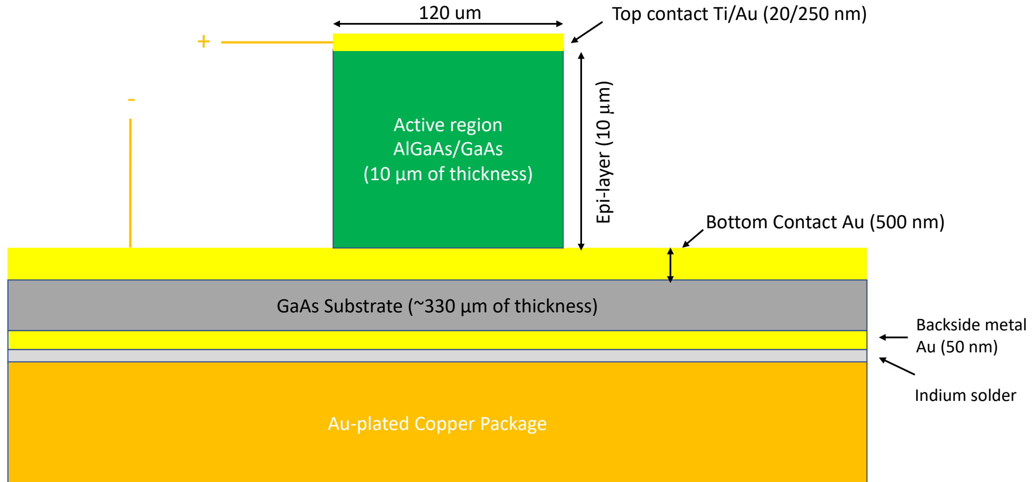

Figure 6.25 Schematic diagram of cross-section view of a typical THz QCL in metal-metal waveguide

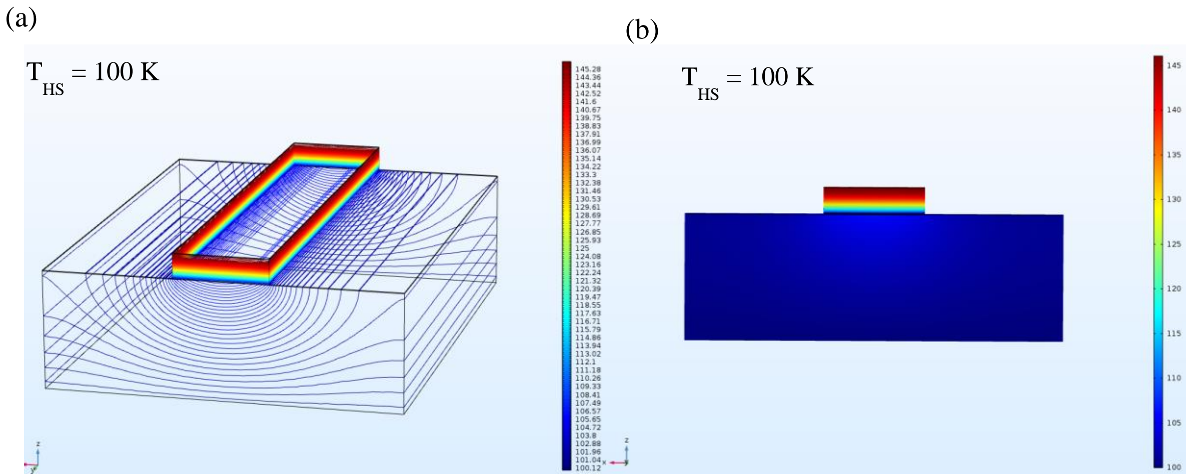

Figure 6.26 3D (a) and 2D (b) temperature profile by COMSOL simulation for the temperature rise in cw mode operation for Au-Au waveguide THz QCLs on GaAs when the heat sink temperature steady at 100 K.

To verify the assumption, a same simulation model is carried out to compare the DC biased temperature rising in the THz QCL's active region on different heat sink submount assembly, when the

heat sink temperature is steady at 100 K. In this simulation, GaAs receptor substrate is replaced as AlN, Si, and diamond (1 μm thick) coated on Si, and the power injection density is 2.56×10^{12} W/m^3 (J = 320 A/cm^2, which is the J_{th} for wafer# G0226 lasing at 100 K). The simulation results show that the AlN as hetero substrate (heat sink submount) has the lowest rising temperature in device's active region, which produce 10.44 K of average temperature rise and 14.71 K of maximum temperature rise. Similarly, diamond coated on Si appears to be the second lowest temperature rising in active region, followed by pure Si substrate. This is probably due to the extreme high thermal conductivity of diamond in contrast with other materials. Nevertheless, since there is only thin film layer of diamond onto Si, the temperature rising is still slightly higher compared with AlN in this certain bias condition. In comparison, GaAs itself has substrate gives much higher temperature rise in active region compared with other three materials. These simulation results verify the assumption that AlN as heat sink submount produces superior thermal properties.

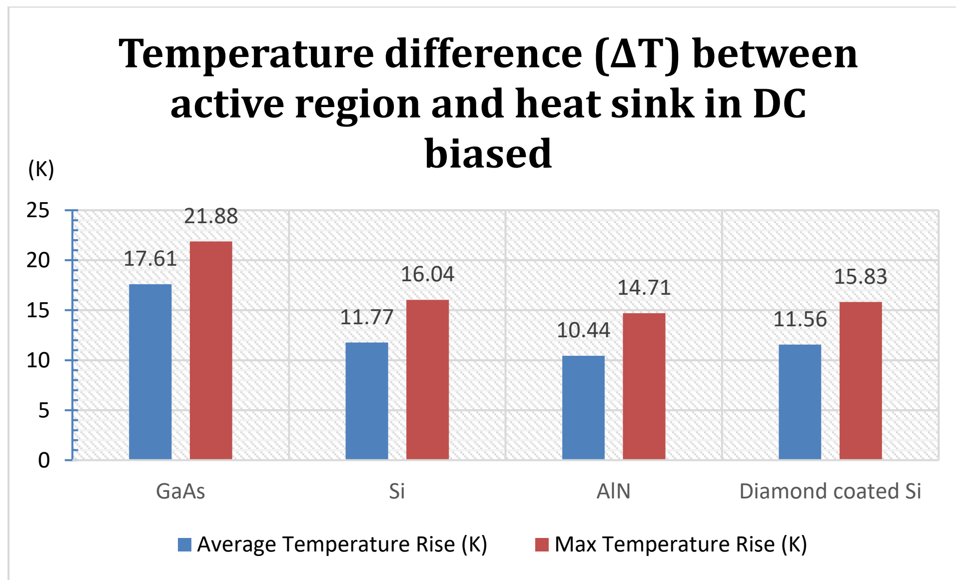

Figure 6.27 Average (blue) and max (orange) temperature rise above heat sink temperature (set to100 K) of THz QCLs (Au-Au bonding) on different heat sink submount of GaAs, Si, AlN, and diamond coated (1 μm) Si, respectively. The power injection density is at 2.56×10^{12} W/m^3 (J = 320 A/cm^2).

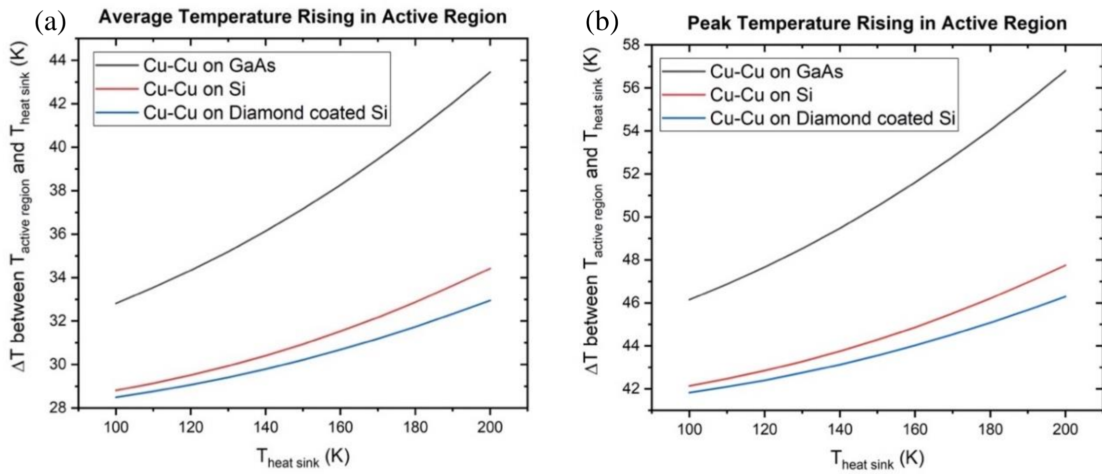

Figure 6.28 Average temperature rising (a) and peak temperature rising (b) in active region with different heat sink temperature on DC biased (cw mode).

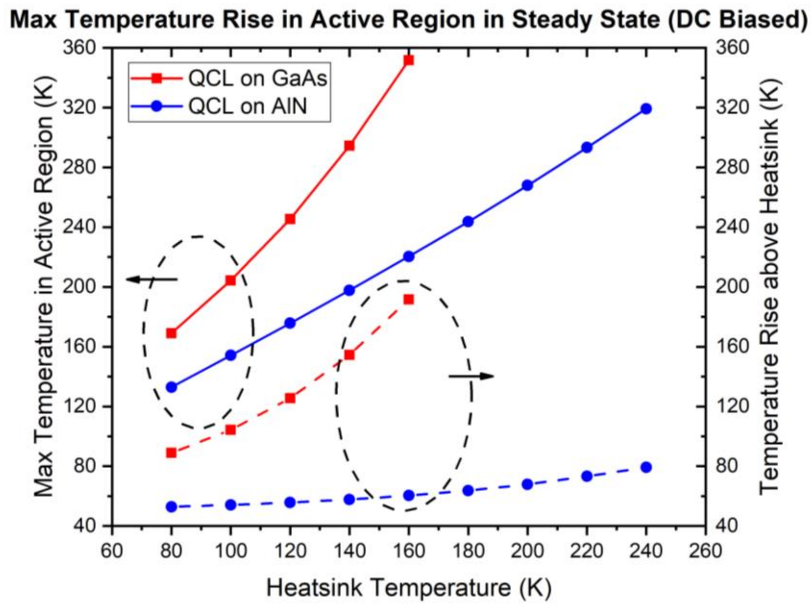

Figure 6.29 Simulated maximum temperature rise (left axis) and the temperature rise above heatsink temperature (right axis) in active region when THz QCL is in DC biased (injected power density is 8.00×10^{12} W/m^3)

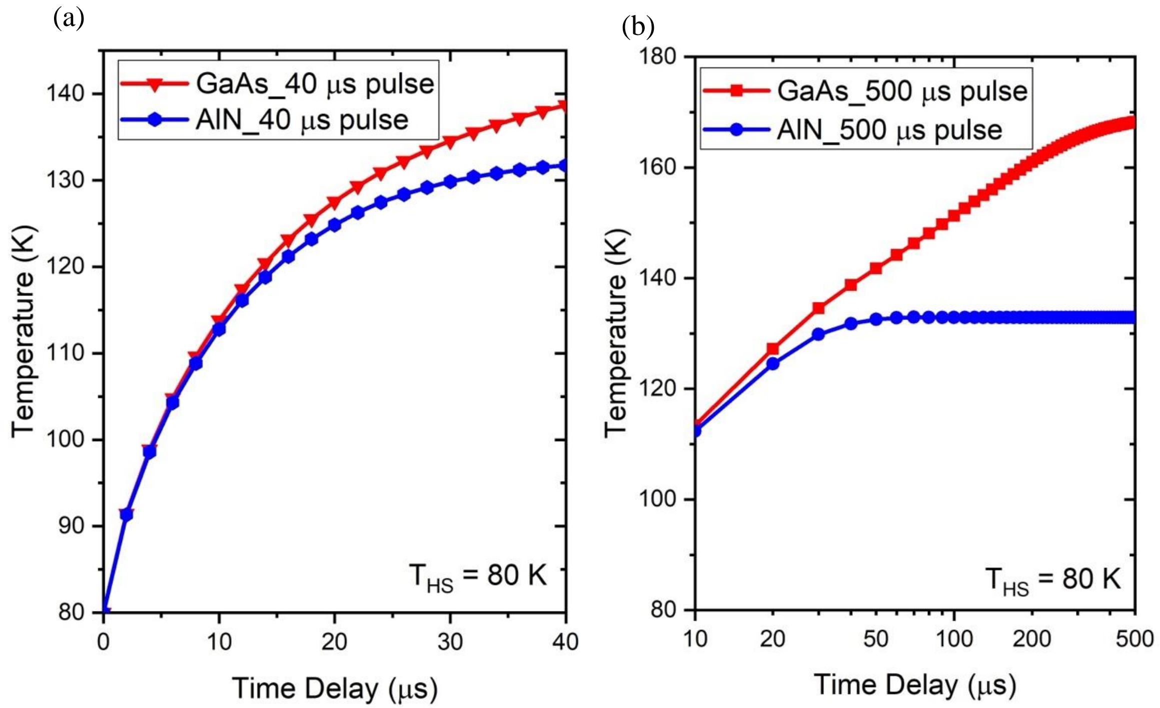

Figure 6.30 Simulated internal active region temperature rises of THz QCL bonded on GaAs (red line) and AlN (blue line) when the pulse injection at 40 μs (a) and 500 μs (b). The heatsink temperature is kept at 80 K and the injected peak power density is 8.00 $\times 10^{12}$ W/m^3.

6.6 Summary

To summarize, THz QCLs are fabricated in Au-Au ridge waveguides and hetero bonded on AlN substrate successfully. The L-J-V characterization in a short pulse injection (250 ns) shows the temperature dependent J_{th} and T_{max} for THz QCLs on AlN are comparable to the measured results from the same device wafer fabricated in Au-Au ridge waveguides bonded on GaAs receptor substrate. The pulse duration dependent L-J-V measurements show the normalized light intensity (light intensity per pulse width) drops much faster for THz QCLs on GaAs compared to THz QCLs on AlN substrate at higher heat sink temperature (e.g., 80 K), and it eventually leads to lasing quenching when the pulse duration above 30 μs at 80 K, which could be attributed to Joule heating. These results indicate that THz QCLs in MM waveguides hetero bonded on AlN perform efficient heat extraction and dissipation, which is promising for breaking the T_{max} towards cw operation.

Chapter 7
Conclusion

7.1 Summary of This Dissertation

This dissertation represents systematic studies on thermal dynamic imaging and thermal management on mid-infrared quantum cascade lasers (MIR QCLs) and terahertz quantum cascade lasers (THz QCLs) towards higher optical performance in higher heat dissipation efficiency. The main results of this dissertation are summarized as follows.

1. Time-resolved (TR) temperature profile of actively-biased MIR QCLs was measured by using charge-coupled-device (CCD)-based spatially resolved time-domain thermoreflectance (SR-TDTR) microscopy with an ultrafast temporal resolution of 50 ns and a high spatial resolution of 390 nm. Based on the measured TR two-dimensional (2D) temperature profiles, the heat generation and dissipation dynamics within the lasers have been investigated. It is found that the active-region temperature increases quickly to a peak value (up to ~100 °C above ambient room temperature) within 500 ns upon pulsed current injection of 6 A. The heat dissipation to the top and bottom cladding layers of the device is initially comparable, yet it evolves differently with time. Within 1-2 μs, the heat dissipation to the top cladding is substantially reduced and most of the heat is drained to the substrate through the bottom cladding layer. This constrained heat dissipation is confirmed by experimental light-current-voltage (L-I-V) measurement and theoretical thermal modeling. The results show that the internal temperature rise in the active region, much above the heatsink temperature, can eventually lead to thermal quenching for lasing operation. The SR-TDTR is a powerful tool for probing internal thermal dynamics of many active electronic and photonic devices, particularly for those needing special heat and thermal arrangement.

2. Spatially resolved transient temporal profile to observe 3D thermodynamics of MIR QCLs. It is clearly observed that there is strong localized Joule heating occurring on the laser facet, especially on the edge of electroplated gold (EP-Au) layer above the top cladding layer close to the facet. It is also observed that stronger Joule heating situates on the rough surface of EP-Au, leading to higher temperature rise (hot spots). Three sets of devices were characterized for the thermal properties (thermal resistance and thermal conductance per unit area). Comparing to the dissipation channel towards top EP-Au layer through the top cladding layer, it is found that most of heat is dissipating

towards to the heatsink through bottom cladding layer – substrate channel. Thicker EP-Au layer does not have strong effects on enhancing the thermal dissipation efficiency based on the epi-layer up mounting. In comparison, the narrow ridge waveguide could have a more efficient way for thermal dissipation. This evidence leads a guidance for improving thermal management on MIR QCLs based on packaging strategies.

3. Reversible lasing performance degradation of an actively-biased mid-infrared quantum cascade laser (MIR-QCL) is investigated under an accelerated aging burn-in test for 30 hours in the ambient atmosphere, followed by 10 minutes of hydrogen plasma treatment. The thermal dynamics of the localized facet Joule heating from the facet-uncoated $GaAs/Al_{0.45}Ga_{0.55}As$ MIR-QCL is visualized by spatially resolved time-domain thermoreflectance (SR-TDTR) imaging system during the reversible optical degradation process. It is found that the thermal-induced facet oxidation is the main reason for the rapid degradation of the lasing performance. The high aluminum compound of the active region on the facet can easily be oxidized in a thermal-stress condition, which has a strong absorption at the MIR-QCL's lasing wavelength ($\lambda \sim 9$ μm). The temperature rises on the laser facet reduce after 30 hours of an accelerated aging burn-in test, along with a degradation of the optical performance. On the contrary, the facet temperature rise increases after 10 minutes of hydrogen plasma treatment, along with the resuming of the lasing optical performance. On the other hand, the temperature rises along the laser cavity is negligible before and after aging test, indicating insignificant degradation inside the laser cavity. It is found that the optical degradation localizes on the device facet, and the lasing performance degrades from the additional localized facet Joule heating due to the oxidation layer reabsorption on the facet. These results verify that thermal-induced facet oxidation is the main reason for the rapid degradation of the lasing performance in the early aging stage.

4. THz QCLs are fabricated in Au-Au ridge waveguides and hetero bonded on Si and AlN substrate successfully. The L-J-V characterization in a short pulse injection (250 ns) shows the temperature dependent J_{th} and T_{max} for THz QCLs on AlN are comparable to the measured results from the same device wafer fabricated in Au-Au ridge waveguides bonded on GaAs receptor substrate. The pulse duration dependent L-J-V measurements show the normalized light intensity (light intensity per pulse width) drops much faster for THz QCL on GaAs than on AlN substrate at higher heat sink temperature (e.g., 80 K), and it eventually leads to lasing quenching when the pulse duration above 30 μs at 80 K, which could be attributed to Joule heating. These preliminary results indicate that

THz QCLs in MM waveguides hetero bonded on AlN perform efficient heat extraction and dissipation, which is promising for breaking the T_{max} towards cw operation.

7.2 Future Work and Perspectives

THz QCLs suffer from divergent far-field beam pattern, which make it difficult to be coupled and modulated externally. Conventionally, an external silicon lens has been widely used to shape the THz light, but the centimeters-scale could be poor for miniaturization. On the other hand, on-chip silicon waveguides with metal cladding layers have the unique properties of lower optical loss than III-V materials. As a result, the silicon-based hybrid platform could be an ideal solution for coupling THz QCLs with silicon wafer waveguide, which can optimize near-field and far-field beam pattern towards on-chip photonics integration.

In this work, substantial improvement of far-field beam pattern for terahertz quantum cascade lasers (THz QCLs) by heterogenous integration of THz QCLs with high-resistance (HR) silicon waveguide will be demonstrated. The THz QCLs are transfer bonded on silicon (Si) substrate followed by substrate liftoff process. The results shows that the far-field beam pattern quality can be optimized by Au coating on Si sidewall, which enhance the coupling efficiency and uniform the mode distribution. This project has a potential application for on-chip terahertz source towards terahertz band silicon photonics. Simulation results are shown from Figure 7.1 to Figure 7.4, and the fabrication procedures and preliminary results are shown in Appendix C.

Simulation: QCL coupling to Si Waveguide

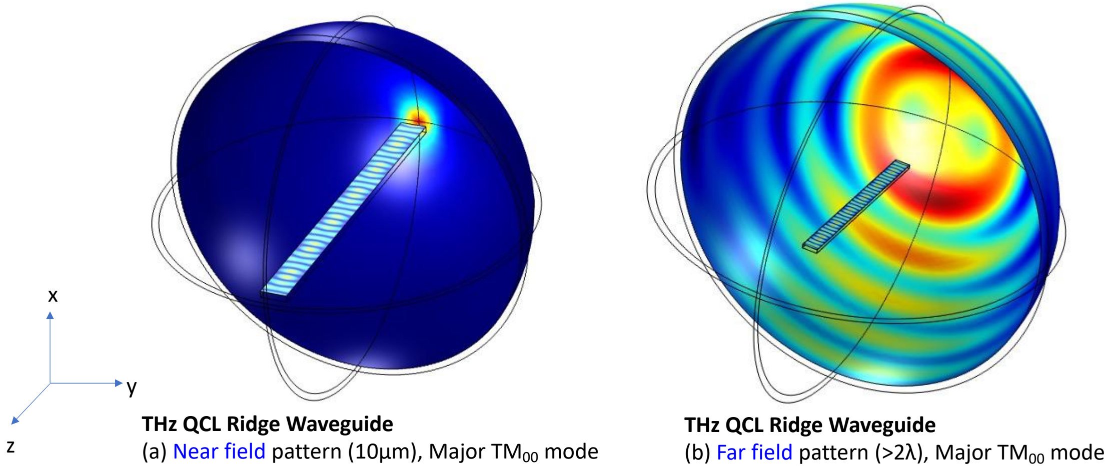

Figure 7.1 Schematic diagram of THz QCL ridge waveguide in near field pattern (a) and far field pattern (b).

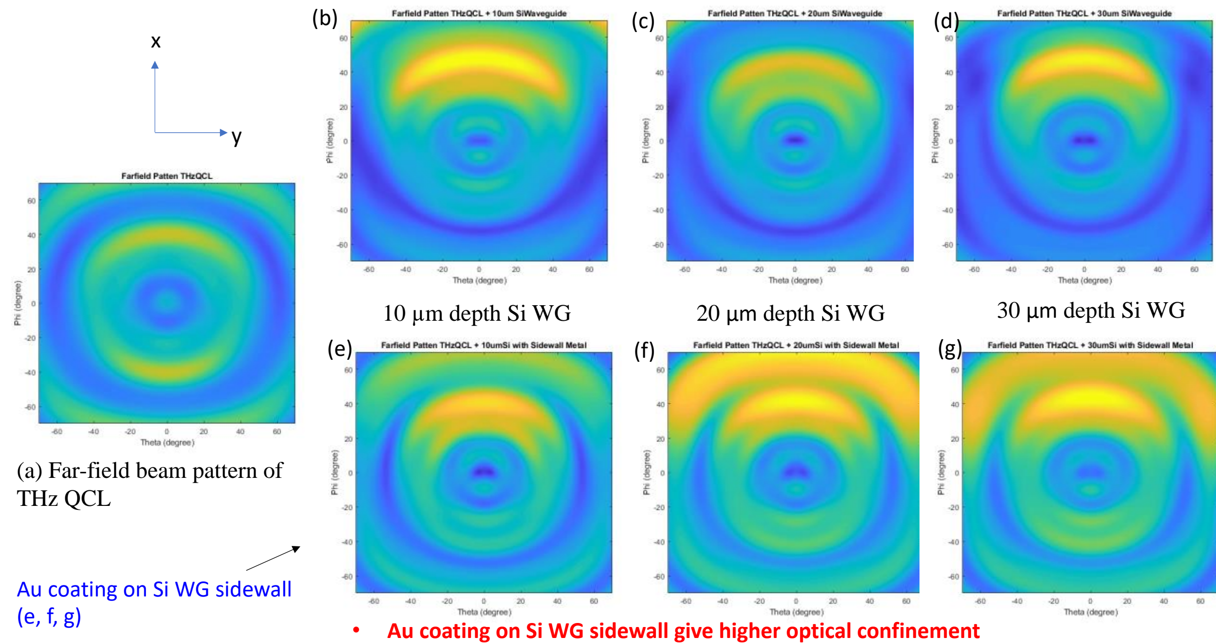

Figure 7.2 Simulation of far-field pattern of THz QCL coupling with Si Waveguide (Si WG), the lateral gap between THz QCL and Si WG is optimized at 10 µm: (a) Far-field beam pattern of THz QCL with 40 µm of ridge width of and 10 µm of depth without Si waveguide coupling; (b) Far-field beam pattern of THz QCL coupling with Si waveguide with 10 µm depth (without metal coating on Si WG sidewall); (c) Far-field beam pattern of THz QCL coupling with Si waveguide with 20 µm depth (without metal coating on Si WG sidewall); (d) Far-field beam pattern of THz QCL coupling with Si waveguide with 30 µm depth (without metal coating on Si WG sidewall); (e) Far-field beam pattern of THz QCL coupling with Si waveguide with 10 µm depth (Au coating on Si WG sidewall); (f) Far-field beam pattern of THz QCL coupling with Si waveguide with 20 µm depth (Au coating on Si WG sidewall); (g) Far-field beam pattern of THz QCL coupling with Si waveguide with 30 µm depth (Au coating on Si WG sidewall).

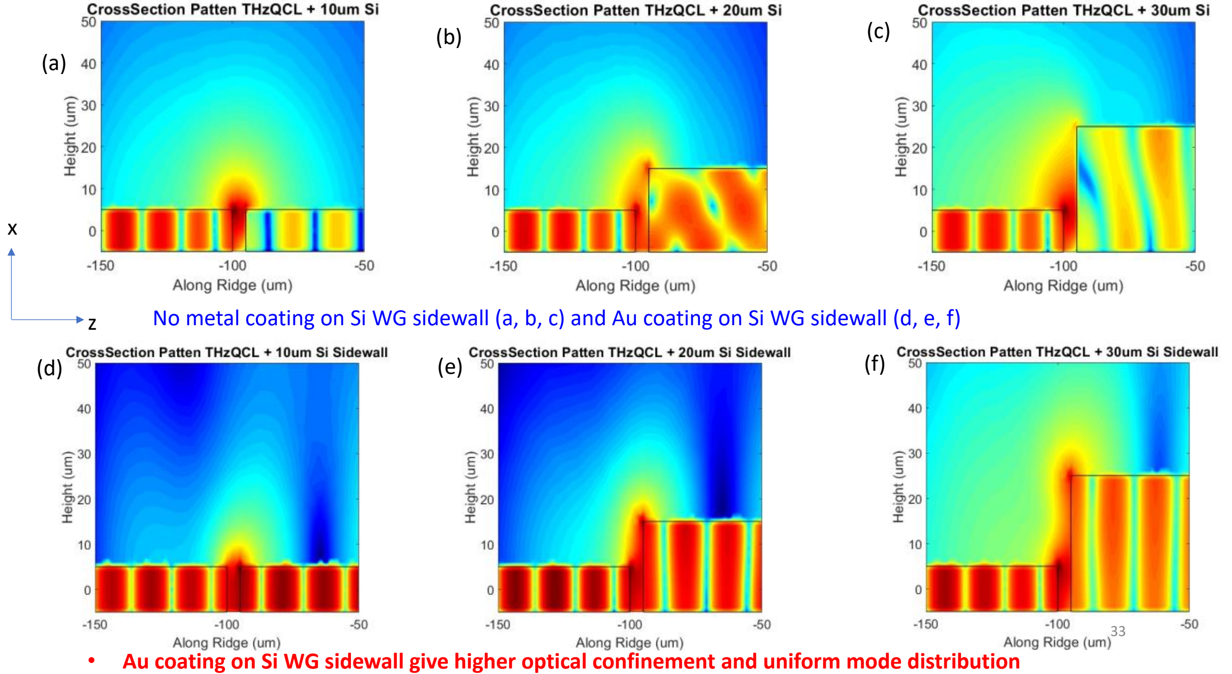

Figure 7.3 Mode propagation along THz QCL ridge waveguide towards Si Waveguide (Si WG): (a) Mode propagation along THz QCL ridge waveguide towards Si WG with 10 µm depth (without metal coating on Si WG sidewall); (b) Mode propagation along THz QCL ridge waveguide towards Si WG with 20 µm depth (without metal coating on Si WG sidewall); (c) Mode propagation along THz QCL ridge waveguide towards Si WG with 30 µm depth (without metal coating on Si WG sidewall); (d) Mode propagation along THz QCL ridge waveguide towards Si WG with 10 µm depth (Au metal coating on Si WG sidewall); (e) Mode propagation along THz QCL ridge waveguide towards Si WG with 20 µm depth (Au metal coating on Si WG sidewall); (f) Mode propagation along THz QCL ridge waveguide towards Si WG with 30 µm depth (Au metal coating on Si WG sidewall).

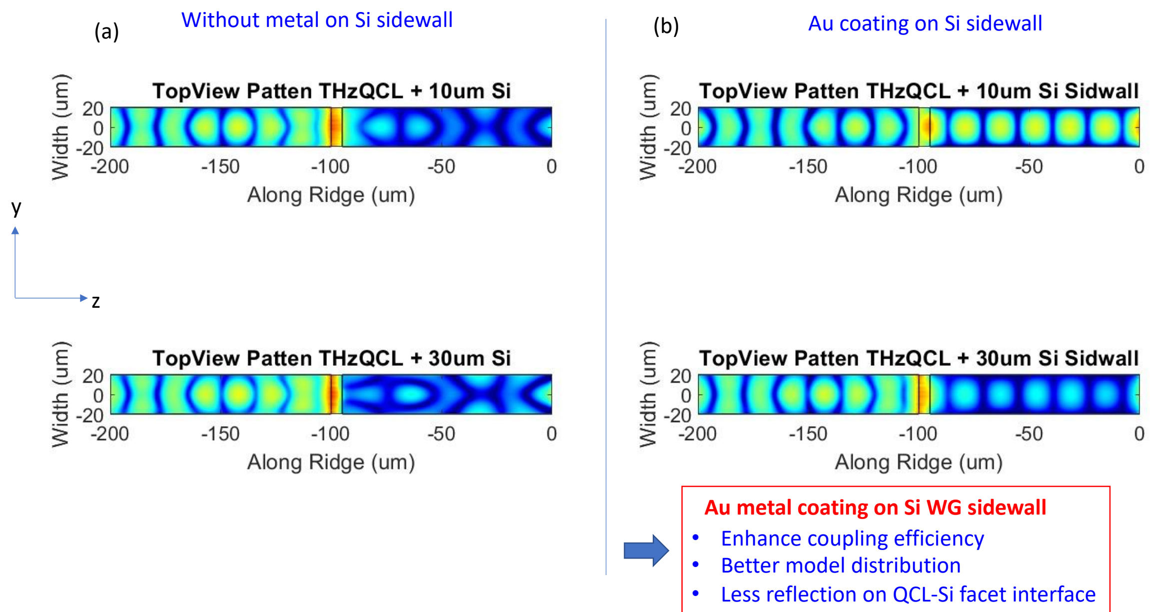

Figure 7.4 Top view pattern distribution along THz QCL ridge waveguide towards Si Waveguide (Si WG): (a) without metal coating on Si sidewall; (b) with Au coating on Si sidewall

Bibliography

[1] J. Faist, F. Capasso, D. L. Sivco, C. Sirtori, A. L. Hutchinson, and A. Y. Cho, "Quantum Cascade Laser," *Science* **264**(5158), 553–556 (1994).

[2] N. Zhuo, F. Liu, and Z. Wang, "Quantum cascade lasers: from sketch to mainstream in the mid and far infrared," *Journal of Semiconductors* **41**(1), 010301 (2020).

[3] C. Sirtori, "Bridge for the terahertz gap," *Nature* **417**(6885), 132-133 (2002).

[4] R. Köhler, A. Tredicucci, F. Beltram, H. E. Beere, E. H. Linfield, A. G. Davies, D. A. Ritchie, R. C. Iotti, and F. Rossi, "Terahertz semiconductor-heterostructure laser," *Nature* **417**(6885), 156-159 (2002).

[5] F. Wang, S. Slivken, D. H. Wu, and M. Razeghi, "Room temperature quantum cascade laser with∼ 31% wall-plug efficiency," *AIP Advances* **10**(7), 075012 (2020).

[6] M. S. Vitiello, G. Scamarcio, V. Spagnolo, S. S. Dhillon, and C. Sirtori, "Terahertz quantum cascade lasers with large wall-plug efficiency," *Applied Physics Letters* **90**(19), 191115 (2007).

[7] A. Knigge, G. Erbert, J. Jönsson, W. Pittroff, R. Staske, B. Sumpf, M. Weyers, and G. Tränkle, "Passively cooled 940 nm laser bars with 73% wall-plug efficiency at 70 W and 25°C," *Electronics Letters* **41**(5), 250 (2005).

[8] R. Kazarinov, "Possibility of amplification of electromagnetic waves in a semiconductor with superlattice," *Sov. Phys.-Semicond.* **5**(4), 707-709 (1971).

[9] A. Y. Cho. *Molecular Beam Epitaxy*. (Woodbury, NY: AIP Press) (1997).

[10] M. Razeghi. *The MOCVD Challenge: A survey of GaInAsP-InP and GaInAsP-GaAs for photonic and electronic device applications*. CRC Press (2010).

[11] M. Beck, D. Hofstetter, T. Aellen, J. Faist, U. Oesterle, M. Ilegems, E. Gini, and H. Melchior, "Continuous wave operation of a mid-infrared semiconductor laser at room temperature," *Science* **295**(5553), 301-305 (2002).

[12] F. Wang, S. Slivken, D. H. Wu, and M. Razeghi, "Room temperature quantum cascade lasers with 22% wall plug efficiency in continuous-wave operation," *Opt. Express* **28**(12), 17532-17538 (2020).

[13] Y. Yao, A. J. Hoffman, and C. F. Gmachl, "Mid-infrared quantum cascade lasers," *Nature Photonics*, **6**(7), 432-439 (2012).

[14] B. Wen and D. Ban. "High-temperature terahertz quantum cascade lasers." *Progress in Quantum Electronics* **80**, 100363 (2021).

[15] B. S. Williams, "Terahertz quantum-cascade lasers," *Nature Photonics* **1**(9), 517-525 (2007).

[16] G. Liang, T. Liu, and Q. J. Wang, "Recent developments of terahertz quantum cascade lasers," *IEEE Journal of Selected Topics in Quantum Electronics* **23**(4), 1-18 (2016).

[17] M. A. Belkin, F. Capasso, A. Belyanin, D. L. Sivco, A. Y. Cho, D. C. Oakley, C. J. Vineis, and G. W. Turner, "Terahertz quantum-cascade-laser source based on intracavity difference-frequency generation," *Nature Photonics* **1**(5), 288-292 (2007).

[18] K. Fujita, S. Jung, Y. Jiang, J. H. Kim, A. Nakanishi, A. Ito, M. Hitaka, T. Edamura, and M. A. Belkin, "Recent progress in terahertz difference-frequency quantum cascade laser sources," *Nanophotonics* **7**(11), 1795-1817 (2018).

[19] L. Li, L. Chen, J. Zhu, J. Freeman, P. Dean, A. Valavanis, A. G. Davies, and E. H. Linfield, "Terahertz quantum cascade lasers with> 1 W output powers," *Electronics Letters* **50**(4), 309-311 (2014).

[20] G. Scalari, L. Ajili, J. Faist, H. Beere, E. Linfield, D. Ritchie, and G. Davies, "Far-infrared (λ≃ 87 μm) bound-to-continuum quantum-cascade lasers operating up to 90 K," *Applied Physics Letters* **82**(19), 3165-3167 (2003).

[21] B. S. Williams, H. Callebaut, S. Kumar, Q. Hu, and J. L. Reno, "3.4-THz quantum cascade laser based on longitudinal-optical-phonon scattering for depopulation," *Applied Physics Letters* **82**(7), 1015-1017 (2003).

[22] S. Kumar, C. W. I. Chan, Q. Hu, and J. L. Reno, "A 1.8-THz quantum cascade laser operating significantly above the temperature of ℏω/kB," *Nature Physics* **7**(2), 166-171 (2011).

[23] E. Dupont, S. Fathololoumi, Z. R. Wasilewski, G. Aers, S. R. Laframboise, M. Lindskog, S. G. Razavipour, A. Wacker, D. Ban, and H. C. Liu, "A phonon scattering assisted injection and extraction based terahertz quantum cascade laser," *Journal of Applied Physics* **111**(7), 073111 (2012).

[24] L. Bosco, M. Franckié, G. Scalari, M. Beck, A. Wacker, and J. Faist, "Thermoelectrically cooled THz quantum cascade laser operating up to 210 K," *Applied Physics Letters* **115**(1), 010601 (2019).

[25] S. Fathololoumi, E. Dupont, C. W. I. Chan, Z. R. Wasilewski, S. R. Laframboise, D. Ban, A. Mátyás, C. Jirauschek, Q. Hu, and H. C. Liu, "Terahertz quantum cascade lasers operating up to∼

200 K with optimized oscillator strength and improved injection tunneling," *Optics Express* **20**(4), 3866-3876 (2012).

[26] A. Khalatpour, A. K. Paulsen, C. Deimert, Z. R. Wasilewski, and Q. Hu, "High-power portable terahertz laser systems," *Nature Photonics* **15**(1), 16-20 (2021).

[27] M. Razeghi, Q. Y. Lu, N. Bandyopadhyay, W. Zhou, D. Heydari, Y. Bai, and S. Slivken, "Quantum cascade lasers: from tool to product," *Optics Express* **23**(7), 8462-8475 (2015).

[28] S. Rassel, C. Xu, S. Zhang, and D. Ban, "Noninvasive blood glucose detection using a quantum cascade laser," *Analyst*, **145**(7), 2441 (2020).

[29] L. J. Mawst and D. Botez, "High-Power Mid-Infrared (λ~ 3-6 μm) Quantum Cascade Lasers," *IEEE Photonics Journal* **14**(1), 1-25, (2021).

[30] A. Tsekoun, R. Go, M. Pushkarsky, M. Razeghi, and C. K. N. Patel, "Improved performance of quantum cascade lasers through a scalable, manufacturable epitaxial-side-down mounting process," *Proceedings of the National Academy of Sciences* **103**(13), 4831-4835 (2006).

[31] F. Wang, S. Slivken, D. H. Wu, Q. Y. Lu, and M. Razeghi, "Continuous wave quantum cascade lasers with 5.6 W output power at room temperature and 41% wall-plug efficiency in cryogenic operation," *AIP Advances* **10**(5), 055120 (2020).

[32] Y. Sin, Z. Lingley, M. Brodie, B. Knipfer, C. Sigler, C. Boyle, J. D. Kirch, K. Oresick, H. Kim, D. Botez, L. J. Mawst, D. Lindberg, and T. Earles, "Catastrophic degradation in high-power buried heterostructure quantum cascade lasers." *CLEO: Science and Innovations* (pp. SW3N-3). Optical Society of America (2019).

[33] A. Evans, S. R. Darvish, S. Slivken, J. Nguyen, Y. Bai, and M. Razeghi, "Buried heterostructure quantum cascade lasers with high continuous-wave wall plug efficiency," *Applied physics letters* **91**(7), 071101 (2007).

[34] M. Tonouchi, "Cutting-edge terahertz technology," *Nature photonics* **1**(2), 97-105 (2007).

[35] A. Y. Pawar, D. D. Sonawane, K. B. Erande, and D. V. Derle, "Terahertz technology and its applications," *Drug invention today* **5**(2) 157-163 (2013).

[36] S. Jung, J. H. Kim, Y. Jiang, K. Vijayraghavan, and M. A. Belkin, "Terahertz difference-frequency quantum cascade laser sources on silicon," *Optica* **4**(1), 38-43 (2017).

[37] M. Wienold, B. Röben, L. Schrottke, R. Sharma, A. Tahraoui, K. Biermann, and H. T. Grahn, "High-temperature, continuous-wave operation of terahertz quantum-cascade lasers with metal-metal waveguides and third-order distributed feedback," *Optics Express* **22**(3), 3334-3348 (2014).

[38] B. S. Williams, S. Kumar, Q. Hu, and J. L. Reno, "Operation of terahertz quantum-cascade lasers at 164 K in pulsed mode and at 117 K in continuous-wave mode," *Optics Express* **13**(9), 3331-3339 (2005).

[39] D. R. Lide, "CRC Handbook of Chemistry and Physics 85th Ed CRC Press," *Boca Raton* (2004): 8-141. (pp. 2296-2314)

[40] R. O. Carlson, G. A. Slack, and S. J. Silverman, "Thermal Conductivity of GaAs and $GaAs_{1-x}P_x$ Laser Semiconductors," *Journal of Applied Physics* **36**(2), 505-507 (1965).

[41] J. S. Blakemore, "Semiconducting and other major properties of gallium arsenide," *Journal of Applied Physics* **53**(10), R123-R181 (1982).

[42] M. Soltanolkotabi, G. L. Bennis, and R. Gupta, "Temperature dependence of the thermal diffusivity of GaAs in the 100–305 K range measured by the pulsed photothermal displacement technique," *Journal of Applied Physics* **85**(2), 794-798 (1999).

[43] C. J. Glassbrenner and G. A. Slack, "Thermal conductivity of silicon and germanium from 3 K to the melting point," *Physical Review* **134**(4A), A1058 (1964).

[44] A. S. Okhotin, A. S. Pushkarskij, and V. V. Gorbachev, "Thermophysical properties of semiconductors," (1972).

[45] G. A. Slack, R. A. Tanzilli, R. O. Pohl, and J. W. Vandersande, "The intrinsic thermal conductivity of AlN," *Journal of Physics and Chemistry of Solids* **48**(7), 641-647 (1987).

[46] E. R. Dobrovinskaya, L. A. Lytvynov, and V. Pishchik, "Sapphire: material, manufacturing, applications," *Springer Science & Business Media* (2009).

[47] S. Barman and G. P. Srivastava, "Temperature dependence of the thermal conductivity of different forms of diamond," *Journal of Applied Physics* **101**(12), 123507 (2007).

[48] A. C. Victor, "Heat capacity of diamond at high temperatures," *The Journal of Chemical Physics* **36**(7), 1903-1911 (1962).

[49] K. S. Pitzer, "The heat capacity of diamond from 70 to 300 K," *The Journal of Chemical Physics* **6**(2), 68-70 (1938).

[50] T. L. Bergman, F. P. Incropera, D. P. Dewitt, and A. S. Lavine, "Fundamentals of heat and mass transfer," *John Wiley & Sons* (2011).

[51] M. S. Vitiello, G. Scamarcio, and V. Spagnolo, "Temperature dependence of thermal conductivity and boundary resistance in THz quantum cascade lasers," *IEEE Journal of Selected Topics in Quantum Electronics*, **14**(2), 431-435 (2008).

[52] S. Mei and I. Knezevic, "Thermal conductivity of III-V semiconductor superlattices," *Journal of Applied Physics* **118**(17), 175101 (2015).

[53] W. S. Capinski, H. J. Maris, T. Ruf, M. Cardona, K. Ploog, and D. S. Katzer, "Thermal-conductivity measurements of GaAs/AlAs superlattices using a picosecond optical pump-and-probe technique," *Physical Review B* **59**(12), 8105 (1999).

[54] S. Fathololoumi, E. Dupont, D. Ban, M. Graf, S. R. Laframboise, Z. R. Wasilewski, and H. C. Liu, "Time-resolved thermal quenching of THz quantum cascade lasers," *IEEE J. Quantum Electron.* **46**(3), 396-404 (2010).

[55] S. Wang, C. Xu, F. Duan, B. Wen, S. S. Rassel, M. C. Tam, Z. Wasilewski, L. Wei, and D. Ban, "Thermal dynamic imaging of mid-infrared quantum cascade lasers with high temporal–spatial resolution." *Journal of Applied Physics* **128**(8), 083106 (2020).

[56] D. H. Olson, J. L. Braun, and P. E. Hopkins, "Spatially resolved thermoreflectance techniques for thermal conductivity measurements from the nanoscale to the mesoscale," *Journal of Applied Physics* **126**(15), 150901 (2019).

[57] P. K. Chan, K. P. Pipe, J. J. Plant, R. B. Swint, and P. W. Juodawlkis, "Temperature mapping and thermal lensing in large-mode, high-power laser diodes," *Applied Physics Letters* **89**(20), 201110 (2006).

[58] D. Pierścińska, "Thermoreflectance spectroscopy—Analysis of thermal processes in semiconductor lasers," *Journal of Physics D: Applied Physics* **51**(1), 013001 (2017).

[59] P. Jiang, X. Qian, and R. Yang, "Tutorial: Time-domain thermoreflectance (TDTR) for thermal property characterization of bulk and thin film materials," *Journal of Applied Physics* **124**(16), 161103 (2018).

[60] J. L. Braun, D. H. Olson, J. T. Gaskins, and P. E. Hopkins, "A steady-state thermoreflectance method to measure thermal conductivity," *Review of Scientific Instruments*, **90**(2), 024905 (2019).

[61] T. Favaloro, J. H. Bahk, and A. Shakouri, "Characterization of the temperature dependence of the thermoreflectance coefficient for conductive thin films," *Review of Scientific Instruments* **86**(2), 024903 (2015).

[62] Zurich Instruments, "Principles of Boxcar Averaging", white paper released in December 2021, https://www.zhinst.com/americas/en/resources/principles-of-boxcar-averaging

[63] K. Maize and A. Shakouri, "Transient thermal imaging using thermoreflectance," in *2008 Twenty-Fourth Annual IEEE Semiconductor Thermal Measurement and Management Symposium* (IEEE, San Jose, CA, 2008), pp. 55-58.

[64] K. Yazawa, D. Kendig, and A. Shakouri, "Time-resolved thermoreflectance imaging for thermal testing and analysis," in *39th International Symposium for Testing and Failure Analysis* (ASM International, San Jose, CA, 2013), pp. 194-202.

[65] F. Duan, K. Chen, S. Wang, L. Wei, Y. Yu, and D. Ban, "Temperature profile and transient response of thermally tunable ridge waveguides with laterally sup- ported suspension," *Applied Physics Letters* **116**(1), 011102 (2020).

[66] H. Page, C. Becker, A. Robertson, G. Glastre, V. Ortiz, and C. Sirtori, "300 K operation of a GaAs-based quantum-cascade laser at $\lambda \approx 9$ μm," *Applied Physics Letters* **78**(22), 3529 (2001).

[67] M. Bugajski, T. Piwoński, D. Wawer, T. Ochalski, E. Deichsel, P. Unger, and B. Corbett, "Thermoreflectance study of facet heating in semiconductor lasers," *Materials Science in Semiconductor Processing* **9**(1), 188 (2006).

[68] N. Becher, M. Farzaneh, B. Knipfer, C. Sigler, J. Kirch, C. Boyle, D. Botez, L. J. Mawst, D. F. Lindberg, and T. Earles, "Thermal imaging of buried heterostructure quantum cascade lasers (QCLs) and QCL arrays using CCD-based thermoreflectance microscopy," *Journal of Applied Physics* **125**(3), 033102 (2019).

[69] C. A. Evans, V. D. Jovanovic, D. Indjin, Z. Ikonic, and P. Harrison, "Investigation of thermal effects in quantum-cascade lasers," *IEEE J. Quantum Electron*. **42**(9), 857 (2006).

[70] V. Spagnolo, G. Scamarcio, H. Page, and C. Sirtori, "Simultaneous measurement of the electronic and lattice temperatures in $GaAs/Al_{0.45}Ga_{0.55}As$ quantum-cascade lasers: influence on the optical performance," *Applied Physics Letters* **84**(18), 3690 (2004).

[71] V. Spagnolo, M. Troccoli, G. Scamarcio, C. Becker, G. Glastre, and C. Sirtori, "Thermal resistance and temperature characteristics of GaAs/$Al_{0.33}Ga_{0.67}As$ quantum-cascade lasers," *Applied Physics Letters* **78**(9), 1177 (2001).

[72] M. S. Vitiello, G. Scamarcio, V. Spagnolo, C. Worrall, H. E. Beere, D. A. Ritchie, C. Sirtori, J. Alton, and S. Barbieri, "Subband electronic temperatures and electron-lattice energy relaxation in terahertz quantum cascade lasers with different conduction band offsets," *Applied Physics Letters* **89**(13), 131114 (2006).

[73] Q. Zhang, F. Q. Liu, W. Zhang, Q. Lu, L. Wang, L. Li, and Z. Wang, "Thermal induced facet destructive feature of quantum cascade lasers," *Applied Physics Letters* **96**(14), 141117 (2010).

[74] D. Pierścińska, K. Pierściński, M. Płuska, G. Sobczak, A. Kuźmicz, P. Gutowski, and M. Bugajski, "Temperature induced degradation mechanisms of AlInAs/InGaAs/InP quantum cascade lasers," *Materials Research Express* **5**(1), 016204 (2018).

[75] Y. Hu, Q. Zhang, and J. Li, "The thermal failure process of the quantum cascade laser," *Optical and Quantum Electronics* **47**(10), 3419-3426 (2015).

[76] F. Xie, H. K. Nguyen, H. Leblanc, L. Hughes, J. Wang, J. Wen, D. J. Miller, and K. Lascola, "Long term reliability study and life time model of quantum cascade lasers," *Applied Physics Letters* **109**(12), 121111 (2016).

[77] D. Hathaway, M. Shahzad, T. S. Sakthivel, M. Suttinger, R. Go, E. Sanchez, S. Seal, H. Shu, A. Lyakh, "Output facet heating mechanism for uncoated high power long wave infrared quantum cascade lasers," *AIP Advances* **10**(8), 085104 (2020).

[78] N. Korner, E. Beck, A. Dommann, N. Onda, and J. Ramm, "Hydrogen plasma chemical cleaning of metallic substrates and silicon wafers," *Surface and Coatings Technology* **76**, 731-737 (1995).

[79] J. Kischkat, S. Peters, B. Gruska, M. Semtsiv, M. Chashnikova, M. Klinkmüller, O. Fedosenko, S. Machulik, A. Aleksandrova, G. Monastyrskyi, Y. Flores, and W. T. Masselink, "Mid-infrared optical properties of thin films of aluminum oxide, titanium dioxide, silicon dioxide, aluminum nitride, and silicon nitride," *Applied Optics* **51**(28), 6789-6798 (2012).

[80] M. Rösch, G. Scalari, M. Beck, and J. Faist, "Octave-spanning semiconductor laser," *Nature Photonics* **9**(1), 42-47 (2015).

[81] M. Rösch, M. Beck, M. J. Süess, D. Bachmann, K. Unterrainer, J. Faist, and G. Scalari, "Heterogeneous terahertz quantum cascade lasers exceeding 1.9 THz spectral bandwidth and featuring dual comb operation," *Nanophotonics* **7**(1), 237-242 (2018).

[82] Chao Xu, "Toward High Performance Broad-band Frequency Comb Operation of Terahertz Quantum Cascade Lasers," Ph.D. dissertation, *University of Waterloo* (2017).

[83] S. Fathololoumi, E. Dupont, S. G. Razavipour, S. R. Laframboise, G. Parent, Z. Wasilewski, H. C. Liu, and D. Ban, "On metal contacts of terahertz quantum cascade lasers with a metal–metal waveguide," *Semiconductor science and technology* **26**(10), 105021 (2011).

[84] Y. Zeng, B. Qiang, and Q. J. Wang, "Photonic engineering technology for the development of terahertz quantum cascade lasers," *Advanced Optical Materials* **8**(3), 1900573 (2020).

[85] C. M. Liu, H. W. Lin, Y. S. Huang, Y. C. Chu, C. Chen, D. R. Lyu, K. N. Chen, and K. N. Tu, "Low-temperature direct copper-to-copper bonding enabled by creep on (111) surfaces of nanotwinned Cu," *Scientific reports* **5**(1), 1-11 (2015).

[86] J. A. Wu, C. Y. Huang, W. W. Wu, and C. Chen, "Fabrication of (111)-oriented nanotwinned Au films for Au-to-Au direct bonding," *Materials* **11**(11), 2287 (2018).

[87] K. Booker, Y. O. Mayon, C. Jones, M. Stocks, and A. Blakers, "Deep, vertical etching for GaAs using inductively coupled plasma/reactive ion etching," *Journal of Vacuum Science & Technology B, Nanotechnology and Microelectronics: Materials, Processing, Measurement, and Phenomena* **38**(1), 012206 (2020).

[88] M. Volatier, D. Duchesne, R. Morandotti, R. Ares, and V. Aimez, "Extremely high aspect ratio GaAs and GaAs/AlGaAs nanowaveguides fabricated using chlorine ICP etching with N_2-promoted passivation," *Nanotechnology* **21**(13), 134014 (2010).

[89] R. Wang, P. Täschler, Z. Wang, E. Gini, M. Beck, and J. Faist, "Monolithic integration of mid-infrared quantum cascade lasers and frequency combs with passive waveguides," *ACS Photonics* **9**(2), 426-431 (2022).

[90] S. Jung, D. Palaferri, K. Zhang, F. Xie, Y. Okuno, C. Pinzone, K. Lascola, and M. A. Belkin, "Homogeneous photonic integration of mid-infrared quantum cascade lasers with low-loss passive waveguides on an InP platform," *Optica* **6**(8), 1023-1030 (2019).

[91] Y. Sun, K. Zhou, Q. Sun, J. Liu, M. Feng, Z. Li, Y. Zhou, L. Zhang, D. Li, S. Zhang, and M. Ikeda, "Room-temperature continuous-wave electrically injected InGaN-based laser directly grown on Si," *Nature Photonics* **10**(9), 595-599 (2016).

[92] D. Liang and J. E. Bowers, "Recent progress in lasers on silicon," *Nature photonics* **4**(8), 511-517 (2010).

[93] D. Pasquariello and K. Hjort, "Plasma-assisted InP-to-Si low temperature wafer bonding," *IEEE Journal of Selected Topics in Quantum Electronics* **8**(1) 118-131 (2002).

[94] A. Spott, J. Peters, M. L. Davenport, E. J. Stanton, C. D. Merritt, W. W. Bewley, I. Vurgaftman, C. S. Kim, J. R. Meyer, J. Kirch, L. J. Mawst, D. Botez, and J. E. Bowers, "Quantum cascade laser on silicon," *Optica* **3**(5), 545-551 (2016).

[95] A. Spott, E. J. Stanton, N. Volet, J. D. Peters, J. R. Meyer, and J. E. Bowers, "Heterogeneous integration for mid-infrared silicon photonics," *IEEE Journal of Selected Topics in Quantum Electronics* **23**(6), 1-10 (2017).

[96] P. Kaur, A. Boes, G. Ren, T. G. Nguyen, G. Roelkens, and A. Mitchell, "Hybrid and heterogeneous photonic integration," *APL Photonics* **6**(6), 061102 (2021).

[97] S. Jung, J. Kirch, J. H. Kim, L. J. Mawst, D. Botez, and M. A. Belkin, "Quantum cascade lasers transfer-printed on silicon-on-sapphire," *Applied physics letters* **111**(21), 211102 (2017).

[98] O. Krüger, S. Kreutzmann, D. Prasai, M. Wienold, R. Sharma, W. Pittroff, L. Weixelbaum, W. John, K. Biermann, L. Schrottke, F. Schnieder, G. Erbert, H. T. Grahn, G. Tränkle, "Epitaxial-side mounting of terahertz quantum-cascade lasers for improved heat management," *IEEE Photonics Technology Letters* **25**(16), 1570-1573 (2013).

[99] Y. Li, T. Wang, S. Zhai, J. Liu, F. Liu, and Z. Wang, "High-power epitaxial-side down mounted terahertz quantum cascade lasers," *Electronics Letters* **52**(16), 1401-1402 (2016).

[100] S. Wang, C. Xu, Z. Wasilewski, and D. Ban, "Heterogeneous integration of transfer bonded terahertz quantum cascade lasers for improved heat management and light coupling," *Optoelectronic Devices and Integration X* (Vol. 11894, pp. 158-165), SPIE, October 2021.

[101] J. Justice, C. Bower, M. Meitl, M. B. Mooney, M. A. Gubbins, and B. Corbett, "Wafer-scale integration of group III-V lasers on silicon using transfer printing of epitaxial layers," *Nature Photonics* **6**(9), 610-614 (2012).

[102] X. Sheng, C. Robert, S. Wang, G. Pakeltis, B. Corbett, and J. A. Rogers, "Transfer printing of fully formed thin-film microscale GaAs lasers on silicon with a thermally conductive interface material," *Laser & Photonics Reviews* **9**(4), L17-L22 (2015).

[103] J. Zhang, G. Muliuk, J. Juvert, S. Kumari, J. Goyvaerts, B. Haq, C. Op de Beeck, B. Kuyken, G. Morthier, D. Van Thourhout, and R. Baets, "III-V-on-Si photonic integrated circuits realized using micro-transfer-printing," *APL photonics* **4**(11), 110803 (2019).

[104] S. Fathololoumi, E. Dupont, Z. R. Wasilewski, C. W. I. Chan, S. G. Razavipour, S. R. Laframboise, S. Huang, Q. Hu, D. Ban, and H. C. Liu, "Effect of oscillator strength and intermediate resonance on the performance of resonant phonon-based terahertz quantum cascade lasers," *Journal of Applied Physics* **113**(11), 113109 (2013).

[105] D. Turčinková, G. Scalari, F. Castellano, M. I. Amanti, M. Beck, and J. Faist, "Ultra-broadband heterogeneous quantum cascade laser emitting from 2.2 to 3.2 THz," *Applied Physics Letters* **99**(19), 191104 (2011).

[106] S. Wang, C. Xu, Z. Wasilewski, and D. Ban, "Localized Facet Joule Heating of Mid-infrared Quantum Cascade Lasers," *2022 Photonics North (PN)*, IEEE, 2022.

[107] B. S. Williams, S. Kumar, H. Callebaut, Q. Hu, and J. L. Reno, "Terahertz quantum-cascade laser at λ≈ 100 μm using metal waveguide for mode confinement," *Applied Physics Letters* **83**(11), 2124-2126 (2003).

[108] Boyu Wen, "Development of Terahertz Quantum Cascade Lasers with Novel Quantum Designs," Ph.D. dissertation, *University of Waterloo* (2021).

[109] C. Xu, S. G. Razavipour, Z. Wasilewski, and D. Ban, "An investigation on optimum ridge width and exposed side strips width of terahertz quantum cascade lasers with metal-metal waveguides," *Optics Express* **21**(26), 31951-31959 (2013).

[110] F. Castellano, L. Li, E. H. Linfield, A. G. Davies, and M. S. Vitiello, "Frequency and amplitude modulation of ultra-compact terahertz quantum cascade lasers using an integrated avalanche diode oscillator," *Scientific reports* **6**(1), 1-10 (2016).

[111] B. S. Williams, S. Kumar, Q. Hu, and J. L. Reno, "High-power terahertz quantum-cascade lasers," *Electronics letters* **42**(2), 89-91 (2006).

[112] M. A. Belkin and F. Capasso, "New frontiers in quantum cascade lasers: high performance room temperature terahertz sources," *Physica Scripta* **90**(11), 118002 (2015).

[113] V. Spagnolo, A. Lops, G. Scamarcio, M. S. Vitiello, and C. D. Franco, "Improved thermal management of mid-IR quantum cascade lasers," *Journal of Applied Physics* **103**(4), 043103 (2008).

[114] V. Spagnolo, G. Scamarcio, D. Marano, H. Page, and C. Sirtori, "Thermoelastic stress in GaAs/AlGaAs quantum cascade lasers," *Applied physics letters* **82**(26), 4639-4641 (2003).

[115] B. S. Williams, "Terahertz quantum cascade lasers," Ph.D. dissertation, *MIT* (2003).

[116] S. Fathololoumi, "Terahertz Quantum Cascade Lasers: towards high performance operation," Ph.D. dissertation, *University of Waterloo* (2010).

[117] S. G. Razavipour, "Design, Analysis, and Characterization of Indirectly-pumped Terahertz Quantum Cascade Lasers," Ph.D. dissertation, *University of Waterloo* (2013).

[118] C. C. Lee, C. Y. Wang, and G. Matijasevic, "Au-In bonding below the eutectic temperature," *IEEE Transactions on components, hybrids, and manufacturing technology* **16**(3), 311-316 (1993).

[119] S. Kumar, B. S. Williams, S. Kohen, Q. Hu, and J. L. Reno, "Continuous-wave operation of terahertz quantum-cascade lasers above liquid-nitrogen temperature," *Applied Physics Letters* **84**(14), 2494-2496 (2004).

[120] H. Li, P. Laffaille, D. Gacemi, M. Apfel, C. Sirtori, J. Leonardon, G. Santarelli, M. Rösch, G. Scalari, M. Beck, and J. Faist, "Dynamics of ultra-broadband terahertz quantum cascade lasers for comb operation," *Optics Express* **23**(26), 33270-33294 (2015).

[121] D. Bachmann, N. Leder, M. Rösch, G. Scalari, M. Beck, H. Arthaber, J. Faist, K. Unterrainer, and J. Darmo, "Broadband terahertz amplification in a heterogeneous quantum cascade laser," *Optics Express* **23**(3), 3117-3125, (2015).

[122] D. Bachmann, M. Rösch, G. Scalari, M. Beck, J. Faist, K. Unterrainer, and J. Darmo, "Dispersion in a broadband terahertz quantum cascade laser," *Applied Physics Letters* **109**(22), 221107 (2016).

[123] W. Maineult, P. Gellie, A. Andronico, P. Filloux, G. Leo, C. Sirtori, S. Barbieri, E. Peytavit, T. Akalin, J. F. Lampin, and H. E. Beere, "Metal-metal terahertz quantum cascade laser with micro-transverse-electromagnetic-horn antenna," *Applied Physics Letters* **93**(18), 183508 (2008).

[124] W. J. Wan, H. Li, and J. C. Cao, "Homogeneous spectral broadening of pulsed terahertz quantum cascade lasers by radio frequency modulation," *Optics Express* **26**(2), 980-989 (2018).

Appendices

Appendix A. Fabrication Procedures of THz QCLs

Table A.1 Fabrication procedures of conventional THz QCLs structure in metal-metal waveguide on GaAs

Process steps of conventional THz QCLs structure in metal-metal waveguide on GaAs			
No.	**Step**	**Equipment Used**	**Metrology Data**
1	Cleave and clean	Solvent Bench	Acetone/IPA/Acetone/IPA
2	Bonding metal deposition (Ti/Au: 20/250 nm) on device and carriers	Evaporator: E-beam [ANGSTROM-Ebeam]	Ti/Au (20/250 nm)
3	Thermocompression Au-Au bonding between QCL device and GaAs carrier substrate via oven	Vacuum Oven	300 C, 3 Mpa, 60 min
4	Mechanical Lapping	Lapping machine	8 rpm (2 and 1/2 rounds, substrate thickness 100-120 um remained estimated)
5	Wet Chemical Etching	Wet bench with fume hood	Citric acid + hydrogen peroxide (4:1 by volume) for 4-5 hours until etch stop layer fully exposed
6	Etch stop removal by HF (49%)	HF Acids Bench [HFACID]	Concentrated HF (49%) for 60 seconds
7	Pattern for top metal	Spin Coat [REYNOLDSTECH-twincoater], UV Direct Write [HEIDELBERG-MLA], UV Resist Develop [DEVELOPUV]	Photoresist: nLof 2035
8	High doped layer removal by wet etching [H_2SO_4:H_2O_2:H_2O (1:8:160)]	Acid bench	H_2SO_4:H_2O_2:H_2O (1:8:160) for 15 seconds (50 nm etched off estimated)
9	Top metal deposition (Ti/Au: 20/250 nm) and liftoff	Evaporator: E-beam [ANGSTROM-Ebeam]	Ti/Au (20/250 nm)
11	Pattern for dry etch mask (AZP 4620)	Spin Coat [REYNOLDSTECH-twincoater], UV Direct Write [HEIDELBERG-MLA], UV Resist Develop [DEVELOPUV]	Photoresist: AZP 4620
12	GaAs/AlGaAs mesa dry etch (AZP 4620 as mask) and clean	RIE: Metals & III-V [OXFORD-metalRIE]	OPT: AlGaAs/GaAs etch (mix of Cl_2, BCl_3, and Ar)
13	BHF dip to remove post-etched residue	HF Acids Bench [HFACID]	BOE (1:10), 30 seconds
14	Backside metal deposition (Ti/Au: 20/50 nm)	Evaporator: E-beam [ANGSTROM-Ebeam]	Ti/Au (20/50 nm)
15	Cleave and packaging	Wirebonder: Manual Wedge/Ball [WESTBOND-wirebond1]	Au wire, ball/wedge bonding

Table A.2 Fabrication procedures of hybrid integration of THz QCLs on hetero substrates

Process Steps for Hetero Bonding of THz QCLs			
No.	**Step**	**Equipment Used**	**Metrology Data**
1	Pattern for contact metal	Spin Coat [REYNOLDSTECH-twincoater], UV Direct Write [HEIDELBERG-MLA], UV Resist Develop [DEVELOPUV]	Photoresist: nLof 2035
2	Contact metal deposition and liftoff process	Evaporator: E-beam [ANGSTROM-Ebeam]	Ti/Au (20/250 nm)
3	SiNx deposition for dry etch mask	ALD/PECVD Cluster [OXFORD-cluster]	SiNx: ~800 nm
4	Pattern SiNx for mesa dry etch hard mask	Spin Coat [REYNOLDSTECH-twincoater], UV Direct Write [HEIDELBERG-MLA], UV Resist Develop [DEVELOPUV], Evaporator: E-beam [ANGSTROM-Ebeam]	Photoresist: nLof 2035, Al (50 nm)
5	Etch SiNx for mesa dry etch hard mask	RIE: Metals & III-V [OXFORD-metalRIE]	OPT: SiNx etch (SF_6 only)
6	Dry etch for mesa (ridge waveguide)	RIE: Metals & III-V [OXFORD-metalRIE]	OPT: AlGaAs/GaAs etch (mix of Cl_2, BCl_3, and Ar)
7	SiNx mask removal	HF Acids Only [HFACID]	BOE (1:10), 3 min
8	Substrate thin down	Wet bench	Citric acid + hydrogen peroxide (4:1 by volume) for 12 hours to thin down GaAs substrate to ~300-350 um (etch off ~300 um)
9	Dicing and cleaving	Dicing Saw [DISCO-saw], cleaving diamond pen	2.4 × 3 mm for each die
10	Metal-metal thermocompression bonding	Die Bonder [TRESKY-diebond]	300 C, 3 Mpa, 60 min
11	Substrate liftoff process	HF Acids Only [HFACID]	Concentrated HF (49%), 3 min
12	Pattern for top metal	Spin Coat [REYNOLDSTECH-twincoater], UV Direct Write [HEIDELBERG-MLA], UV Resist Develop [DEVELOPUV]	Photoresist: nLof 2035
13	Top metal deposition and liftoff	Evaporator: E-beam [ANGSTROM-Ebeam]	Ti/Au (20/250 nm)
14	Backside metal deposition	Evaporator: E-beam [ANGSTROM-Ebeam]	Ti/Au (20/50 nm)
15	Packaging and wire-bonding	Wirebonder: Manual Wedge/Ball [WESTBOND-wirebond1]	Au wire, ball/wedge bonding

Appendix B. Process Flow of THz QCLs Hybrid Bonded on Hetero Substrate

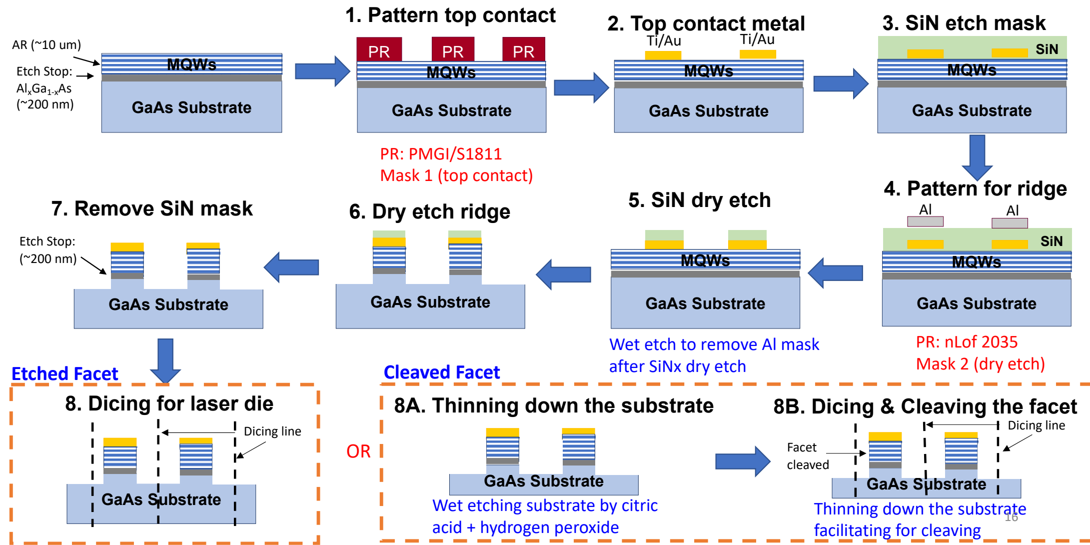

Figure B.1 Schematic diagram of the fabrication process flow of THz QCLs in hetero bonding process (1)

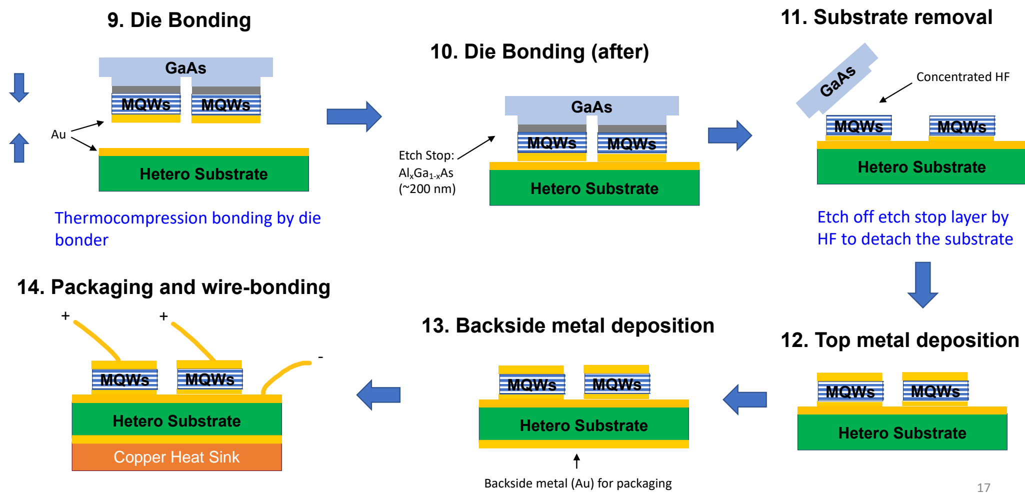

Figure B.2 Schematic diagram of the fabrication process flow of THz QCLs in hetero bonding process (2)

Appendix C. Process Flow of THz QCLs Integrated with Si Waveguide on Si Substrate

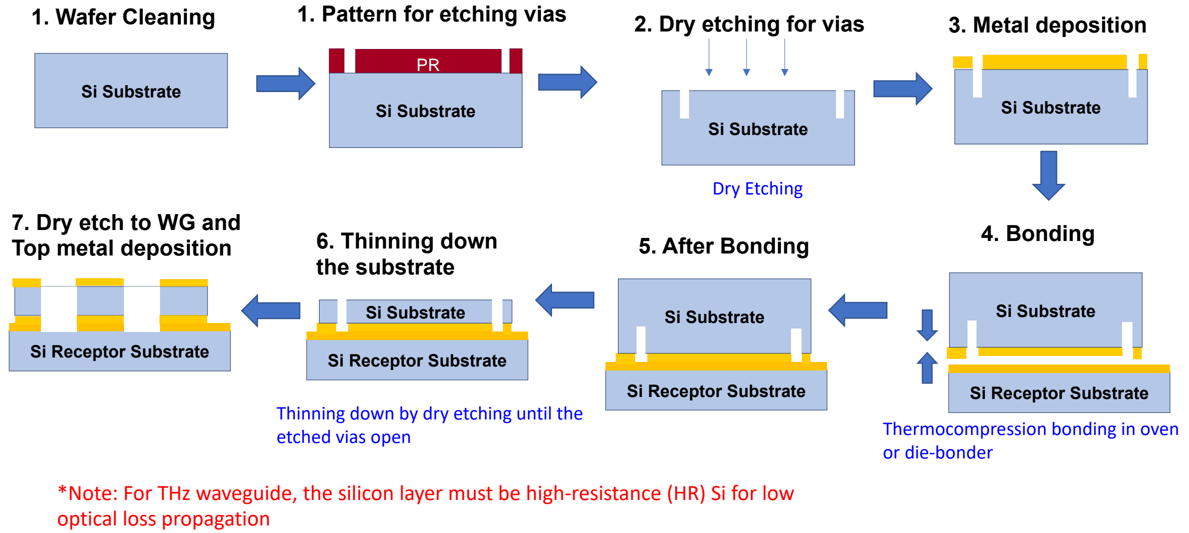

Figure C.1 Schematic diagram of process flow (1): Si Waveguide on Si

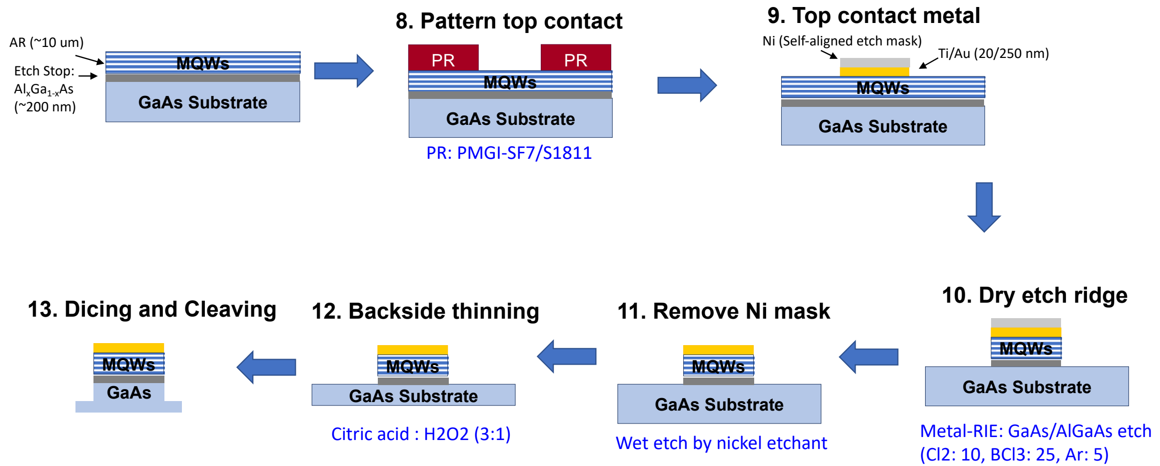

Figure C.2 Schematic diagram of process flow (2): Fabrication of THz QCL

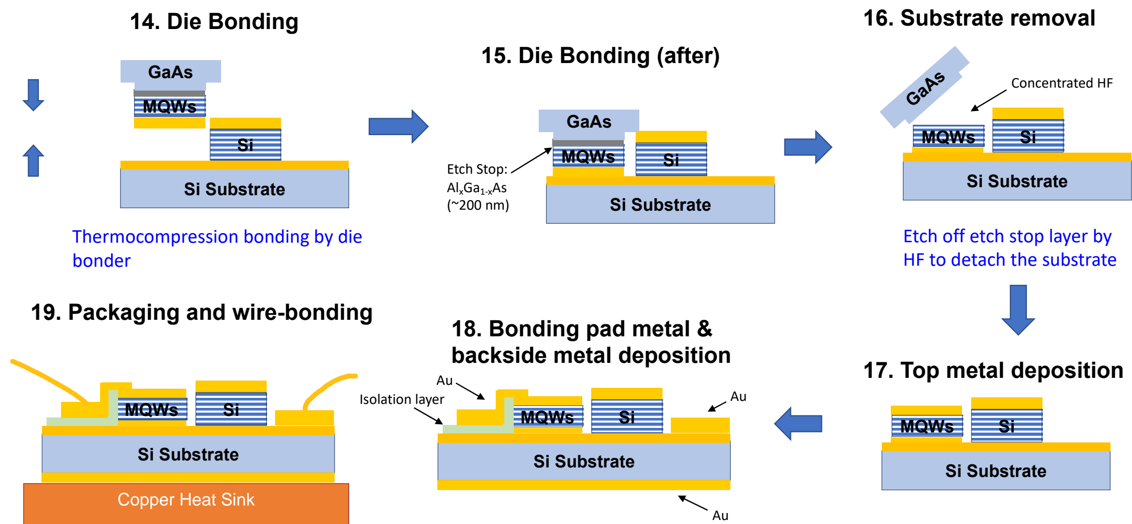

Figure C.3 Schematic diagram of process flow (3): Transfer THz QCL on Si

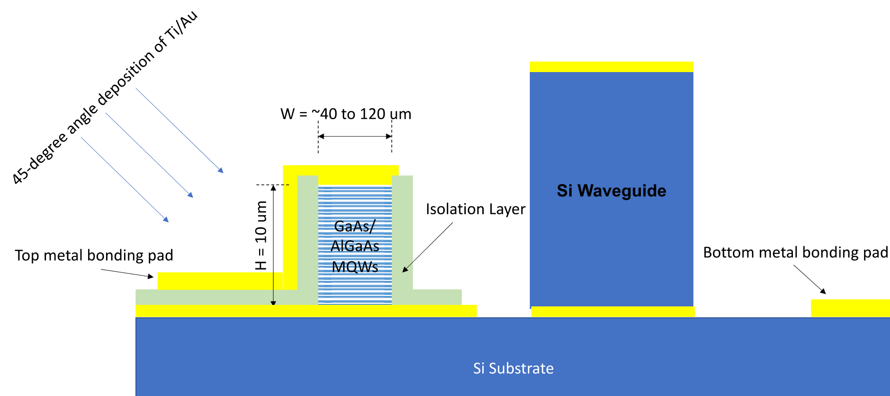

Figure C.4 Schematic diagram of the cross-section view of the device

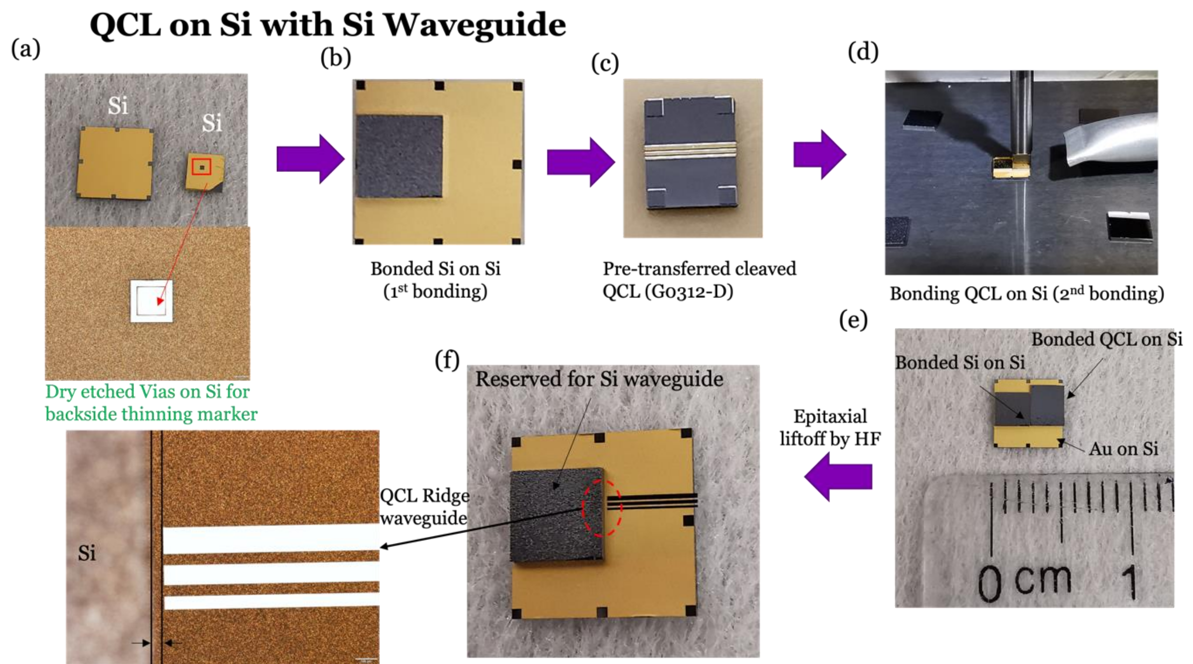

Figure C.5 Fabrication process for QCL on Si with Si Waveguide

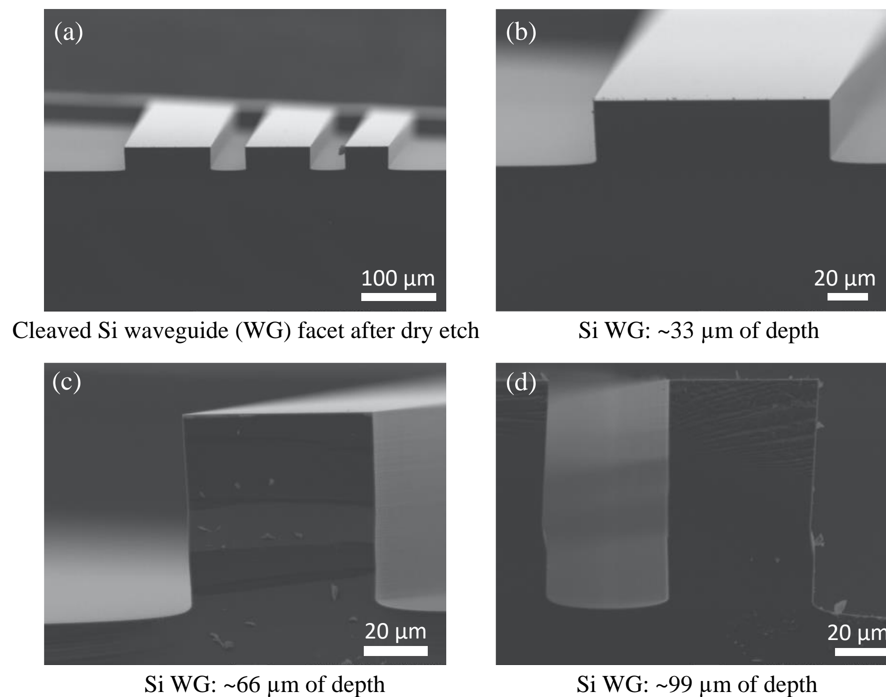

Figure C.6 Dry-etched Si ridge waveguide with cleaved facet for integration in different ridge height (etch-depth)

Appendix D. Wafer Growth Sheet

Table D.1 Wafer# G0241 (MIR QCLs) Growth Sheet

Repeats	Comment	Material	x	Thickness [Å]	doping N [cm^{-3}]	reps
	N+ 2-3 E18 GaAs substrate					
	Emitter Contact (ground)	GaAs:Si		10000	6.00E+18	
	N- GaAs cladding	GaAs:Si		35000	4.60E+16	
	thin barrier for injection	$Al_xGa_{1-x}As$	0.45	15		
		GaAs		34		
		$Al_xGa_{1-x}As$	0.45	17		
		GaAs:Si		30		
		$Al_xGa_{1-x}As$	0.45	18	3.96E+17	
		GaAs:Si		28	3.96E+17	
		$Al_xGa_{1-x}As$	0.45	20	3.96E+17	
		GaAs:Si		30	3.96E+17	
		$Al_xGa_{1-x}As$	0.45	26		
		GaAs		30		
× 36	injection Barrier	$Al_xGa_{1-x}As$	0.45	46		36
		GaAs		19		36
		$Al_xGa_{1-x}As$	0.45	11		36
		GaAs		54		36
		$Al_xGa_{1-x}As$	0.45	11		36
		GaAs		48		36
		$Al_xGa_{1-x}As$	0.45	28		36
		GaAs		34		36
		$Al_xGa_{1-x}As$	0.456	17		36
		GaAs		30		36
		$Al_xGa_{1-x}As$:Si	0.45	18	3.96E+17	36
		GaAs:Si		28	3.96E+17	36
		$Al_xGa_{1-x}As$:Si	0.45	20	3.96E+17	36
		GaAs:Si		30	3.96E+17	36
		$Al_xGa_{1-x}As$	0.45	26		36
		GaAs		30		36
	Exit Barrier	$Al_xGa_{1-x}As$	0.45	30		
	N- GaAs cladding	GaAs:Si		35000	4.60E+16	
	Collector Contact (Positive bias)	GaAs:Si		10000	6.00E+18	

Superlattice period (Å)	450	
3D Average doping (cm^{-3})	8.44E+16	
2D doping (cm^{-2})	3.80E+11	(Given)
Doping wells/barriers (cm^{-3})	3.96E+17	
Total MBE thickness (Å)	1.0648E+05	

Table D.2 Wafer# G0226 (THz QCLs) Growth Sheet

Repeats		Comment	Material	x	Thickness [Å]	doping N [cm-3]	reps
		Semi Insulating (SI) GaAs					
		Buffer	GaAs		1000	-	1
	-	Etch Stop	$Al_xGa_{1-x}As$	0.97	3000		1
	-	Positive Bias	GaAs		1000	3.00E+18	1
	-	Spacer	GaAs		200		1
C	×30	Injector Barrier, b4	$Al_xGa_{1-x}As$	0.15	55		30
		Phonon Well, w4	GaAs		184	1.70E+16	30
		Phonon Well, b3	$Al_xGa_{1-x}As$	0.15	42		30
		Lower Lasing Double Well, w3	GaAs		94		30
		Lower Lasing Double Well, b2	$Al_xGa_{1-x}As$	0.15	38		30
		Lower Lasing Double Well, w2	GaAs		105		30
		Lasing Barrier, b1	$Al_xGa_{1-x}As$	0.15	18		30
		Upper Lasing Well, w1	GaAs		120		30
B	×60	Injector Barrier, b4	$Al_xGa_{1-x}As$	0.15	55		60
		Phonon Well, w4	GaAs		184	1.70E+16	60
		Phonon Well, b3	$Al_xGa_{1-x}As$	0.15	42		60
		Lower Lasing Double Well, w3	GaAs		94		60
		Lower Lasing Double Well, b2	$Al_xGa_{1-x}As$	0.15	38		60
		Lower Lasing Double Well, w2	GaAs		113		60
		Lasing Barrier, b1	$Al_xGa_{1-x}As$	0.15	18		60
		Upper Lasing Well, w1	GaAs		113		60
C	×30	Injector Barrier, b4	$Al_xGa_{1-x}As$	0.15	55		30
		Phonon Well, w4	GaAs		184	1.70E+16	30
		Phonon Well, b3	$Al_xGa_{1-x}As$	0.15	42		30
		Lower Lasing Double Well, w3	GaAs		94		30
		Lower Lasing Double Well, b2	$Al_xGa_{1-x}As$	0.15	38		30
		Lower Lasing Double Well, w2	GaAs		105		30
		Lasing Barrier, b1	$Al_xGa_{1-x}As$	0.15	18		30
		Upper Lasing Well, w1	GaAs		120		30
A	×30	Injector Barrier, b4	$Al_xGa_{1-x}As$	0.15	55		30
		Phonon Well, w4	GaAs		184	1.70E+16	30
		Phonon Well, b3	$Al_xGa_{1-x}As$	0.15	42		30
		Lower Lasing Double Well, w3	GaAs		94		30
		Lower Lasing Double Well, b2	$Al_xGa_{1-x}As$	0.15	38		30
		Lower Lasing Double Well, w2	GaAs		115		30
		Lasing Barrier, b1	$Al_xGa_{1-x}As$	0.15	18		30
		Upper Lasing Well, w1	GaAs		110		30
	-	Injector Barrier	$Al_xGa_{1-x}As$	0.15	55		1
	-	Spacer (Fermi level adjustment)	GaAs		400	5.20E+17	1
	-	Bottom Contact A (Ground) Injection Side	GaAs:Si		500	5.00E+18	1
	-	Bottom Contact B	GaAs:Si		100	4.00E+19	1
	-	Bottom Contact C	LT GaAs		35		1

Period A (Å)	656
Period B (Å)	657
Period C (Å)	656
Requested well homogeneous doping in w4 (cm^{-3})	1.70E+16
Desired average doping (cm^{-2})	3.13E+10
Total MBE thickness (Å)	9.85E+04

Table D.3 Wafer# G0312 (THz QCLs) Growth Sheet

Repeats	Comment	Material	Thickness [Å]	doping N [cm^{-3}]	reps
	Semi Insulating (SI) GaAs				
	Buffer	GaAs	2000		
	High temp. cap	AlAs	30		
	Etch Stop	$Al_{0.97}Ga_{0.03}As$	2000		
	Positive bias	GaAs: Si	1000	5.00E+18	
	Spacer	GaAs	100		
× 222	Injector Barrier	$Al_{0.15}Ga_{0.85}As$	46		222
	Phonon Well 1_2	GaAs	49		222
	Si- Delta-doping	GaAs: Si	20	1.50E+17	222
	Phonon Well 1_1	GaAs	89		222
	Extraction Barrier	$Al_{0.15}Ga_{0.85}As$	46		222
	Well 2	GaAs	83		222
	Radiative Barrier	$Al_{0.15}Ga_{0.85}As$	31.7		222
	Well 1	GaAs	86		222
	Injection Barrier	$Al_{0.15}Ga_{0.85}As$	46		
	Phonon Well 1_2	GaAs	49		
	Si-doping	GaAs: Si	20	1.50E+17	
	Phonon Well 1_1	GaAs	89		
	Extraction Barrier	$Al_{0.15}Ga_{0.85}As$	46		
	Spacer	GaAs	100		
	Top Contact A	GaAs: Si	500	5.00E+18	
	Top Contact B	GaAs: Si	100	4.00E+19	
	Top Contact C	LT-GaAs	35		

Superlattice period (Å)	450.7
Well Doping (cm^{-3})	1.50E+17
Total MBE thickness (Å)	1.061704E+05

Table D.4 Wafer# G0405 (THz QCLs) Growth Sheet

Repeats	Comment	Material	Thickness [Å]	doping N [cm^{-3}]	reps
	Semi Insulating (SI) GaAs				
	Buffer	GaAs	2000		
	High temp. cap	AlAs	30		
	Etch Stop	$Al_{0.55}Ga_{0.45}As$	3000		
	Positive bias	GaAs: Si	1000	5.00E+18	
	Spacer	GaAs	100		
× 222	Injector Barrier	$Al_{0.15}Ga_{0.85}As$	46		222
	Phonon Well 1_2	GaAs	49		222
	Si- Delta-doping	GaAs: Si	20	1.50E+17	222
	Phonon Well 1_1	GaAs	89		222
	Extraction Barrier	$Al_{0.15}Ga_{0.85}As$	46		222
	Well 2	GaAs	83		222
	Radiative Barrier	$Al_{0.15}Ga_{0.85}As$	31.7		222
	Well 1	GaAs	86		222
	Injection Barrier	$Al_{0.15}Ga_{0.85}As$	46		
	Phonon Well 1_2	GaAs	49		
	Si-doping	GaAs: Si	20	1.50E+17	
	Phonon Well 1_1	GaAs	89		
	Extraction Barrier	$Al_{0.15}Ga_{0.85}As$	46		
	Spacer	GaAs	100		
	Top Contact A	GaAs: Si	500	5.00E+18	
	Top Contact B	GaAs: Si	100	4.00E+19	
	Top Contact C	LT-GaAs	35		

Superlattice period (Å)	450.7
Well Doping (cm^{-3})	1.50E+17
Total MBE thickness (Å)	1.071704E+05